The origin and evolution of amorphous silica coatings on young Hawaiian basalts

Thesis by

Steven Michael Chemtob

In Partial Fulfillment of the Requirements for the degree of

Doctor of Philosophy

CALIFORNIA INSTITUTE OF TECHNOLOGY

Pasadena, California

2013

(Defended November 12, 2012)

ACKNOWLEDGEMENTS

One of the most important lessons I learned over the course of my doctoral work is that science is not a solo effort. My time at Caltech has been enriched greatly by many interactions with mentors and colleagues, and to these fine scientists and people I am grateful. I first thank my advisor, George Rossman, who was an incredibly available and supportive mentor throughout my time at Caltech. George taught me the procedures for many experimental and analytical techniques, but also taught me the importance of developing a knack for improvisation. He knew when to spend hands-on time with me in the lab or on a manuscript, and when to leave me to figure something out myself. Even as my thesis evolved in new and unexpected directions away from his primary research focus, George was always willing to chat and argue about any problems I encountered or findings that excited me. I am a better scientist because of him.

I have benefitted greatly from discussions with my thesis advisory committee members, Ed Stolper, Bethany Ehlmann, and especially John Eiler, whom I credit for introducing me to the weird and wonderful world of isotope geochemistry. I also thank Woody Fischer, Paul Asimow, Oded Aharonson, and Jason Saleeby for kindness and useful discussion.

My thesis work involved learning and using a large number of laboratory and analytical techniques, which would not have been possible without generous assistance from Chi Ma, Yunbin Guan, Mike Baker, Jed Mosenfelder, and Lindsey Hedges.

I am very fortunate to have developed productive collaborations with scientists at other institutions, and appreciate their willingness to offer their time and lab resources to work on a few interesting samples from Hawaii. My interactions with Jonathan Stebbins (Stanford), Joel Hurowitz (JPL), Albert Yen (JPL), Ed Young (UCLA), Karen Ziegler (UNM), Tim Glotch (Stony Brook), Ken Hon (UH-Hilo), and Tim Orr (HVO-USGS) were all invaluable to my graduate student experience.

My personal development over the last six years took place as much outside the work sphere as inside it. My parents, Stuart and Helen Chemtob, have been a constant source of support, love, and general life advice. I'm incredibly grateful for their interest in my research and willingness to talk through matters personal and scientific. During my time in Los Angeles, music performance has become an increasingly important part of my identity, and so I thank Desiree LaVertu, Nancy Sulahian, Delores Bing, Gregg Geiger, and Grant Gershon for fostering my musical development.

Lastly, many friends have made this period of my life enjoyable and memorable. They include, but are not limited to Aaron Wolf, Gretchen Keppel-Aleks, Brian Cornelius, Melanie Channon, Megan Newcombe, the Cummingtonites (a.k.a. Alan Chapman, Andrew Matzen, & Steve Kidder), Dan and Danielle Bower, June Wicks, Meg Rosenburg and Jon Wolfe, Janet Nippell, and (especially) Kate Yandell.

ABSTRACT

Young basaltic lavas on the Big Island of Hawaii frequently feature brightly colored surface coatings. These coatings, the product of interaction of volcanically-derived acidic fluids with basaltic substrates, provide an opportunity to study the rates and mechanisms of early onset chemical weathering in a natural setting. Lava flows of various ages, from hours to ~40 years, at sites along Kilauea's southwest and east rift zones and at Mauna Loa were visited and sampled to determine the nature and extent of this alteration phenomenon. The coatings are composed of a layer of amorphous silica, 1–80 μm thick, capped in some cases by a 1 μm layer of Fe-Ti oxide. Raman, infrared, and ^{29}Si nuclear magnetic resonance (NMR) spectra indicate that the coating is structurally identical to hydrous silica gel and contains unusually high structural Si-OH contents for a natural silica sample (5.4 wt% as H_2O). Opaque coatings were observed on surfaces as young as one year old, and incipient siliceous alteration was observed to begin within days. Coating thickness varies with flow age, proximity to acid sources such as volcanic plumes emanating from Kilauea Caldera and Pu'u O'o, and climate. Coatings form preferentially on lavas with glassy surface layers, such as dense pahoehoe and spatter ramparts.

The silicon isotope compositions of silica coatings and basalts were measured to determine the degree of Si mobility during coating formation. Coatings are enriched in ^{30}Si/^{28}Si by 1–1.5‰ relative to their basalt substrates. This fractionation is opposite in direction to that previously reported for opal precipitation, suggesting that aqueous Si speciation may strongly affect the sign and magnitude of the fractionation factor. Experiments in which fresh basalt glass was partially dissolved in dilute hydrochloric or hydrofluoric acid reproduced Hawaiian silica coating morphologies. Fluids collected from all experiments displayed δ^{30}Si fractionations, but the direction of fractionation depended on fluid chemistry.

The morphologic, spectroscopic and geochemical observations presented here are most consistent with a dissolution-reprecipitation mechanism for silica coating formation. Acidic solutions dissolved near-surface basalt, then precipitated *in situ* a portion of the dissolved Si as amorphous silica.

TABLE OF CONTENTS

LIST OF FIGURES AND TABLES

Chapter II

Chapter III

Chapter IV

Chapter V

Chapter I. Introduction

Chemical weathering is a ubiquitous process that exerts a fundamental control on the chemistry, morphology, and mineralogy of landscapes. These controls are observed or inferred to operate at a number of physical scales, from molecular-scale processes of mineral breakdown and replacement, to meter-scale processes of soil development, to km-scale processes controlling the morphology of landforms. The minerals that form as a result of weathering are a function of the substrate composition and numerous environmental factors, including temperature, pH, water-rock ratio, and timescale of alteration. Thus, studying the properties of secondary or alteration minerals where they occur in the geologic record can help constrain past climatic and geologic conditions at the time of their formation.

The occurrence, distribution, and chemistry of secondary minerals have been used as proxies for past environmental conditions in many geologic settings. On Earth, trace element and stable isotope ratios (e.g. Ge/Si, REE, δ^{7}Li, δ^{24}Mg, δ^{30}Si) of sedimentary or metasedimentary rocks may be used to establish sediment provenance, intensity of weathering, and climatic conditions (Hamade et al., 2003; Teng et al., 2010; many others). On Mars, hydrated minerals and their distribution as identified by *in situ* instruments and orbital spectrometers have been used to reconstruct the climate, water availability, and potential habitability of the martian surface (Poulet et al., 2005; Bibring et al., 2006; Ehlmann et al., 2008; many others). However, effective use of mineralogical or geochemical proxies for ancient weathering environments requires a strong understanding of the development of those proxies during modern weathering. Thermodynamic modeling and laboratory experiments to measure weathering rates, products and geochemical fractionations are invaluable but may not match the signatures observed during *in situ* weathering (White and Brantley, 2003). Studies of weathering in modern field settings are an important complement to modeling and lab-based techniques for the establishment of effective weathering proxies.

The Hawaiian Islands are an especially instructive natural laboratory to study the rates, mechanisms, and products of chemical weathering. The Big Island of Hawaii presents a continuous record of volcanic activity from over 700,000 years ago to the present day. These volcanic products are primarily lava flows, ash deposits, and hyaloclastites dominated by tholeiitic basalt compositions. Chemical fractionation trends derived from primary igneous processes are well documented in Hawaiian lavas, but except in rare cases, these fractionations are small in magnitude compared to the range of compositions that may be accessed by secondary weathering processes. Thus, the subaerial portion of Hawaii comprises lavas with a relatively homogenous range of primary compositions but vastly varying ages and environmental conditions (i.e., annual rainfall, temperature, influence of volcanic gases). These climatic conditions have been shown to affect mineral weathering rates (Gordon, 2005). Rates of chemical weathering can be determined not only by field studies of modern weathering fluxes but also by proxy studies of flows of increasing age. Additionally, active volcanic landscapes like Hawaii feature a range of chemical environments. Weathering near Hawaiian volcanic vents may be dominated by sulfuric, hydrochloric and hydrofluoric acids, instead of carbonic and organic acids that drive most terrestrial weathering. Therefore, the effects of fluid chemistry on weathering rates and alteration mineralogy can be observed directly.

This thesis is focused on understanding one particular weathering phenomenon observed on the Big Island of Hawaii. Young basalts frequently feature brightly colored white, blue, yellow, red, or orange surface coatings[1] composed primarily of amorphous silica. In this work, opaque coatings were observed on lava surfaces as young as one year old, and incipient alteration was observed to begin within hours or days. As highly visible natural phenomena on lava flows at one of the most active and famous volcanoes on Earth, silica coatings are of potential interest to a broad range of visitors to the island. The coatings provide a context to study the early onset of basaltic glass dissolution and alteration in a natural setting. The mechanisms and rates of glass dissolution are important for understanding many geologic settings, including both subaerial and oceanic environments, as well as for many industrial and material science applications and issues related to long-term storage of toxic waste.

The study of Hawaiian alteration processes may also provide special insight on chemical weathering on Mars. Hawaii has long been considered a potentially viable analog for Mars because of its dominantly basaltic composition and acid-sulfate driven weathering processes. Opaline silica has been identified on Mars by both *in situ* and orbital measurements (Squyres et al., 2008; Milliken et al., 2008) and is one of a number

---

[1] A note: Throughout this thesis, I refer to the brightly colored silica-rich alteration layers on the surfaces of Hawaiian basalt flows as "coatings." I use this term for these materials partly in deference to past literature on the topic (Farr and Adams, 1984; Curtiss et al., 1985; Dorn, 1998; Minitti et al., 2007) and partly because it aptly describes their macroscopic morphological appearance. In calling the silica layers "coatings," I do not intend to imply a particular process for their formation. Indeed, the preponderance of evidence presented in this document suggests that the "coatings" are residual products of leaching, rather than externally deposited material.

of identified hydrated minerals that suggest a warmer and wetter climate early in martian history. Understanding the formation of silica deposits in a terrestrial environment may constrain the formation conditions for martian silica. Additionally, thin coatings may substantially alter the spectroscopic signature of planetary surfaces as probed by remote sensing. The spectral contributions of coated substrate rocks may be masked in visible/near-infrared reflectance spectra for coatings as thin as 2–3 µm (Minitti et al., 2007) and in thermal infrared spectra for coatings as thin as 5–10 µm (Kraft et al., 2003). Thus, effective interpretation of Mars orbital datasets depends on understanding the factors that control the distribution of alteration coatings.

The following four chapters comprise an integrated effort to understand the development and evolution of silica coatings on young lava flows at Kilauea and Mauna Loa. The specific objectives of the work are to characterize the material properties of the coatings; to determine the timescale, mechanism, and environmental conditions associated with coating formation; to understand the factors controlling the heterogeneous distribution of coatings across the Hawaiian landscape; and to establish the stable isotopic signatures of coating formation. I combined field observations, laboratory experiments, and a variety of geochemical and microanalytical techniques to reconstruct the history of these materials and to achieve a mechanistic understanding of their formation.

In Chapter II, I present detailed analyses of silica coated basalts from the December 1974 flow along Kilauea's Southwest Rift Zone, the "type locality" of these coatings for my thesis. I used a variety of techniques to characterize these materials, including scanning electron microscopy (SEM), electron probe microanalysis (EPMA), Raman and infrared spectroscopy, and elemental and oxygen isotopic analysis by secondary ion mass spectrometry (SIMS). I conclude here, as in other chapters, that the coatings are residual products of near-surface basalt leaching rather than products of deposition of externally derived silica. These results were previously published in the *Journal of Geophysical Research* and are reproduced with permission.

The results from Chapter II provide a detailed picture of coating formation in a single region but do not provide strong constraints on formation timescales or the spatial distribution of coatings. In Chapter III, I expand the field observations of Chapter II to include lava surfaces of a variety of ages (several hours through 42 years) from Kilauea's southwest and east rift zones and Mauna Loa's northeast rift zone. I present detailed field and microanalytical descriptions of silica coatings at these field sites. Using this information, I determine the timescale and rates of coating formation, evaluate likely sources of the acidity fueling the chemical weathering process, assess the origins of coating heterogeneity, and illustrate the mechanism of coating formation.

Chapter IV, the product of a collaboration with Prof. Jonathan Stebbins of Stanford University, contains detailed structural characterization by ^{29}Si magic-angle spinning nuclear magnetic resonance spectroscopy (^{29}Si MAS NMR) and vibrational spectroscopy of silica coatings from Pu'u O'o and other analog amorphous silica samples. We determined that the Hawaiian silica coating sample is structurally identical to hydrous silica gel and has unusually high structural water content for a natural silica (~5.5 wt%). These results indicate complete structural resetting in the coatings relative to the basaltic substrate. The text of this chapter was previously published in *American Mineralogist* and is reproduced with permission. Prof. Stebbins performed the ^{29}Si MAS NMR measurements and wrote sections of the paper relating to NMR results; I prepared samples, performed Raman and infrared spectroscopic analyses, and wrote the introduction, methods, Raman and IR results, and discussion.

In Chapter V, I use the example of Hawaiian silica coatings and cements to address a wider issue: the silicon isotope signature of basalt weathering. Si isotopes have come into increasing prominence as a method for probing low-temperature aqueous systems, but fractionation factors are poorly constrained. We measured δ^{30}Si of silica coatings and their basalt substrates by multi-collector inductively coupled plasma mass spectrometry (MC-ICP-MS) and by SIMS to determine the isotopic fractionation associated with coating formation. We determined that silica coatings are enriched in ^{30}Si relative to their basalt substrates. This is the opposite sense of fractionation observed during clay and opal precipitation in most sedimentary systems and suggests that Si speciation may dramatically change the direction and magnitude of Si isotope fractionation. I also present the results of partial-dissolution experiments of basalt glass in HCl and HF that were conducted to replicate natural coating morphology and to explore the effects of fluid chemistry on Si isotope fractionation. These experiments produced amorphous silica alteration layers and confirmed that Si speciation changes the fractionation factor associated with weathering. These results may have important implications for the use of Si isotopes in the study of modern and ancient aqueous systems.

Works Cited

Bibring, J.-P. et al. (2006) Global mineralogical and aqueous Mars history derived from OMEGA/Mars Express data. *Science*, **312**, 400–404.

Curtiss B., J. B. Adams, and M. S. Ghiorso (1985) Origin, development and chemistry of silica-alumina rock coatings from the semi-arid regions of the island of Hawaii. *Geochimica et Cosmochimica Acta*, **49**, 49–56.

Dorn, R. I. (1998) *Rock coatings*, 444 p., Elsevier, New York.

Ehlmann, B. L., Mustard, J. F., Fassett, C. I., Schon, S. C., Head, J. W., Des Marais, D. J., Grant, J. A., and Murchie, S. L. (2008) Clay minerals in delta deposits and organic preservation potential on Mars. *Nat. Geosci.*, **1**, 355–358.

Farr, T. G., and J. B. Adams (1984) Rock coatings in Hawaii. *GSA Bulletin*, **95**, 1077–1083.

Gordon, S. J. (2005) Effect of environmental factors on the chemical weathering of plagioclase in Hawaiian basalt. *Phys. Geography*, **26**, 69–84.

Hamade, T., Konhauser, K. O., Raiswell, R., Goldsmith, S., and Morris, R. C. (2003) Using Ge/Si ratios to decouple iron and silica fluxes in Precambrian banded iron formations. *Geology*, **31**, 35–38.

Kraft, M. D., J. R. Michalski, and T. G. Sharp (2003) Effects of pure silica coatings on thermal emission spectra of basaltic rocks: considerations for Martian surface mineralogy. *Geophys. Res. Lett.*, **30**, doi:10.1029/2003GL018848.

Milliken, R. E., G. A. Swayze, R. E. Arvidson, J. L. Bishop, R. N. Clark, B. L. Ehlmann, R. O. Green, J. P. Grotzinger, R. V. Morris, S. L. Murchie, J. F. Mustard, and C. Weitz (2008) Opaline silica in young deposits on Mars. *Geology*, **36**, 847–850.

Minitti, M. E., C. M. Weitz, M. D. Lane, and J. L. Bishop (2007) Morphology, chemistry, and spectral properties of Hawaiian rock coatings and implications for Mars. *JGR*, **112**, doi:10.1029/2006JE002839.

Poulet, F., Bibring, J.-P., Mustard, J. F., Gendrin, A., Mangold, N., Langevin, Y., Arvidson, R. E., Gondet, B., and Gomez, C. (2005) Phyllosilicates on Mars and implications for early martian climate. *Nature*, **438**, 623–627.

Seelos, K. D., R. E. Arvidson, B. L. Jolliff, S. M. Chemtob, R. V. Morris, D. W. Ming, and G. A. Swayze (2009) Silica in a Mars analog environment: Ka'u Desert, Kilauea Volcano, Hawai'i. *JGR*, **115**, E00D15, doi:10.1029/2009JE003347.

Squyres, S. W., R. E. Arvidson, S. Ruff, R. Gellert, R. V. Morris, D. V. Ming, L. Crumpler, J. Farmer, D. J. Des Marais, A. Yen, S. M. McLennan, W. Calvin, J. F. Bell, III, B. C. Clark, and A. Wang (2008) Discovery of silica-rich deposits on Mars by the Spirit rover. *Science*, **320,** 1063–1067.

Teng, F.-Z., Li, W.-Y., Rudnick, R. L., and Gardner, R. (2010) Contrasting lithium and magnesium isotope fractionation during continental weathering. *EPSL*, **300**, 63–71.

Chapter II. Silica Coatings in the Ka'u Desert, Hawaii

Originally published as:
Chemtob, S. M., B. L. Jolliff, G. R. Rossman, J. M. Eiler, and R. E. Arvidson (2010) Silica coatings in the Ka'u Desert, Hawaii, a Mars analog terrain: a micromorphological, spectral, chemical and isotopic study. *Journal of Geophysical Research*, **115**, E04001, doi:10.1029/2009JE003473.

Abstract

High-silica materials have been observed on Mars, both from orbit by the CRISM spectrometer and *in situ* by the Spirit rover at Gusev Crater. These observations potentially imply a wet, geologically active Martian surface. To understand silica formation on Mars, it is useful to study analogous terrestrial silica deposits. We studied silica coatings that occur on the 1974 Kilauea flow in the Ka'u Desert, Hawaii. These coatings are typically composed of two layers: a ~10 µm layer of amorphous silica, capped by a ~1 µm layer of Fe-Ti oxide. The oxide coating is composed of ~100 nm spherules, suggesting formation by chemical deposition. Raman spectroscopy indicates altered silica glass as the dominant phase in the silica coating, and anatase and rutile as dominant phases in the Fe-Ti coating; jarosite also occurs within the coatings. Oxygen isotopic contents of the coatings were determined by secondary ion mass spectrometry (Cameca 7f and NanoSIMS). The measured values, $\delta^{18}O_{Fe\text{-}Ti} = 14.6 \pm 2.1‰$, and $\delta^{18}O_{silica} = 12.1 \pm 2.2‰$ (relative to SMOW), are enriched in ^{18}O relative to the basalt substrate. The observations presented are consistent with a residual formation mechanism for the silica coating. Acid-sulfate solutions leached away divalent and trivalent cations, leaving a silica-enriched layer behind. Micrometer-scale dissolution and reprecipitation may have also occurred within the coatings. Chemical similarities

between the Hawaiian samples and the high-silica deposits at Gusev suggest that the Martian deposits are the product of extended periods of similar acid-sulfate leaching.

1. Introduction

Surface coatings on rocks are ubiquitous on Earth, and have been observed on the surface of Mars (Christensen et al., 2004). Coatings record physical and chemical interactions between the substrate and the surrounding environment (Dorn, 1998). Silica coatings are a common type of surface deposit that forms on Earth in a variety of geologic environments through a variety of mechanisms. Most silica coatings form in semi-arid environments, such as Hawaii and the Snake River Plain (Farr and Adams, 1984), but such coatings can also form in hydrothermal and epithermal spring settings (Rodgers et al., 2002). Silica is also a common component of desert varnish (Perry et al., 2006). Documented mechanisms of silica coating formation include dissolution of wind-blown particulates and re-precipitation of silica (Curtiss et al., 1985), leaching of divalent and trivalent cations from volcanic glass (Minitti et al., 2007), growth in solution followed by gravity deposition (Darragh et al., 1966), and vapor deposition (Gu et al., 2002). The chemistry and morphology of silica deposits can be influenced by the deposition mechanism (Rodgers et al., 2002).

Coatings influence spectral measurements in remote sensing and *in situ* analyses. Thin silica coatings have been shown to mask the spectral signature of a basaltic substrate in thermal infrared analyses (Crisp et al., 1990; Kraft et al., 2003) and visible and near-infrared reflectance analyses (Abrams et al., 1991; Seelos et al., 2009). Although spectral analyses of coated surfaces can produce geologically valuable information, such as relative ages of flow surfaces (Evans et al., 1981), they may hinder understanding of the “true” substrate lithology.

Secondary silica has been predicted to be mobile on the surface of Mars, a result of alteration of olivine, pyroxene and volcanic glass (McLennan et al., 2003). Recently, those predictions have been confirmed by *in situ* observations; in particular, high-silica materials (> 90% SiO_2) thought to be the products of hydrothermal alteration have been discovered by the Spirit rover at Home Plate (Arvidson et al., 2008; Squyres et al., 2007; Squyres et al, 2008). Orbital spectra of the martian surface have also suggested the presence of secondary silica. The presence of hydrated silica-rich material, as indicated by Si-OH vibrational bands at 2.21–2.25 μm in CRISM spectra, has been confirmed in bedded units near Valles Marineris (Milliken et al., 2008) and in highland craters at Nili Fossae (Mustard et al., 2008; Ehlmann et al., 2009). Thermal Emission Spectrometer (TES) data have been used to identify two compositionally distinct surface types (Bandfield et al., 2000). Surface Type 2 (ST2) was initially modeled as an andesitic composition, but is also consistent with phyllosilicate-bearing weathered basalt (Wyatt and McSween, 2002), palagonitized basalt (Morris et al., 2003), or opaline silica-coated basalt (Kraft et al., 2003). The wide spatial domain of ST2 indicates that silica coatings may be common on the martian surface. These detections of silica imply a wet, thermally active and potentially habitable environment on the martian surface, at least in localized areas. Additionally, silica deposits may also be among the most favorable lithologies for preserving microbial fossils on Mars (Farmer and Des Marais, 1999). Understanding the nature of these coatings can provide vital information on past climatic and atmospheric conditions, as well as geologic context.

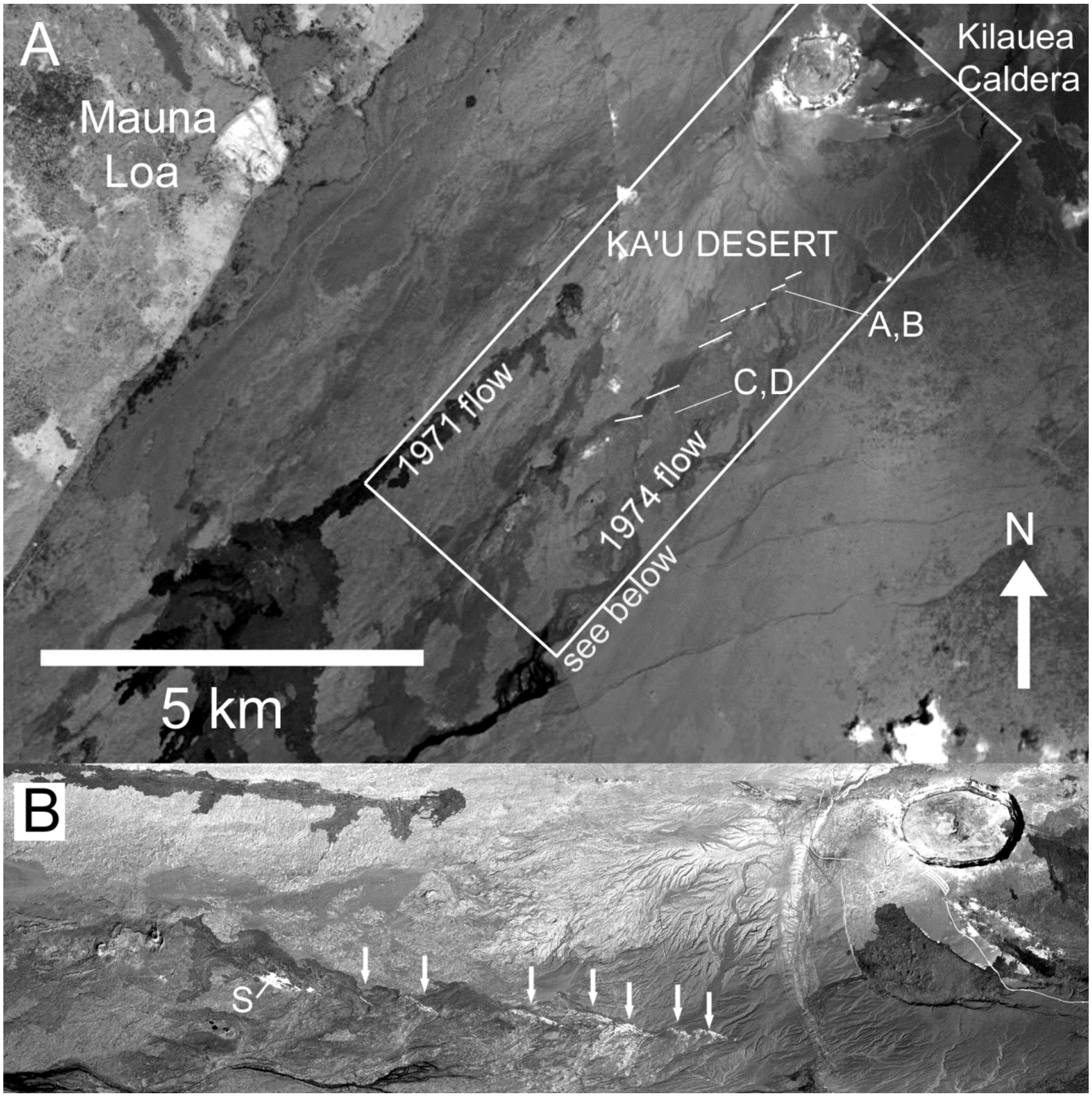

Figure 1. a) Google Earth imagery of the Ka'u Desert. A–D indicate locations of photos and hand samples shown in Figures 2a–d; red lines indicate approximate locations of 1974 flow fissure vents. b) AVIRIS false-color composite image of 1974 flow, using 1.24, 0.66 and 0.48 µm as RGB, respectively. Red arrows indicate 1974 fissure vents. "S" indicates an active solfatara, not discussed further in this paper. (Adapted from Seelos et al., 2009.)

Without sample return of high-silica materials from Mars, we rely on analog materials to better understand martian geochemical processes. Hawaii has long been considered a viable physical and chemical analog to Mars (e.g., Bell et al., 1993).

Specifically, the Ka’u Desert, on the southwestern flank of Kilauea, is a robust analog because of its young surface age and acid-sulfate driven alteration processes (Seelos et al., 2009) (**Figure 1**). In addition, Airborne Visible/Near Infrared Imaging Spectrometer (AVIRIS) has collected hyperspectral reflectance datasets of the Ka’u Desert at the same spatial resolution as CRISM, allowing for direct comparison of dataset analyses. Hawaiian silica coatings, therefore, are ideal subjects of study to understand the processes that may have occurred on Mars to produce secondary silica deposits. Previous researchers have analyzed a variety of silica coatings from all five volcanoes on the Big Island (e.g., Minitti et al., 2007; Farr and Adams, 1984; Curtiss et al., 1985). We focus on a single suite of samples from the Ka’u Desert, employing a variety of techniques for in-depth characterization of the coatings at multiple scales. These include chemical analysis, high-resolution imagery, Raman and transmission IR spectroscopic analysis, and the first (to our knowledge) oxygen isotopic measurements of Hawaiian basalt coatings. The goal of this study is to characterize these coatings, determine their formation mechanism, and describe the implications for silica mobility in the Hawaiian and martian systems.

2. Materials and Methods

This study focuses primarily on a suite of coated basalt samples from the Kilauea December 1974 pahoehoe flow, collected in the Ka’u Desert in 2002 and 2003 (**Figure 1**). This flow originated from several fissure vents near the Southwest Rift and displays heterogeneous surface morphology (Soule et al., 2004). Rock samples were collected at

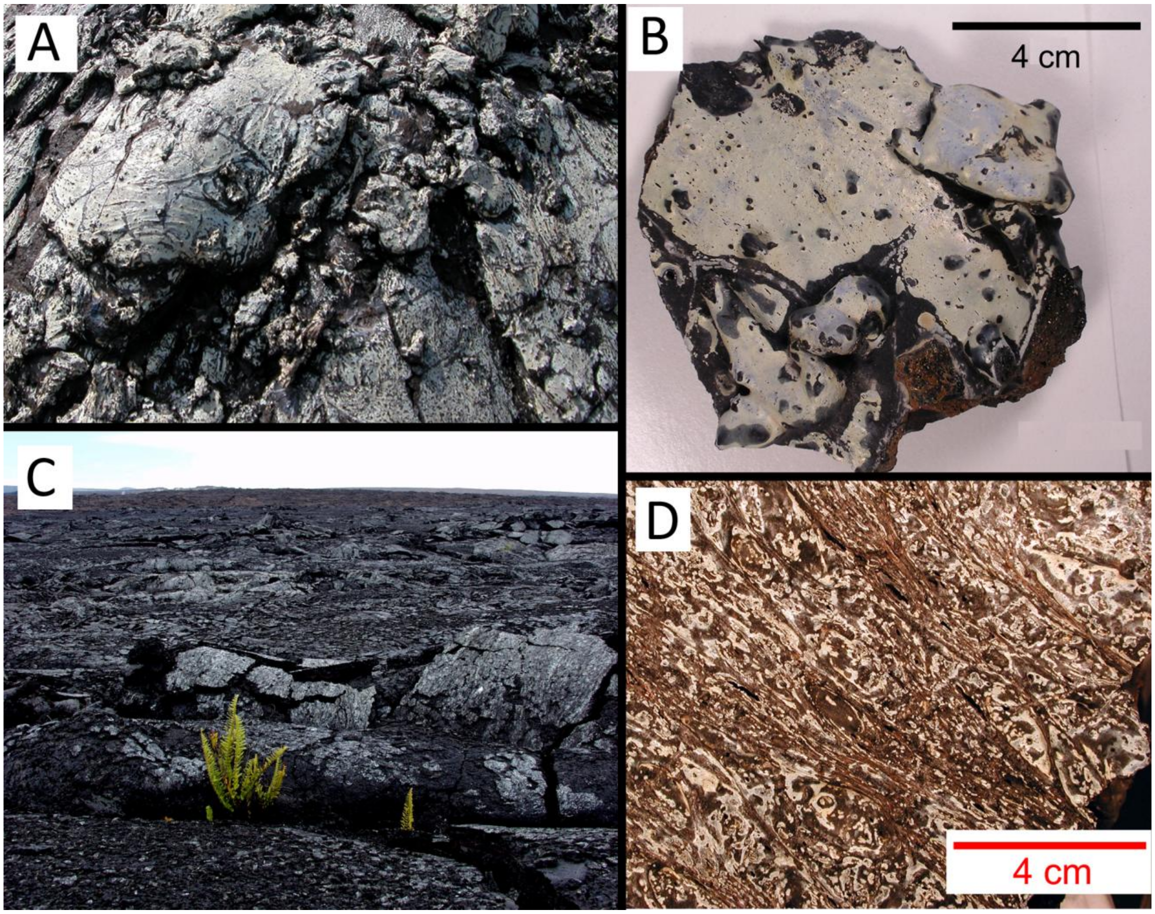

Figure 2. Macroscopic coating morphology. a) Coated spatter “pancakes” on the 1974 Kilauea flow. Field of view is ~2 m across. b) Hand sample of coated spatter rampart. Bright surface areas feature the Fe-Ti coating. c) Distal end of 1974 flow. Note that surfaces exposed by spallation appear fresh and uncoated. d) Coated sample collected on distal end of 1974 flow, on which the Fe-Ti coatings are sparser.

two sites on the 1974 flow: 1) near the fissure vents closest to Kilauea Caldera, on heavily coated spatter ramparts, and 2) close to the distal end of the flow, where the pahoehoe transitions into a’a. Additional description of Ka’u Desert collection locales can be found in Seelos et al. (2009). Additional analyses were performed on coated samples from the Mauna Ulu 1974 flow, collected just north of the Chain of Craters Road. Samples were stored at room temperature after their collection; humidity was not controlled.

Samples were analyzed by Raman spectroscopy, using a HoloLab 5000 Raman system with a 632.8 nm He-Ne laser at Washington University, and using a Renishaw M1000 micro Raman spectrometer with a 514.5 nm argon laser at Caltech. The spot size used was typically ~1 µm. Mineral identifications based on Raman spectra were performed using the Washington University Raman database and the UA-Caltech RRUFF database.

In order to determine water content and speciation within the coatings, transmission IR spectra were acquired with a Nicolet Magna-IR spectrometer at Caltech, using a liquid-N_2 cooled mercury cadmium telluride (MCT-A) detector and a KBr beamsplitter. Spectra were collected in the 2000–4000 cm^{-1} range. Wafers of coated and uncoated basalts were prepared by polishing to a thickness of 50–100 µm. Transmission spectra were acquired through the wafers, perpendicular to the basalt-coating interface.

Major and minor element compositional data was acquired by electron probe microanalysis (EPMA) using a JEOL 733 Superprobe with Advanced Microbeam Inc. automation, at Washington University. Quantitative data were acquired using wavelength dispersive spectrometry, operating at 15 kV accelerating voltage and beam currents of either 20 nA or 30 nA. Nominal spot sizes ranged from 1 to 10 µm in diameter; the smallest analytical volumes were likely around 3–4 µm across. Glasses of varying composition, including Hawaiian basalt and fused silica glass, were used for standardization. Both cross-sectional thick sections and natural flat surfaces of coated basalts were analyzed. The use of natural surfaces with irregular geometries led to occasional charging effects and low totals, but preserved the integrity of the thin, friable coatings. Additional chemical imaging was conducted by NanoSIMS at Caltech, using a duoplasmatron (O_2^-) primary beam for mapping the distribution of metals and transition metals and a Cs^+ primary beam for mapping non-metals. Backscattered electron (BSE) images were obtained both by electron microprobe and with a LEO 1550 VP field emission SEM at Caltech. Secondary electron (SE) images were also obtained by SEM at magnifications ranging from 250 to 50,000×. An Oxford Inca X-ray energy dispersive spectrometer (EDS) was used for concurrent elemental analyses.

Oxygen isotopic analyses were conducted on a Cameca 7f ion microprobe and by NanoSIMS at Caltech. A chip of the Hawaiian coating was polished at a small angle relative to the surface to expose large regions of the coating for analysis and to minimize topography on the sample surface. Analyzed standards included HSQ glass (pure SiO_2), described in Eiler et al. (1997), and laboratory silica glass. In addition, two Ti-oxide samples, a synthetic rutile from Russia and an ilmenite ore sample from Baie St. Paul, Quebec, Canada, were mounted as standards. Samples and standards were coated with 50 nm Au before analysis. Cameca 7f measurements were made with a Cs^+ primary beam, focused to a ~40 μm spot. Secondary $^{16}O^-$ and $^{18}O^-$ ions were pseudo-simultaneously measured by magnetic peak switching and with two Faraday cups. Typical count rates were around $2 \cdot 10^9$ cps for ^{16}O and $4 \cdot 10^6$ cps for ^{18}O. NanoSIMS measurements were made with a Cs^+ primary beam and a 6 μm raster size. Typical ^{16}O count rates were around $5 \cdot 10^8$ cps. The oxygen isotope compositions of the silica glass and Ti-oxide standards, as well as the bulk basaltic glass of the sample, were determined by conventional laser fluorination techniques (Valley et al., 1995).

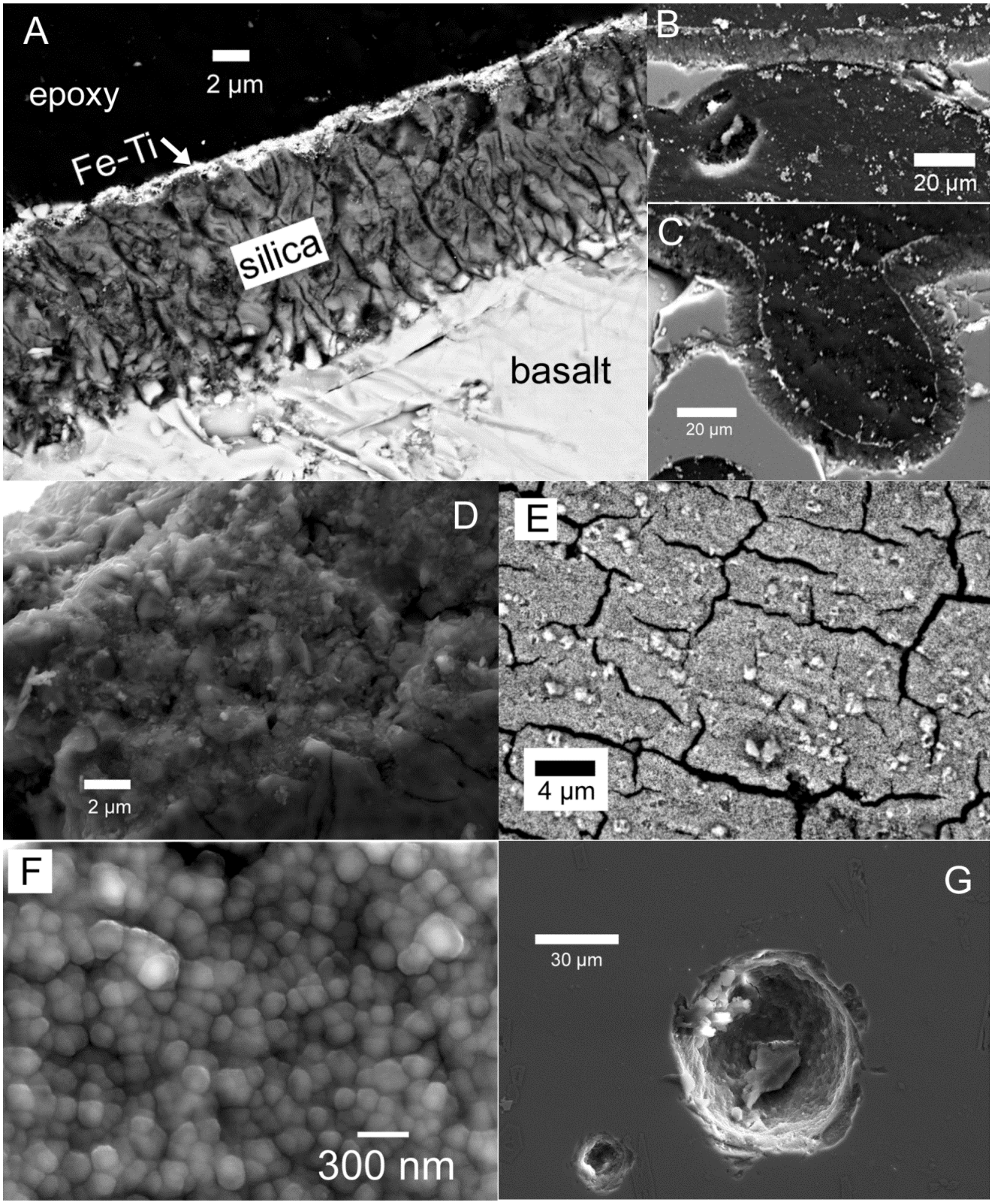

Figure 3. SEM and BSE imagery of coating morphologies. a) Backscatter electron image of typical coating morphology; unaltered basalt substrate, with a ~10 µm silica coating on top, capped by a ~1 µm Fe-Ti oxide coating. b) In places, the coating overlies near-surface vesicles, implying a residual rather than depositional formation. c) Near-surface vesicle featuring coating on all sides, again implying a residual formation mechanism. d) SE image of porous, irregular silica material. e) BSE image of natural coating surface, illustrating granular, sometimes ridged surface appearance with desiccation cracks. f) Spheroidal aggregate morphology of Fe-Ti coating on surface. g) An interior vesicle with thin (~ 1 µm) silica coating, as identified by EDS.

3. Results

3. 1. Coating Morphology

The 1974 Kilauea flow prominently features discontinuous opaque coatings, colored white, pale yellow, pale-blue or pale orange, on many subaerial surfaces within several hundred meters of the source vents. These pale surfaces correspond to the Fe- and Ti- rich coating layer, as described below. The Fe-Ti coatings cover high areal proportions of the surfaces of spatter ramparts lining the fissure vents (**Figure 2a,b**); the areal proportion of coverage drops with distance from the vents (**Figure 2c,d**). The gradient in pale coating coverage away from the fissures is manifested in remote visible/near-infrared (VNIR) images as a gradient in brightness (**Figure 1b)**. On samples where areal coverage is less than full, the pale coating appears to form primarily in topographic lows. Nearly all subaerial surfaces also feature a colorless coating layer of near-pure SiO_2 that underlies the pale, visually prominent Fe-Ti coating. These silica coatings are difficult to identify by sight in the field, but are identifiable by absorption features associated with Si-OH and H_2O fundamental and overtone vibrations in field and remote reflectance spectra (Seelos et al., 2009). In places where the glassy flow surface has cracked or spalled away by physical weathering, the exposed basalt surfaces appear fresh and uncoated (**Figure 2c**). Some leeward edges of the 1974 flow have no apparent coating, the result of abrasion by windblown ash deposits (Seelos et al., 2009) (**Figure 1b**).

SEM and BSE images of polished cross-sections of coated basalt samples indicate two prominent coating layers. A layer of amorphous silica directly overlies the basaltic glass substrate (**Figure 3a–d**). A second, thinner (< 1.5 μm) layer, not always present,

				Representative normalized endmembers	
	Basalt	**Silica coating**	**Fe-Ti coating**	**Silica coating**	**Fe-Ti coating**
SiO_2	51.87	94.87	0.88	97.36	0
TiO_2	2.48	0.19	59.44	0.19	77.05
Al_2O_3	13.3	0.12	0.02	0.12	0.02
FeO*	10.59	0.28	14.16	0.29	18.35
MnO	0.17	0.06	0	0.06	0
MgO	7.44	0.33	0.02	0.34	0.02
CaO	11.02	0.06	0.22	0.06	0.28
Na_2O	2.71	0.03	0.05	0.03	0.06
K_2O	0.47	0.03	0.02	0.03	0.02
P_2O_5	0.25	0.02	2.04	0.02	2.64
Cr_2O_3	0.06	0.04	0.03	0.04	0.04
SO_3	0.045	1.41	1.19	1.45	1.53
Total	100.405	97.44	78.07		

Table 1. Representative electron microprobe measurements of coatings on 1974 Kilauea flow. Endmember compositions are normalized to 100%; Fe-Ti normalized endmember calculated assuming zero SiO_2.

appears bright in BSE images and is composed primarily of iron-titanium oxides. The glass substrate appears physically unaltered up to the coating boundary. The silica-basalt boundary is sharp but undulating and appears to be made up of crisscrossing fractures dissecting the glass surface. This veined texture continues through the entire silica layer, and veins apparently contribute to increased porosity at the outer edges of the layer. The thickness of the silica coating of samples analyzed for this study was fairly constant around ~10 μm; other researchers have reported more variable thicknesses of 5–70 μm (Minitti et al., 2007). Although we did not collect samples with sufficient spatial resolution to characterize coating thickness gradients away from the vents in detail, analyses of samples from our two collection sites suggest that silica coating thickness is uncorrelated to the areal coverage of the Fe-Ti coating. In addition to the surface coatings, some interior vesicles, hundreds of microns below the surface and surrounded by otherwise unaltered basaltic glass, are lined with high-Si material **(Figure 3g)**.

SEM images of the coating surface and of natural broken surfaces were also collected. The coating surface is an aggregate of spherules 50–150 nm in diameter (**Figure 3e–f**). In places, these spherules congeal together into larger globules up to 1 μm across. EDS analysis of the spherules indicate high Fe and Ti content. On some coating surfaces, Ti-rich and Si-rich materials form alternating bands or lamellae. Fractures, possibly formed by shrinkage during cooling or by dessication, dissect the surface into polygonal platelets ~10 μm across **(Figure 3e**). Flecks of uncoated basaltic glass overlie the coating surface, likely ash particles post-dating the coating formation. Examination of broken surfaces of the coating indicates that the lower coating layer does not share the same spheroidal aggregate morphology. Instead, the lower layer is angular, irregular and porous (**Figure 3d**). The textural boundary likely corresponds to the compositional boundary between SiO_2-rich and Fe-Ti-rich material.

Spheroidal aggregrate morphology is commonly associated with opaline silica, but has also been observed in deposited films of anatase (Shimizu et al., 1999; Sankapal et al., 2005) and amorphous titania (Oguri et al., 1988). In opals, spheroidal aggregate morphology is observed to form in a variety of environments, including precipitates in groundwater systems, vapor deposition, and fabricated thin films (Gu et al., 2002). Although spheroidal aggregates can occur in residual environments (Rodgers et al., 2002), the texture is generally associated with depositional processes. Based on the

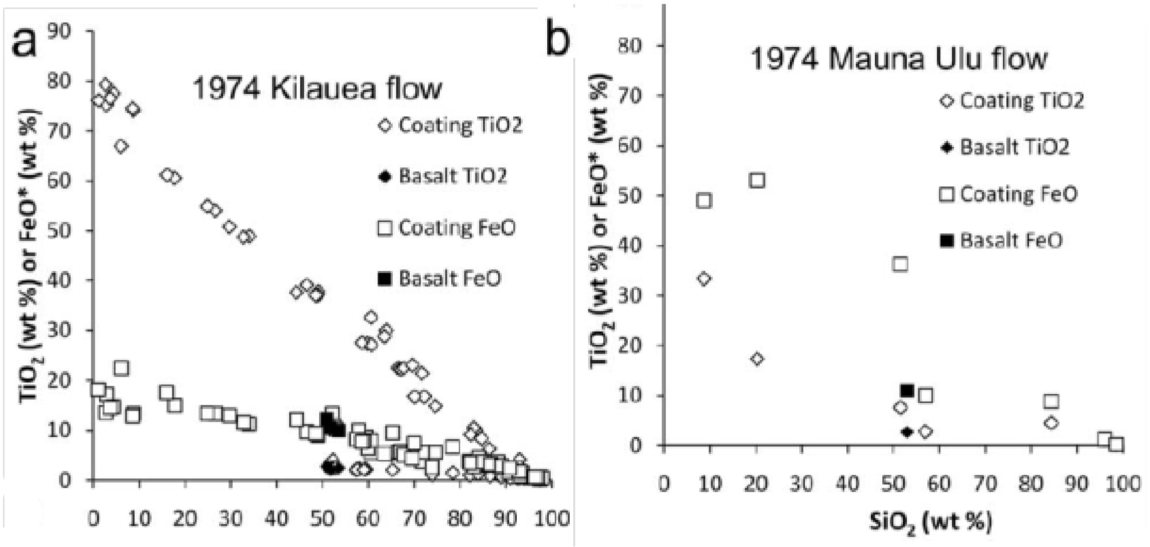

Figure 4. Compositional analyses. TiO_2 and FeO* concentrations are displayed as diamonds and squares respectively. Basalt substrate analyses are represented by filled symbols; coating analyses are open symbols. a) 1974 Kilauea flow analyses. The observed trends can be explained by two mixing trends; between basalt and silica coating endmembers, and between silica coating and Fe-Ti oxide endmembers. b) 1974 Mauna Ulu flow analyses. The Fe/Ti ratio of the Fe-Ti oxide endmember is lower and more variable than that of the Kilauea coatings.

variations in composition of the coating surface as indicated by EDS, we interpret the spheres as deposited amorphous Fe-Ti oxides. The variations in sphere size may relate to variations in water-rock ratio and other conditions of deposition.

3.2. Coating Chemistry

Electron microprobe analyses of the Ka’u Desert coatings indicate three compositional endmembers: unaltered basaltic glass, and two coating compositions (**Table 1**). The basaltic substrate is an olivine-normative tholeiite. The basaltic glass is unchanged in composition even < 2 μm from the edge of the silica coating, indicating the absence of a leaching profile at the spatial resolution of the electron microprobe. The compositions of spot analyses on the coatings are linear mixtures of two endmembers (**Figure 4a**). The opaline layer is typically 93–100 wt% SiO_2, with minor concentrations of Al_2O_3, MgO, FeO*, and CaO and enrichments in SO_3. Because the outer opaque coating layer is so thin, it was difficult to isolate it in a single beam diameter during EPMA. An ideal, SiO_2-free endmember composition was calculated as ~75% TiO_2 and ~20% FeO*, with percent-level enrichments in SO_3 and P_2O_5. This Ti/Fe ratio does not correspond to the stoichiometry of any single Fe-Ti oxide phase; it lies between pure TiO_2 and the pseudobrookite-ferropseudobrookite join. Many spot analyses of coating surfaces suffer from low totals, likely the result of non-ideal topography, porosity, and significant water content of the coating (as verified by transmission IR spectroscopy below).

EPMA traverses across the coatings reveal concentration gradients in basaltic cations (Al^{3+}, Mg^{2+}, Ca^{2+}, Na^{+}) away from the basalt-coating interface (**Figure 5**). All of these elements display similar depletion factors across the coating, leading to parallel trends on a log-scale plot of concentration. Both the opaline layer and the outer layer are enriched in S; the sulfur content of the coating increases continuously with distance from the basalt substrate, and does not vary much across the silica-TiO_2 boundary (**Figure 5**).

To test regional homogeneity of Ka’u Desert coatings, samples collected from the Mauna Ulu 1974 flow, roughly 10 km east, were also analyzed. Although the morphology of the Mauna Ulu coatings is similar to that of the Ka’u Desert coatings, their chemistry is distinct. Compositional analyses of Mauna Ulu coatings cannot be explained by mixing of two endmembers, indicating heterogeneity in the Ti/Fe ratio in the outer coating layer (**Figure 4b**). The Ti/Fe ratio of the outer layer is significantly lower than that of the Ka’u Desert coatings; the most Si-poor analysis featured ~35%

TiO_2 and ~50% FeO*. This ratio implies a different mineralogy, potentially a mixture of anatase and hematite.

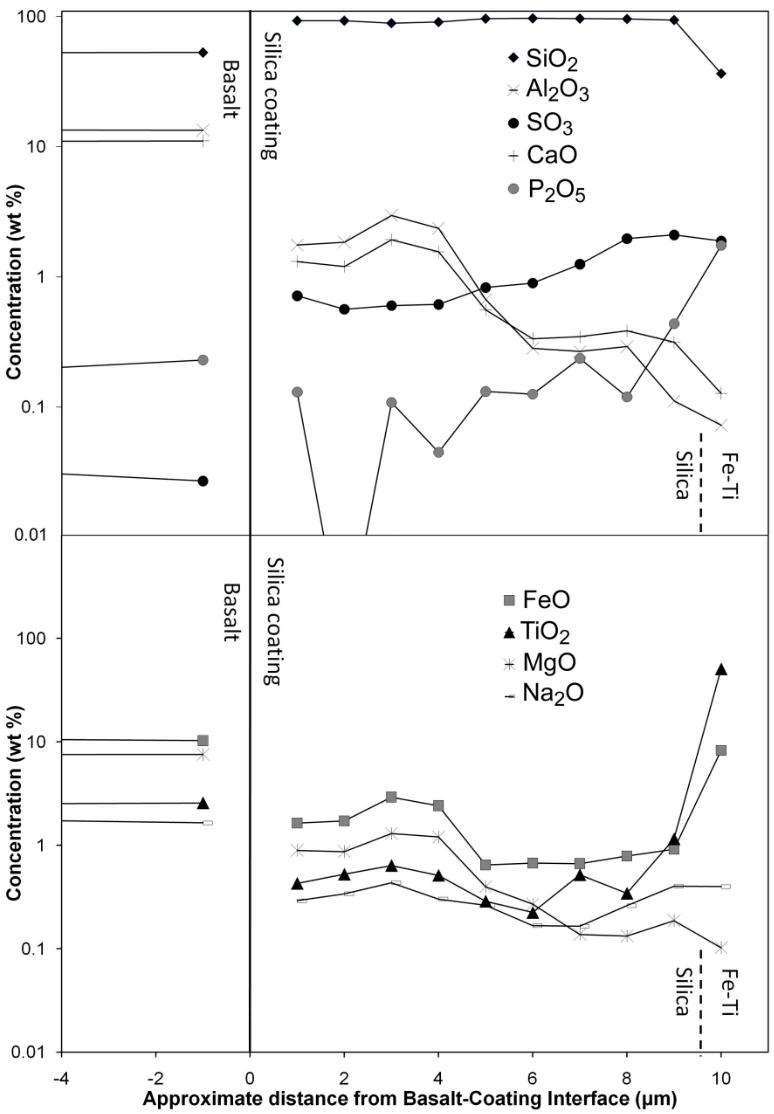

Figure 5. Microprobe traverse across cross-section of Kilauea 1974 coating, for a) SiO_2, Al_2O_3, SO_3, CaO, and P_2O_5, and b) FeO, TiO_2, MgO, and Na_2O. All analyses are normalized to 100%. Basaltic elements are depleted in the silica coating; depletion factors for each element are similar. S concentration varies smoothly through coating and increases towards Fe-Ti-rich edge.

Spatial variations in coating composition were explored by NanoSIMS mapping. Spatial resolution of images acquired with the O_2^- source was determined to be ~1 µm (**Figure 6**). The Si map confirms that the lower coating layer is enriched in Si. The intensity of the Si counts decreases with distance from the substrate, suggesting an increase in void or pore space away from the edge. Maps of Ca, Al, and Mg (not pictured), elements associated with the basaltic substrate, indicate that these elements are depleted in the coating materials.

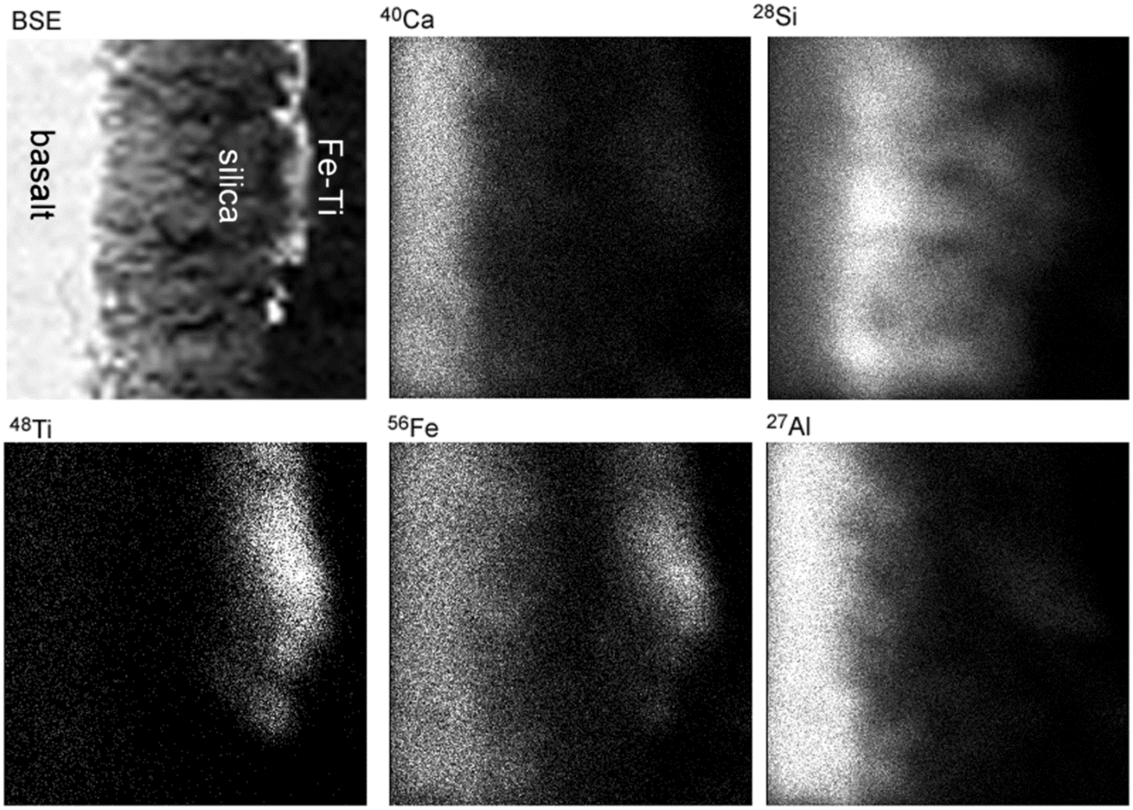

Figure 6. NanoSIMS elemental maps collected with O_2^-, with BSE image for comparison. Each map is 20 x 20 µm. Spatial resolution is ~1.5 µm.

Concentration gradients in these elements are apparent near the basalt substrate edge, corroborating EPMA traverse results (**Figure 5**); in the outer half of the silica coating layer, these basaltic elements are nearly absent. The outer coating layer is strongly enriched in Ti and Fe. The interface between the two coating layers is not sharp, but this may be an analytical artifact.

The distribution of various non-metals in the coating was determined by NanoSIMS mapping using the Cs^+ source; spatial resolution of these images was ~500 nm (**Figure 7**). Each element was ratioed to ^{16}O because oxygen concentration is roughly constant across silicates. Variations in ^{16}O intensity (not pictured) were the result of void space in the material and matrix effects. The Cs^+ maps indicate strong F

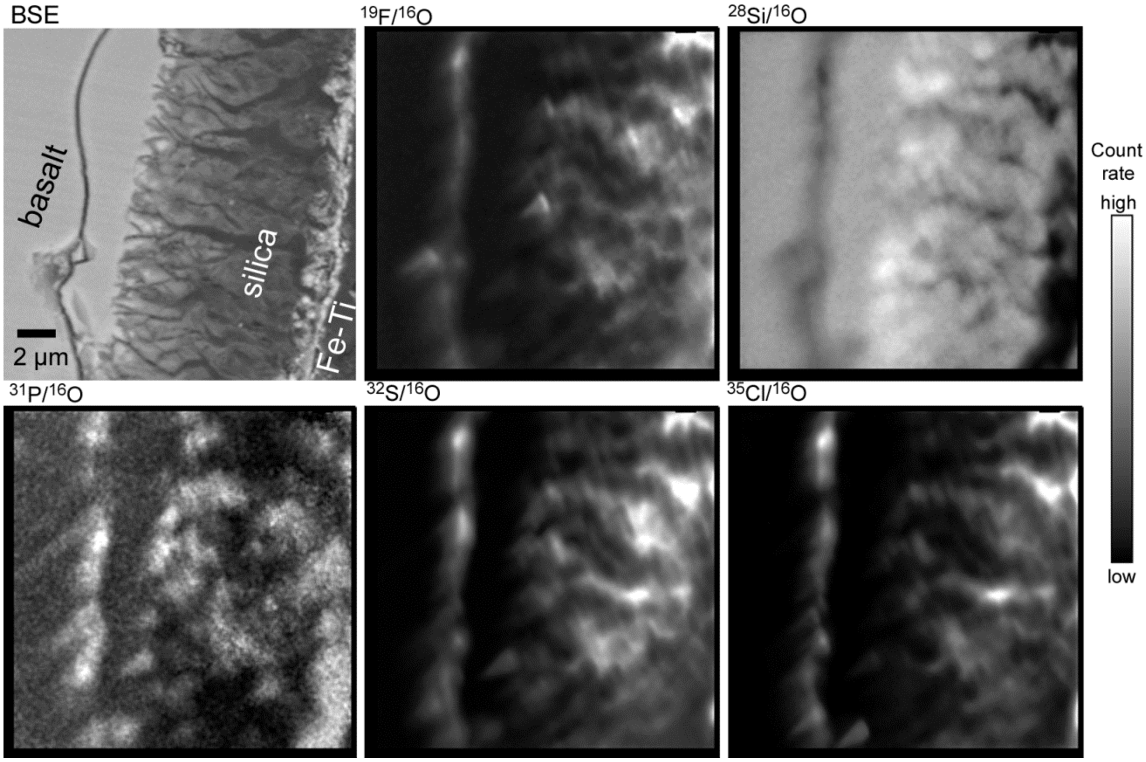

Figure 7. NanoSIMS elemental ratio maps collected with Cs^+ beam, with BSE image for comparison. Each element is ratioed to ^{16}O because oxygen concentration is roughly constant across the coating gradient. The linear feature present on the right side of each map is a crack in the basalt substrate. Each map is 20 x 20 µm; spatial resolution is ~500 nm.

enrichment in the outer, Ti-rich coating. This enrichment suggests that the deposition of the Ti-rich coating occurred in a halide-rich environment and may have involved Ti-halide complexes (Barsukova et al., 1979). Chlorine is largely absent from the outer layer; this absence could be the result of post-depositional dissolution and removal, as most chlorides are soluble. The outer coating also features enrichments in phosphorus, which commonly has limited mobility in weathering environments. Sulfur occurs only at low concentrations in the Fe-Ti coating and is instead concentrated heterogeneously within the silica layer. The relative absence of S in the outer coating suggests that S remained soluble in the solutions from which the Fe-Ti oxide was chemically

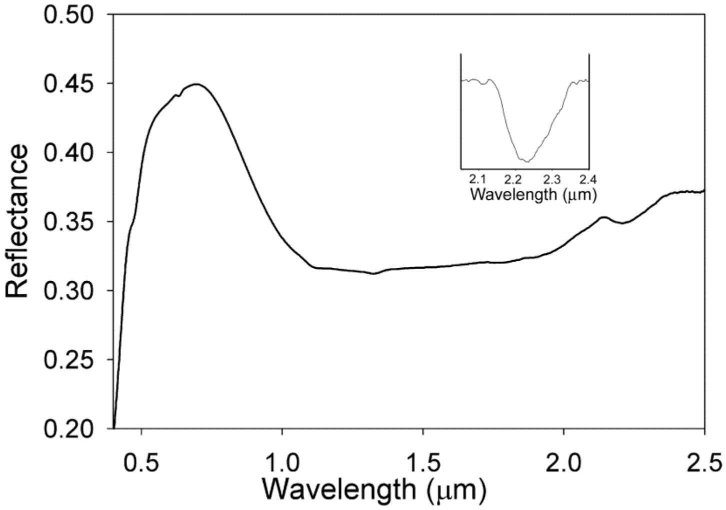

Figure 8. Reflectance spectrum of coated Kilauea basalt. Prominent spectral features include an Fe^{3+} absorption edge and an Si-OH vibrational feature at 2.23 μm indicating opaline silica. The inset shows the Si-OH feature with baseline removed. Adapted from Seelos et al. (2010).

precipitated. Sulfur hotspots may represent locations where jarosite (as identified by Raman, discussed below) is present.

3.3. Spectral Properties and Mineralogy

3.3.1. Reflectance Spectroscopy

The results of field and laboratory reflectance spectra in the visible and near-IR regions (0.4–2.5 μm) of coating samples from the Ka'u Desert are described in detail elsewhere (Seelos et al., 2010). Absorption features in these spectra include an absorption edge centered at 0.4 μm and a broad band at 1.0 μm, both the result of ferric iron in the sample. Molecular water is indicated by absorptions at 1.4 and 1.9 μm, and structural OH in opaline silica (Si-OH vibration) is indicated by a band at 2.23 μm (**Figure 8**). Thinner coating samples displayed a negative slope in reflectance towards longer wavelengths, but thick coating samples did not display this feature. This negative slope is possibly the result of absorption by the basaltic substrate underneath an optically thin coating. The spectral features described above, particularly the ferric iron absorption edge and the 2.23 μm silica absorption, are also observed in remote AVIRIS spectra of the 1974 flow (Seelos et al., 2010).

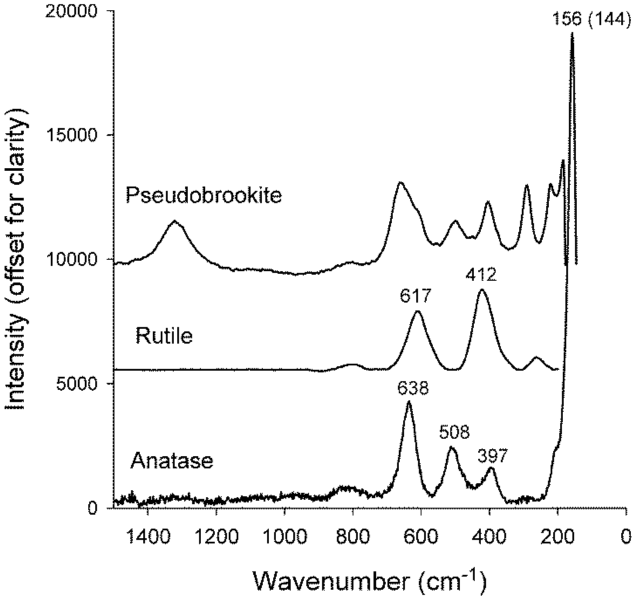

Figure 9. Selection of Raman spectra of Fe-Ti-rich coating. Definitive identifications include anatase and rutile; however, peak shifts in the spectra of both phases from previously published spectra may indicate varying degrees of crystallinity and Fe^{3+}-substitution. Another spectrum is consistent with an Fe-Ti oxide in the pseudobrookite family.

3.3.2. Raman Spectroscopy

Because the Fe-Ti coating is optically opaque at the wavelength of our Raman laser, Raman spectral analyses of the coating surface are dominated by the mineralogy of the Fe-Ti phase. Signatures of the opaline silica coating and of the unaltered basalt are masked by the strong absorptions of the titanium oxides. At least three different phases were identified in the Fe-Ti-rich layer (**Figure 9**). One spectrum is indicative of anatase, although peak positions are commonly shifted from those previously documented and calculated for pure crystalline anatase (Ohsaka et al., 1978). The intense band corresponding to the ν_6 vibrational mode, normally found at 144 cm^{-1}, is present but is cut off due to low instrument sensitivity below 150 cm^{-1}. Peaks at 397 cm^{-1}, 508 cm^{-1}, and 638 cm^{-1} correspond to the ν_4, ν_3, and ν_1 vibrational modes, respectively. The FWHMs of these peaks are larger than those of published spectra of crystalline anatase. The peak shifts and increased peak width can potentially be explained by variable degrees of crystallinity and by solid solution of Fe^{3+} in the anatase structure. Although

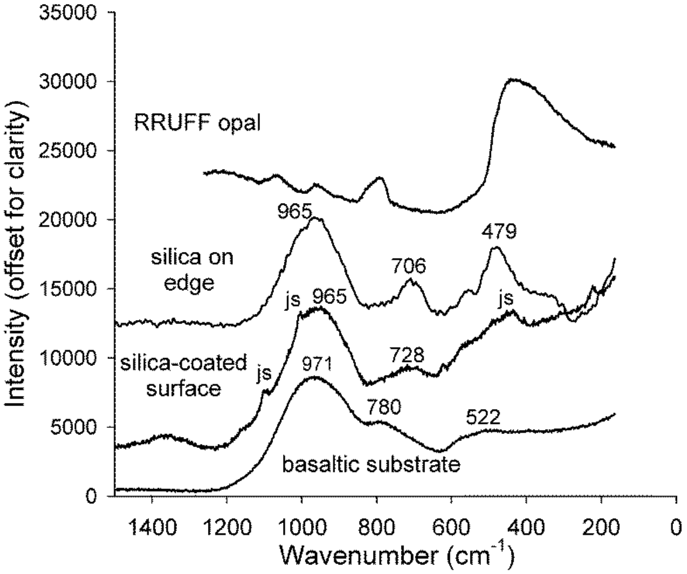

Figure 10. Selection of Raman spectra of amorphous silica coating, with an opal from the RRUFF library for comparison. Silica-rich materials are inconsistent with opal, and are most consistent with leached basaltic glass. Jarosite (js) was also detected in analyses of silica-coated surfaces (see also Figure 11).

most natural anatase samples previously analyzed include only 1–3 wt% Fe_2O_3 (Liu et al., 1992), synthetic anatases have been precipitated containing up to Fe/(Ti+Fe) 0.1 mol/mol (Schwertmann et al., 1995). Substitution of other metals for titanium in natural rutiles has been documented to shift Raman peak positions (Smith and Perseil, 1996). Charge balance is likely accomplished by substitution of hydroxyl for oxygen, in the form $Fe_xTi_{(1-x)}O_{(2-x)}(OH)_x$ (Schwertmann et al., 1995). Scraped coating shavings were analyzed by powder XRD to confirm the Raman mineral identification; weak, sharp peaks observed at $2\theta = 25.1°$ and $47.5°$ confirm the presence of crystalline, non-x-ray-amorphous anatase.

Another frequently observed surface Raman spectrum also featured the intense ν_6 band at 156 cm^{-1} associated with anatase, but had substantial peak shifts in the other TiO_2 vibrational bands (**Figure 9**). The ν_1 band normally found around 638 cm^{-1} is instead located at 617 cm^{-1}, the ν_4 band is located at 412 cm^{-1}, and the ν_3 band at 508 cm^{-1} is weak or non-existent. This spectrum is consistent with a mixture of variably crystalline anatase and rutile; amorphous titania films may contain microcrystals of rutile even when deposited at low temperature (Hsu et al., 1986). A third phase has no exact match in the RRUFF spectral library; its closest matches of the appropriate chemistry are members of the pseudobrookite group (i.e., Fe_2TiO_5).

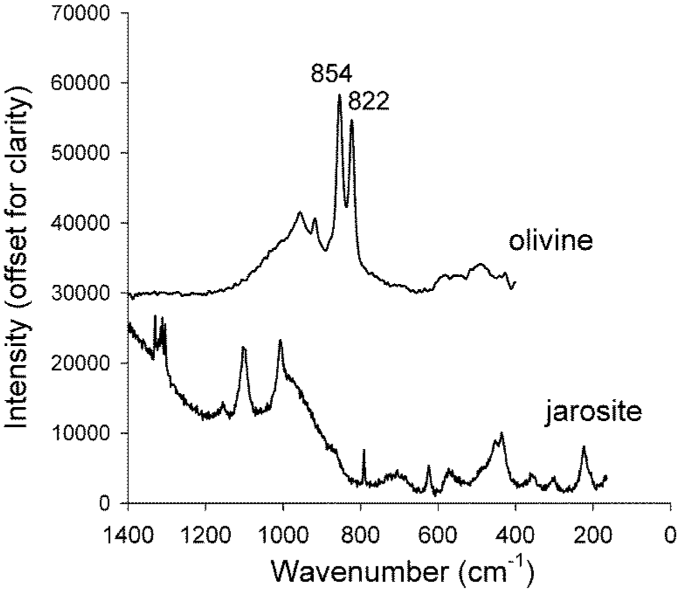

Figure 11. Raman spectra of other phases associated with the coatings. Olivine was rarely detected and may represent relict phenocrysts or occasional embedded ash particles. Jarosite was detected in association with the silica coating.

Raman spectra of the lower SiO_2-rich coating are generally characterized by broad peaks, indicating that the coating material is amorphous (**Figure 10**). However, the spectra are inconsistent with previously reported Raman spectra of common and gem-quality opals (Ilieva et al., 2007; Smallwood et al., 2007). Instead, the spectrum of the SiO_2-rich coating most resembles that of a glass (Bertoluzza et al., 1982), and bears similarities to the spectrum of the basaltic substrate. The Raman spectrum of the basaltic glass features broad peaks at 522 cm^{-1}, 780 cm^{-1}, and 971 cm^{-1}, corresponding to the O-Si-O bending mode, symmetric stretch and asymmetric stretch, respectively (McMillan, 1984) (**Figure 10**). The position of the O-Si-O asymmetric stretch in silicate glasses is a function of the degree of polymerization; the 971 cm^{-1} position, as expected, corresponds to a metasilicate composition (McMillan, 1984). In the silica coating, the asymmetric stretch band occurs around 965 cm^{-1}, rather than 1060 cm^{-1} as previously documented for silica glass. The silica coating also features shifts to lower frequencies of the dominant bending mode (479 cm^{-1}) and symmetric stretch mode (706–728 cm^{-1}). The retention of the characteristic basalt O-Si-O asymmetric stretch position in the silica coating suggests that the silica is a residual product of leaching, and that as network-modifying cations were removed, the degree of polymerization was not affected.

Some Raman spectra of silica-coated surfaces featured peaks at 1008 cm^{-1} and 1105 cm^{-1}, corresponding to a member of the jarosite subgroup (**Figure 10**). This jarosite group member was also isolated as an independent phase within the silica coating (**Figure 11**). The particular species could not be definitively determined, but the Raman spectrum is most consistent with the potassium endmember, jarosite itself. The detection of jarosite in the silica coatings is not unexpected, given the high SO_3 contents of the coating materials as determined by EPMA and common remote and *in situ* detections of jarosite in Hawaiian volcanic deposits (i.e. Morris et al., 2005, Guinness et al., 2007). The spectral signature of olivine, characterized by strong peaks at 822 cm^{-1} and 854 cm^{-1}) was also rarely detected associated with the coatings (**Figure 11**). This detection is surprising because olivine has been determined to dissolve more quickly than basaltic glass at low pH (Hausrath et al., 2008). The olivine may represent partially dissolved olivine phenocrysts, or it may derive from contamination by olivine-bearing ash.

3.3.3. Transmission IR Spectroscopy

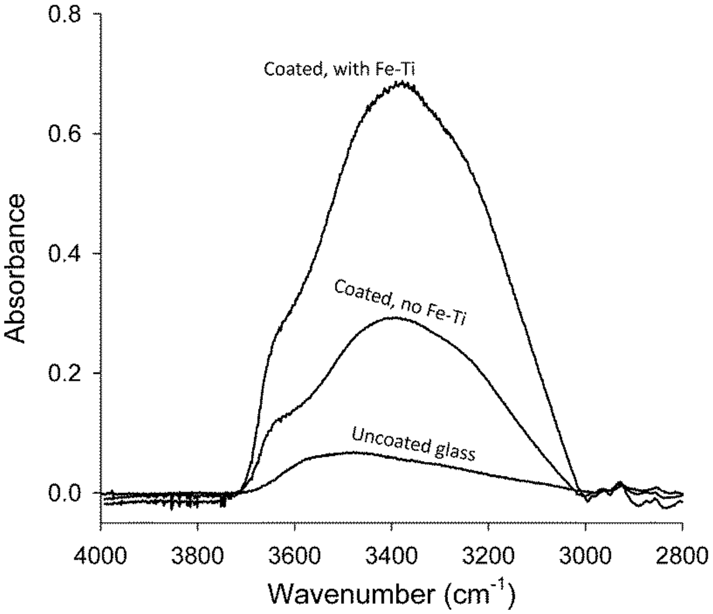

Figure 12. Transmission infrared spectra. The unaltered glass was determined to contain 0.01–0.10 wt% water. The coatings were calculated to contain 1.1–3.5% water.

Transmission spectra of uncoated basalt wafers feature an asymmetric OH fundamental vibration peak at around 3543 cm^{-1} (**Figure 12**). Based on the value 67 L·mol^{-1}·cm^{-1} for molar absorptivity of water in basaltic glass (Stolper, 1982), the water content of the basalt was determined to vary between 0.01–0.10 wt%. This water content

was judged to be sufficiently low that it would not have an interfering impact on the measurement of the coating water content. The transmission spectrum of uncoated basalt was subtracted from coated basalt spectra in proportion to the thickness of basalt for each coated wafer.

The transmission spectra of the coatings typically featured a broad, asymmetric peak centered at ~3370 cm^{-1}, with a shoulder at approximately 3635 cm^{-1} (**Figure 12**). This peak was typically well fit by the superposition of three Gaussians centered at 3230 cm^{-1}, 3413 cm^{-1} and 3633 cm^{-1}; these bands likely correspond to the first overtone of the H_2O bend, the H_2O symmetric stretch, and H_2O asymmetric stretch, respectively. Because the silica coating is so thin, attempts to quantify the proportions of H_2O and OH in the opal using the combination bands at ~4500 cm^{-1} and 5200 cm^{-1} (as in Ohlhorst et al., 2001) were unsuccessful. However, recent reports indicate that siliceous glasses hydrated at near-ambient temperature should contain little or no hydroxyl (Anovitz et al., 2008). Using the value of integrated molar absorptivity for the 3570 cm^{-1} band given for H_2O from Newman et al. (1986) (26300 ± 2200 $L \cdot mol^{-1} \cdot cm^{-2}$), water content of the coating was determined to vary between 1.1 and 3.5 wt%. Water content is a strong function of the presence or absence of a significant Fe-Ti oxide layer; analyzed spots with a pale coating layer present tended to have higher water content. This observation cannot be explained by high water contents in the Fe-Ti coating. Since the outer coating is only ~1 μm thick, explaining the excess water by assigning it to the Fe-Ti layer would require an outer coating water content of up to ~24 wt%, an unreasonable value. A more reasonable explanation is that the silica coating has dehydrated since formation, and that the outer coating layer prevented or slowed dehydration. This dehydration could have occurred in the field after coating formation or in the laboratory since collection in 2003.

3.4. Isotopic Characteristics

The oxygen isotope composition of the Fe-Ti oxide standards and the Hawaiian basalt substrate were determined via laser fluorination analysis. The measured $\delta^{18}O_{SMOW}$ values of the rutile and ilmenite were 29.7±0.3‰ and 5.8±0.22‰, respectively. The measured value of $\delta^{18}O_{SMOW}$ of the basalt substrate was 5.1±0.07‰. This value of $\delta^{18}O$ is comparable to most Hawaiian basaltic glasses (Eiler et al., 1996).

SIMS oxygen isotope analyses of Fe-Ti oxide standards were successful and reproducible with standard deviations of 0.3–0.6‰. By comparing $\delta^{18}O$ measured by

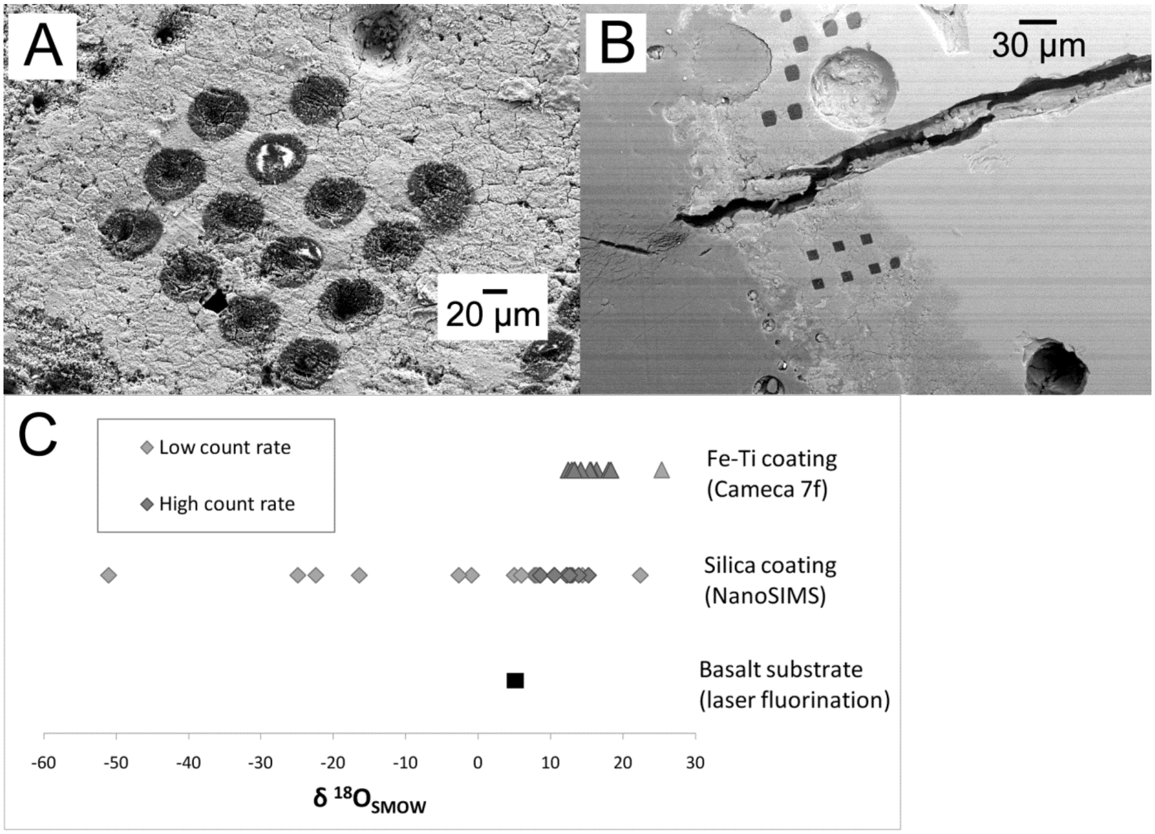

Figure 13. SIMS oxygen isotopic results. a) Cameca 7f pits on natural coated surface for analysis of Fe-Ti coating. b) NanoSIMS pits of polished section for analysis of silica coating. c) $\delta^{18}O_{SMOW}$ measurements, post-standardization. Both data sets feature a wide spread of oxygen isotopic values, but many suffer from low count rates, indicating the effects of topography. Filtering the data by count rate produces a more tightly clustered set of measurements.

laser fluorination to the SIMS analyses, instrumental mass fractionations (IMF) were calculated; for ilmenite, 1000 ln α_{SIMS} = -0.1‰, and for rutile 1000 ln α_{SIMS} = -6.2‰. This difference in IMF is likely the result of a compositional matrix effect; iron content of oxides has previously been shown to strongly influence matrix effects (Riciputi et al., 1998; Eiler et al., 1997). Assuming that the magnitude of the SIMS matrix effect in Fe-Ti oxides is, to first order, a function of composition along the $FeTiO_3$-TiO_2 join, the calculated fractionation for the composition of the Fe-Ti coating is 1000 ln α_{SIMS} = -2.1‰. NanoSIMS analysis of the silica glass standard indicated an IMF for amorphous silica of 1000 ln α_{SIMS} = 22.5‰.

Cameca 7f measurements of the Fe-Ti coating were performed on natural, unpolished coating surfaces, with a ~40 μm spot size (**Figure 13a**); NanoSIMS analyses of the silica coating were performed on polished thick sections, with a ~6 μm spot size (**Figure 13b**). SIMS and NanoSIMS analyses of the natural Hawaiian samples were commonly highly variable (**Figure 13c, Supplemental Table 1**). Most Cameca 7f IMF-corrected measurements of $\delta^{18}O$ of the Fe-Ti coating clustered around 14‰, with an outlier measurement at 25.3‰. NanoSIMS analyses of the silica coating showed a wide spread of $\delta^{18}O$ values, with a cluster around 9‰. In both datasets, outlying measurements also featured low count rates, suggesting the effects of topography (up to tens of micrometers) on the natural sample surface. Based on this observation, the datasets were filtered by minimum count rate, producing more tightly clustered values; we focus our interpretations on these clusters comprising the majority of the data.

Using the IMF previously calculated for the Fe-Ti oxide composition and the mean of the clustered data, we determine $\delta^{18}O_{SMOW}$ of the Fe-Ti coating to be 14.6±2.1‰. Similarly, we calculate the $\delta^{18}O_{SMOW}$ of the silica coating layer to be 12.1±2.2‰ (**Figure 13c**).

4. Discussion

4.1. Interpretation of Isotopic Data

4.1.1. Available Water Sources

As described above, the coating layers are progressively enriched in ^{18}O relative to the basalt substrate. The oxygen isotopic composition of the water from which the coating layers formed is unknown, but can be constrained by the $\delta^{18}O$ of available water

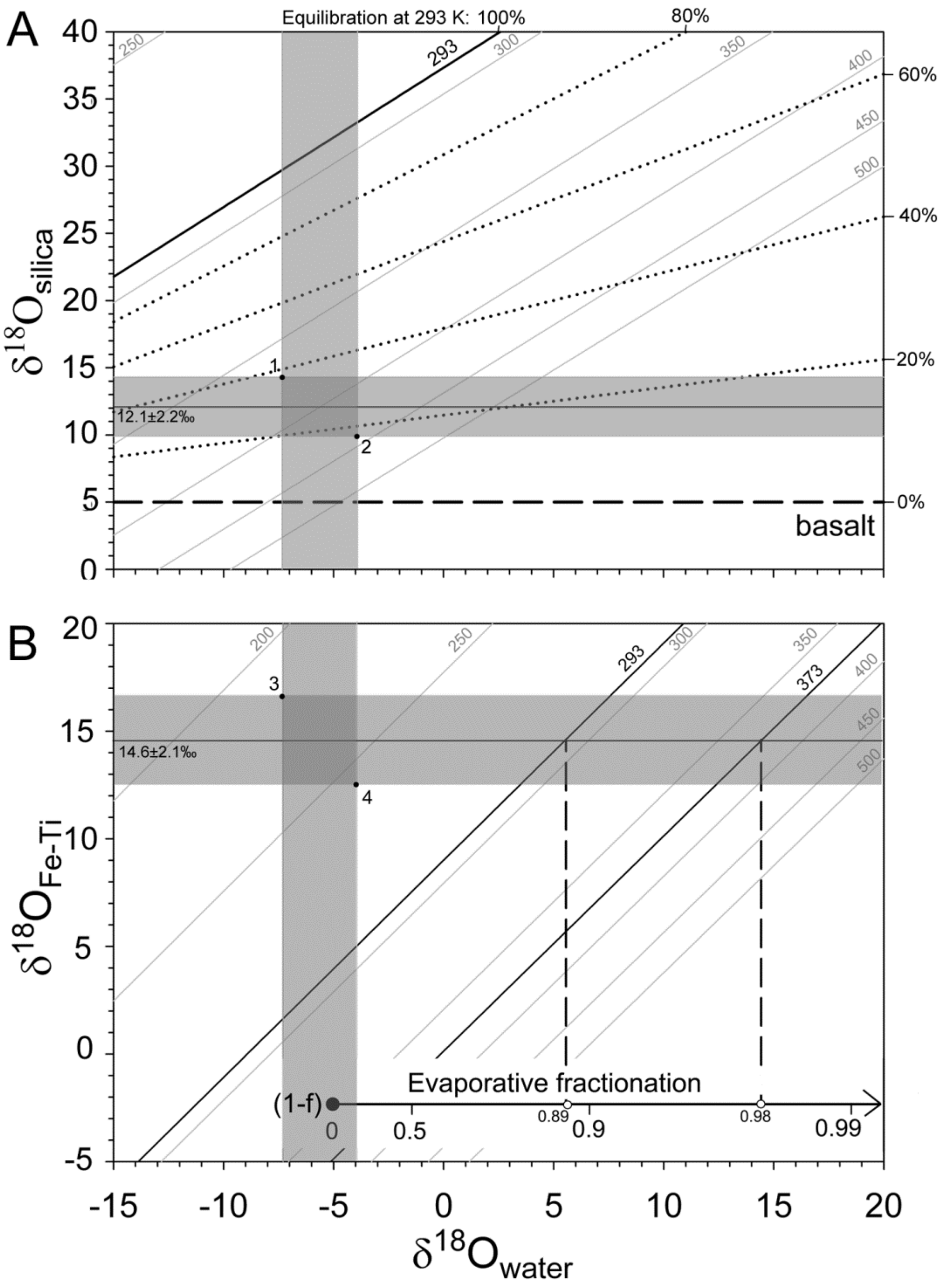

Figure 14. Geothermometry. In each plot, the horizontal shaded bar represents the SIMS measurement (±1σ), and the vertical shaded bar represents the range of meteoric waters in the Ka'u Desert (Scholl et al., 1995). A) Silica coating. Solid contours are isotherms (in Kelvins) calculated for the amorphous silica-water geothermometer from Kita et al. (1985). Dotted contours represent mixing at 293 K between the basaltic substrate (0% equilibration) and the equilibrium silica composition at 293 K (100% equilibration). The rectangle defined by (1) and (2) represents the range in T for equilibrium formation (369–440 K), and the range in f_{equil} for non-equilibrium formation (17–37%). B) Fe-Ti coating. Solid contours are isotherms (in Kelvin) calculated for the anatase-water geothermometer from Bird et al. (1993). The rectangle defined by (3) and (4) represents range in equilibrium temperature (211–255 K); these T are unreasonably low. The evaporative fractionation line defines conditions under which the Fe-Ti coating could have been deposited at ambient or elevated temperatures (see text).

sources, which include rainwater, groundwater, and steam emitted at the vent and by the degassing flow. Precipitation collected in the Ka'u Desert between spring 1992 and spring 1993 varied between -7.3‰ and -3.9‰ (Scholl et al., 1995). Groundwater collected from a Kilauea summit borehole in the same season had $\delta^{18}O$ = -5.6‰ (Scholl et al., 1995). Waters collected from fumaroles near the south rim of the Halemaumau pit crater had $\delta^{18}O$ values of -11.0‰ and -4.3‰, indicating that these fumarolic waters are dominated by recycled meteoric water, with no magmatic water signal (Hinkley et al., 1995). Therefore, the enriched coating $\delta^{18}O$ cannot be the product of simple isotopic exchange between the basaltic substrate and available water sources. Below, we consider equilibrium and non-equilibrium formation scenarios consistent with the observed fractionations.

4.1.2. Geothermometry

Under the assumption that the coatings formed in equilibrium with local meteoric water, we apply published geothermometers to estimate the temperatures associated with each layer. We consider the results of a silica-water geothermometer derived for amorphous silica (Kita, Taguchi and Matsubaya, 1985 (KTM)). Considering the observed range of meteoric $\delta^{18}O$ and the measured silica coating $\delta^{18}O$, the KTM thermometer indicates a temperature range of 369–440 K (**Figure 14a**). Another geothermometer derived for cryptocrystalline silica (Knauth and Epstein, 1976) produces a similar range of 353–425 K. For the Fe-Ti oxide coating $\delta^{18}O$, we consider the low-temperature anatase-water and rutile-water geothermometers published by Bird et al. (1993). The observed fractionations correspond to a temperature range of 228–255 K for the anatase-water thermometer, and 211–237 K for the rutile-water geothermometer (**Figure 14b**).

The geothermometry results described above indicate that the two coating layers cannot have formed at the same temperature in equilibrium with water of meteoric composition. The geothermometer results suggest that the silica coatings formed well above ambient temperatures, near the boiling point of water. However, the assumption of mineral-water equilibrium during formation may be unrealistic in a low water-to-rock ratio environment, especially for the silica coating, which has chemical and textural characteristics consistent with a leaching residue. The observed $\delta^{18}O_{silica}$ may also be explained by isotopic mixing between the basaltic substrate and meteoric water. For example, if the silica coating formed at ambient temperature (293 K), the observed $\delta^{18}O_{silica}$ would indicate just 17–37% equilibration between the basaltic substrate and the water source (**Figure 14a**). Given that the silica probably did not achieve full equilibration with the water source, the temperatures measured by geothermometry then represent upper bounds on the temperature of formation.

The assumption of mineral-water equilibrium is more reasonable for the Fe-Ti coating, which was chemically deposited from solution. However, the unreasonably low, sub-freezing temperatures indicated by the anatase geothermometer suggest that depositional solutions, originally of meteoric composition, were subject to evaporative fractionation. At T = 373 K, equilibrium liquid-water fractionation is described by $\alpha_{l\text{-}v} =$ 1.0051 (Horita and Wesolowski, 1994). Assuming equilibrium Rayleigh evaporation at 100% humidity, and neglecting Craig-Gordon effects (Craig et al., 1963; Criss, 1999), a fractionation of the required magnitude would require ~98% evaporation (f = 0.02) of the solution before precipitation of the Fe-Ti coating (**Figure 14b**). At ambient temperature, the observed fractionation requires ~89% Rayleigh evaporation (assuming the same $\alpha_{l\text{-}v}$).

To summarize the above considerations, the $\delta^{18}O$ measurements of the coating layers are consistent with both ambient and elevated temperatures. The silica coating $\delta^{18}O$ indicates equilibrium formation temperatures as high as 440 K, but this temperature represents an upper limit because of likely incomplete equilibration. The Fe-Ti coating equilibrated with water that had undergone extreme evaporative fractionation.

4.2. Formation Mechanism

4.2.1. Field Relations

There is no universal mechanism for the formation of silica coatings (Dorn, 1998); indeed, previous studies of Hawaiian silica coatings have illustrated that multiple mechanisms of formation operate on Hawaii alone. The presence of jarosite and the apparent mobility of Fe and Ti strongly suggest that the coatings on the 1974 flow are the product of acid-sulfate alteration. Field morphologies place constraints on the source of acidity. An obvious potential source of acidity is the nearby Kilauea Caldera, which typically emits 100–400 metric tons SO_2/day (Casadevall et al., 1987). Magmatic SO_2 is converted to sulfuric acid aerosol and is blown downwind up to several kilometers into the Ka’u Desert, where it interacts with basaltic materials and produces amorphous silica (Schiffman et al., 2006). In this region, silica deposits removed by physical weathering are continuously renewed (Schiffman et al., 2006); thus, this model suggests steady growth of the silica layer over the 28 years between flow emplacement and collection. The regional “acid fog” model effectively describes much of the acid-sulfate alteration occurring in the Ka'u Desert, but it is inconsistent with several observations for the 1974 flow coatings. Areas on the pahoehoe flow where glass surfaces have spalled away show no apparent coating regrowth (**Figure 2c**). Silica coatings on the walls of interior vesicles require hot, syneruptional deposition (**Figure 3g**). Finally, it is difficult to explain the gradients in Fe-Ti areal coverage away from the 1974 spatter ramparts with acidity derived solely from the main caldera.

The Fe-Ti gradient away from the spatter ramparts suggest that the fissure vents that produced those ramparts were also important sources of acidic vapors. The post-eruptive gas emission history of the fissure vents is unknown; at the time our field work in 2002, activity had ceased. However, the vents certainly had their strongest gas emissions during and following the 1974 eruption; thus, our preferred interpretation involves coating formation over a period of weeks or months while the fissure vents were active. Oxygen isotopes constrain the temperature of formation of both coatings to around the boiling point of water or below. Some alteration, including the interior vesicle coatings, must have occurred at high temperature, implying short timescales. Such short timescales are reasonable; alteration by volcanic vapors can produce noticeable leaching and silica enrichment of basaltic glass in as little as an hour (Spadaro et al., 2002). The majority of alteration may have occurred at ambient temperature, after the erupted basalt had cooled but before the vents had stopped steaming. The main caldera may have also contributed acidity. The onset of the 1983 P'u Ō'ō eruption, 20 km away from Kilauea Caldera on the east rift zone, was accompanied by a ~2x increase in SO_2 emissions from the main caldera (Casadevall et al., 1987); similarly, the onset of the 1974 eruption along the SW rift zone was likely accompanied by a jump in gas flux at the caldera. A weakness of this interpretation is that our sampling was too sparse to identify variations in the thickness of the silica layer away from the vents. Additional field work is required to identify and characterize any thickness gradients and gauge the relative importance of regional, caldera-derived vapors and local, fissure vent-derived vapors.

4.2.2. Silica Coating

We consider two classes of micro-scale formation pathways for the 1974 Ka'u Desert silica coatings: 1) direct deposition, 2) residual leaching and dissolution.

Direct deposition: A direct depositional mechanism requires an external source of silica and a method for chemical deposition on the basalt surface. Proposed solid sources for the silica in Hawaiian silica coatings include phytolith-bearing atmospheric dust (Farr and Adams, 1984) and wind-blown volcanic ash and tephra (Curtiss et al., 1985). These wind-blown materials then undergo partial dissolution during wetting events, and amorphous silica precipitates (Curtiss et al., 1985). This mechanism is unlikely for the formation of the 1974 coatings, which are laterally homogenous and show no evidence of embedded clasts. External silica can be derived by dissolution of the rock substrate and transportation in solution as monosilicic acid ($Si(OH)_4$) (Dorn, 1998), or as colloidal silica (Krauskopf, 1956). Dissolved silica is the primary silica source for more volumetrically significant deposits like siliceous sinters (Rodgers et al., 2002). Silica may also be carried in steam, but its solubility is low at near-surface pressures (Macdonald, 1944; Brady, 1953). SiF_4 has been proposed as a volatile gaseous phase present during the cooling of Hawaiian basalt flows, but such volatilization produces local Si depletions, not enrichments (White and Hochella, 1992); therefore, a vapor depositional mechanism seems unlikely. We restrict further consideration to depositional mechanisms involving aqueous solution.

The strongest evidence supporting a depositional mechanism is the sharp boundary between the silica coating and the basaltic substrate, and the lack of an obvious chemical gradient within the glass near the coating. However, chemical boundary layers produced by short-term leaching of silicate glasses can be just tens of nanometers wide, undetectable at the spatial resolution of EPMA (Smets and Lommen, 1982). The presence of an apparently sharp boundary, therefore, does not prove a depositional mechanism. Other observations are inconsistent with deposition. The first mineral phase deposited in hydrothermal sinter environments is opal-A (Herdianita et al., 2000); the absence of spheroidal texture in the silica layer, together with Raman spectroscopic evidence, indicate that opal-A is not present. Amorphous, non-opaline silica can be deposited from solution (Fournier and Rowe, 1966), but opal is the norm in depositional environments. Finally, the coating, in places, directly overlies near-surface vesicles with no basaltic substrate underneath (**Figure 3b)**. The coatings could not have been deposited here, as there was no surface on which to deposit. In other places, vertical and horizontal walls of surface vesicles feature coatings of uniform thickness, an implausible geometry for a depositional scenario (**Figure 3c**). Based on these observations, we do not favor a depositional mechanism for the formation of the silica coatings.

Residual leaching and dissolution: The silica coating might also have formed through alteration of the basaltic glass substrate, either by leaching (by hydrothermal fluids or meteoric water), or by total dissolution and reprecipitation. Under low pH conditions (2–3), Si^{4+} is relatively insoluble in solution and lower valence basaltic cations

(Mg^{2+}, Ca^{2+}, Al^{3+}, Na^{+}) are mobile and easily exchanged for protons in solution; thus, basalt leaching could leave behind a silica-enriched layer (El-Shamy et al., 1972; Minitti et al., 2007). Highly acidic conditions have frequently been invoked for the genesis of Hawaiian alteration products (e.g., Schiffman et al., 2006; Macdonald, 1944). Because basalt weathering consumes acidity, a leaching mechanism must operate either in an environment with a high water-rock ratio or with continuously renewed acidity (Minitti et al., 2007).

The observations presented in this study are most consistent with a leaching formation mechanism for the 1974 silica coating; given the presence of jarosite, this leaching is likely facilitated by acid-sulfate alteration. The hypothesis of a residual nature for the silica layer is supported by its porous texture, low concentrations of elements in basaltic proportions, and glass-like mineralogy as determined by Raman spectroscopy. We have not been able to definitively identify the leaching agent; vapor alteration has been proposed as a mechanism for the production of secondary silica in volcanic environments (Tosca et al., 2004), but liquids are likely required for the removal of lower valence cations from the system (Squyres et al., 2008).

The above evidence indicates that acid-sulfate leaching is the dominant mechanism involved in the coating formation; however, other mechanisms must also be operating to explain the lack of obvious diffusive profiles in leached elements and the enriched $\delta^{18}O$ signature. Oxygen diffusion through glass is exceedingly slow at ambient and epithermal temperatures (e.g. Rawal and Cooper, 1979), so any enrichment suggests that oxygen transport was facilitated by small-scale dissolution and reprecipitation. Such small-scale dissolution might erase concentration gradients within the coating. In addition, thin silica deposits observed on the walls of interior vesicles are likely the product of vapor deposition. Thus, although silica was primarily immobile during leaching, there is evidence for silica mobility on length scales of a few micrometers.

4.2.3. Fe-Ti Coating

The observations presented in this study provide considerable constraints on the origin of the Fe-Ti coating layer. The spheroidal aggregate texture necessitates a depositional mechanism; the varying spherule size (**Figure 3f**) is likely a result of numerous environmental factors, including variable water-rock ratio and pH of solution. Vapor deposition of Fe-Ti oxides has been recorded in stalactites within a lava tube (Baird et al., 1985), and Ti has been detected in measurable quantities in aerosols in volcanic plumes (Hinkley, 1991). However, it is difficult to explain the relative homogeneity of the Fe-Ti coating and the evaporative oxygen isotopic signature with a vapor depositional mechanism; therefore, our preferred explanation involves chemical deposition of the Fe-Ti oxides from aqueous solution.

The source of the chemical constituents of the Fe-Ti coating and their transport in solution are not fully understood. The mobility of Ti in sedimentary systems near neutral pH is limited, often less than 1 μm (Tilley and Eggleton, 2005). Fe and Ti were likely released into solution by chemical weathering of basaltic glass or accessory phases such as titanomagnetite. The high areal proportions of Fe-Ti coating coverage near the vents was achieved either by thicker leaching zones on the surfaces of erupting basalts (although thicker silica coatings have not been observed), or by leaching of basalts around the vent walls and transport of dissolved basaltic cations in volcanic fluids.

Titanomagnetites have been shown to dissolve readily at low pH (Arlauckas and McLennan, 2005; Tosca et al., 2004). However, Fe-Ti oxides tend to dissolve non-stoichiometrically, with Ti being considerably less mobile in solution than Fe (Arlauckas and McLennan, 2005). There are two possible explanations for high Ti/Fe ratios in the coating. One possibility is that Ti was transported in solution as hydroxy-sulfate complexes like $Ti(OH)SO_4^{2+}$ (Agapova et al., 1989) or as hydroxy-halide complexes like $Ti(OH)_2F_4^{2-}$ (Barsukova et al., 1979). NanoSIMS mapping indicated F enrichment in the Fe-Ti layer (**Figure 7**), and Kilauean gases are F- and Cl- bearing (Naughton et al., 1980). If complexation did occur, Ti might be transported for large distances before deposition. A second explanation for the high Ti/Fe ratios is that the Ti and Fe were carried in solution for very short distances (i.e., micrometers) before precipitation, such that Ti could not fractionate out. This scenario is supported by the high concentrations of P in the Fe-Ti coating, another highly immobile element found in the basaltic glass. The formation of the Mauna Ulu Fe-Ti coating, which has a higher and more variable Fe/Ti ratio, must have featured longer characteristic transport distances and less efficient transport of Ti in solution.

The depositional texture and stratigraphic position of the Fe-Ti coating requires that it formed concurrently with or after silica coating formation. The enriched $\delta^{18}O$ is consistent with deposition near ambient temperature from a highly evaporated solution. The poor crystallinity of the Fe-Ti layer is also consistent with low-temperature deposition (Hsu et al., 1986), suggesting a depositional window after basalt cooling but before vent activity ceased. The simplest and most general explanation consistent our observations is that both coating materials formed from an isotopically evolving water body in a single chain of events. Acidic fluids leached the upper layer of basalt glass, leaving a silica-enriched layer behind and releasing Fe and Ti into solution. The solution evaporated, precipitating the Fe-Ti oxide overlying the silica.

5. Implications for Mars

5.1. Silica Deposits at Gusev Crater

No martian silica deposit has been studied in greater detail than those discovered at Gusev Crater. These deposits consist of light-toned soils and nodular outcrops in the vicinity of Home Plate, an ~80 m wide ovate landform featuring platy layered outcrops interpreted as altered volcanic tuff deposits (Squyres et al., 2007; Arvidson et al., 2008). The most silica-enriched soil site, Gertrude Weise, is composed of over 90% SiO_2 (Squyres et al., 2008). These soils are sometimes associated with ferric sulfates (e.g., Tyrone), but Gertrude Weise is also highly depleted in sulfur. Mini-TES spectra of the high-silica soils contain vibrational absorption features at 475 cm^{-1} and 1110 cm^{-1} consistent with the Si-O stretching and bending modes in opal-A (Squyres et al., 2008; Michalski et al., 2003). The Home Plate high-silica materials, like the Ka'u Desert silica coatings, have been interpreted as the products of acid-sulfate alteration, but it is unclear whether they are residual or were transported and deposited as a siliceous sinter (Squyres et al., 2008). The occurrence of the high-silica materials in soils suggests the deposits were subjected to post-depositional reworking, probably under a dry atmosphere (Squyres et al., 2008).

Compositional comparison between the Gertrude Weise (GW) soil sample and the 1974 silica coatings may provide additional clues about martian alteration conditions.

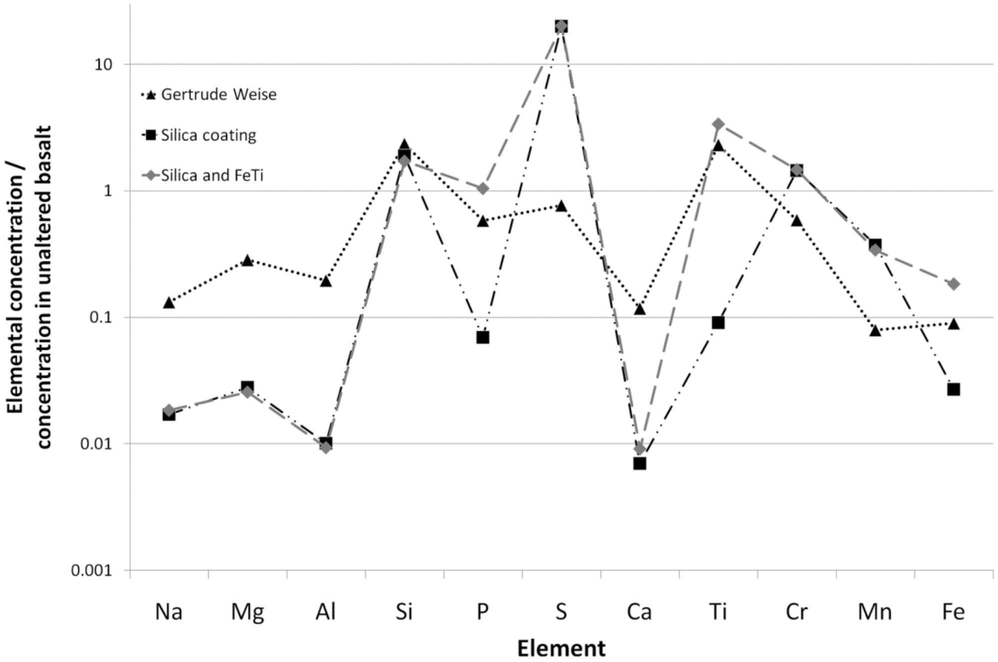

Figure 15. Composition of silica-rich materials from Hawaii and Mars relative to their respective unaltered basalt composition. The Gertrude Weise ratios are calculated relative to Adirondack class basalt (Ming et al., 2006). 'Silica coating' refers to the endmember composition of the silica layer alone; 'Silica and FeTi' was calculated by a weighted average of the silica endmember and the Fe-Ti oxide endmember (10:1).

The bulk composition of the Hawaiian coating material was estimated by weighting electron microprobe analyses of the silica coating and the Fe-Ti coating in a 10:1 ratio, roughly corresponding to their respective thicknesses. Elemental ratios of each alteration product to their respective unaltered basalt indicate that both GW and the coating materials are enriched in Si and Ti and strongly depleted in Na, Mg, Al, Mn and Fe (**Figure 15**). The depletions of basaltic elements are more extreme in the Hawaiian samples than in GW, suggesting unusually efficient leaching or possible subsequent remobilization events. The most noticeable differences in major element chemistry between the two deposits are in S, P, and Cr. The Hawaiian coatings are strongly enriched in S; Gertrude Weise is moderately depleted in S relative to unaltered basalt. This apparent depletion is partially the result of high initial S concentrations in Martian basalt (Ming et al. 2006), but the depletion also indicates that GW is a late-stage leaching product. P and Cr are moderately enriched in the Hawaiian coatings, but are moderately depleted in GW. These two elements are generally immobile in solution, so the GW depletion may indicate longer characteristic transport distances than the Hawaiian Fe-Ti coatings.

A major difference in the character of the two deposits is the volume of alteration. The Ka'u Desert coatings in this study are only ~10 μm thick, whereas observations at Gusev Crater indicate outcrop-scale alteration at least several cm deep (Squyres et al., 2008). This difference in alteration volume is likely a function of both the length and intensity of alteration. The coatings on the 1974 flow formed in no longer than 30 years, and likely in a much shorter time period; older coatings on Hawaiian lava flows are often thicker, up to several hundred micrometers (Farr and Adams, 1984; Minitti et al., 2007). Hawaiian samples collected near fumaroles at Halema'uma'u Crater and Sulfur Bank, where exposure to acidic fluids is more consistent and intense, show volume alteration similar to that seen at Home Plate (Macdonald, 1944; Morris et al., 2000). Volume alteration may also indicate percolation of fluids and vapors through a substrate along fractures and grain boundaries (Morris et al., 2000), instead of only surface interaction as observed on the 1974 flow. Therefore, the morphology and distribution of the high-silica materials near Home Plate suggests long-lived (decades to centuries), intense acid-sulfate alteration in close proximity to a hydrothermal or fumarolic vent.

5.2. Global Processes

Orbital detections of Si-OH and Si-O vibrations in thermal infrared spectra and VNIR reflectance spectra suggest that opaline silica may be present on Mars at much larger spatial scales than represented by the Home Plate deposits. Opaline silica, as identified by CRISM, is associated with light-toned bedded deposits in Valles Marineris that extend for tens or hundreds of kilometers (Milliken et al., 2008). These spectral detections of opaline silica are often associated with jarosite, a robust indicator of acid-sulfate formation conditions. The volumetric extent of these secondary minerals in the deposits is unknown; the spectral signature could be produced by volume-altered ash deposits (Milliken et al., 2008), or thin silica coatings or weathering rinds, which mask the spectral signature of their unaltered substrate (Seelos et al., 2009; Minitti et al., 2007). Regardless of the extent of alteration in these layered units, a formation mechanism similar to that of the Hawaiian coating seems unlikely. Alteration on the 1974 Kilauea flow occurred over a spatial domain of several kilometers; the source of acidity for this alteration was one or several volcanic vents. Pervasive volcanic alteration in distinct bedded layers over several hundred kilometers would likely require intense regional volcanism with many active vents. No obvious volcanic vents have been observed via HiRISE imagery in the area of these deposits, suggesting an aqueous, nonvolcanic origin (Milliken et al., 2008). Mechanisms more likely to produce pervasive regional opaline silica include deposition from an evaporating, acidic water body and groundwater infiltration. Elsewhere on Mars, hydrated silica has been detected in highlands craters in the Nili Fossae region, often in association with other hydrated minerals including phyllosilicates and zeolites (Ehlmann et al., 2009). These mineral assemblages indicate regional hydrothermal or low-grade metamorphic alteration at near-neutral pH, implying an environment dissimilar to the Ka’u Desert. The CRISM silica detections indicate that silica formation on Mars, as on Earth, occurs over a wide range of water-rock ratios and environmental conditions.

In addition to the targeted spectral detections described above, hydrated silica coatings have been suggested as regionally or globally occurring phenomena to explain more widespread spectral observations. Surface Type 2, a unit defined by TES spectra that characterizes most of the dark surfaces in the martian northern lowlands, has a spectral component corresponding to hydrous or high-silica glass (Bandfield et al., 2000). This spectral component is consistent with silica coatings capping unaltered basalt (Kraft et al., 2003). Silica coatings have also been invoked as a global phenomenon to explain muting of the high-calcium pyroxene signature in CRISM spectra from Hesperian compositionally distinct ejecta (Skok et al., 2008). If silica coatings do occur on a global scale on the martian surface, a volcanic acid-sulfate origin as described in this paper is unlikely; volcanic vapors probably only act as alteration agents on the spatial scale of kilometers. Any plausible formation mechanism involves water, but the putative widespread occurrence of silica coatings in the northern lowlands does not distinguish between mechanisms involving an ancient ocean (Head et al., 1999) and mechanisms involving thin film wetting and alteration (Kraft et al., 2004).

Acknowledgements

This work was supported by funding from NASA grants NAG5-12684 (B. Jolliff) and NNX06AB20G (G. Rossman), as well as Gordon and Betty Moore Foundation funding for the Caltech Center for Microanalysis (J. Eiler). The manuscript was significantly improved by the input of Kim Seelos and an anonymous reviewer. We thank Chi Ma for assistance with collection of SEM imagery, Naomi Levin for assistance with laser fluorination measurements, and Yunbin Guan for assistance in the use of the NanoSIMS and Cameca 7f.

Works Cited

Abrams, M., E. Abbott, and A. Kahle (1991) Combined use of visible, reflected infrared, and thermal infrared images for mapping Hawaiian lava flows. *JGR*, **96**, 475–484.

Agapova, G., I. Modnikov, Y. Shmariovich (1989) Experimental study of the behavior of titanium in hot sulfide-carbonate solutions. *Int'l Geo. Rev.*, **31**, 4424–4430.

Anovitz, L. M., D. R. Cole, and M. Fayek (2008) Mechanisms of rhyolitic glass hydration below the glass transition. *Am. Min.*, **93**, 1166–1178.

Arlauckas, S., and S. McLennan (2005) Dissolution rates and weathering products of iron-titanium oxides: pH and temperature dependence, *LPSC XXXVI*, #2011.

Arvidson, R. E., and 32 others (2008) Spirit Mars Rover Mission to the Columbia Hills, Gusev Crater: Mission overview and selected results from the Cumberland Ridge to Home Plate. *J. Geophys. Res.*, **113**, E12S33, doi:10.1029/2008JE003183.

Baird A. K., D.C. Mohrig, and E.E. Welday (1985) Vapor deposition in basaltic stalactites, Kilauea, Hawaii. *Lithos*, **18**, 151–160.

Bandfield, J. L., V. E. Hamilton, and P. E. Christensen (2000) A global view of martian surface composition from MGS-TES. *Science*, **287**, 1626–1630.

Barsukova, M. L., V. A. Kuznetsov, V. A. Dorofeyeva, and L. I. Khodakovskiy (1979) Measurement of the solubility of rutile TiO_2 in fluoride solutions at elevated temperatures. *Geochemistry International*, **16** (4), 41–-49.

Bell, J. F. III, R. V. Morris, and J. B. Adams (1993) Thermally altered palagonitic tephra – a spectral and process analog to the soil and dust of Mars. *JGR*, **98**, E2, 3373–3385.

Bertoluzza, A., C. Fagnano, M. A. Morelli, V. Gottardi, and M. Guglielmi (1982) Raman and infrared spectra on silica gel evolving toward glass. *J. Non-Crystalline Solids*, **48**, 117–128.

Bird, M. I., F. J. Longstaffe, and W. S. Fyfe (1993) Oxygen-isotope fractionation in titanium-oxide minerals at low temperature. *Geochim. Cosmochim. Acta*, **57**, 3083–3091.

Brady, E. L. (1953) Chemical nature of silica carried by steam. *J. Phys. Chem.*, **57**, 706–710.

Casadevall, T.J., Stokes, J.B., Greenland, L.P., Malinconico, L.L., Casadevall, J.R., and Furukawa, B.T. (1987) SO_2 and CO_2 emission rates at Kilauea Volcano, 1979-1984, chap. 29 in Decker, R.W., Wright, T.L., and Stauffer, P.H., eds., Volcanism in Hawaii: U.S. Geological Survey Professional Paper 1350, **1**, 771–780.

Christensen, P.R., and 27 others (2004) Initial Results from the Mini-TES Experiment in Gusev Crater from the Spirit Rover. *Science*, **305**, 837–841.

Craig, H., L. J. Gordon, and Y. Horibe (1963) Isotopic exchange effects in the evaporation of water. *JGR*, **68**, 5079–5087.

Crisp, J., A. Kahle, and E. A. Abbott (1990) Thermal infrared spectral character of Hawaiian basaltic glasses. *JGR*, **95**, 21657–21669.

Criss, R. E. (1999) *Principles of stable isotope distribution*. 254 p., Oxford University Press, New York.

Curtiss B., J. B. Adams, and M. S. Ghiorso (1985) Origin, development and chemistry of silica-alumina rock coatings from the semi-arid regions of the island of Hawaii. *Geochimica et Cosmochimica Acta*, **49**, 49–56.

Darragh, P. J., A. J. Gaskin, B. C. Terrell, and J. V. Sanders (1966) Origin of precious opal. *Nature*, **209**, 13–16.

Dorn, R. I. (1998) *Rock coatings*, 444 p., Elsevier, New York.

Eiler, J. M., K. A. Farley, J. W. Valley, A. W. Hofmann, and E. M. Stolper (1996) Oxygen isotope constraints on the sources of Hawaiian volcanism. *EPSL*, **144**, 453–468.

Eiler, J. M., C. Graham and J. W. Valley (1997) SIMS analysis of oxygen isotopes: matrix effects in complex minerals and glasses. *Chem. Geol.*, **138**, 221–244.

Ehlmann, B. L., J. Mustard, G. A. Swayze, R. N. Clark, J. L. Bishop, F. Poulet, D. J. Des Marais, L. H. Roach, R. Milliken, J. J. Wray, O. S. Barnouin-Jha, and S. Murchie (2009) Identification of hydrated silicate minerals on Mars using MRO-CRISM: geologic context near Nili Fossae and implications for aqueous alteration. *JGR*, doi:10.1029/2009JE003339.

El-Shamy, T. M., J. Lewins, and R. W. Douglas (1972) The dependence of the pH of the decomposition of glasses by aqueous solutions. *Glass Tech.*, **13**, 81–87.

Evans, D. L., T. G. Farr, and J. B. Adams (1981) Spectral reflectance of weathered terrestrial and martian surfaces. *Proc. Lunar Planet. Sci.*, **12B**, 1473–1479.

Farmer, J. D., and D. J. Des Marais (1999) Exploring for a record of ancient Martian life. *JGR*, **104** (E11), 26977–26995.

Farr, T. G., and J. B. Adams (1984) Rock coatings in Hawaii. *GSA Bulletin*, **95**, 1077–1083.

Fournier, R. O. and J. J. Rowe (1966) The deposition of silica in hot springs. *Bull. Volcanol.*, **29**, 585–587.

Gu, Z., A. Fujishima, and O. Sato (2002) Fabrication of high-quality opal films with controllable thickness. *Chem. Mater.*, **14**, 760–765.

Guinness, E. A., R. Arvidson, B. Jolliff, K. Seelos, F. Seelos, IV, D. Ming, R. Morris, and T. Graff (2007) Hyperspectral reflectance mapping of cinder cones at the summit of Mauna Kea and implications for equivalent observations on Mars, *J. Geophys. Res.*, **112**, E08S11, doi:10.1029/2006JE002822

Hausrath, E. M., A. K. Navarre-Sitchler, P. B. Sak, C. I. Steefel, and S. L. Brantley (2008) Basalt weathering rates on Earth and the duration of liquid water on the plains of Gusev Crater, Mars. *Geology*, **36**, 67–70.

Head, J. W., III, H. Hiesinger, M. A. Ivanov, M. A. Kreslavsky, S. Pratt, and B. J. Thomson (1999) Possible ancient oceans on Mars: evidence from Laser Orbiter Altimeter data. *Science*, **286**, 2134–2137.

Herdianita, N. R., P. R. L. Browne, K. A. Rodgers, and K. A. Campbell (2000) Mineralogical and textural changes accompanying ageing of silica sinter. *Mineralium Deposita*, **35**, 48–62.

Hinkley, T. K. (1991) Distribution of metals between particulate and gaseous forms in a volcanic plume. *Bull. Volcanol.*, **53**, 395–400.

Hinkley, T. K., J. E. Quick, R. T. Gregory, and T. M. Gerlach (1995) Hydrogen and oxygen isotopic composition of waters from fumaroles at Kilauea summit, Hawaii. *Bull. Volcanol.*, **57,** 44–51.

Horita, J. D. and D. J. Wesolowski (1994) Liquid-vapor fractionation of oxygen and hydrogen isotopes of water from the freezing to the critical temperature. *Geochim. Cosmochim. Acta*, **58**, 3425–3437.

Hsu, L. S., R. Rujkorakarn, J. R. Sites, and C. Y. She (1986) Thermally induced crystallization of amorphous-titania films. *J. Appl. Phys.*, **59**, 3475–3480.

Ilieva, A., B. Mihailova, Z. Tsintsov, and O. Petrov (2007) Structural state of microcrystalline opals: a Raman spectroscopic study. *Am. Min.*, **92**, 2007.

Irvine, W. M. and J. B. Pollack (1968) Infrared optical properties of water and ice spheres. *Icarus*, **8**, 324–360.

Kita, I., S. Taguchi and O. Matsubaya (1985) Oxygen isotope fractionation between amorphous silica and water at 34-93° C. *Nature*, **314**, 83–84.

Knauth, L. P., and S. Epstein (1976) Hydrogen and oxygen isotope ratios in nodular and bedded cherts. *Geochim. Cosmochim. Acta*, **40**, 1095–1108

Kraft, M. D., J. R. Michalski, and T. G. Sharp (2003) Effects of pure silica coatings on thermal emission spectra of basaltic rocks: considerations for Martian surface mineralogy. *Geophys. Res. Lett.*, **30**, doi:10.1029/2003GL018848.

Kraft, M. D., J. R. Michalski, and T. G. Sharp (2004) High-silica rock coatings: TES surface-type 2 and chemical weathering of Mars. *LPSC XXXV*, #1936.

Krauskopf, K. B. (1956) Dissolution and precipitation of silica at low temperatures. *Geochim. Cosmochim. Acta*, **10**, 1–26.

Liu, L. and T. P. Mernagh (1992) Phase transitions and Raman spectra of anatase and rutile at high pressures and room temperature. *Eur. J. Mineral.*, **4**, 45–52.

Macdonald, G. A. (1944) Solfataric alteration of rocks at Kilauea volcano. *Am. J. Sci.*, **242**, 496–505.

McLennan, S. M. (2003) Sedimentary silica on Mars. *Geology*, **31**, 315–318.

McMillan, P. (1984) Structural studies of silicate glasses and melts – applications and limitations of Raman spectroscopy. *Am. Min.*, **69**, 622–644.

Michalski, J. R., M. D. Kraft, T. Diedrich, T. G. Sharp, and P. R. Christensen (2003) Thermal emission spectroscopy of the silica polymorphs and considerations for remote sensing of Mars. *Geophys. Res. Lett.*, **30**, doi:10.1029/2003GL018354.

Milliken, R. E., G. A. Swayze, R. E. Arvidson, J. L. Bishop, R. N. Clark, B. L. Ehlmann, R. O. Green, J. P. Grotzinger, R. V. Morris, S. L. Murchie, J. F. Mustard, and C. Weitz (2008) Opaline silica in young deposits on Mars. *Geology*, **36**, 847-850.

Ming, D. W., D. W. Mittlefehldt, R. V. Morris, D. C. Golden, R. Gellert, A. Yen, B. C. Clark, S. W. Squyres, W. H. Farrand, S. W. Ruff, R. E. Arvidson, G. Klingelhöfer, H. Y. McSween, D. S. Rodionov, C. Schröder, P. A. de Souza Jr., and A. Wang (2006) Geochemical and mineralogical indicators for aqueous processes in the Columbia Hills of Gusev crater, Mars. *JGR*, **111**, doi: 10.1029/2005JE002560.

Minitti, M. E., C. M. Weitz, M. D. Lane, and J. L. Bishop (2007) Morphology, chemistry, and spectral properties of Hawaiian rock coatings and implications for Mars. *JGR*, **112**, doi:10.1029/2006JE002839.

Morris, R. V., T. Graff, M. D. Lane, D. C. Golden, C. S. Schwandt, T. D. Shelfer, D. W. Ming, S. A. Mertzman, J. F. Bell, J. Crisp, and P. R. Christensen (2000) Acid sulfate alteration products of a tholeiitic basalt: implications for interpretation of martian thermal emission spectra. *LPSC XXXI*, #2014.

Morris, R. V., D. W. Ming, T. G. Graff, R. E. Arvidson, J. F. Bell III, S. W. Squyres, S. A. Mertzman, J. E. Gruener, D. C. Golden, L. Le and G. A. Robinson (2005) Hematite spherules in basaltic tephra altered under aqueous, acid-sulfate conditions on Mauna Kea volcano, Hawaii: possible clues for the occurrence of hematite-rich spherules in the Burns formation at Meridiani Planum, Mars. *EPSL*, **240**, 168–178.

Mustard, J. F., and 35 others (2008) Hydrated silicate minerals on Mars observed by the Mars Reconnaissance Orbiter CRISM instrument. *Nature*, **454**, 305–309.

Naughton, J. J. (1980) Composition of come components in gas collected during the 1977 eruption at Kilauea, Hawaii. *J. Volcanol. Geotherm. Res.*, **7**, 319–322.

Newman, S., E. M. Stolper, and S. Epstein (1986) Measurement of water in rhyolitic glasses: calibration of an infrared spectroscopic technique. *Am. Min.*, **71**, 1527–1541.

Oguri, Y., R. E. Riman, and H. K. Bowen (1988) Processing of anatase prepared from hydrothermally treated alkoxy-derived hydrous titania. *J. Mat. Sci.*, **23**, 2897–2904.

Ohlhorst, S., H. Behrens, F. Holtz (2001) Compositional dependence of molar absorptivities of near-infrared OH- and H_2O bands in rhyolitic to basaltic glasses. *Chemical Geology*, **174**, 5–20.

Ohsaka, T., F. Izumi, and Y. Fujiki (1978) Raman spectrum of anatase, TiO_2. *J. Raman Spec.*, **7**, 321–324.

Perry, R. S., B. Y. Lynne, M. A. Sephton, V. M. Kolb, C. C. Perry, and J. T. Staley (2006) Baking black opal in the desert sun: the importance of silica in desert varnish. *Geology*, **34**, 537-540.

Rawal, B. S. and A. R. Cooper (1979) Oxygen self-diffusion in a potassium strontium silicate glass using proton activation analysis. *J. Mat. Sci.*, **14**, 1425-1432.

Riciputi, L. R., B. A. Paterson, and R. L. Ripperdan (1998) Measurement of light stable isotopes by SIMS: matrix effects for oxygen, carbon, and sulfur isotopes in minerals. *Int'l. J. Mass Spec.*, **178**, 81–112.

Rodgers, K. A., K. L. Cook, P. R. L. Browne, and K. A. Campbell (2002) The mineralogy, texture and significance of silica derived from alteration by steam condensate in three New Zealand geothermal fields. *Clay Minerals*, **37**, 299–322.

Sankapal, B. R., M. C. Lux-Steiner, and A. Ennaoui (2005) Synthesis and characterization of anatase-TiO_2 thin films. *Applied Surface Science*, **239**, 165–170.

Schiffman, P., R. Zierenberg, N. Marks, J. L. Bishop, and M. D. Dyar (2006) Acid-fog deposition at Kilauea volcano: a possible mechanism for the formation of siliceous-sulfate rock coatings on Mars. *Geology*, **34**, 921–924.

Scholl, M. A., S. E. Ingebritsen, C. J. Janik, and J. P. Kauahikaua (1995) An isotope hydrology study of the Kilauea volcano area, Hawaii. U.S. Geological Survey Water Resources Investigations Report 95–4213, 44 p.

Schwertmann, U., J. Friedl, G. Pfab, and A. U. Gehring (1995) Iron substitution in soil and synthetic anatase. *Clays and Clay Minerals*, **43**, 599–606.

Seelos, K. D., R. E. Arvidson, B. L. Jolliff, S. M. Chemtob, R. V. Morris, D. W. Ming, and G. A. Swayze (2009) Silica in a Mars analog environment: Ka'u Desert, Kilauea Volcano, Hawai'i. *JGR*, **115**, E00D15, doi:10.1029/2009JE003347.

Skok, J. R., J. F. Mustard, S. L. Murchie, and M. B. Wyatt (2008) CRISM-OMEGA observations of compositionally distinct crater ejecta in the Syrtis Major region of Mars. Abstract P43A-1384, presented at the American Geophysical Union 2008 Fall Meeting, San Francisco, CA.

Shimizu, K., H. Imai, H. Hirashima, and K. Tsukuma (1999) Low-temperature synthesis of anatase thin films on glass and organic substrates by direct deposition from aqueous solutions. *Thin Solid Films*, **351**, 220–224.

Smallwood, A. G., P. S. Thomas, and A. S. Ray (1997) Characterisation of sedimentary opals by Fourier transform Raman spectroscopy. *Spectrochimica Acta Part A*, **53**, 2341–2345.

Smets, B. M. J., and T. P. A. Lommen (1982) The leaching of sodium aluminosilicate glasses studied by secondary ion mass spectrometry. *Phys. Chem. Glasses*, **23**, 83–87.

Smith, D.C. and E. A. Perseil (1996) The Sb^{5+}+R^{3+}=2 Ti^{4+} substitution in natural titanites and rutiles from St. Marcel, Aosta Valley, Italy, observed with Raman spectroscopy. *GeoRaman 96 Proceedings*, 11.

Soule, S. A., K. V. Cashman, and J. P. Kauahikaua (2004) Examining flow emplacement through the surface morphology of three rapidly emplaced, solidified lava flows, Kilauea Volcano, Hawai'i. *Bull. Volcanol.*, **66**, 1–14.

Spadaro, F. R., R. A. Lefèvre, and P. Ausset (2002) Experimental rapid alteration of basaltic glass: implications for the origins of atmospheric particulates. *Geology*, **30**, 671–674.

Squyres, S. W., and 27 others (2007) Pyroclastic activity at Home Plate in Gusev Crater, Mars. *Science*, **316**, 738–742.

Squyres, S. W., R. E. Arvidson, S. Ruff, R. Gellert, R. V. Morris, D. V. Ming, L. Crumpler, J. Farmer, D. J. Des Marais, A. Yen, S. M. McLennan, W. Calvin, J. F. Bell, III, B. C. Clark, and A. Wang (2008) Discovery of silica-rich deposits on Mars by the Spirit rover. *Science*, **320,** 1063–1067.

Stolper, E. M. (1982) Water in silicate glasses: an infrared spectroscopic study. *Contrib. Mineral. Petrol.*, **81**, 1–17.

Tilley, D. B. and R. A. Eggleton (2005) Titanite low-temperature alteration and Ti mobility. *Clays and Clay Minerals*, **53**, 100–107.

Tosca, N. J., S. M. McLennan, D. H. Lindsley, and M. A. A. Schoonen (2004) Acid-sulfate weathering of synthetic Martian basalt: the acid-fog model revisited. *JGR*, **109**, E05003 05010.01029/02003JE002218.

Valley, J. W., N. Kitchen, M. J. Kohn, C. R. Niendorff and M. J. Spicuzza (1995) Strategies for high precision oxygen isotope analysis by laser fluorination. *Geochim. Cosmochim. Acta*, **59**, 5223–5231.

White A. F. and M. F. Hochella (1992) Surface chemistry associated with the cooling and subaerial weathering of recent basalt flows, *Geochimica et Cosmochimica Acta*, **56**, 3711–3721.

Wyatt, M. B. and H. Y. McSween (2002) Spectral evidence for weathered basalt as an alternative to andesite in the northern lowlands of Mars. *Nature*, **417**, 263–266.

Filename	**^{18}O/^{16}O**	**δ^{18}O, corrected**	**Error, 1σ**	**^{16}O counts**
silica_A1_1	0.0020684	8.59	0.94	5.38E+08
silica_A1_2	0.0020667	7.76	1.56	3.40E+08
silica_A1_3	0.0019461	-51.05	2.78	6.65E+07
silica_A1_5	0.0020048	-22.42	5.76	9.19E+07
silica_A1_6	0.0020967	22.39	17.8	2.33E+07
silica_A1_8	0.0019997	-24.91	1.67	1.86E+08
silica_A1_9	0.002067	7.91	1.27	3.11E+08
silica_A1_10	0.0020775	13.03	1.32	3.29E+08
silica_A2_1	0.0020821	15.27	0.86	6.54E+08
silica_A2_2	0.0020771	12.83	1.03	4.61E+08
silica_A2_3	0.002076	12.29	1.02	4.96E+08
silica_A2_4	0.0020803	14.39	12.6	3.56E+08
silica_A2_5	0.0020674	8.1	1.38	3.45E+08
silica_A2_6	0.0020171	-16.43	4.6	3.54E+07
silica_A3_1	0.0020793	13.9	0.81	7.20E+08
silica_A3_2	0.0020758	12.2	0.86	6.56E+08
silica_A3_3	0.0020767	12.64	0.87	6.42E+08
silica_A3_4	0.0020723	10.49	0.96	5.25E+08
silica_A4_1	0.0020724	10.54	1	4.64E+08
silica_A4_2	0.002061	4.98	1.12	3.84E+08
silica_A4_3	0.0020489	-0.92	2.27	1.16E+08
silica_A4_4	0.002063	5.96	1.11	3.94E+08
silica_A4_5	0.0020453	-2.68	1.6	2.09E+08
silica_A4_6	0.0020681	8.44	1.35	2.72E+08
FeTi_082108_01	0.002024814	12.44	0.21	1.64E+09
FeTi_082108_01@2	0.002032642	16.35	0.22	1.66E+09
FeTi_082108_01@3	0.002025803	12.93	0.2	1.79E+09
FeTi_082108_01@4	0.002050591	25.32	0.48	1.50E+09
FeTi_082108_01@5	0.002026639	13.35	0.18	1.62E+09
FeTi_082108_02	0.002035984	18.02	0.21	1.73E+09
FeTi_082108_02@1	0.002031118	15.59	0.13	1.81E+09
FeTi_082108_02@2	0.0020308	15.43	0.28	1.68E+09
FeTi_082108_02@3	0.002036583	18.32	0.26	1.68E+09
FeTi_082108_02@4	0.002028281	14.17	0.14	1.77E+09
FeTi_082108_02@5	0.002026476	13.27	0.21	1.73E+09

Supplementary Table 1. Oxygen isotope measurements of silica coatings, conducted on the NanoSIMS, and of Fe-Ti oxide coatings, conducted on the Cameca 7f.

Chapter III. Distribution and Temporal Evolution of Hawaiian Silica Coatings

Abstract

Young Hawaiian basalts frequently feature colorful surface coatings composed of amorphous silica and Fe-Ti oxides. The process by which these coatings form—chemical weathering of near-surface basalt by volcanically-derived acidic fluids—has been previously documented, but the timescale of coating formation and factors controlling coating coverage heterogeneity were largely unconstrained. Young lava flows (of varying ages, from hours to ~40 years) along Kilauea's southwest and east rift zones and at Mauna Loa were visited and investigated to determine the extent of silica coating distribution. Coating thickness varies as a function of flow age, flow surface type, proximity to acid sources like regional volcanic plumes, and climatic parameters such as rainfall and average annual temperature. Siliceous alteration was observed on basalt surfaces as young as 8 days old. Implied rates of silica coating growth observed in this study were as high as 3–5 µm/year. Coatings form preferentially on flow surfaces with glassy outer layers, including spatter ramparts, volcanic bombs and dense pahoehoe breakouts, potentially because these layers have been strain-weakened by deformation during cooling. Physical erosion removes the coatings from surfaces with mm-scale topography. The observations presented here are most consistent with coating formation by dissolution of near-surface basalt, coupled with *in situ* precipitation of amorphous silica.

1. Introduction

Young Hawaiian lava flows frequently feature white, yellow, blue, orange or red surface coatings (Farr and Adams, 1984; Curtiss et al., 1985; Dorn, 1995; Minitti et al., 2007; Chemtob et al., 2010). The coatings are composed primarily of amorphous silica and are understood to represent chemical weathering products resulting from interaction of volcanically derived acids with fresh basaltic surfaces. The presence of silica coatings modifies the visual appearance and thermal infrared and visible/near-IR reflectance spectroscopic signatures of the basalt substrate (Kraft et al., 2003; Seelos et al., 2010). Along with physical weathering and other chemical reactions such as oxidation, the development of silica coatings produces a predictable spectral evolution of basalt surfaces that allows remote mapping and relative dating of lava flow fields (Kahle et al., 1988; Crisp et al., 1990; Abrams et al., 1991; Byrnes et al., 2004). Similar coatings have been reported on basalts in other active volcanic landscapes (Fulignati et al., 2006; Prinsloo et al., 2010) and have been suggested to occur on the surface of Mars (Skok et al., 2010). Thus, understanding the properties, formation mechanisms, and formation rates of Hawaiian silica coatings may contribute to problems related to landscape evolution and chemical weathering in a variety of geological settings.

Numerous formation mechanisms have been demonstrated and/or proposed for the formation of silica coatings and cements on young Hawaiian flows, including leaching of near surface glasses (Minitti et al., 2007; Chemtob et al., 2010), dissolution-reprecipitation of windblown particulates (Farr and Adams, 1984; Curtiss et al., 1985), and transport and deposition of externally derived Si in solution (Schiffman et al., 2006). However, a number of issues regarding the formation and distribution of silica coatings remain poorly understood. First, the timing and rate of coating formation are poorly constrained. The dissolution rates of basaltic glass have been studied experimentally by many researchers (Oelkers and Gislason, 2001; Gislason and Oelkers, 2003; Tosca et al., 2004; Hurowitz et al., 2005); however, *in situ* weathering rates may be orders of magnitude lower than those measured experimentally (White and Brantley, 2003). Reports of rates of silica coating formation on fresh basalts vary widely. Just-erupted Pele's tears and hairs from Masaya Volcano, Nicaragua, featured siliceous alteration layers several μm thick, formed within hours from exposure to the plume (Moune et al., 2007). In an experiment in which basaltic glass spherules were exposed to the acid plume of Etna, Murano, Italy, chemical alteration was visible after just 4 hours and ~10 μm Si-rich leached layers were present after 63 days (Spadaro et al., 2002). In contrast, Crisp et al. (1990) observed the remote spectral signature of amorphous silica coatings only on lava flows at least three years old. Also poorly understood is the physical and chemical evolution of the coatings post-formation.

In a previous study, we observed the chemistry, mineralogy and morphology of silica coatings from a single lava flow in the Ka'u Desert, along the Southwest Rift Zone (SWRZ) of Kilauea (Chemtob et al., 2010). In this chapter, we expand these observations to include field and laboratory descriptions of alteration products of basaltic samples from several Kilauea and Mauna Loa locales of a variety of ages. We document how the chemistry and morphology of these coatings vary as a function of age, proximity to acid sources, and environmental conditions. This information is used to assess the rates and mechanism of coating formation and to understand the post-depositional history and present-day distribution of coatings across the Hawaiian landscape.

Sampling Location/ *Sample Name*	**Sample Description**	**Eruptive age**	**Collection Date**	**Age Upon Collection**	**Waypoint number**
Ka'u Desert, Kilauea SWRZ					
KD-003a	Spatter rampart with white coatings	1974	2010	36 years	1
KD-003c	Traverse: pahoehoe, 1 m NW of rampart				
KD-003e	Traverse: pahoehoe, 10 m NW of rampart				
KD-003g	Traverse: pahoehoe, 40 m NW of rampart				2
KD-Mar10-004	Coated pahoehoe at southeast edge of 1974 flow				3
Keanakakoi Crater					
KK	Spatter ramparts near southeast rim of crater	1974	2012	38 years	4
Mauna Ulu, summit region					
MU-014	Pahoehoe slab from walls of near-summit channel	1969	2010	41 years	5
MU-017c	Shelly pahoehoe with coatings on shell underside	1969-73	2010	37-41 yrs.	6
Mauna Ulu, medial flow field					
MU-029	P-type pahoehoe breakouts with bright coatings	1969-73	2010	37-41 yrs.	7
Napau Crater, Episode 54 eruption					
NC-97-011b	Spatter rampart in center of Napau Crater	1997	2010	13 years	8
Pu'u O'o summit lavas, Episode 55					
Jul10-PU-009	Volcanic bombs strewn on overflow lava surface	1998[a]	2010	< 12 years[a]	9
Jul10-PU-010	Doubly-coated shelly pahoehoe	1998	2010	12 years	
Pu'u O'o summit lavas, Episode 58					
Jul10-PU-011	Spatter adjacent to fissure vent, initial Episode 58 activity	2007	2010	3 years	10

Table 1. Sampling locations and samples discussed in this study. Waypoint coordinates are presented in Table A1.

[a] These bombs were deposited on 1998 lavas, therefore postdating them, but their eruptive age is unknown.

Sampling Location/ *Sample Name*	**Sample Description**	**Eruptive age**	**Collection Date**	**Age Upon Collection**	**Waypoint number**
Episode 58 distal flow field					
TEB-020	Hornito sample	April 2010	July 2010	3 months	11
KP-017	Dense blue pahoehoe on near-shore lava plains	2007	2010	3 years	12
Kamoamoa 2011 eruption					
KE59-2941[b]	Spatter deposited on older tephra, collected while still hot	Mar. 6, 2011	Mar. 6, 2011	< 1 day	13
KE59-2952[b]	Spatter deposited on older tephra	Mar. 5, 2011	Mar. 6, 2011	1 day	14
KE59-2970[b]	Spatter deposited on older tephra	Mar. 5, 2011	Mar. 10, 2011	5 days	
KE59-2979[b]	Spatter deposited on older tephra	Mar. 6, 2011	Mar. 14, 2011	8 days	15
KE59-2980[b]	Spatter deposited on older tephra	Mar. 9, 2011	Mar. 14, 2011	5 days	16
NC-11-008	Iridescent lava from main spatter rampart	March 2011	March 2012	1 year	17
NC-11-010	Volcanic bomb adjacent to main spatter rampart				
NC-11-015	Spatter deposited on older tephra				18
Mauna Loa, 1984 eruption					
Mar12-ML-NS-024	Lava from near-summit spatter rampart	1984	2012	28 years	20
Mar12-ML-PL-001	A'a with powdery white deposit				21
Mar12-ML-PL-005	Rafted pahoehoe chunk with orange-red color				22

Table 1. (continued)

[b] Samples collected and provided by Tim Orr (HVO-USGS)

2. Sampling Locations

Basalt samples were collected in and around Hawaii Volcanoes National Park during three field seasons in March 2010, July-August 2010, and March 2012. Sampling sites are mapped in Figures 1, 2, 3 and 4 and described in Table 1 and Table A1. Sites were selected to provide a range in flow surface age, flow surface type, proximity to gas plumes, and climatic conditions. Flow ages at the time of collection ranged from essentially zero (still-flowing lavas near Kalapana and spatter samples at Kamoamoa) to 42 years (Mauna Ulu flows). Except for the active flows on the pali above Kalapana, which were accessed by helicopter, all sampling sites were accessed by foot. All samples were collected by the author, except for spatter samples from the 2011 Kamoamoa eruption collected days after emplacement by HVO-USGS personnel.

3. Analytical Methods

Micro-images of Hawaiian samples were acquired by scanning electron microscopy (SEM), using a LEO 1550 VP field emission SEM at Caltech. Both cross-sectional thick sections and natural surfaces of basalts were observed. Thick sections were prepared using Burnham Petroepoxy resin and curing agent and were polished to 0.3 μm using diamond and alumina polishing papers. Backscattered electron (BSE) and secondary electron (SE) images were acquired at a 9–12 mm working distance and at a range of magnifications, using 10 kV accelerating voltage. Kα x-ray intensity maps of Si, Mg, Al, Ca, Fe, Ti, Na, F, and/or K were collected using an Oxford X-Max SDD energy-dispersive spectrometer (EDS) system.

Coating thicknesses were determined by one of several methods. For select samples, thicknesses were measured directly by SEM from cross-sectional thick sections, prepared as described above. Coating thicknesses could also be estimated from SEM images of natural surfaces by finding the edges of coated regions and measuring the length of the exposed coating edge (e.g., **Fig. 18c**). For other samples, a “scratch

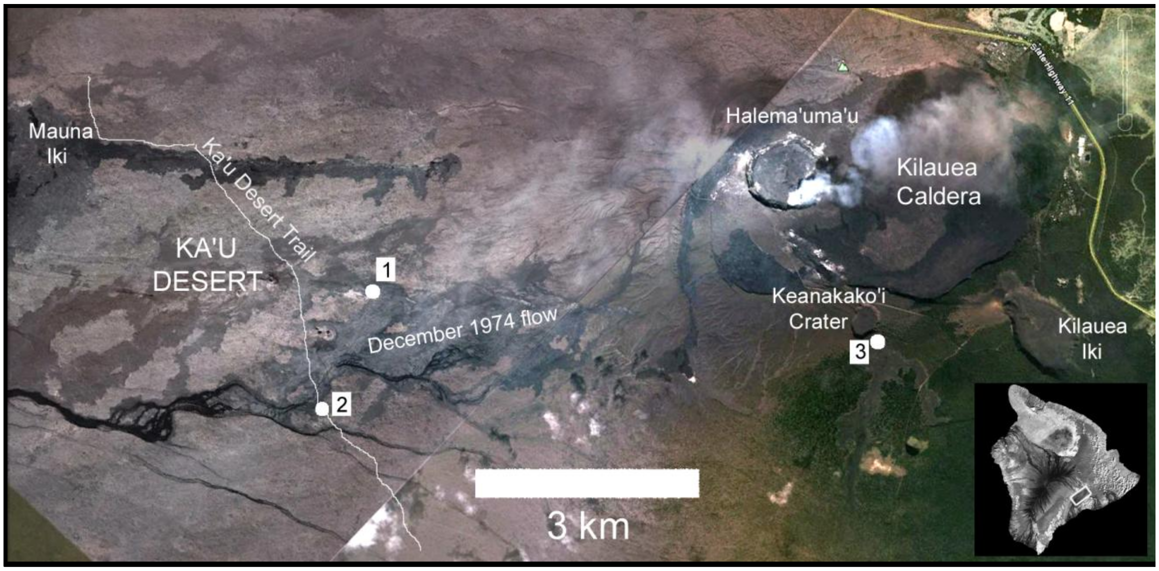

Figure 1. Google Earth imagery of Kilauea's summit and southwest rift zone. Sampling sites 1, 2, and 3 are indicated. Landsat image of Hawai'i provided as reference.

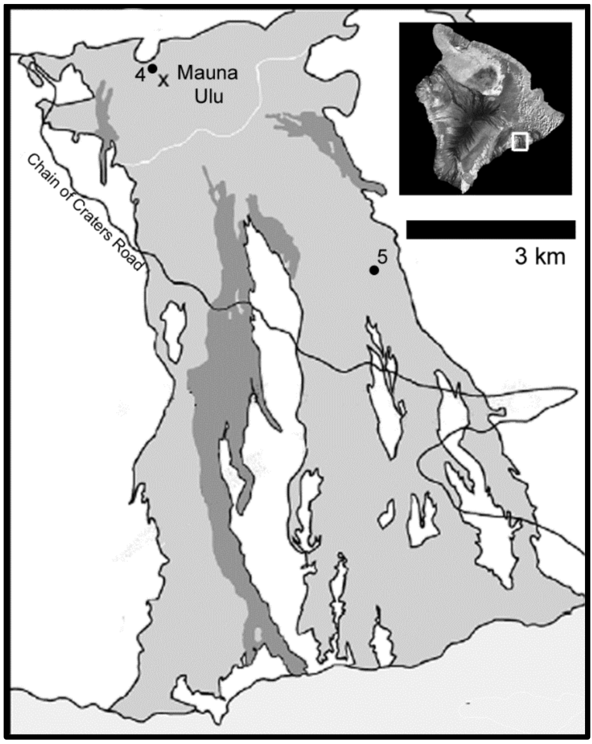

Figure 2. Sketch map of the Mauna Ulu flow field, modified from Byrnes et al. (2004). Dark gray regions are a'a lobes. Sampling sites 4 and 5 are indicated.

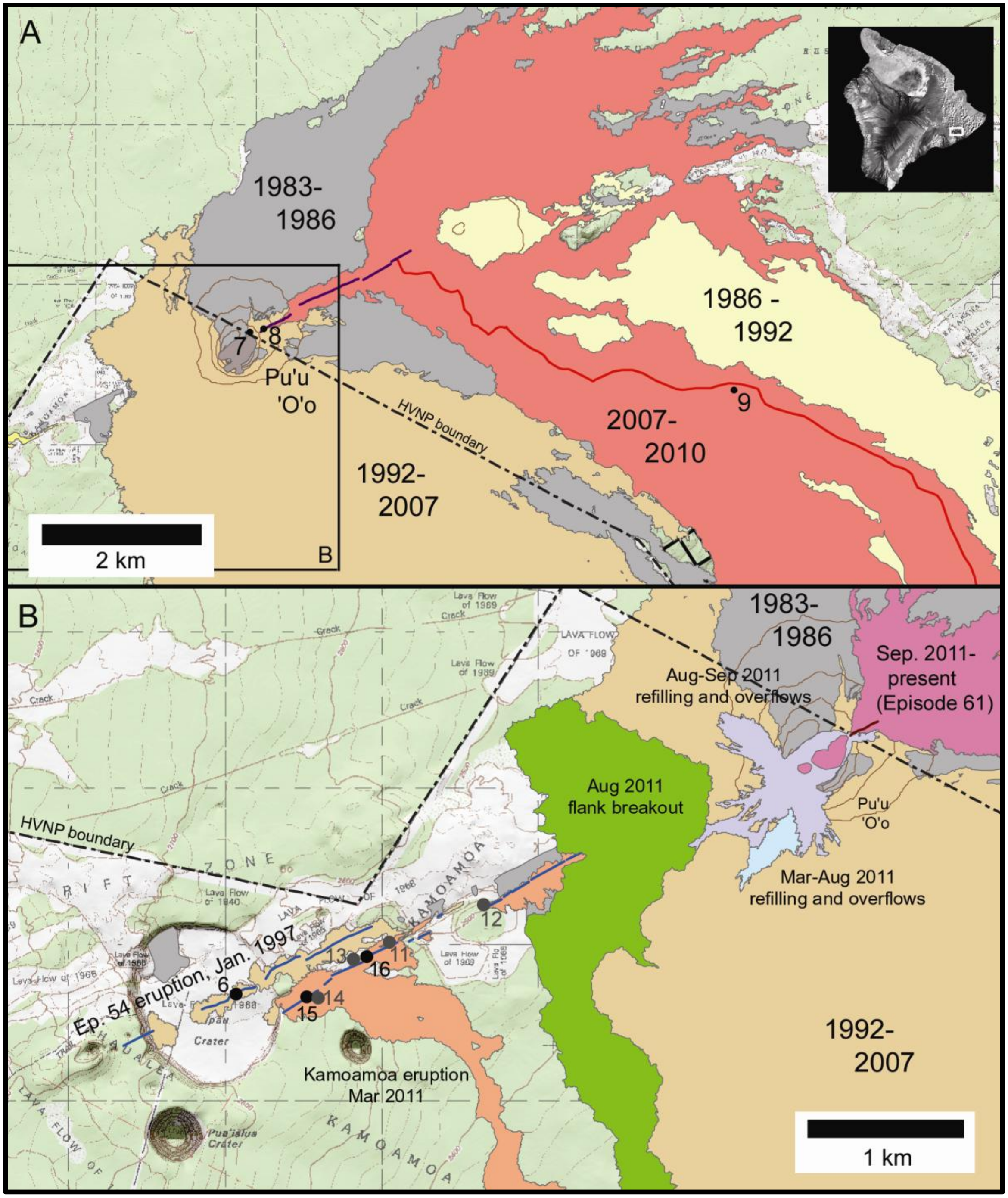

Figure 3. Geologic maps of the Pu'u O'o region of Kilauea's East Rift Zone, courtesy of Tim Orr (HVO-USGS). a) Summit of Pu'u O'o as it appeared in July 2010. Sampling sites 7, 8, and 9 are indicated. The dashed line is the national park boundary. The black box indicates the region depicted in the next map. b) Napau Crater, Kamoamoa and Pu'u O'o as they appeared in October 2012. Sampling sites 6 and 11–16 are indicated. Sites 11–14 (depicted in dark gray) were sampled during and immediately after the 2011 Kamoamoa eruption by USGS personnel. Samples at sites 15 and 16 were collected one year after eruption. Note that the currently active Episode 61 flow field has buried sampling site 8 (formerly on the NE face of Pu'u O'o)

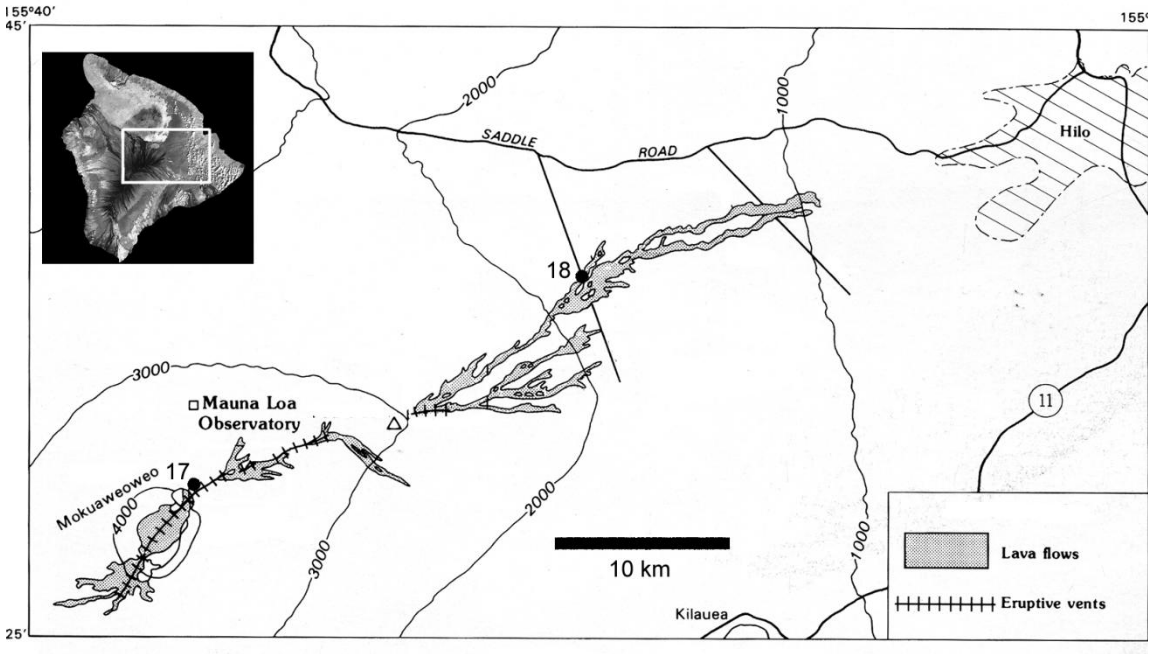

Figure 4. Sketch map of the 1984 flow along the northeast rift zone of Mauna Loa, modified from Lockwood et al. (1987). Sampling sites 17 and 18 are indicated.

test" was employed to determine coating thickness. Natural coated surfaces were abraded using an iron needle or paper clip, removing the coating but leaving the basalt substrate undamaged. Coating thicknesses were then estimated by incremental z-adjustments of the sample stage on a Nikon petrographic microscope.

Major and minor element compositional data of silica coatings and basalts were acquired by electron probe microanalysis (EPMA) using a JEOL JXA-8200 at Caltech. Phase identification of alteration materials was achieved by Raman spectroscopy.

4. Results

4.1. Sample Descriptions

Field and SEM imagery of sites and samples investigated in this study are given in Figures 5-19. Detailed descriptions of these sites and samples can be found in the Appendix. These results are summarized in Table 2 and discussed below.

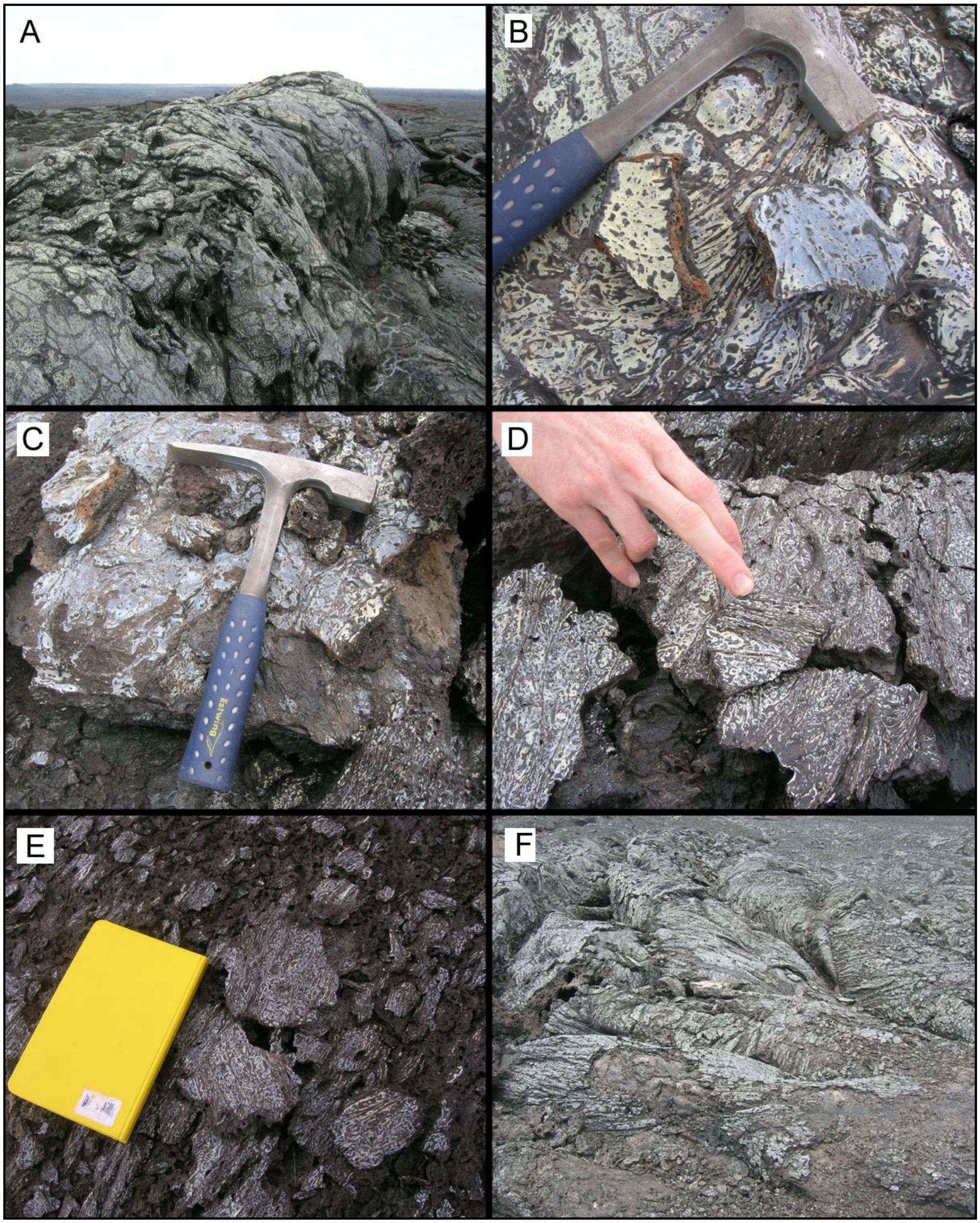

Figure 5. December 1974 flow, Ka'u Desert, Kilauea SW Rift Zone. a) A coated spatter rampart. b) The surface of the spatter rampart from (a). A traverse was conducted perpendicular to the trace of the spatter rampart to observe changes in morphology: coated lavas c) 1 m, d) 10 m and e) 40 m NW of the spatter rampart in (a). f) Coatings on SE edge of 1974 flow, 1.5 km from trace of the SWRZ.

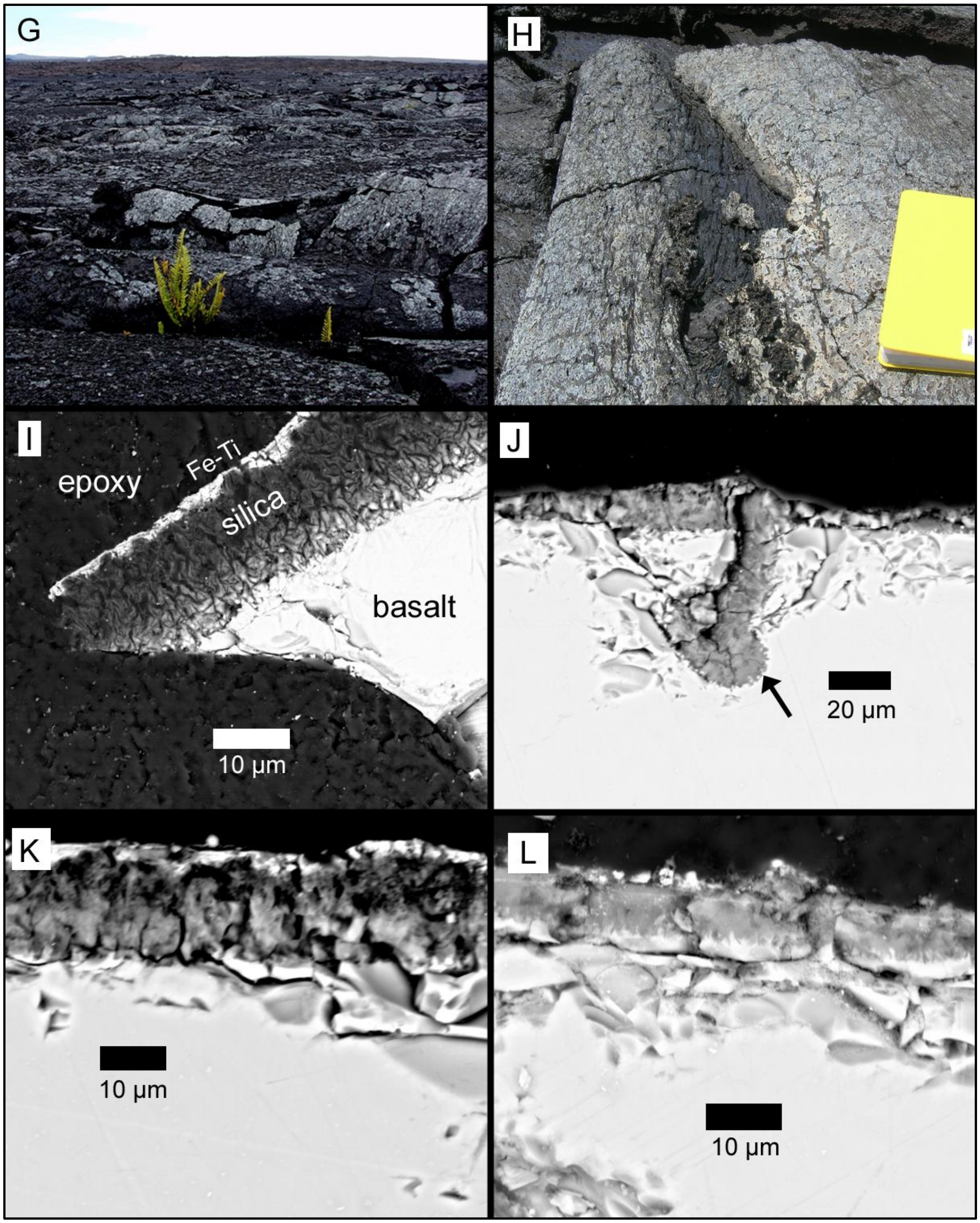

Figure 5 (continued). g) Coatings in the Ka'u Desert are slow to form or re-form on spalled surfaces. h) Topographic control on heterogeneous coating coverage. i) BSE image of silica coating morphology from the spatter rampart. j) Penetration of silica layer into basalt substrate along a surface crack. k) Silica coating of sample KD-003e, shown in (d). l) Coating morphology of sample KD-003g, shown in (e).

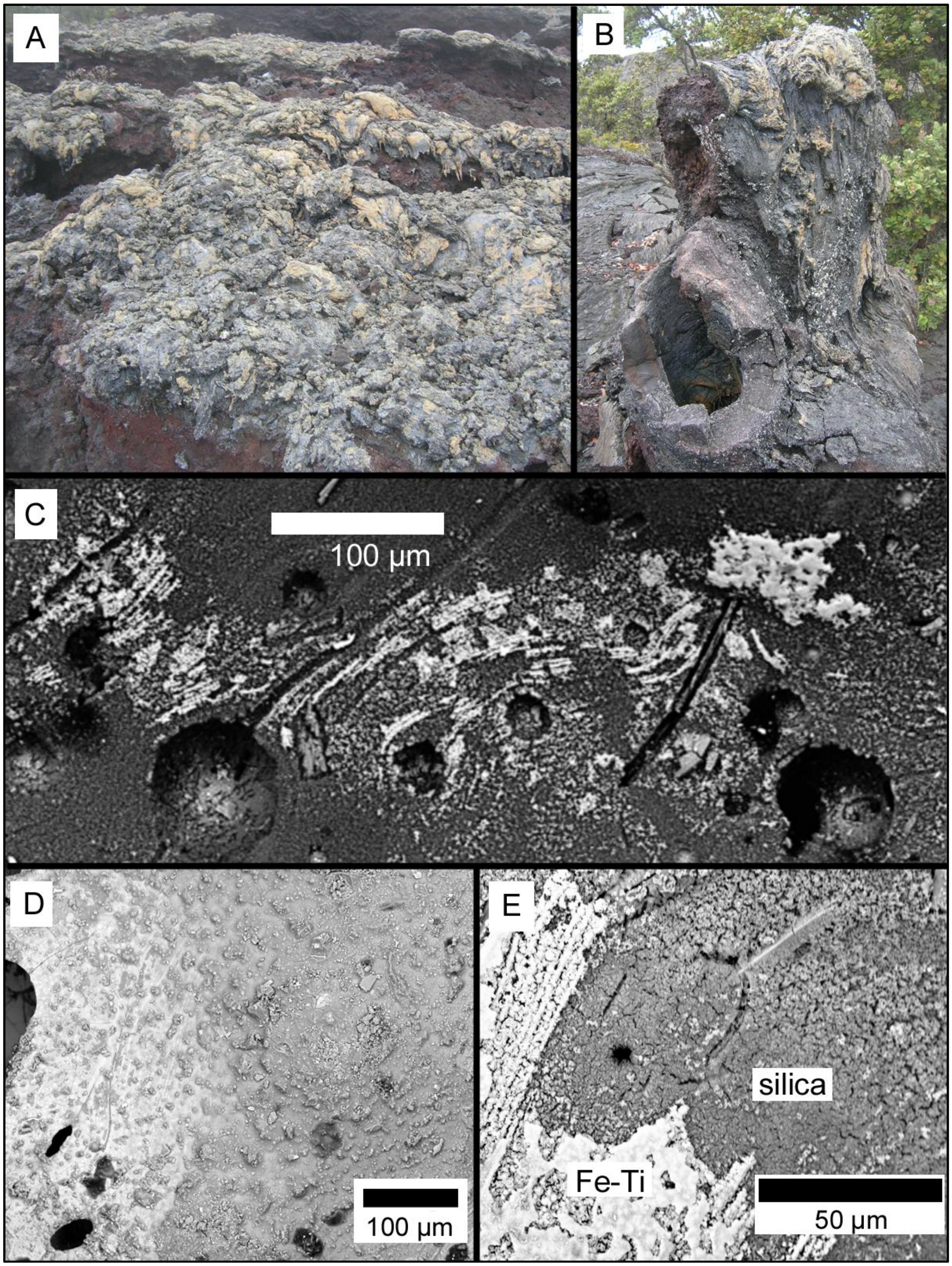

Figure 6. South rim of Keanakakoi Crater, 1973 lavas. a) Coated spatter ramparts. b) Coatings forming on dripping spatter on a lava tree. c) BSE image of the natural surface of sample KK. Fe-Ti coating is the bright material; at right, the coating appears massive, but to the left it appears lineated. d) Coated surface of sample KK. Bright material at left is Fe-Ti rich; glazed surface with particulate nubs at right is amorphous silica. e) Alternate silica coating morphology, with abundant desiccation cracks and "popcorn" texture, capped by Fe-Ti coating.

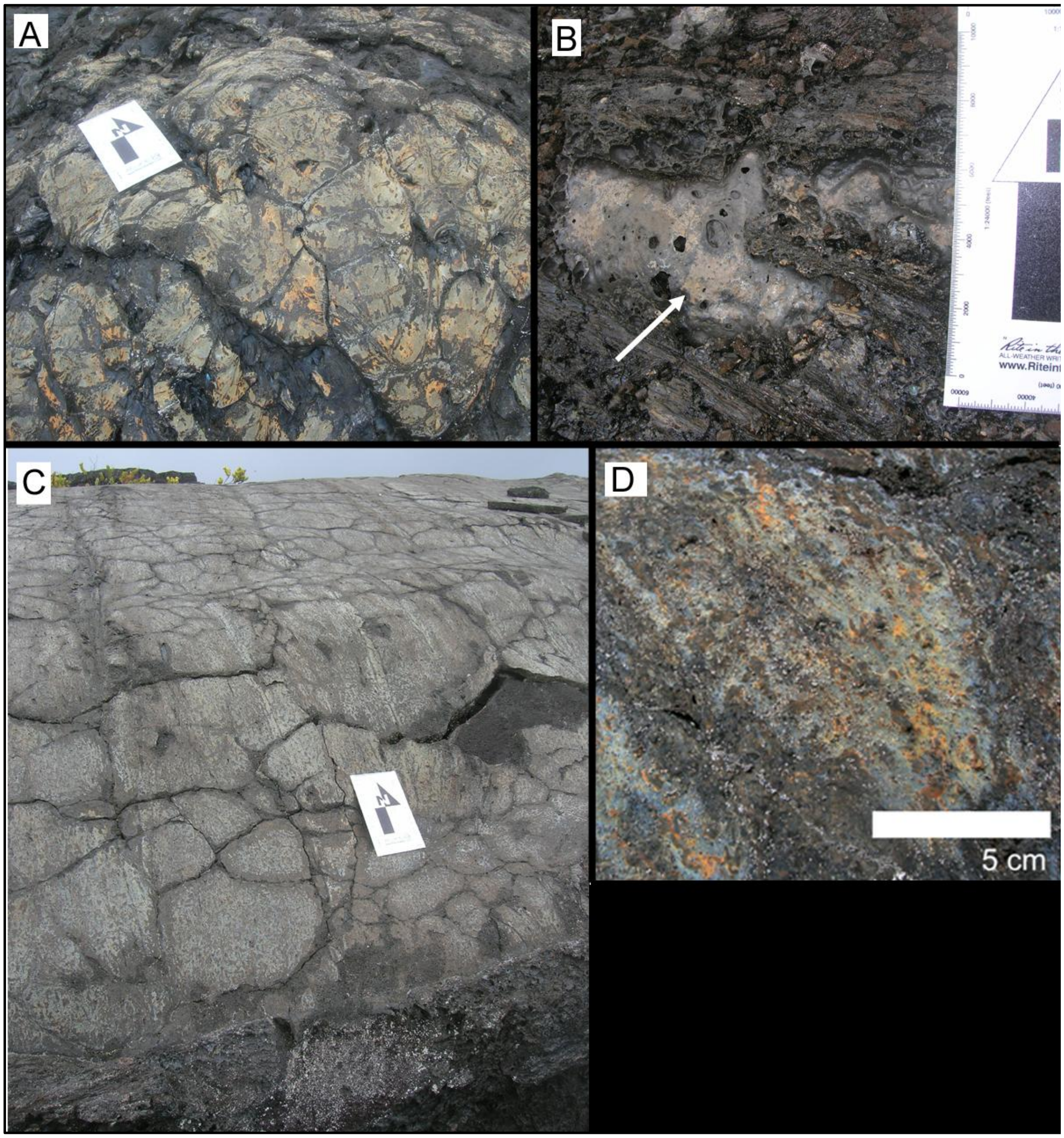

Figure 7. Mauna Ulu, near-summit region. a) Coatings on spatter rampart at 1969 fissure west of summit. b) Pale coatings re-forming on spalled surface, 100 m south of spatter rampart from (a). c) Walls of lava channel on north slope of Mauna Ulu summit. d) Micro-topographic control on coating alteration and removal.

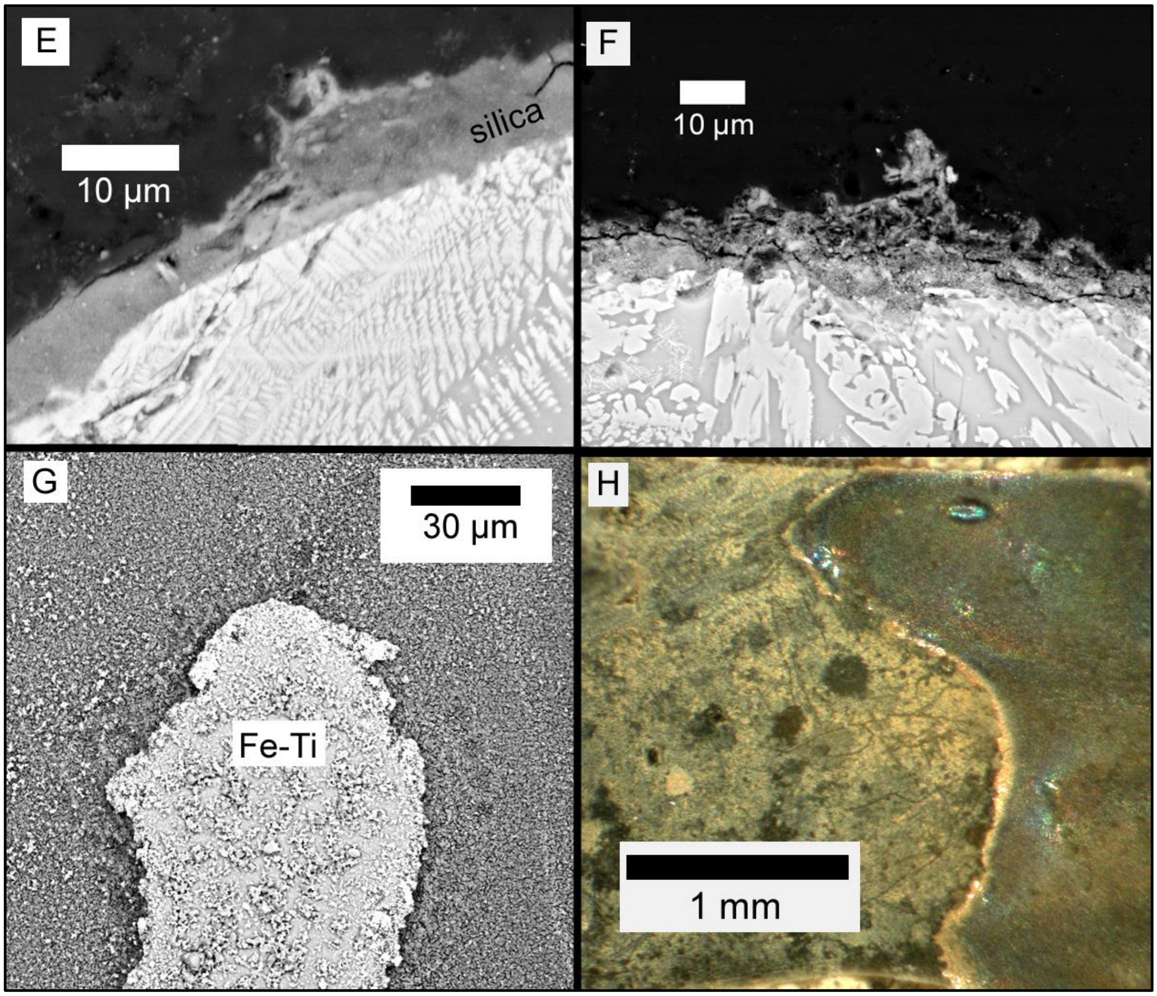

Figure 7 (continued). e) BSE image of silica coating on sample MU-017c. f) BSE image of silica coating on sample MU-017c, with some evidence for selective dissolution of glass, leaving dendritic pyroxenes intact. g) BSE image of natural surface of sample MU-014, with bright Fe-Ti coating strip capping silica-coated surface. h) Deflational texture on Mauna Ulu summit sample, in which surface regions with minimal alteration (right) sit several μm higher than regions with more extensive silica coatings (left).

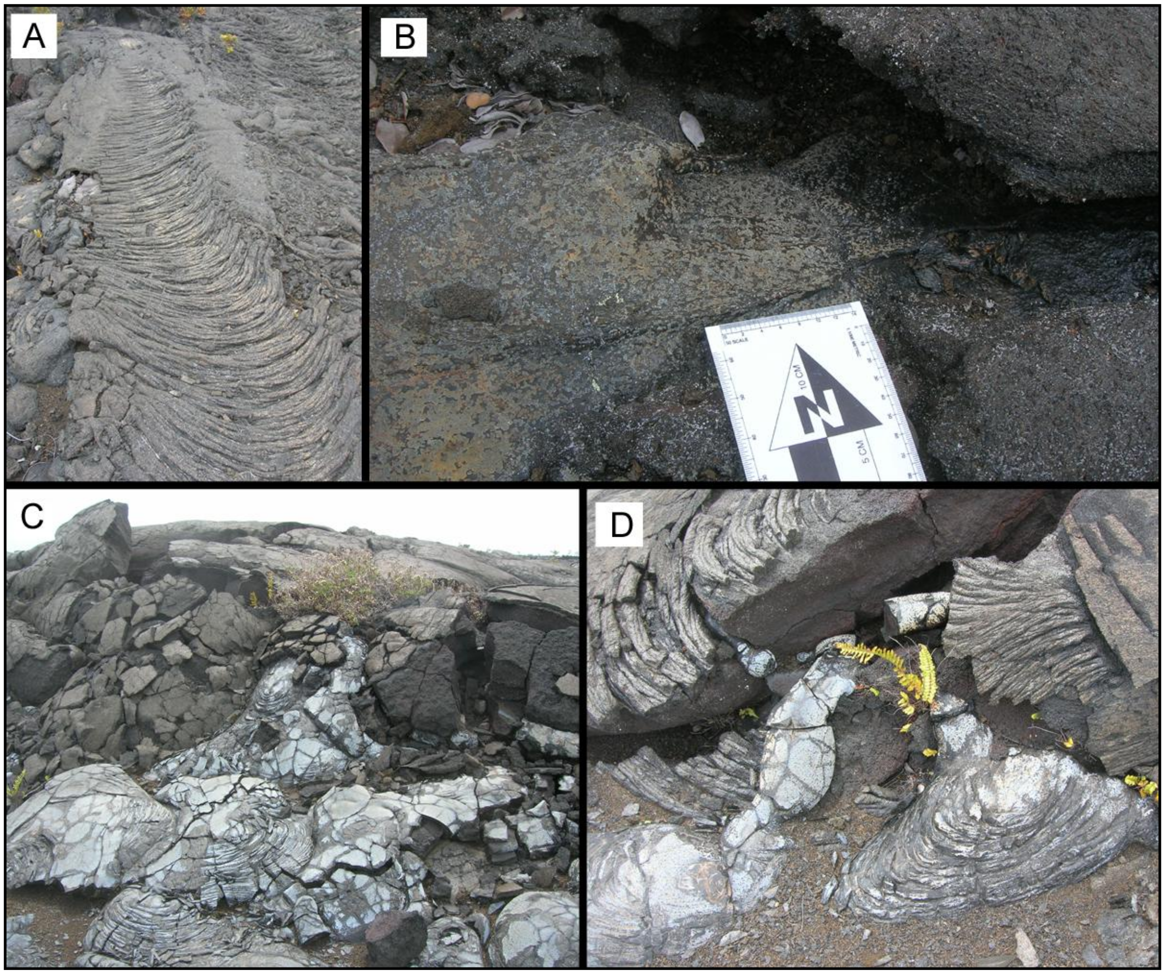

Figure 8. Mauna Ulu distal flow field. a) Coatings preferentially formed or preserved on flow axis of pahoehoe ropes. b) Coating petering out underneath lava awning. c) Dense, highly degassed, heavily coated lavas extruding from a tumulus. d) Detail of site of extrusion from (c).

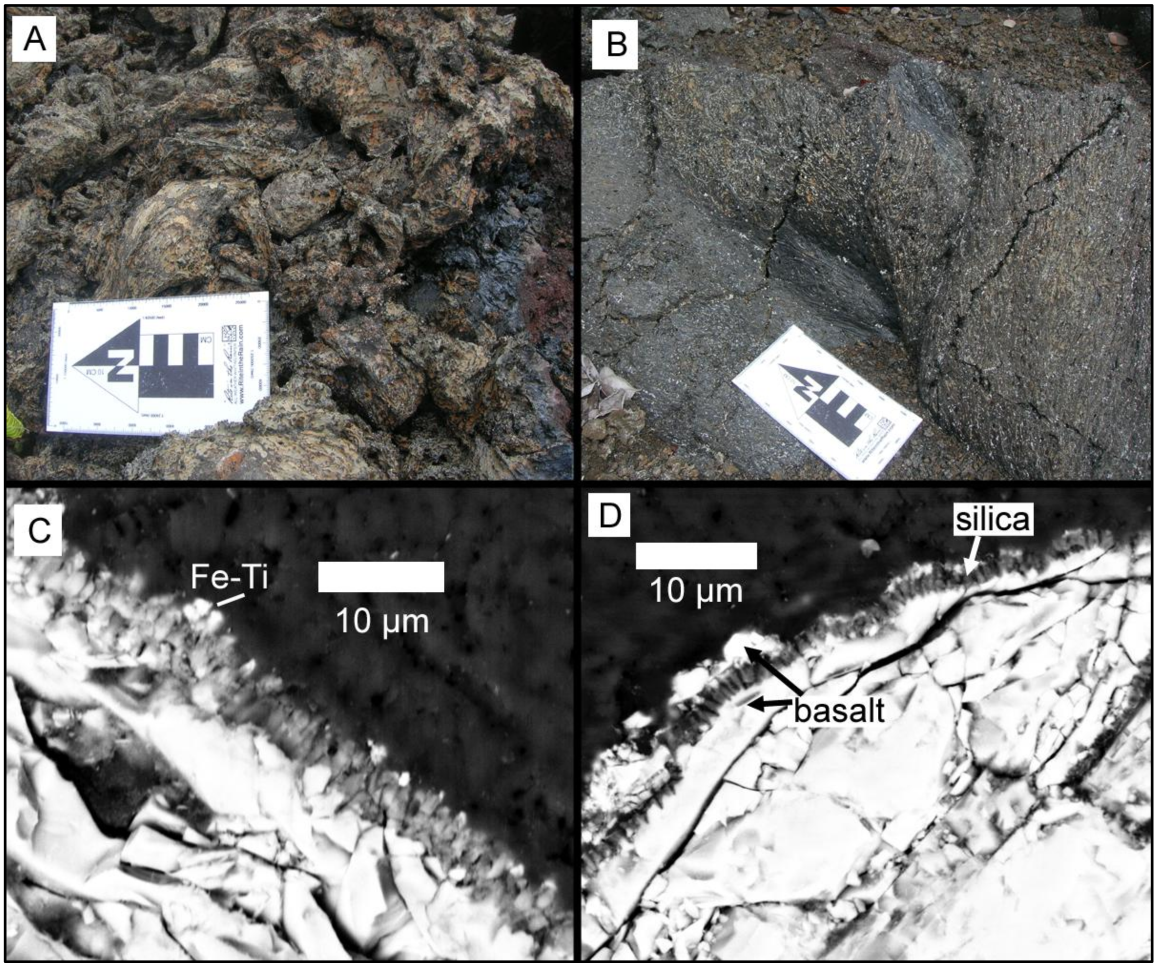

Figure 9. Napau Crater 1997 fissure eruption. a) Coated spatter ramparts along fissure. b) Sparse coatings on pahoehoe toes at northernmost extent flow, ~100 m from fissure. c) BSE image of thin silica coatings with bright Fe-Ti oxides at edge. d) Silica alteration penetrates a near surface crack at left.

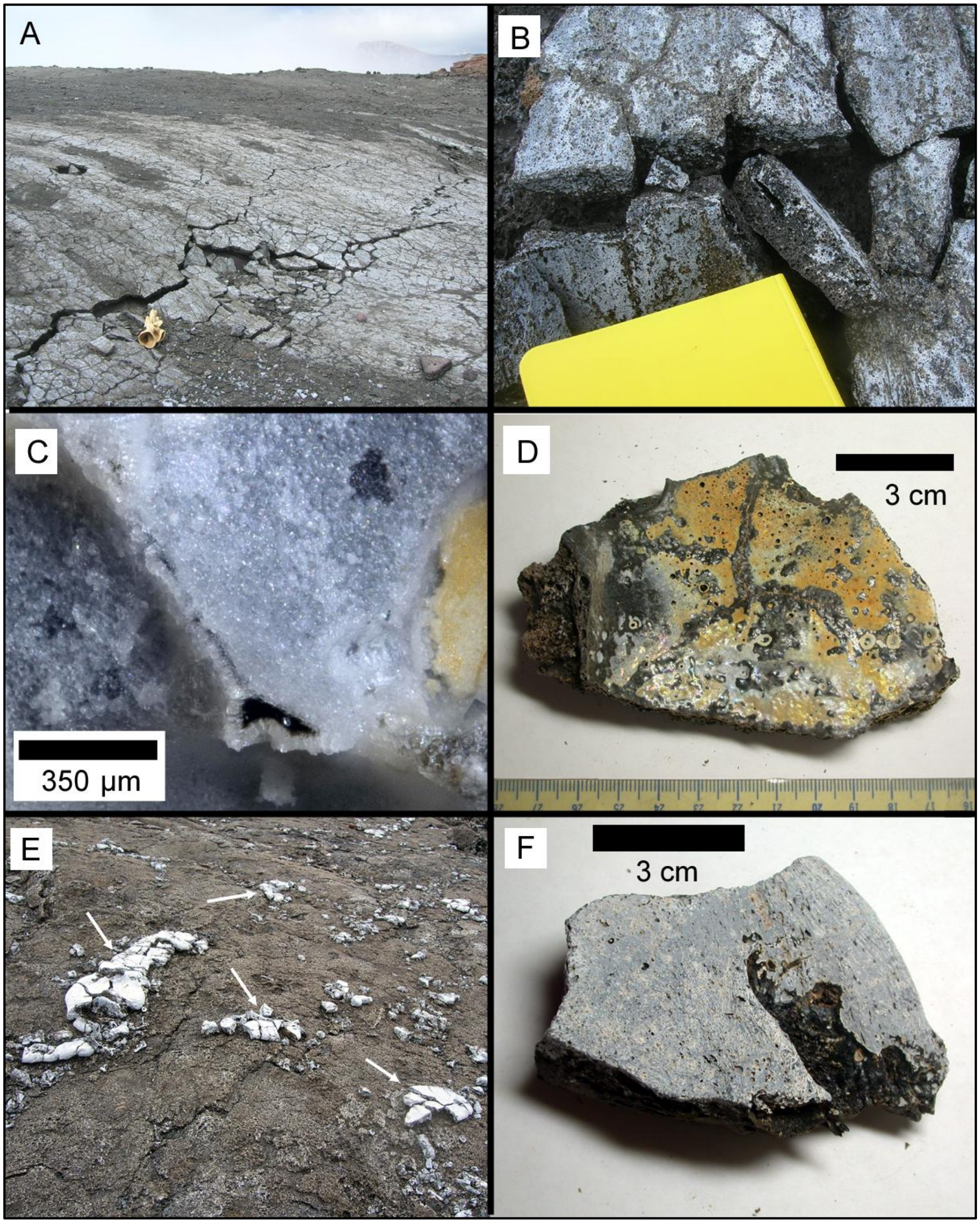

Figure 10. Pu'u O'o summit, 1998 overflow lavas. a) Bright, highly visible coatings at summit. Pu'u O'o rim visible in background. b) Field appearance of coatings on 1998 overflow lavas. Coatings appear along major surface cracks. Notebook for scale. c) Visible light image of coatings on sample PU-010, collected with a long-focus digital microscope. d) Underside of PU-010 pahoehoe shell, displaying white, yellow and orange coatings. e) Volcanic bombs of unknown age strewn across the near-rim surface. f) Sample PU-009, one of the volcanic bomb fragments from (e).

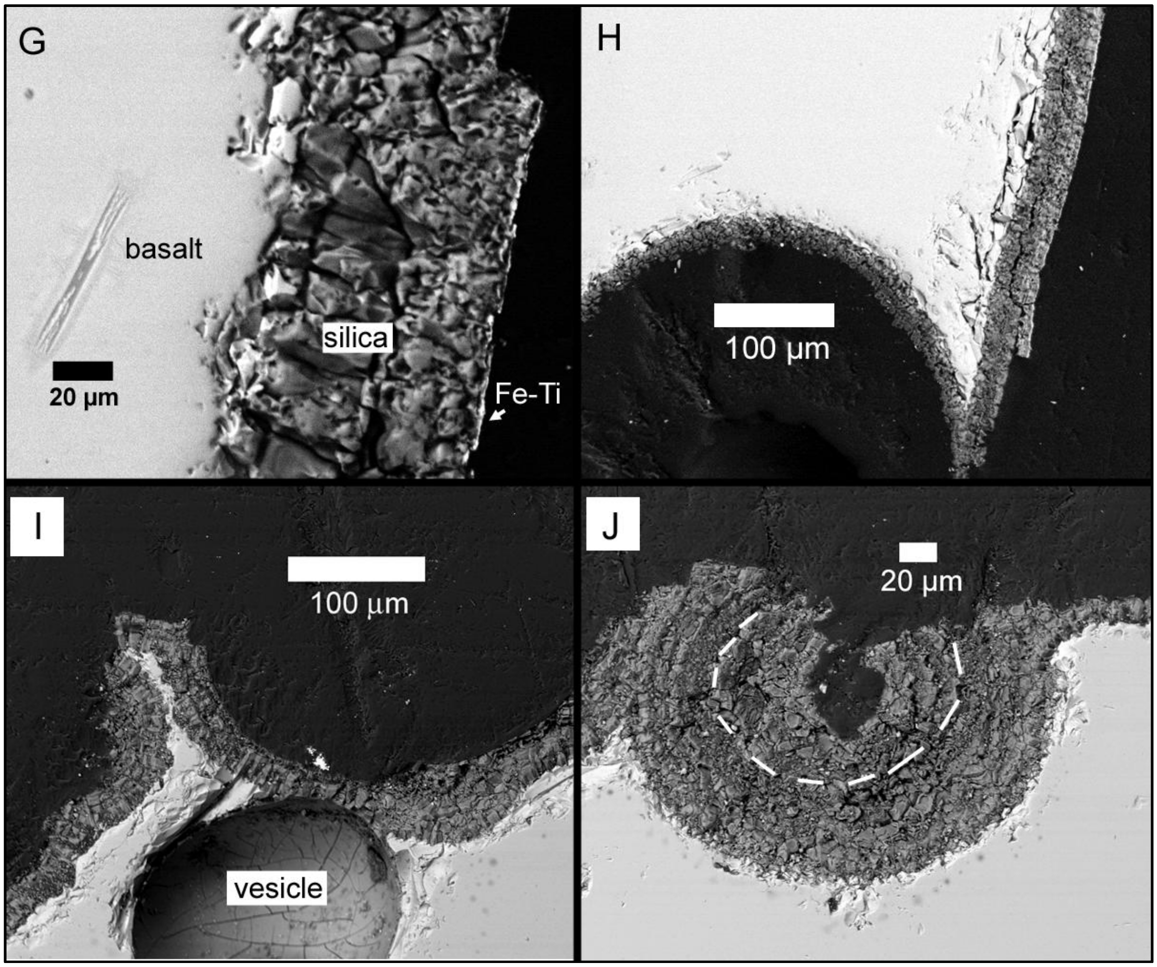

Figure 10 (continued). g) BSE image of silica coating on underside of sample PU-010. h) BSE image of silica coatings on upside of sample PU-010. i) BSE image of silica coating on sample PU-009. The silica coating bridges a near-surface vesicle, consistent with a residual or replacement mechanism. j) Silica-infilled vesicle on sample PU-009. Concentric layers are apparent in the silica deposit (one layer is marked by the white dotted line), suggesting chemical deposition.

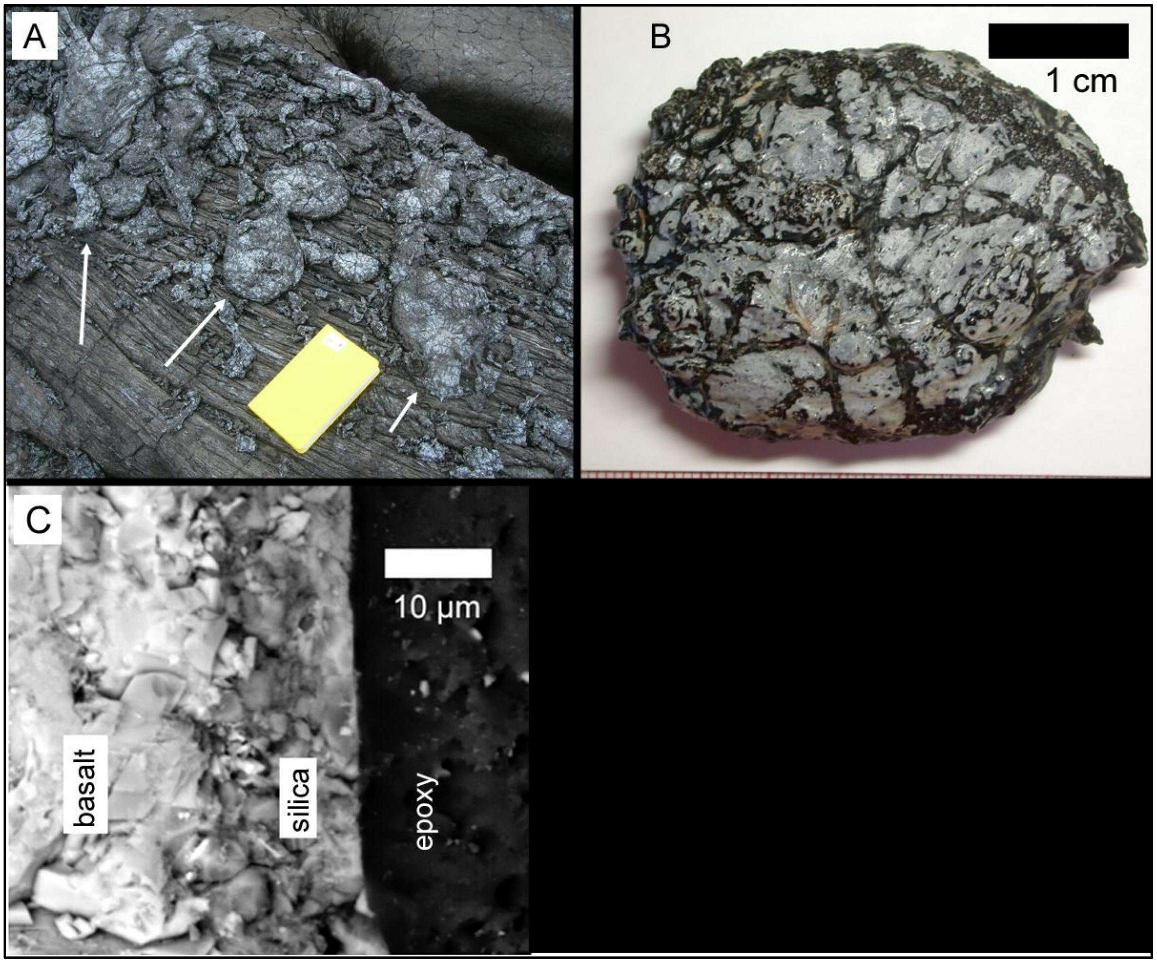

Figure 11. Pu'u O'o summit, Episode 58 initial eruptive activity, 2007 lavas. a) Brightly coated spatter adjacent to fissure vent (marked by arrows). b) Sample PU-011, spatter collected as in (a). c) BSE image of silica coating on sample PU-011.

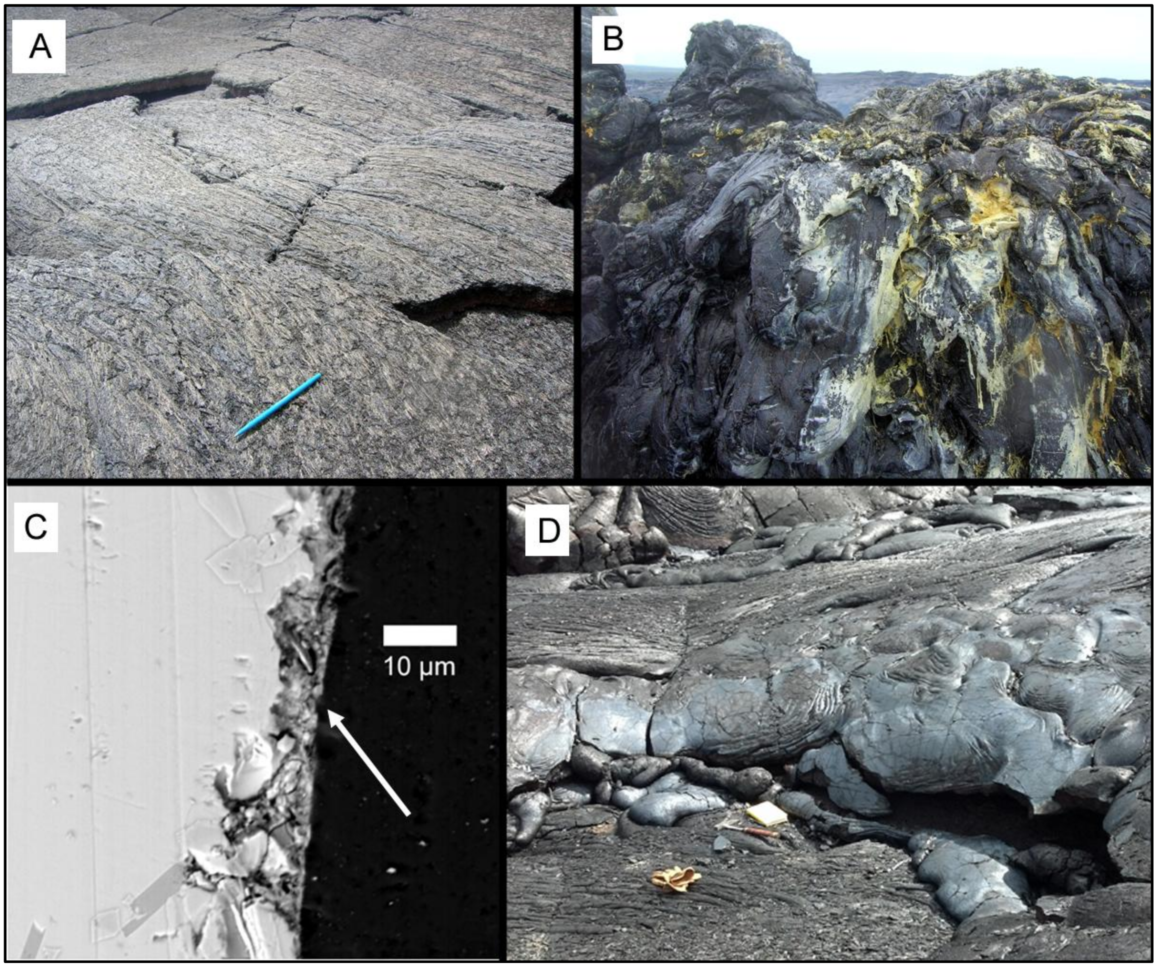

Figure 12. Episode 58 distal flow field lavas, 2007-2010. a) Spalled S-type pahoehoe with no apparent alteration. b) Hornito on distal flow field, 1 month old at time of study. White and yellow material is sulfur. c) Irregular Si-rich coating on sample TEB-020, dark basalt from hornito surface. d) Dense blue pahoehoe, emplaced in 2007, near Kalapana coast.

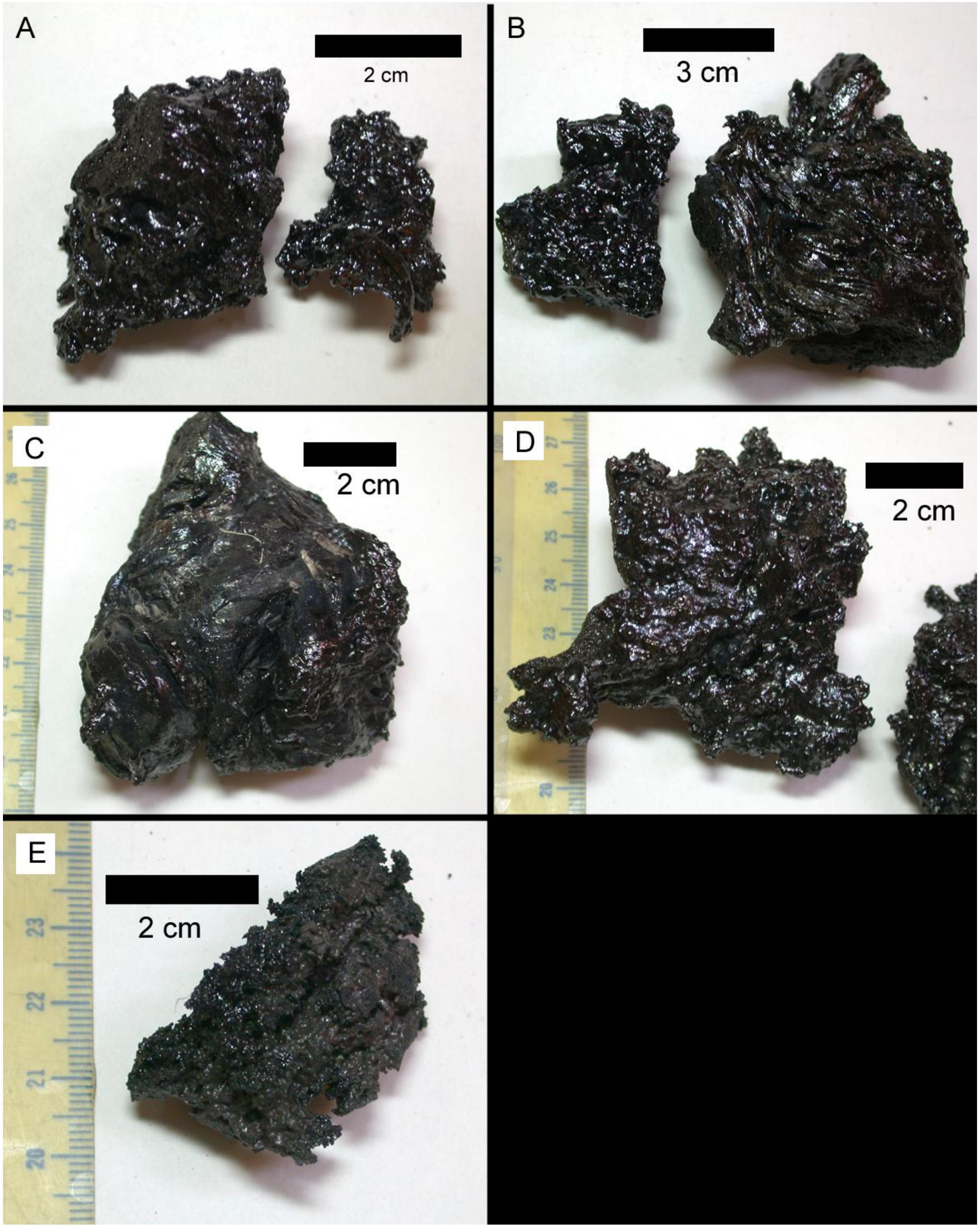

Figure 13. Spatter samples from Kamoamoa 2011 eruption, collected by Tim Orr (USGS). a) Sample KE59-2941, collected while still warm. b) Sample KE59-2952, 24 hours old at time of collection. c) Sample KE59-2970, 5 days old at time of collection. d) Sample KE59-2979, 8 days old at time of collection. e) Sample KE59-2980, 5 days old at time of colleciton.

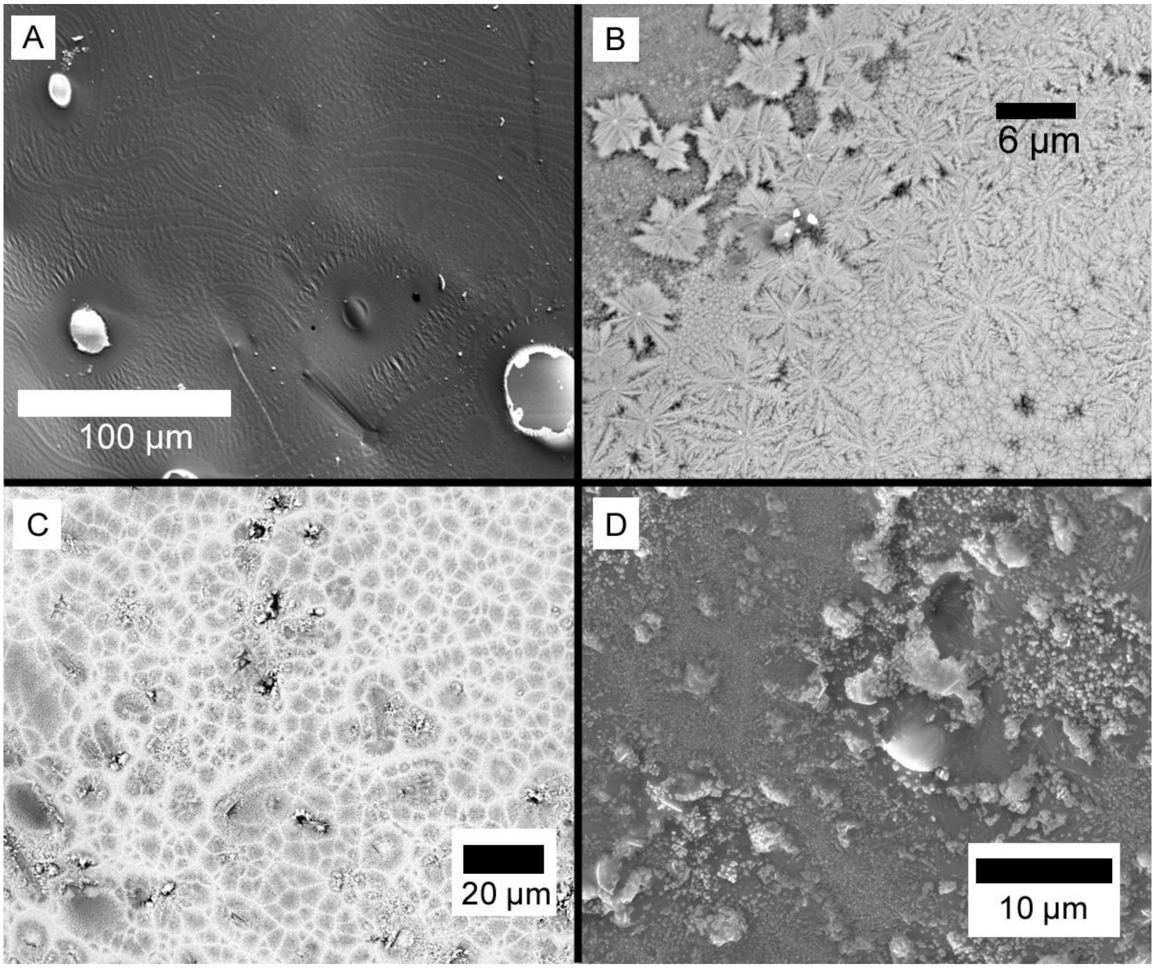

Figure 14. Micro-morphology of fresh Kamoamoa spatter samples. a) Secondary electron image of KE59-2941, showing crinkle ridge morphology. b) BSE image of KE59-2970. Bright material is Fe-rich coating, present both as bunches of dendritic crystals and as amorphous masses. c) Fe-rich material on sample KE59-2980. d) Particulate matter on surface of KE59-2980.

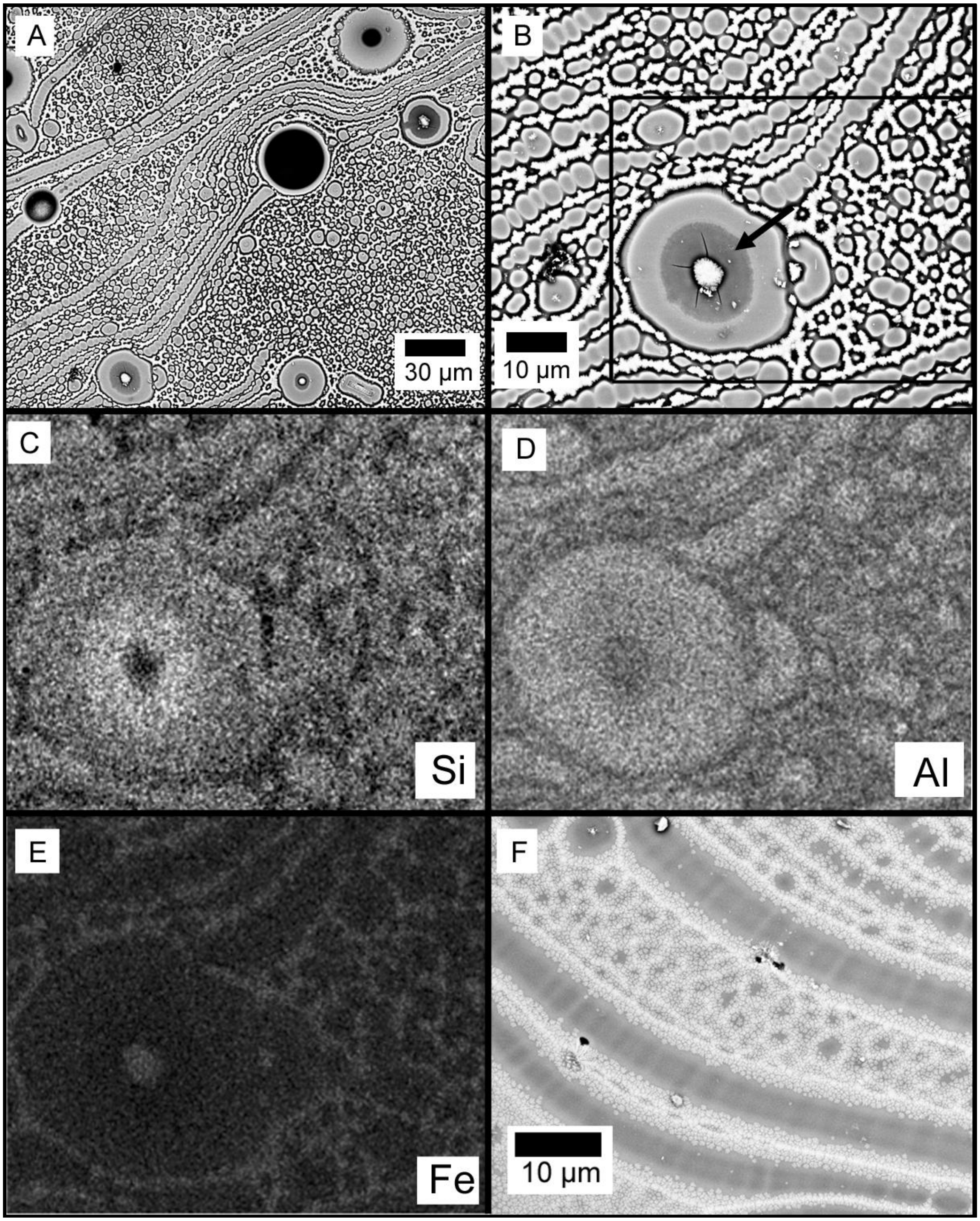

Figure 15. Micro-morphology and chemistry of sample KE59-2979. a) Pockmark-covered surface, showing primary deformation lineation texture. b) Zoomed view of large pockmark at lower left of (a). Dark material with desiccation cracks in center is amorphous silica. Bright material appearing between pockmarks is apparently fine-grained bunches of Fe-rich material. EDS elemental maps of the region indicated by the box are shown for the following elements: c) Si, d) Al, and e) Fe. f) Polygonal platelet morphology of Fe-rich material.

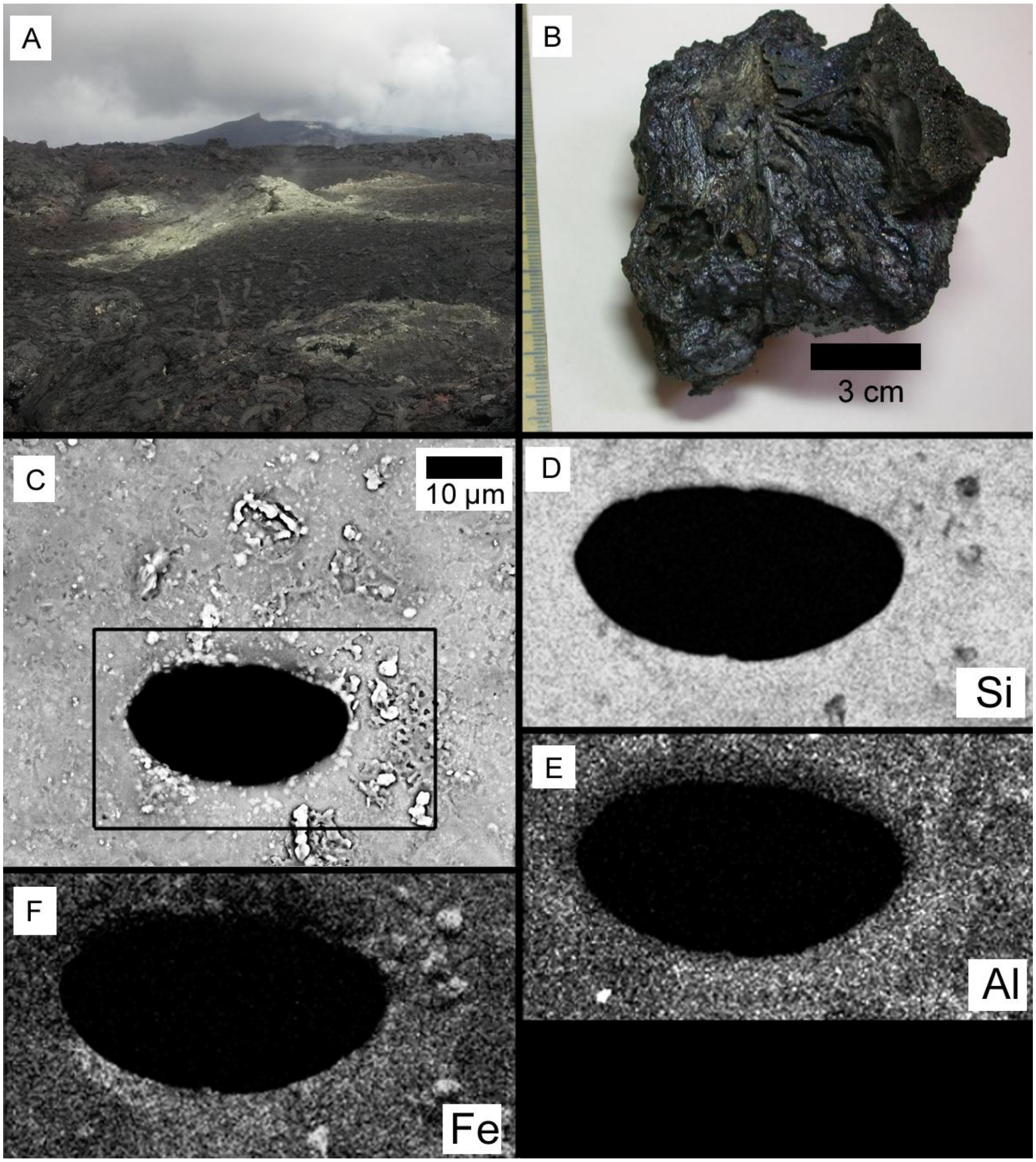

Figure 16. Kamoamoa 2011 eruption site as it appeared in March 2012. a) Sulfur mineralization at still-active fumarole. Pu'u O'o cone visible in background. b) Sample NC-11-008, collected from on-axis spatter rampart. Iridescent colors (blue) visible on surface. c) Secondary electron image of natural surface of NC-11-008. EDS elemental maps of the region indicated by the box are given for the following elements: d) Si, e) Al, and f) Fe.

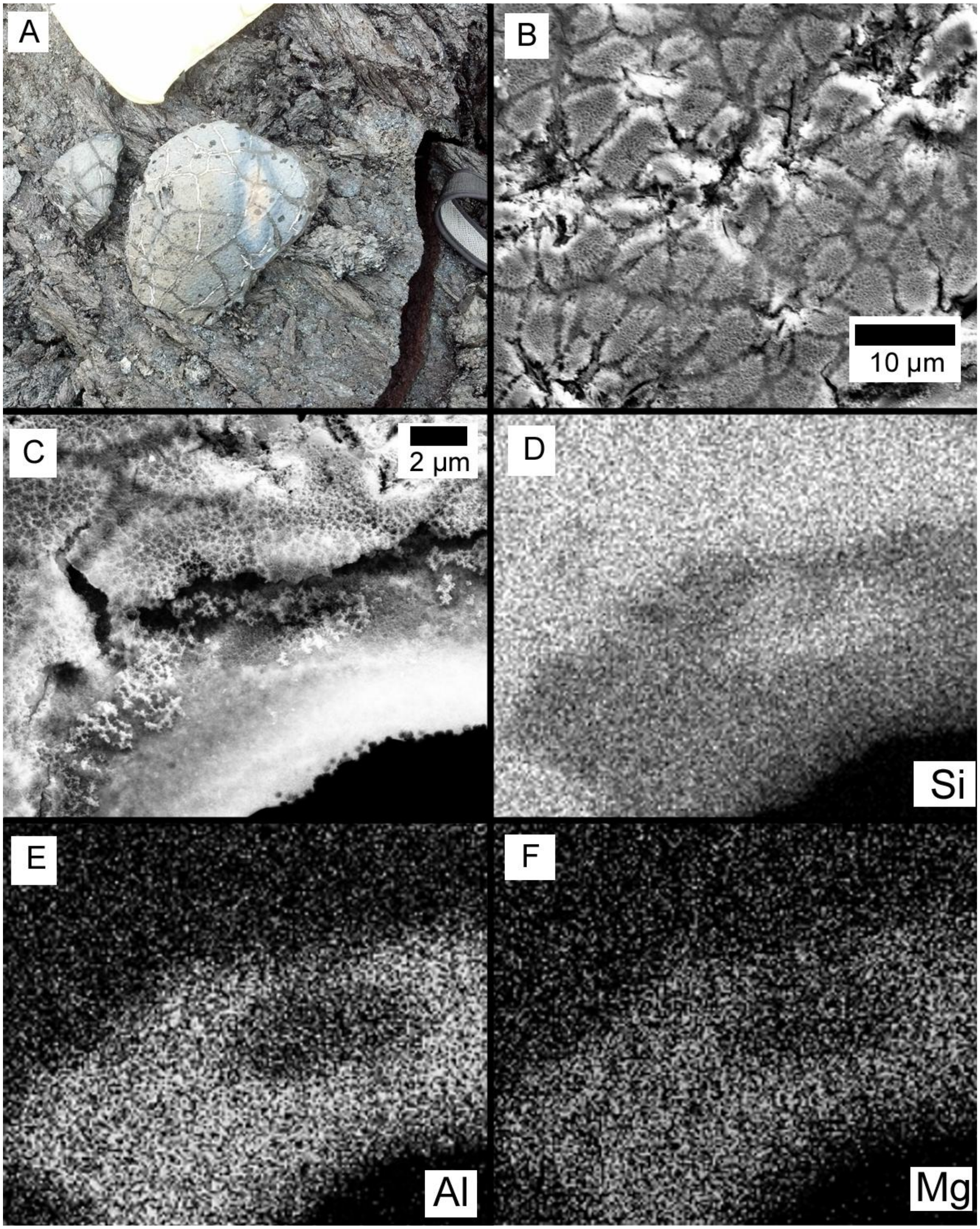

Figure 17. a) Sample NC-11-010, a volcanic bomb collected adjacent to the on-axis spatter rampart at the Kamoamoa eruption site. b) Secondary electron image of altered surface of NC-11-010. c) Higher magnification SE image of silica coating and uncoated edge of vesicle on NC-11-010. EDS elemental maps of this region are given for the following elements: d) Si, e) Al, and f) Mg.

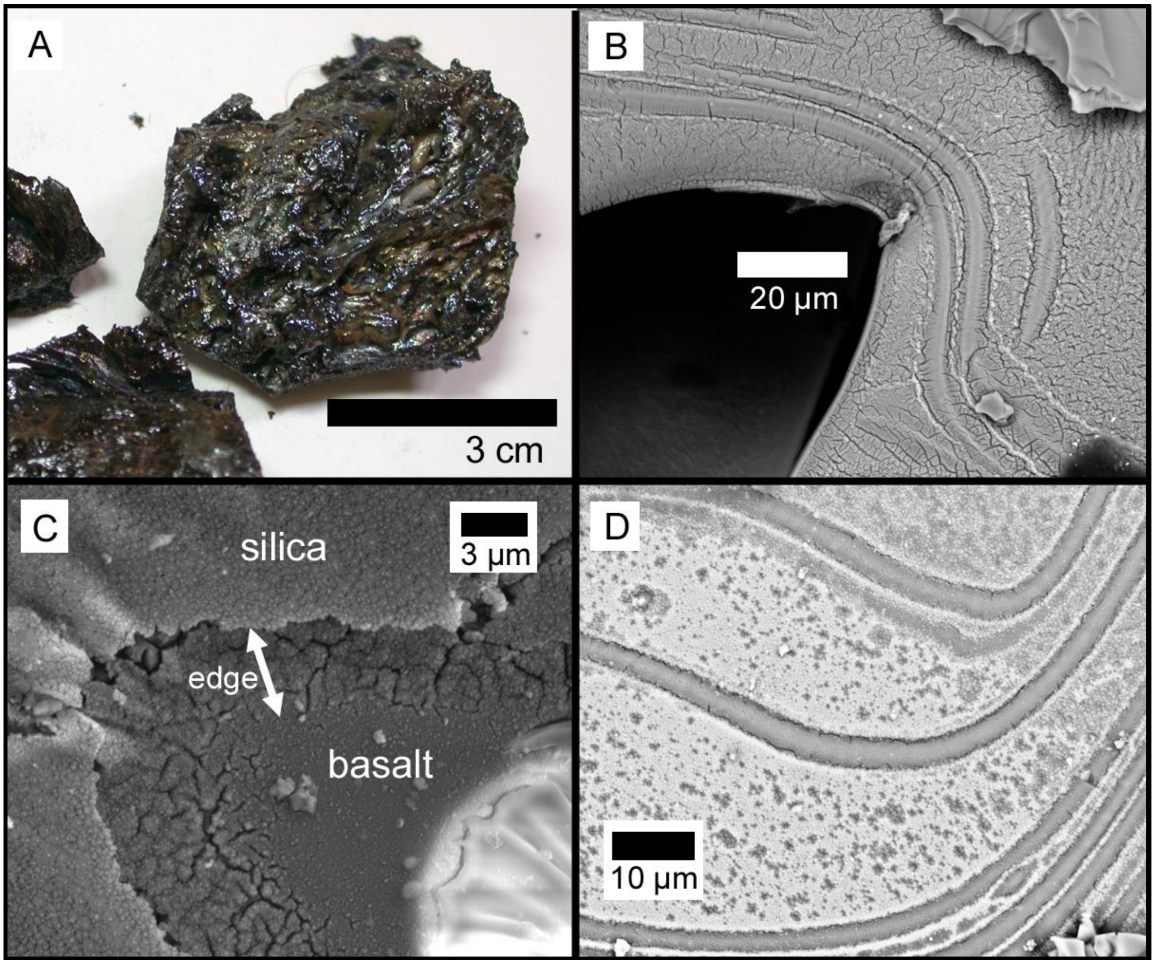

Figure 18. a) Sample NC-11-015, spatter from the Kamoamoa eruption that landed on older tephra to the north of the fissure. b) SE image of spatter surface, with amorphous silica coating and lineations related to primary deformation. c) Edge of silica coating near vesicle, implying 3–5 μm coating thickness. d) Fe-rich polyhedra on NC-11-015 surface.

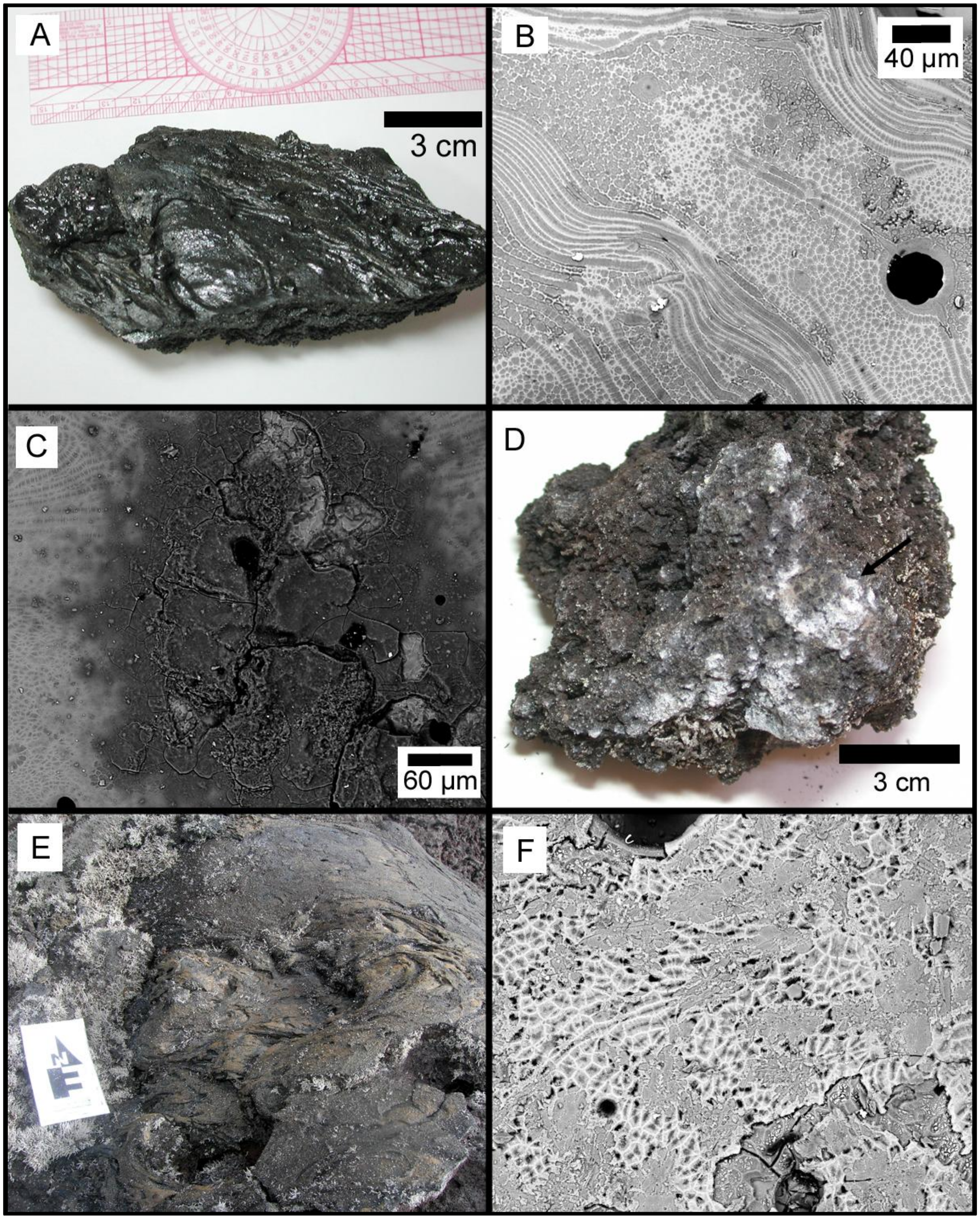

Figure 19. Samples from Mauna Loa 1984 eruption. a) Sample ML-NS-024, collected from spatter ramparts near the summit caldera. b) Surface morphology of sample ML-NS-024, illustrating lineations and pockmarks related to primary deformation. c) BSE image of patch of amorphous silica on ML-NS-024 surface. Amorphous silica patches were uncommon on this sample. Apparent thickness of silica patch is ~2 μm. d) Sample ML-PL-001, collected from distal 1984 a'a flow at an elevation of 1750 m. White powdery material was identified by Raman as amorphous silica. White-yellow growths on far right side of sample is lichen. e) Orange-red discoloration on rafted pahoehoe chunk from distal a'a flow (sample ML-PL-005). f) BSE image of ML-PL-005 surface. Bright material is a Fe-rich coating identified by Raman spectroscopy as lepidocrocite.

Sampling Location/ *Sample Name*	**Surface Appearance**	**Coating Coverage**	**Max Silica Thickness (μm)**	**Micro-morphology**
Kau Desert, Kilauea SWRZ				
KD-003a, spatter rampart	White, yellow and blue opaque coatings	Contiguous on spatter rampart, appears sparser on adjacent pahoehoe; absent where spalled	13	Silica layer capped by well-developed Fe-Ti layer; silica penetrates substrate along cracks
KD-003c, 1 m NW of rampart			not determined	
KD-003e, 10 m NW of rampart			16	
KD-003g, 40 m NW of rampart			7	
KD-Mar10-004			4	
Keanakakoi Crater				
KK	Yellow and orange opaque coatings	Prominent and contiguous on rafted spatter and lava trees; not present on lava lake surfaces	3.5	Silica appears as glaze or as "popcorn" texture; Fe-Ti coverage is irregular
Mauna Ulu, summit region				
MU-014	Dull white, yellow and orange opaque coatings	Present on spatter rampart and smooth pahoehoe surfaces, undergoing oxidation and removal; absent where spalled	5	Fe-Ti coating occurs in 30-100 μm bands on surface
MU-017c	Powdery white and yellow coatings	Contiguous on underside of shelly pahoehoe		Silica may preferentially replace glass over pyroxenes
Mauna Ulu, medial flow field				
MU-029	Bright white, yellow and orange opaque coatings	Contiguous on dense breakout pahohoe toes; spotty and surface dependent on spongy pahoehoe	6	Not investigated

Table 2. Summary of field and sample descriptions from the Appendix.

Sampling Location/ *Sample Name*	**Surface Appearance**	**Coating Coverage**	**Max Silica Thickness (μm)**	**Micro-morphology**
Napau Crater, Episode 54 eruption				
NC-97-011b	Yellow and orange opaque coatings	Prominent and contiguous on spatter rampart; present but sparse on pahoehoe toes ~100 m away	3	Fe-Ti coating particulate rather than continuous; silica layer penetrates basalt along cracks
Pu'u O'o summit lavas, Episode 55				
PU-009	Thick, translucent white coatings; on underside, opaque white, yellow, or blue material, or colorless glazes	Contiguous and heavy coatings on volcanic bombs, most pahoehoe surfaces, and shell undersides; absent where spalled and on 1983-86 rim lavas	26; up to 100 in depositional morphology	Silica layers bridge near-surface vesicles; apparent deposition within some surface vesicles
PU-010			80 (underside); 35 (outer surface)	Thin Fe-Ti coating present capping thick silica coatings
Pu'u O'o summit lavas, Episode 58				
PU-011	Translucent white coatings	Contiguous on spatter next to fissure vent; sparse but present on pahoehoe of same age	14	No discrete Fe-Ti layer observed; some Fe-Ti enrichment within silica layer
Episode 58 distal flow field				
TEB-020	Glassy hornito surface with sulfur condensates, but no visible coatings	No coatings on spalled S-type pahoehoe; sparse Si-rich layers on hornito detectable only by SEM	6	Thin, irregular Si-rich coating identifiable by SEM
KP-017	Silvery blue surface, no bright coatings	Not present	0	No detectable chemical heterogeneities at surface
Kamoamoa, 2011 eruption				
KE59-2941	black glassy spatter, no visually obvious alteration	not applicable; hand samples	0	primary lineation and crinkle texture
KE59-2952				

Table 2 (continued).

Sampling Location/ *Sample Name*	**Surface Appearance**	**Coating Coverage**	**Max Silica Thickness (µm)**	**Micro-morphology**
Kamoamoa, 2011 eruption (continued)				
KE59-2970	black glassy spatter, no visually obvious alteration	not applicable; hand samples	0	Fe-rich dendritic precipitate on surface
KE59-2979			< 1	primary lineation and crinkle texture; Fe-rich material on surface; incipient amorphous silica alteration
KE59-2980			0	Fe-rich material in subequant polygonal pattern
Kamoamoa, 2011 eruption (collected 1 year later)				
NC-11-008	iridescent colors on spatter rampart	Heterogeneous; matte coatings on some surfaces but absent on most	< 2	Topographically smooth; no Fe-Ti
NC-11-010	dull white, yellow, blue opaque coatings		3	Highly porous surface cut by shallow cracks
NC-11-015	Dull opaque blue or brown surface coloration	Contiguous over spatter surface; not apparent on older underlying spatter	4	primary lineation texture; surface covered in silica desiccation cracks; Fe-rich polygonal deposits
Mauna Loa, 1984 eruption				
ML-NS-024	black glassy spatter, no visually obvious alteration	No visually obvious coatings	2	Primary lineation texture, localized Si-rich alteration
ML-PL-001	White powdery deposit on a'a	A'a surfaces primarily uncoated	localized nodule	White powder identified as amorphous silica
ML-PL-005	Orange-red coloration on pahoehoe chunk		0	Color derives from ~1 µm lepidocrocite layer on surface

Table 2 (continued).

4.2. General Field Observations

Siliceous alteration layers were present on some lava flow surfaces at nearly every field site visited in this study. The coatings are often brightly colored; white, blue, yellow, orange and red colors are common (**Fig. 20a**). Incipient or very thin coatings may be colorless and/ or invisible upon macroscopic inspection. The coatings display a variety of textures, either appearing as a matte, opaque surface glaze or as a powdery white material. Surfaces with brightly colored coatings frequently appear dark along surface cracks (**Fig. 5a**).

The occurrence and visual prominence of brightly colored coatings is dependent on surface properties. Wilmoth and Walker (1991) distinguish two main types of Hawaiian pahoehoe lava. S-type (spongy) pahoehoe, the most abundant variety, has a high vesicle content and tends to spall its glassy surface layer (Wilmoth and Walker, 1991; Hon et al., 1994). P-type (pipe vesicle-bearing) pahoehoe is typically found on flat lava deltas where tumuli and lava rises are common and forms through long residence times in lava tubes. P-type lavas are dense, vesicle-poor and may display a silvery blue color when fresh (Oze and Winter, 2005). Brightly colored coatings form prominently on P-type pahoehoe surfaces and other lava surfaces with smooth, glassy exteriors, such as spatter ramparts (**Fig. 5a**), spatter adhering to lava trees and tree molds (**Fig. 6b**), and volcanic bombs (**Fig. 10e**). Coatings may form on the undersides of hollow pahoehoe shells and spatter chunks. Coatings may be present on less smooth ropey pahoehoe or sheet pahoehoe surfaces, but tend to be sparser in their surface coverage (**Fig. 5e**). Pahoehoe ropes sometimes displayed coatings only along their flow axis (**Fig. 8a**).

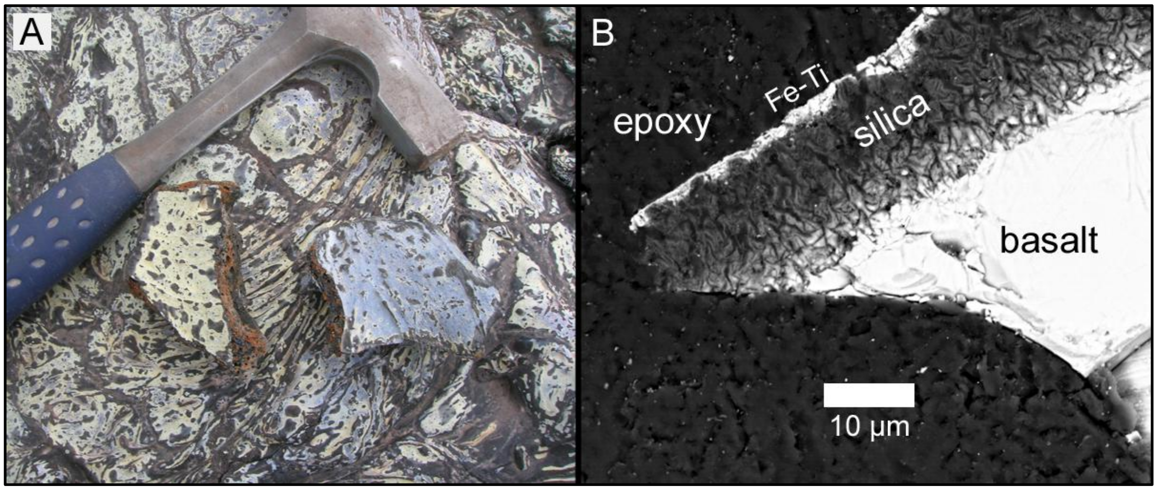

Figure 20. Typical morphology of colorful silica coatings as seen in the Ka'u Desert, along Kilauea's Southwest Rift Zone. A) White and blue coatings on a spatter rampart. The colored coating is not present on cracks that cover the surface. B) Backscatter electron image of a polished cross section of the coatings on the same spatter rampart. The bright region is the basaltic glass substrate, capped by a two-layer coating: a ~13 μm layer of amorphous silica (gray), capped by a 1 μm layer of Fe-Ti oxide (bright)

Brightly colored coatings are rare on a'a and on flow surfaces that have spalled their outer glassy layer (**Fig. 5g**)

Lava surfaces frequently display heterogeneity in coating coverage over short spatial scales. These heterogeneities appear to result both from physical abrasion and surface-selective formation. Coating distribution appears to be influenced by surface topography, including cm-to-m scale lava flow morphology and μm-to-mm scale irregularities of the lava flow surface. At the cm-to-m scale, coatings may be absent immediately adjacent to topographic barriers like pahoehoe flow fronts and underneath lava "awnings" (**Fig. 5h**) At the smaller scale, coatings were often observed to be absent or actively eroding on surfaces with ~0.1–5 mm roughness. Bright coatings on older flows often appeared to be eroding and oxidizing concentrically away from topographic nubs (**Fig. 7d**)

4.3. General Micro-Scale Observations

BSE images of polished cross sections of coated basalt indicate that the coatings consist of a layer of amorphous silica, 1–80 µm thick, capped in some cases by a ~1 µm layer of Fe-Ti oxide (**Fig. 20b**). Based on its distribution, the Fe-Ti oxide layer appears to be responsible for the bright colors and opaque pigmentation observed on coated basalts in the field. The silica coating layer is nearly pure SiO_2, with occasional sulfur enrichment (Chemtob et al., 2010), and has a high Si-OH content as determined by ^{29}Si NMR and IR methods (5.4 wt% as H_2O in the PU-009 coating; Chemtob et al., 2012). Fe-Ti coatings on samples from the Ka’u Desert have ~78% TiO_2, ~20% FeO* (total Fe expressed as ferrous iron oxide) and percent-level enrichment of sulfur and phosphorus (Chemtob et al., 2010). The Fe/Ti ratio in the coatings at other sites is higher and more variable. The mineralogy of the Fe/Ti coatings in the Ka’u Desert is dominated by anatase and rutile; pseudobrookite, hematite and lepidocrocite have also been identified. SEM images of cross sectional surfaces and natural surfaces of the silica coating frequently show cracks, likely representing desiccation after coating formation or within the SEM. The boundary of the siliceous layer is undulating but chemically sharp (**Fig. 20b**). Basalt immediately adjacent to the coating is visually unaltered and chemically identical to far interior basalt. The silica layer may penetrate the basalt substrate along near-surface cracks (**Fig. 5j**).

Imagery of unpolished natural surfaces provides additional information about the alteration processes. Fresh, unaltered spatter surfaces frequently display lineations or crenulations with 3-5 µm spacing and pockmarks, 1-25 µm in diameter (**Fig. 14a, Fig. 15a**). These textures are attributable to primary deformation of the lava surface as it cools. On aged spatter surfaces, the same primary deformation textures frequently define compositional heterogeneity. Silica alteration layers developed along lineations and at the centers of pockmarks, presumably reflecting regions of the surface that experienced maximum strain (**Fig. 15b, Fig. 19b**). Even as silica coatings develop and cover the majority of a lava surface, primary deformation textures are in some cases still visible. Well-developed silica coatings may appear either as smooth, continuous glazes (**Fig. 6d**) or as a porous, highly irregular "popcorn" textured material (**Fig. 7g; Fig. 17c**). Surface regions with more extensive silica coatings were frequently low-lying or deflated relative to regions with less alteration material (**Fig. 7h**).

Fe-Ti oxide coatings on decades-old coated surfaces occur in distinct patches across the surface. In places, the Fe-Ti coating displays fine internal lineations similar in scale to primary lineations observed on fresh surfaces; elsewhere, the Fe-Ti oxides appear massive and amorphous (**Fig. 6c**). Fe-Ti coatings on one Ka'u Desert sample was shown to be composed of microspheroids, ~100 nm in diameter (Chemtob et al., 2010). Very young (days old) lava surfaces may also display Fe-rich crystallites, occurring as dendritic bundles, polygonal tiles or amorphous masses (**Fig. 14b,c; Fig. 15b,f**). Whether these initial Fe-rich deposits are precursors to Fe-Ti coatings on surfaces that have also developed silica coatings is unclear.

5. Discussion

5.1. Timescale of Coating Formation

Because many parameters may affect the formation rate and properties of silica coatings, including proximity to acid sources, lava surface type, and environmental conditions, assessing the timescale of coating formation merely by plotting coating thickness against age may be misleading. Instead, we focus our interpretation of coating growth rate on sample pairs from near-identical collection locations with different ages: spatter collected in 2011 and 2012 from the Kamoamoa eruption, and 1998 and 2007 lavas at the summit of Pu’u O’o.

Fresh spatter samples (collected days after emplacement) from the Kamoamoa eruption site are not visibly macroscopically altered but display progressive incipient alteration observable by microanalytical techniques. Samples KE59-2941 and KE59-2952, collected several hours and one day after emplacement, respectively, both showed primary surface deformation textures but no chemical alteration on their surfaces (**Fig. 21a**). The surfaces of samples KE59-2970 and KE59-2980, each collected 5 days after their eruption, featured dendritic Fe-rich precipitates identified by electron backscatter diffraction as magnetite and ilmenite, but no apparent silica-rich alteration material (**Fig. 21b; Fig. A1**). Sample KE59-2979, collected 8 days after the eruption, displayed localized spots of amorphous silica alteration, sometimes directly associated with patches of Fe-rich precipitate (**Fig. 21c**). This series of samples indicates that a period of days is required for initial incipient silica coating formation. Observations of siliceous alteration layers on the surface of Pele’s tears forming seconds or minutes after eruption (Moune et al., 2007) are not replicated at this field site.

Samples collected at the Kamoamoa eruption site one year after eruption have a considerably different surface morphology. Some year-old surfaces displayed visually apparent alteration (**Fig. 17a; Fig. 18a**). Sample NC-11-015, spatter collected from the same locale as the fresh spatter sample suite above, displayed a dull brown surface

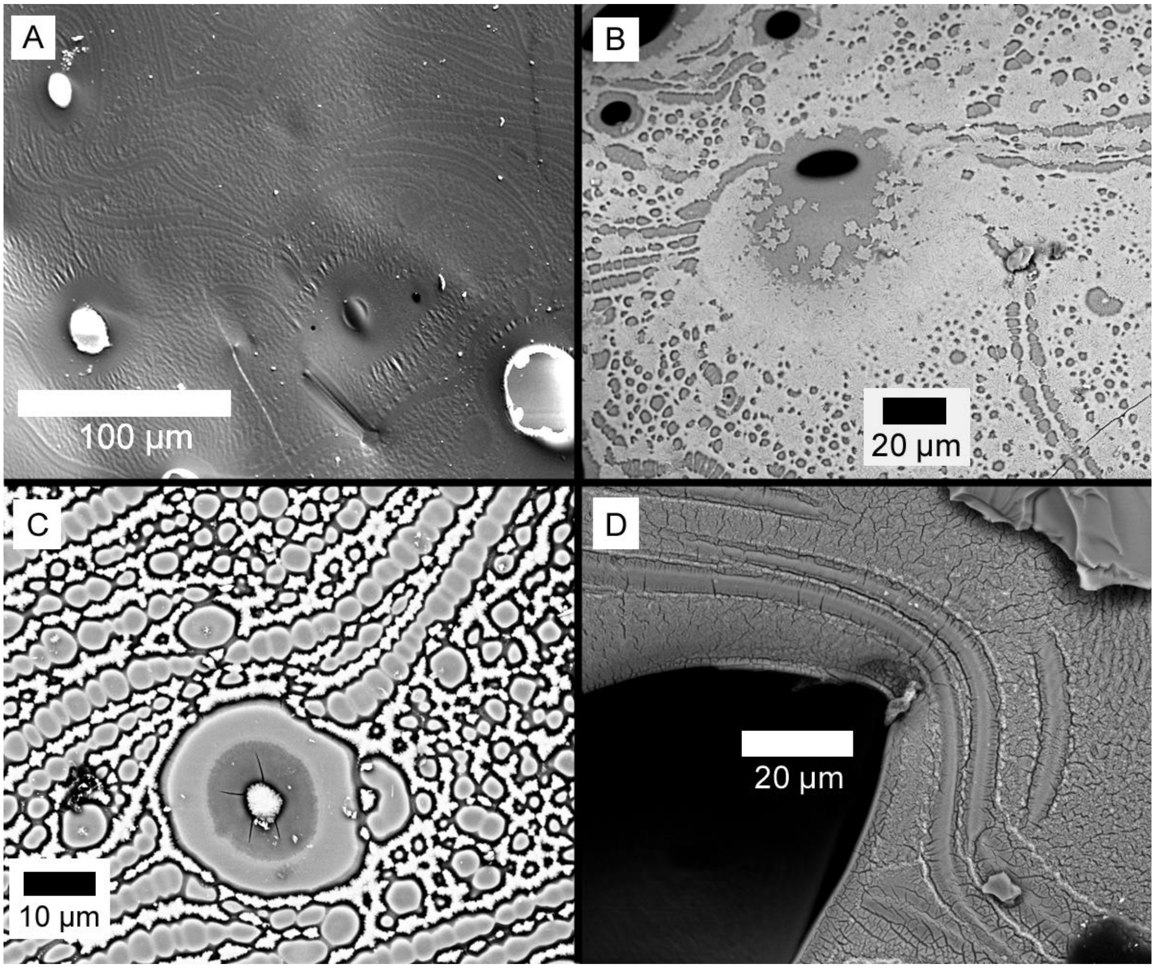

Figure 21. SEM images of Kamoamoa spatter surfaces of various ages. A) Sample KE59-2941, hours old at time of collection. The sample shows deformation texture but no chemical heterogeneity. B) Sample KE59-2970, 5 days old at time of collection. Dendritic Fe-rich crystallites cover the surface, but no siliceous alteration is present. C) Sample KE59-2979, 8 days old at time of collection. Bright material is Fe-rich crystallites; light gray is basalt. Amorphous silica (dark grey with desiccation cracks) has replaced basalt in the central pockmark. D) Sample MU-011-015, collected one year after eruption. Amorphous silica covers most of the surface, but preserves the primary deformation texture.

color with morphology similar to silica coatings observed at other field sites (**Fig. 18a**). SEM-EDS images of NC-11-015 indicate silica coatings over wide swaths of its surface (**Fig. 21d**), estimated from coating edges on the natural surface to be ~4 µm thick (**Fig. 18c**). Primary surface deformation lineations appear to be preserved within the amorphous silica alteration texture, suggesting silica layer formation replacement rather than by external deposition (**Fig. 21d**). A volcanic bomb (sample NC-11-010) with visible discoloration collected immediately adjacent to the primary Kamoamoa vent was shown to have a highly porous silica coating, ~3 μm thick (**Fig. 17**). The coating thicknesses on these year-old samples suggest a silica alteration layer growth rate of a few μm/year.

The suite of altered basalts from the Kamoamoa eruption can be compared with samples from the 1997 Episode 54 fissure eruption, collected ~1 km away in the center of Napau Crater. Coatings on spatter ramparts from that eruption had a maximum thickness of 3 μm, approximately equal to coating thicknesses from the recent eruption (**Fig. 9**). Several factors may contribute to the similarity of coating thicknesses on 1-year- and 13-year-old surfaces. First, the Episode 54 collection site is 1 km further away from the Pu'u O'o vent, implying less input of acidity from regional plumes. Second, the local SO_2 emissions during the Episode 54 and Kamoamoa eruptions differed greatly. SO_2 emissions from the Episode 54 eruption peaked at 260 metric tons / day (mt/d) (Elias et al., 1998); in contrast, maximum SO_2 emissions from the Kamoamoa eruption were ~10000 mt/d (M. Poland, pers. comm.). These two sites illustrate that coating growth rates may vary widely with time and location; specifically, early coating growth rates may depend strongly on the intensity of syneruptional gas emission.

Samples collected in the vicinity of the summit of Pu'u O'o have experienced intense and sustained exposure to a regional acidic plume. Sample PU-010, an Episode 55 lava erupted in 1998, and sample PU-011, an Episode 58 lava emplaced in 2007, display similar coating colors and physical appearances. Although PU-010 and PU-011 were collected at different distances from the rim (~10 m and ~100 m, respectively), both were collected just upwind relative to the plume, so we assert that their formation

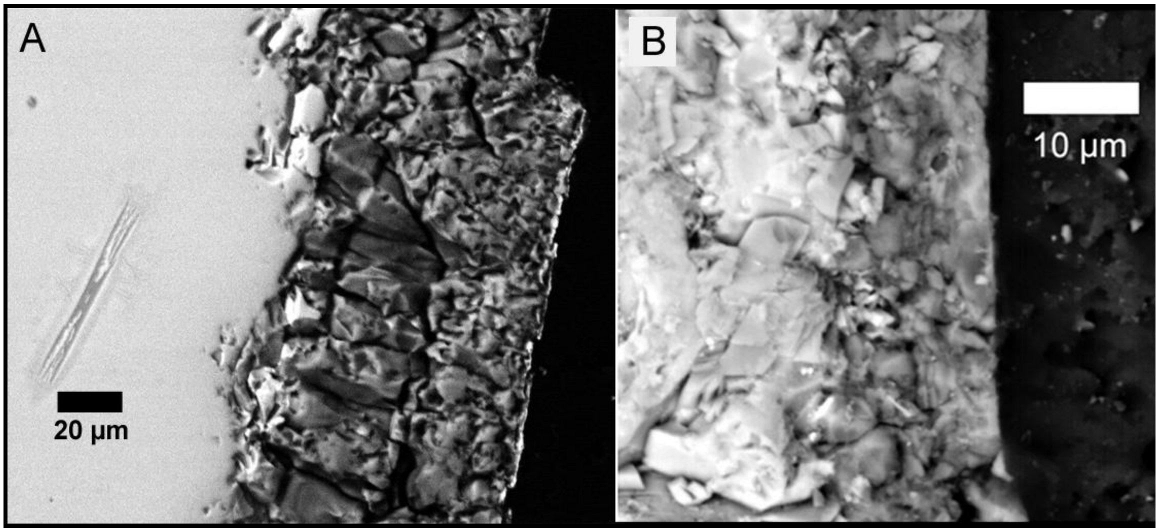

Figure 22. Comparison of near-summit Pu'u O'o lavas from 1998 and 2007. A) Sample PU-010, summit overflow lavas emplaced in 1998. This pahoehoe shell features coatings up to 80 μm thick on both the outside and underside. B) Sample PU-011, spatter emitted from a fissure vent ~100 m from the Pu'u O'o summit in 2007. The sample features a ~12 μm thick silica coating.

conditions are roughly comparable. The maximum coating thicknesses observed for samples PU-010 and PU-011 are 80 μm and 14 μm, respectively (**Fig. 22**). This difference in coating thickness suggests that in the presence of persistent acid sources, coating growth may continue at rates of μm/year for years after lava emplacement.

5.2. Origin of Coating Coverage Heterogeneity

The distribution of silica coatings across the Hawaiian landscape is not uniform. Heterogeneities in silica coating coverage are observable between eruption sites, between different flow surfaces at the same eruption site, and at a microscopic scale on an individual hand sample. Here we discuss three processes—surface-selective formation, erosion, and microenvironmental variability—that demonstrably contribute to the observed heterogeneities.

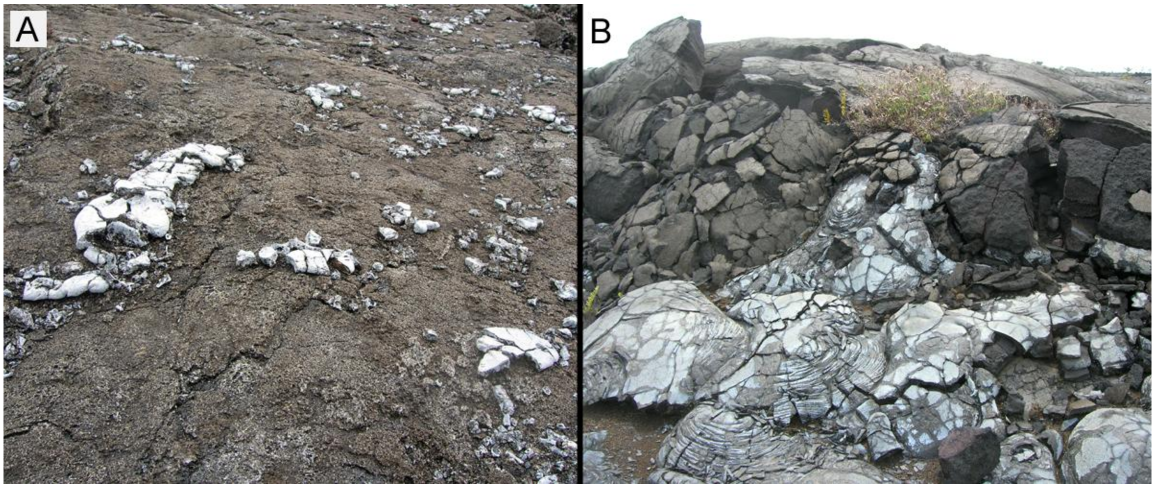

Figure 23. Examples of surface-selective alteration. A) Heavily coated volcanic bombs strewn across the landscape near the rim of Pu'u O'o. The left-most bomb in the foreground is ~20 cm long. B) Bright coatings on P-type pahoehoe breakouts on the distal flow field of Mauna Ulu. Lava surfaces making up the tumulus from which the breakout flows are extruding are minimally coated.

Surface-selective formation: Silica coatings do not form on all surfaces with equal regularity. Coatings were observed to be most prominent on lava with smooth, glassy surfaces, including P-type pahoehoe breakouts, spatter and spatter ramparts, lava trees, and volcanic bombs. The consistency with which these surfaces feature more prominent coatings relative to their surroundings suggests that the glassy surface layers themselves are particularly susceptible to form silica alteration layers (**Fig. 23**). Several factors may contribute to this susceptibility. The interiors of basalt flows may have a higher proportion of phenocrysts than the quenched outer layer. At pH < 2.5, the measured dissolution rate of basaltic glass is higher than that of forsterite, diopside, and plagioclase (Hausrath et al., 2008); thus, in the presence of volcanically-derived sulfuric acid, more glass rich compositions may weather faster.

Another, potentially more important factor in determining surface susceptibility is the degree to which outer glassy layers have undergone strain weakening during lava cooling. We attribute observed lineations, crenulations, and pockmarks on the surfaces of fresh glassy lava are to primary deformation of a solidifying surface over a partially molten interior. Deformed silicate surfaces have a higher density of defects, and silica glass hydrolysis may proceed 100,000 times faster at defect sites than on unstrained Si-O bonds (Bunker, 1994). Evidence in our sample suite for strain-based surface-selective alteration is apparent at both microscopic and macroscopic spatial scales. In days-old spatter from the Kamoamoa eruption and in near-summit spatter from the 1984 Mauna Loa eruption, the microscopic primary deformation texture defines a compositional heterogeneity in which certain parts of the strained surface preferentially developed siliceous alteration (**Fig. 19b; Fig. 21c**). At the macroscopic scale, the morphology of ropey pahoehoe was shown to affect coating coverage. On the Mauna Ulu flow field, bright coatings appeared only along the flow axis of a well-formed set of pahoehoe ropes, the region that experienced the most deformational strain (**Fig. 8a**).

Erosion and preservation bias: Another process leading to the heterogeneity of coating coverage on surfaces is post-formational erosion and removal. The outermost surface of fresh S-type pahoehoe is highly vesicular and therefore less resistant to physical weathering. Coatings regrowth on spalled surfaces is rare, so the rate of spallation of outer glassy layers by wind and water abrasion exerts a strong control on coating distribution.

Silica coatings may also be removed from basalt substrates by abrasion without the complete removal of the glassy layer by spallation. Surface micro-topography strongly influences the rate of abrasion of a coated surface. At Mauna Ulu, we observed concentric coating oxidation and removal around mm-scale topographic nubs (**Fig. 7d**).

Coatings on lavas with relatively smooth, glassy surfaces are preserved relative to neighboring lavas with more roughness.

Microenvironmental variability: Some heterogeneities in coating coverage may result from varying environmental conditions, such as fluid availability and exposure to acid sources, on a localized scale. On the distal Mauna Ulu flow field, coatings are occasionally absent on flow surfaces underneath other basalt obstructions (**Fig. 8b**). Those surfaces may not have received as much rainfall as neighboring exposed surfaces, remaining minimally altered. The degree of alteration of surfaces at the Kamoamoa site one year after eruption was heterogeneous. Some of this heterogeneity can be attributed to surface-selective alteration; dense P-type lavas and volcanic bombs tended to display more colored alteration. However, cases in which lavas of similar surface type displayed different extents of alteration are potentially attributable to heterogeneous exposure to the degassing SO_2 plume during eruption.

5.3. Origin of Acidity

In a previous study, we concluded that silica coatings in the Ka’u Desert result from interaction between a basalt surface and volcanically-derived acidic fluids and vapors (Chemtob et al., 2010). Here we assess the relative importance of possible sources of volcanically-derived acids, including local fissure vents, regional plumes, and volatiles degassed from the lava itself.

Local fissure vents: Coatings on spatter ramparts lining the SWRZ fissure vents appear more contiguous than those on neighboring pahoehoe flows. This difference in coating coverage is apparent in aerial visible-near-IR false color imagery (Seelos et al., 2010). In a previous study (Chemtob et al., 2010) we hypothesized that the fissure vents themselves may be an important source of acidity for coating formation. Variations in syneruptional gas emission rates appear to correlate with coating growth rates (see Section 5.1). Periods of enhanced gas emissions at short-lived fissure eruptions are typically short lived, but emissions may continue at low levels long after the end of lava emplacement. For the Episode 54 fissure eruption at Napau Crater, SO_2 emissions fell from 260 metric tons/day (mt/d) during the eruption to 80 mt/d the following day (Elias et al., 1998). Similarly, the SO_2 emission rates of the 2011 Kamoamoa eruption peaked at ~10000 mt/d at the height of the eruption (March 7–8) but had fallen to ~400 mt/d by March 11 (M. Poland, pers. comm.).

To test the hypothesis that fissure vent emissions influence coating formation, we conducted a traverse perpendicular to the trace of the SWRZ at waypoint 1, collecting coated lavas 1, 10, and 40 m to each side of the spatter rampart (**Fig. 5b-e**). If fissure vents were important sources of acidity, we expect gradients in coating thickness away from the spatter rampart. The maximum coating thicknesses at distances from the spatter rampart of 0, 10, and 40 m were 13, 16, and 7 μm, respectively (**Table 2**). This modest gradient in coating thickness away from the fissure vent suggests that those local vents may be a significant source of acidity. This gradient could reflect early coating formation during the eruptive period of enhanced emissions, or it could indicate that low-level emissions continued after the eruption.

Regional plumes: Field observations indicate that regional acidic plumes are a dominant contributor of acidity leading to silica coating formation. Between 2008 and 2010, typical average SO_2 emission rates varied between 500 and 1000 mt/d at Kilauea summit and between 500 and 2000 mt/d at the ERZ (Elias and Sutton, 2012). The lavas with the thickest coatings observed in the study (80 μm), on the rim of Pu’u O’o, have undergone constant exposure to this acidic plume. Prevailing trade winds carry acidic vapors and condensates from Kilauea towards the southwest over the Ka’u Desert, where they may linger and interact with surface rocks (Schiffman et al., 2006). On days of Kona winds, transport of acidic fluids to the southwest is weakened, and acids may interact with local lava surfaces in all directions. We assess the effect of regional plumes on coating development by comparing three sites of similar age: a location on the 1974 flow near the SWRZ (waypoint 1), the distal toe of that same flow (KD-004; waypoint 2), and the Keanakakoi Crater spatter rampart (waypoint 3) (**Fig. 1**). The maximum silica coating thicknesses measured at those sites (not including the region immediately adjacent to the spatter rampart) were 7, 4, and 3.5 μm, respectively (**Table 2**). Despite being geographically closer to Kilauea Caldera, the Keanakakoi Crater lavas display thinner silica coatings because they were less intensely exposed to the plume. The 1974 flow distal toe was apparently sufficiently far southwest of the main trace of the plume to not develop thick coatings. This gradient and the thick Pu’u O’o coatings indicate that exposure to regional plumes is an important predictor of coating thickness.

Auto-alteration: A final potential source of acidity for alteration of a basalt surface is volatiles degassing from that basalt as it erupts and cools. White and Hochella (1992) observed surface depletion of Si, Fe and Al and enrichment in F on freshly emplaced distal basalt flows, which they attributed to mobilization of fluoride complexes facilitated by degassing. Such “auto-alteration” is a potentially attractive mechanism for explaning coating formation on distal flow fields at Mauna Ulu and Kalapana. However, we do not favor a general auto-alteration hypothesis for silica coating formation for several reasons. First, volatile fluxes from degassing flows on distal flow fields should be far lower than those observed at fissure vents and regional plumes. P-type pahoehoe surfaces that feature the most prominent coatings on distal flow fields are thought to have lost most of their volatile content before eruption (Wilmoth and Walker, 1993). Second, flow degassing ceases within hours of lava emplacement, and observation of Kamoamoa samples indicates that silica coatings do not form in that short period. Volatiles from degassing do not linger on flow surfaces for the period of years required to produce thick silica coatings; F enrichment on fresh surfaces was no longer present after 200 days (White and Hochella, 1992). Instead of auto-alteration, we attribute distal flow alteration primarily to exposure to the diluted regional plume. Alternatively, thin silica coatings have been shown experimentally to form on basalt on timescales of decades, solely through water vapor action (Dorn, 2012). Thus, P-type pahoehoe surfaces prone to alteration may alter with minimal input from acidic plumes, but over longer timescales.

5.4. Climatic Effects

To assess the effects of environmental conditions on the rates and products of chemical weathering of Hawaiian lava flows, we compare the observed alteration in the Ka'u Desert and Mauna Ulu to that of lavas from the 1984 northeast rift zone eruption of Mauna Loa. The summit of Mauna Loa has an average annual temperature around 5° C and receives around 400 mm of precipitation a year; by comparison, Mauna Ulu averages 18-20° C and over 3500 mm of precipitation a year.

A 1984 spatter rampart at the northeast edge of the summit caldera (elevation 3970 m) was not visibly discolored at the time of our visit in March 2012 (**Fig. 19a**). SEM imagery of a sample collected from the spatter rampart (ML-NS-024) indicates that siliceous alteration products occur on the surface in two contexts. First, silica enrichment occurs in zones with primary alteration textures, apparently replacing lineated regions of basaltic composition (**Fig. 19b**). Second, the spatter surface features rare patches, ~300 μm across, composed of contiguous amorphous silica, 1–2 μm thick. (**Fig. 19c**) The location of these patches appears independent of the primary alteration texture.

The total amount of siliceous alteration on near-summit spatter ramparts at Mauna Loa is small compared to spatter ramparts of similar ages at Kilauea. A potential explanation is the removal of much of the silica coatings by physical weathering facilitated by freeze-thaw processes. However, the Mauna Loa spatter samples appear to have retained their glassy outer rinds. Additionally, the edges of the amorphous silica patches on the surface of ML-NS-024 appear gradational rather than erosional. Therefore, it is unlikely that the near-summit spatter ramparts featured thicker and/or more contiguous coatings that were then removed. Instead, we assert that siliceous alteration was muted because of cold, dry climatic conditions. At this time, we cannot deconvolve the separate contributions of temperature and rainfall rate to rates of coating formation.

5.5. Preferred Formation Mechanism

In our previous study (Chemtob et al., 2010), we laid out two potential primary mechanisms for formation of the silica coating: deposition of externally derived silica, and local dissolution of near-surface basalt followed by precipitation of silica. In that study, we favored the latter explanation; based on the new observations of coatings at field sites of various ages, we continue to support that mechanism. The identification of surface-selective alteration at the microscopic and outcrop scale implies that the siliceous alteration is dominantly local (**Fig. 23**). Additionally, identification of coatings bridging near-surface vesicles (**Fig. 10i**) and silica penetrating the surface along cracks (**Fig. 5j**; **Fig. 9d**) support *in situ* incongruent dissolution. However, some select morphologies imply silica mobilization and deposition. One sample, PU-009, featured amorphous silica filling a surface vesicle, preserving concentric microstratigraphy (**Fig. 10j**). This morphology cannot form by *in situ* alteration alone, instead requiring either precipitation of silica from solution or clastic remobilization of previously deposited silica. Thus, although coatings are primarily residual in character, silica may be mobile on local scales.

The dissolution of silica in basalt also releases other cations (Na^+, Ca^{2+}, Mg^{2+}, Al^{3+}, Fe^{3+}, Ti^{4+}) into solution; since these cations are not present in the alteration minerals, they must be removed from the system. Although acids may interact with basalt surfaces both as vapors and liquids, liquid water is required to mobilize and remove these cations. Likely sources of liquid water include condensed water vapor from plume gases and rainwater. There were rain showers every day of the Kamoamoa 2011 eruption (Tim Orr, pers. comm.), indicating that there was no shortage of liquid water for removal of leachates. In cases in which transporting fluids are limited, the dissolved solids may be carried away in stages, forming soluble sulfate, fluoride and chloride salts that are later redissolved.

Replacement of the near-surface basalt by amorphous silica is not an isovolumetric process; deflation of the surface likely occurs during coating formation. We employ a chemical mass balance to determine the thickness of the silica coating produced by dissolving 1 μm of basalt ($\rho_{basalt} = 2.7$ g/cm^3. $X_{SiO2} = 51.7$ wt%; Chemtob, 2012). A typical value for the density of opal is $\rho_{opal} = 2.17$ g/cm^3 (mindat.org). EPMA analyses of the silica coatings routinely produce low totals (Minitti et al., 2007; Chemtob et al., 2010). The low totals are, in part, explained by high structural water content (Chemtob et al., 2012), but may also indicate as much as 15% porosity within the coatings. The effective density of the coatings may be as low as $2.17 \cdot 0.85 = 1.84$ g/cm^3.

Given the above figures, if Si is completely immobile during weathering, then dissolving 1 μm of basalt would produce 0.83 μm of amorphous silica. However, silicon isotopes are fractionated in the silica coatings relative to the basalt substrate (Chemtob, 2012), requiring some Si loss from the system. Based on δ^{30}Si of the PU-009 coating and a model 1000 ln α of +2‰, estimated fractions of Si retained in the coating were $f_{precip} = 0.29$ for steady-state fractionation and $f_{precip} = 0.25$–0.50 for Rayleigh fractionation (Chemtob, 2012). These values would imply just 0.22 μm amorphous silica deposited per 1 μm basalt dissolved for steady-state fractionation, and up to 0.40 μm deposited per 1 μm basalt dissolved for Rayleigh fractionation. Thus, the presence of a 10 μm coating on the surface of a basalt seems to imply that at least 25 μm of basalt was consumed during formation of that coating. This calculation explains the deflational morphology observed on some coated samples (**Fig. 7h**)

We present two hypotheses for the origin of the Fe-Ti oxide coating. In our previous study, we attributed the presence of the Fe-Ti oxide coating to the precipitation

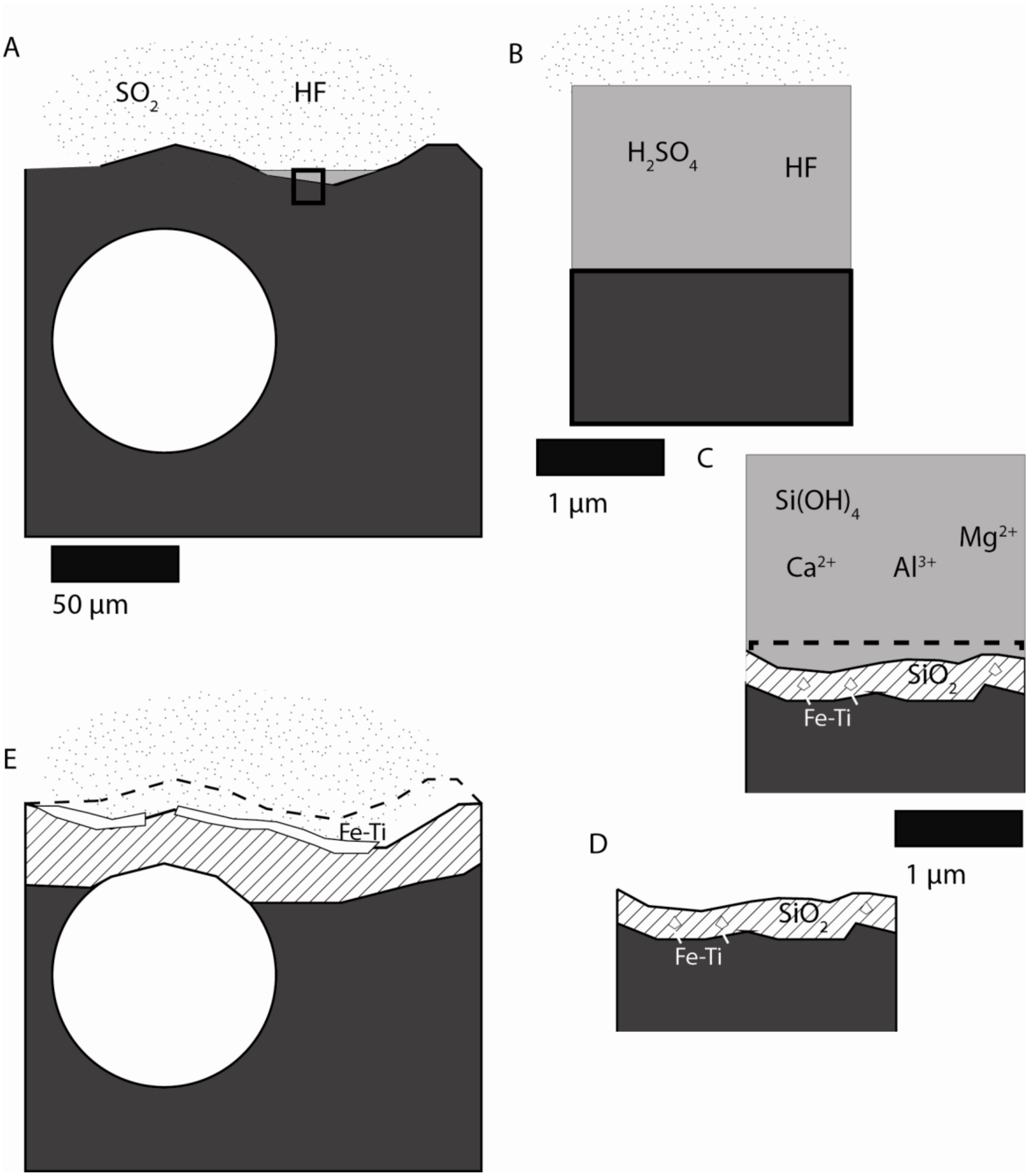

Figure 24. Schematic cartoon depicting coating formation. a) The surface of a fresh, unaltered basalt flow is wetted by rainwater or condensed water vapor in the presence of acidic vapors. b) Surface fluids (light gray) are acidified by the vapors. c) Acidic vapors dissolve a portion of the surface basalt and precipitate amorphous silica in place. Fe and Ti have limited mobility. d) Fluids carrying dissolved load are washed away from the system. e) Silica coatings continue to grow thicker over a period of years. Through that time, Fe-Ti oxides are mobilized and redeposited at the surface. Silica coatings may bridge near-surface vesicles. Because < 1 µm of silica is deposited for every 1 µm basalt dissolved, surfaces may display deflationary morphology (the dotted line represents the original, unaltered basalt surface)

of relatively immobile dissolved Fe^{3+} and Ti^{4+} liberated from the basalt in formation of the silica layer (Chemtob et al., 2010). More mobile elements remain in solution after basalt leaching and are removed from the system, but Fe^{3+} and Ti^{4+} precipitate out quickly. The observation of percent-level enrichment of phosphorus, another immobile element present in basalt glass, lends support to the hypothesis that the Fe-Ti coatings represent material mobilized during basalt leaching. A weakness of this model is that it does not intrinsically explain coating stratigraphy, i.e., the observation that Fe-Ti coatings typically cap the silica alteration layer. To form this capping morphology, Fe^{3+} and Ti^{4+} must be transported by wicking fluids up to tens of μm from their source to the subaerial surface. The mechanism by which these elements are transported to the surface is unclear.

The presence of magnetite and ilmenite crystallites on 5-day old spatter samples (**Fig. 14b**) at Kamoamoa suggests a new hypothesis: that Fe-Ti oxides form by high temperature crystallization during cooling and are later altered along with the underlying glass. Subaerially cooling basalt flows may crystallize near-surface dendritic titanomagnetite crystals, tens of nanometers across, as they quench (G. Rossman, unpublished data; Nadin, 2007). Similarly, 200 nm magnetite crystals on the surface of basalt from Pisgah Volcano, Barstow, California, produce thin film interference colors (G. Rossman, unpublished data). Perhaps the distribution of Fe-Ti coatings observed on coated flows today simply reflects the distribution of early-formed oxide crystallites. This hypothesis would account for both the heterogeneity of Fe-Ti oxide distribution and the capping morphology. However, there are several problems with this hypothesis. The crystallites observed on young Kamoamoa spatter had a higher Fe/Ti ratio (~3–4) than the oxide coatings on silica coated basalts (Fe/Ti as low as ~0.25). The weathering of Fe-Ti oxides mobilizes Fe relative to Ti (Temple, 1966), but even if Ti remains perfectly immobile such an elemental fractionation requires >90% Fe loss. The total volume of Kamoamoa crystallites is not sufficient to sustain this loss and produce observed volumes of Fe-Ti coatings as seen on older flows. Additionally, this mechanism fails to account for the fate of Fe, Ti and P released from the weathered glass layer. Thus, we do not favor a mechanism involving high-T crystallization and subsequent alteration as the sole source of Fe-Ti oxide coatings, but high-T crystallites may contribute in small proportions.

Our preferred coating formation mechanism is illustrated as a cartoon in Figure 24. Liquids on the surface of fresh, unaltered basalts are acidified by volcanically derived vapors. A portion of near-surface basalt is dissolved and replaced *in situ* by amorphous silica. Much of the dissolved load (Mg^{2+}, Ca^{2+}, Na^{+}, Al^{3+}, etc.) remains soluble at low pH and is removed from the system as these fluids are washed away. Titanium and ferric iron have lower mobility and precipitate as Fe-Ti oxides. As acidic alteration of basalt surfaces continue over a period of years, the silica alteration layer grows thicker and Fe and Ti are remobilized to form a contiguous layer at the surface.

6. Conclusions and Implications

Silica coatings are a ubiquitous feature on young lava flows at Kilauea. The coatings consist of a layer of amorphous silica, up to 80 μm thick, capped in some cases by a ~1 μm layer of opaque Fe-Ti oxide. The thickness of these coatings is dependent on the age of the flow, proximity to acid sources, and climatic conditions. Silica layers were observed to form at rates up to microns/year, but vary sharply through time and across the

Hawaiian landscape. The coatings form by acidic dissolution of near-surface basalt, followed by *in situ* precipitation of amorphous silica. Coating formation is surface-selective, occurring most prominently on surfaces with glassy surface layers. Regional plumes are the most important source of acidity driving the breakdown of these glassy layers, but local fissure vents may in some cases be a short-lived but significant contributor.

The set of coatings described in this study are essentially an ephemeral phenomenon, because they are easily removed both by abrasion and by spallation of the glassy layer. However, the coatings described in this study, composed of relatively pure amorphous silica, are one endmember of a broader continuum of coatings on Hawaiian basalts described in the literature. Coatings on lava flows 1,000–2,000 years old are thicker and more alumina-rich; these coatings on older flows typically incorporate wind-blown dust and basaltic ash as well as amorphous silica (Farr and Adams, 1984; Curtiss et al., 1985).

Despite their ubiquity and impact on the appearance of the Hawaiian landscape, surficial silica coatings are not a major contributor to the overall dissolved cation flux entering the ocean due to chemical weathering. Because young lava flows are so porous, rainwater and condensed water vapor rarely interact significantly with the bulk volume of a flow before draining underground. Instead, the geochemical signature of chemical weathering in Hawaiian waters is dominated by groundwater interaction and longer-term breakdown of flows and basaltic soils. Groundwater collected from wells near Kilauea is enriched in sulfate, chlorine and fluorine due to the input of magmatic volatiles; however, the dissolved chemistry implies a more complex mineral assemblage than that observed in this study, consisting of quartz, smectite, calcite and/or chlorite precipitated between 90° and 140° C (Hurwitz et al., 2003). Thus, siliceous surface alteration is a fast-acting reaction that has disproportionately large effects on the appearance of young lava flows, but is not representative of island-wide chemical weathering trends.

7. Acknowledgements

This work was supported by a NASA graduate student fellowship and by the White Rose Foundation. I thank Ken Hon (UH-Hilo) for discussion and for acting as field guide on the visit to the active Episode 58 flow field, Andrew Matzen and Suzanne Birner, who served as field assistants on the July 2010 and March 2012 field trips, respectively, and Tim Orr (HVO-USGS) for providing the Kamoamoa sample suite and geologic maps of the East Rift Zone.

Appendix: Sample Descriptions

Latitude / longitude and UTM coordinates for each sampling site are given in Table A1. Detailed descriptions of each field site and relevant samples collected at each site are given below.

A1. Vicinity of Kilauea Caldera

A1.1. Ka'u Desert, 1974 Flow

A suite of coated basalt samples from the December 1974 flow on Kilauea’s Southwest Rift Zone (SWRZ) was described in a previous study (Chemtob et al., 2010). The author returned to this sample collection site to document changes in silica coating properties along and perpendicular to the SWRZ axis. During the period of this field study, the Ka’u Desert was closed to the northeast of the Ka’u Desert Trail (**Fig. 1**) due to volcanic hazard related to the eruption at Halemaumau Crater beginning in 2009. Therefore, sampling of the December 1974 flow was restricted to regions within 1 km of the Ka’u Desert Trail. Samples from the December 1974 flow ~1 km closer to the crater rim were available from previous studies (Chemtob et al., 2010; Seelos et al., 2010).

White, yellow, and blue coatings appear on many external surfaces of the 1974 flow within the region studied. Previous work suggests that the brightly colored coatings are Fe-Ti oxide layers (Chemtob et al., 2010). At waypoint 1, coatings appear particularly prominent and contiguous on spatter ramparts, composed of basalt blebs with smooth, glassy surface layers, directly along the SWRZ (**Fig. 5a)**. Blebs of spatter ejected meters away from the primary rampart also appear contiguously coated. Cracks crisscrossing the spatter rampart surface were sometimes devoid of the bright coating (**Fig. 5b)**. Within 50

Sampling Location/ *Sample Name*	**UTM (Zone 5Q)**		**Latitude / Longitude**	**Waypoint number**
	E	**N**		
Ka'u Desert, Kilauea SWRZ				
KD-003a	257201	2142656	19.363° N, 155.311° W	1
KD-003c				
KD-003e				
KD-003g				
KD-Mar10-004	257667	2141058	19.349° N, 155.307° W	2
Keanakakoi Crater				
KK	262450	2146534	19.399° N, 155.261° W	3
Mauna Ulu, summit region				
MU-014	268566	2143026	19.368° N, 155.203° W	4
MU-017c	268596	2142839		
Mauna Ulu, medial flow field				
MU-029	272635	2139499	19.337° N, 155.164° W	5
Napau Crater, Episode 54 eruption				
NC-97-011b	275174	2143506	19.373° N, 155.141° W	6
Pu'u O'o summit lavas, Episode 55				
Jul10-PU-009	278937	2145388	19.390° N, 155.105° W	7
Jul10-PU-010				
Pu'u O'o summit lavas, Episode 58				
Jul10-PU-011	279077	2145431	19.391° N, 155.104° W	8
Episode 58 distal flow field				
TEB-020	284974	2144678	19.385° N, 155.047° W	9
KP-017	290757	2140405	19.347° N, 154.992° W	10
Kamoamoa 2011 eruption				
KE59-2941	276060	2144010	19.378° N, 155.132° W	11
KE59-2952	276653	2144210	19.380° N, 155.127° W	12
KE59-2970				
KE59-2979	275556	2143728	19.375° N, 155.137° W	13
KE59-2980	275602	2143808	19.376° N, 155.137° W	14
NC-11-008	275516	2143648	19.374° N, 155.137° W	15
NC-11-010				
NC-11-015	275902	2143939	19.377° N, 155.134° W	16
Mauna Loa, 1984 eruption				
Mar12-ML-NS-024	229603	2157362	19.493° N, 155.576° W	17
Mar12-ML-PL-001	252672	2170675	19.616° N, 155.358° W	18
Mar12-ML-PL-005				

Table A1. UTM and latitude/ longitude coordinates of sites visited for this study.

m of spatter ramparts, coatings are observed on ropey and sheet pahoehoe lavas that retain their glassy surface layer, but they appear sparser (**Fig. 5c–e**). At waypoint 2, the southeast-most extent of the 1974 flow (~1.5 km from the SWRZ), pahoehoe lobes feature similarly sparse but visually detectable coatings (**Fig. 5f)**. In places where the outer glassy layer has spalled away, leaving the rough, vesicular interior exposed, no bright coatings are observed (**Fig. 5g**). Coating coverage is heterogeneous, occasionally over even a single meter-scale outcrop, and appeared to be topographically controlled. Bright coating coverage frequently ceased on surface under overhanging basalt awnings. Additionally, coatings were sometimes absent at the edges of topographic barriers like flow fronts (**Fig. 5h**).

As discussed in Chemtob et al. (2010), the coatings collected at waypoint 1 are composed of a ~10 μm layer of hydrous amorphous silica, capped in many cases by a ~1 μm layer of Fe-Ti oxide **(Fig. 5i)**. The boundary between the silica layer and the basalt substrate is chemically sharp, but typically undulates on a spatial scale of 1 μm. In places, the silica layer penetrates the interior of the substrate along cracks (**Fig. 5j**). Coatings on spatter ramparts ~1 km closer to the caldera were similar in thickness and morphology (Chemtob et al., 2010).

In our previous study, we proposed that the apparent gradient of coating contiguity indicates that local spatter vents may be significant sources of acid. We predicted that if local SWRZ vents were significant sources of acid, a gradient in coating thickness away from the spatter ramparts would be observed. To test this prediction, we collected coated basalt samples 1, 10 and 40 m NW and SE of the SWRZ rampart (Samples KD-003a,c,e, and g; **Fig. 5b–e**). We observed a modest trend in coating thickness with distance from the SWRZ; coating thicknesses 1, 10, and 40 m NW of the rampart were 13, 16, and 7 μm, respectively (**Fig. 5k–l**). Based on this finding, it seems that local spatter vents may be modest contributors of acid for silica coating formation. The regional volcanic plume emanating from Kilauea Caldera may also be an important source of acidity. The plume is carried by trade winds from the caldera to the southwest, roughly following the trace of the SWRZ. Sampling site B, ~1.5 km southeast of the SWRZ, is somewhat removed from the typical path of the plume. Sample KD-Mar10-004, collected at sampling site B ~1.5 km southeast of the SWRZ, had a maximum coating thickness of 4 μm as determined by the "scratch test" method. The decrease in thickness at this site is likely attributable to less intense exposure of the distal end of the 1974 flow to the acidic plume vapors.

A1.2. Keanakakoi Crater

Keanakakoi Crater is a small pit crater on the southeast edge of Kilauea Caldera. A fissure eruption in July 1974 covered parts of the crater floor and produced fire fountains, spatter ramparts, pahoehoe flows and a lava lake on the southeast side of the crater adjacent to the fissure. Spatter ramparts on the southeast edge of the crater collected in March 2012 are brightly and contiguously coated with white, orange and yellow coatings (**Fig. 6a)**. Rafted spatter ramparts transported from their original site of deposition by pahoehoe flows are also coated. Lava trees formed during the fire fountain eruption are frequently covered in dense spatter and also feature colorful coatings (**Fig. 6b**). However, no coatings are observed on the pahoehoe surfaces that make up the majority of the subsided lava lake. These surfaces have largely spalled away their glassy surface layer. Although currently closed to the public and therefore unvisited by this researcher, spatter ramparts on the north side of Keanakakoi Crater also feature bright, visually apparent coatings (J. Saleeby, pers. comm.).

Based on the “scratch test” method, the apparent maximum thickness of the coatings on the surface of the 1974 flows from the vicinity of Keanakakoi Crater is ~3.5 μm. SEM-EDS images of a natural surface of sample KK shows complex relationships between the Fe-Ti and silica coatings. The Fe-Ti oxide coating does not occur uniformly over the surface, but is instead found in irregular patches. In some locations, the Fe-Ti oxide appears to be massive with no internal structure; elsewhere, the Fe-Ti oxide preserves a lineated structure perhaps related to primary deformation texture (**Fig. 6c**). The silica coating appears either as a smooth glazed surface covered with particulate nubs (**Fig. 6d**) or as a rough, popcorn-like surface completely dissected by dessication cracks (**Fig. 6e**).

A2. Vicinity of Mauna Ulu, East Rift Zone, Kilauea

A2.1. Mauna Ulu: Summit Region

The Mauna Ulu eruption lasted from May 1969 until July 1974, with a hiatus between October 1971 and February 1972. The eruption comprised fire fountains, fissure eruptions and large lava flow fields that together comprised the longest and most voluminous historic eruption on record before Pu'u O'o. We observed coatings at two sites near the summit of Mauna Ulu: a December 1969 fissure eruption 1.5 km west of the summit, near the visitor parking lot, and a lava channel and plateau on the northwest side of the summit cone, ~300 m from the caldera edge, next to Pu'u Huluhulu. In the following section, we describe samples collected from the distal flow field, 6 km from the summit.

Many surfaces of the spatter rampart immediately adjacent to the December 1969 fissure vent are brightly coated with white, yellow and orange coatings (**Fig. 7a**). As observed at other sites, the coatings are most prominent on smooth spatter slabs. A traverse perpendicular to the fissure axis was performed to observe changes in coating coverage with distance from the fissure. The coatings appeared equally intense and contiguous on some surfaces 30 m north (where the flow field ended in forest) and hundreds of meters south of the spatter rampart, suggesting that this fissure vent was not a significant source of acidity for coating formation. Generally, coatings were not observed on spalled or eroded surfaces, but, in one location ~100 m south of the fissure, pale brown alteration was observed on a relatively flat surface that had spalled its glassy outer layer (**Fig. 7b**).

The walls of the channel on the northwest side of the Mauna Ulu summit cone consist of lava sheets that represent return flow into the channel after the eruption subsided. These macroscopically smooth sheets feature pale white, yellow or blue coatings on most surfaces; coatings are absent near cracks in the sheet and on spalled surfaces (**Fig. 7c**). Lavas that have not lost their glassy outer layer to spallation, but display greater roughness than the pahoehoe sheets, either display no coatings or have coatings that appear to be abraded and partially removed. Near topographic nubs, white-blue coatings are frequently oxidized to an orange color, suggesting a micro-topographic control on oxidation and removal (**Fig. 7d**). Coatings are also found on the undersides of hollow pahoehoe shells; coatings appear to be more prominent on shell undersides that were previously broken than those that the researchers broke open, suggesting that exposure to the environment plays a factor in coating formation.

Sample MU-017c is a piece of shelly pahoehoe with bright coatings exposed on the shell underside. SEM-EDS images of polished cross-sectional mounts of the shell illustrate that the surface has 3–5 μm coatings of amorphous silica (**Fig. 7e**). The MU-017c basalt substrate consists of dendritic pyroxenes (60%) in a glass matrix (40%). In places, the silica coating may attack the glass around the edges of the pyroxene dendrites, leaving them unaltered (**Fig. 7f**).

The natural surface of sample MU-014, collected from the coated walls of the near-summit lava channel, was examined by SEM-EDS to characterize the distribution of Fe-Ti coatings. Fe-Ti materials occur along localized stripes, 30–100 μm across on the surface, and are not necessarily correlated with the presence of silica coatings (**Fig. 7g**). EPMA analysis of coatings from Mauna Ulu illustrate that the Fe/Ti content of the Fe-Ti coatings is higher and more variable than coatings from the Ka’u Desert (Chemtob et al., 2010).

A2.2. Mauna Ulu: Distal Flow

We traversed the Mauna Ulu distal flow field along the Naulu Trail, starting at Kealakomo on the Chain of Craters Road, to characterize the distribution of coatings ~6 km from the summit vent. Coatings similar in appearance to those seen in the Mauna Ulu summit region were observed on many flow surfaces. Localized variations in coating coverage depended both on surface properties and micro-environmental changes. In places, on the parts of pahoehoe ropes that underwent the most strain during emplacement (i.e., along the axis corresponding to flow direction) displayed discoloration (**Fig. 8a**). Coatings on one smooth surface petered out beneath a lava overhang (**Fig. 8b**).

Particularly intensely colored coatings were observed at a site on the Naulu Trail ~2 km from the Chain of Craters Road. At this site, dense, highly degassed lavas breaking out from tumuli feature bright and contiguous white, yellow and blue coatings (**Fig. 8c–d**). The tumuli themselves from which the dense lavas extrude are typically uncoated. The dense coated lavas appear to be rarely overlain by later pahoehoe lobes, suggesting these lavas were among the last breakouts in this region. Coatings on breakout lavas (sample MU-029) were determined by the “scratch test” to be ~6 μm thick.

A3. Vicinity of Pu’u O’o, East Rift Zone, Kilauea

A3.1. Napau Crater: Episode 54 Eruption

Episode 54 of the Pu'u O'o eruption of Kilauea Volcano occurred on January 30-31, 1997, and consisted of several fissure eruptions within and just to the east of Napau Crater, ~2 km west of the Pu’u O’o cone. These fissures produced lava fountains several tens of meters high and lasted for about 24 hours. In March 2010, we visited the spatter ramparts and pahoehoe flows associated with one of the fissure eruptions in the center of the crater. At the time of the visit, some of the vents associated with the fissure eruptions continued to emit heat and sulfur-rich gas.

Spatter ramparts in the center of Napau Crater from the 1997 eruption displayed prominent, contiguous white, orange and yellow coatings (sample NC-97-011b; **Fig. 9a**). Within ~2 m of the primary fissure, coatings on spatter were more strongly orange in color; away from the fissure, the coatings were paler in color. Ropey pahoehoe flows extend ~100 m in either direction from the fissure, rafting chunks of spatter in some places. Pahoehoe toes at the edge of the 1997 lavas are coated, but appear sparser than than the spatter ramparts (**Fig. 9b**).

SEM imagery of the coatings on the spatter indicate that they consist of a 3-µm-thick layer of amorphous silica, with zones of Fe-Ti oxides near the edge of the coating (**Fig. 9c**). Unlike the coatings from the Ka’u Desert, which featured a thin, continuous layer of Fe-Ti oxide, coatings on the Napau Crater lavas appear to feature more particulate Fe-Ti oxides, 0.3–1.5 µm across, distributed irregularly along the surface. In places, the silica layer appears to penetrate the interior of the basalt along a near-surface crack (**Fig. 9d**).

A3.2. Pu'u O'o Summit Lavas, Episode 55

In July 2010, we traveled by foot via Napau Crater to the summit of the Pu’u O’o vent. We collected samples in two locations from the Episode 55 eruption: 2002–2005 shelly pahoehoe flows that covered the west flank of Pu’u O’o, and 1997–1998 overflow lavas that currently make up the northeast rim of the crater vent. Additionally, we collected samples from the onset of the Episode 58 eruption, comprising spatter and pahoehoe toes from the westernmost fissure of the July 2007 eruption, 200 m northeast of the Pu’u O’o crater vent. Since the sampling trip, some of these sites have been buried by lavas from Episode 61 beginning in 2011.

Both the shelly pahoehoe flows on the west flank of the vent and the overflow lavas on the northeast rim feature a ubiquitous powdery, whitish-blue coating (**Fig. 10a**). This white material is not observed on older surfaces in the immediate vicinity, such as the brown, highly oxidized and spalled lavas from 1983-1986 that make up the edifice on the north crater rim. The white coatings appear most prominently on smooth, flat surfaces, penetrate the surface along prominent surface cracks (**Fig. 10b**), and are not visible in places where the basalt surface has been subjected to physical abrasion or spallation. The coatings are composed of opalescent polygonal material that appears to coat most surfaces with a constant thickness. The basalt cores of coated vesicle rims appear to have been thinned compared to uncoated basalt (**Fig. 10c**). The overflow lavas frequently feature a hollow open space beneath a surficial basalt shell 2–3 cm thick. The undersides of these surficial shells frequently feature a white, yellow or orange pale glazed coating (sample PU-010; **Fig. 10d**). The surface of the flow is littered with volcanic bombs of unknown age ejected from the cone (sample PU-009) (**Fig. 10e–f)**. On their upper surfaces, these bombs are heavily and contiguously coated with the powdery white material, even in cases where the lava on which the bomb sits is spalled and uncoated. The undersides of the bombs also appear to be covered in a yellow or orange glaze-like coating.

SEM images of cross-sections of samples PU-009 and PU-010 indicate that basalts from the 1997–98 Pu'u O'o overflow lavas have hydrous amorphous silica coatings 20–80 µm thick. PU-010, a sample of the coated hollow pahoehoe shell, features ~50 µm silica layers on both sides of the shell (**Fig. 10g–h**). Microprobe analysis of these coatings, like other similar samples, typically have low totals; after normalizing to unity, the analyses indicate that the coatings are 97 wt% SiO_2, with 1 wt% SO_3, 0.5 wt% TiO_2, 0.5 wt% FeO*, and minor quantities of other elements. NMR and infrared analysis indicate that the coating on PU-009 has unusually high structural water content (5.4 wt%

H_2O as Si-OH) for a natural silica sample (Chemtob et al., 2012). The amorphous silica layer is sometimes capped by a thin (< 1 µm), Fe-Ti rich coating layer. Some parts of the surface display residual morphology; for example, in places, the coating bridges near-surface vesicles, implying replacement rather than deposition (Chemtob et al., 2010) (**Fig. 10i**). Other parts of the surface display depositional morphology, such as infilled vesicles (**Fig. 10j**); however, such geometries could also be produced by clastic mobilization and redeposition.

A3.3. Pu'u O'o Summit Lavas, Episode 58

The 2007 lavas were distinguishable from the Episode 55 lavas on which they were deposited by their fresher appearance and darker color. Dense spatter pancakes immediately adjacent to the fissure vent featured a glazed, milky white coating with a similar color as the coatings on the Episode 55 lavas at the rim of Pu'u O'o (**Fig. 11a–b**). Ropey pahoehoe associated with the fissure vents also featured a pale white coating, but coating coverage was sparser than the dense spatter pancakes.

SEM imagery of a cross-sectional mount of one of the 2007 spatter pancakes (sample PU-011) indicates that the spatter features a 6-10 µm-thick amorphous silica coating (**Fig. 11c**). No continuous, discrete Fe-Ti coating layer was observed in SEM images or in Raman spectra of the surface of sample PU-011.

A3.4. Episode 58 Distal Flow Field

In July 2010, we visited sites along the active Episode 58 flow field (an eruption that began in 2007, as described in sections A3.2 and A3.3) to observe the extent of surface alteration on still-active lava and flows up to several months old. We accessed the highest point, at 557 m elevation about 7.5 km east of the Pu'u O'o vent, by helicopter, and parallelled the flow fields to their intersection with the coast near Kalapana.

Most of the lava surfaces on the Episode 58 flow field were S-type pahoehoe that had spalled their glassy surface layer; these spalled surfaces were not visibly altered (**Fig. 12a**). Orange and white mineral deposits were observable along cracks, especially near the trace of the primary lava tube; these deposits were likely iron chlorides (Ken Hon, pers. comm.). Away from cracks, spalled surfaces displayed no obvious alteration products. A 1.5-m-tall hornito at the helicopter access point, ~3 months old at the time of the field visit, featured yellow spattered sublimates of sulfur and white incrustations of thenardite (sodium sulfate) and bloedite (sodium magnesium sulfate) (**Fig. 12b**). A slab from the surface of the hornito (sample TEB-020) displayed a colorless glaze, determined by SEM-EDS to be a Si-rich coating 1–6 µm thick (**Fig. 12c**).

Fresh lava was collected using a steel pole from an open channel at ~390 m elevation. This fresh glass was used as starting material for laboratory dissolution experiments, described in Chemtob (2012). As expected, the fresh lava displayed no signs of alteration. The lava sample (sample KP-fresh) was ~90% glass, with 10% plagioclase phenocrysts.

The Episode 58 flow field intersects the southern coast of Hawaii about 800 m west of Kalapana; most lavas on the plains near the coast were emplaced in 2007. Many surfaces making up these lava plains are S-type pahoehoe, featuring a brittle, "crunchy" surface glass layer. In some places, dense P-type pahoehoe breaks out from small tumuli. P-type pahoehoe surfaces frequently have a distinct blue color, especially in backscattered sunlight (sample KP-017; **Fig. 12d**). Unlike basalt samples with bright colors caused by thin film interference, which typically display a range of colors that vary with the thickness of the film, the blue color of these surfaces does not change appreciably from sample to sample. The constancy of the blue color suggests a compositional origin. Oze and Marshall (2005) suggested nanocrystals of Fe-Ti oxide as a potential chromophore. No silica coatings were detected on these P-type pahoehoe lavas.

A3.5. Kamoamoa 2011 Eruption

On March 5, 2011, the crater floor of the Pu'u O'o cone collapsed due to magma withdrawal. The withdrawn magma fed an eruption along 2 km of the Kamoamoa fissures between Pu'u O'o and Napau Crater. We acquired two sets of samples from this eruption, designated Episode 59 of the Pu'u O'o eruption. USGS scientists collected pahoehoe and spatter samples along the length of the fissure system during and immediately after the eruption. We received a subsample of spatter samples collected off of older tephra 1–8 days after emplacement. Additionally, we visited the westernmost fissure vent of the Kamoamoa eruption in March 2012 and collected pahoehoe toe lavas, spatter directly adjacent to the main vent, and spatter that was ejected onto older tephra.

Fresh spatter samples: The surfaces of 1–8 day old spatter samples collected from Kamoamoa all displayed a black, glossy surface under visual inspection (**Fig. 13a–e**). Polished cross-sectional mounts of the spatter samples showed no contiguous surface alteration layers when observed by SEM-EDS. However, natural surfaces of these samples showed considerable textural and chemical heterogeneity, potentially related to heterogeneity of primary processes rather than postdepositional alteration.

Sample KE59-2941, collected while still hot from the easternmost end of the west fissure system, displayed no surface chemical heterogeneity. The surface was macroscopically smooth but displayed crinkle textures and zones of lineations with 3–5 µm spacing (**Fig. 14a**). These textures are related to deformation of the surface glass as it cools and solidifies. Sample KE59-2952, collected from the westernmost end of the east fissure system ~24 hours after emplacement, similarly displayed crinkle textures and lineations but no chemical heterogeneity.

Sample KE59-2970 was collected from the westernmost end of the east fissure system 5 days after emplacement. Much of the surface is covered by a thin layer (< 1 µm) of Fe-rich material (**Fig. 14b**), identified by EBSD as a mixture of magnetite and ilmenite crystals (**Fig. A1**). In places, the Fe-rich material appears as radial bunches of dentritic crystals, ~100–200 nm wide and up to 5 µm long; elsewhere, the material appears as an amorphous mass. The magnetite-ilmenite masses are not present in areas immediately adjacent to surface vesicles and along some lineations similar to those seen in samples KE59-2941 and KE59-2952. In regions not covered by the Fe-rich material, SEM-EDS indicates that the surface has typical basalt composition. No Si-rich compositions indicating amorphous silica were observed on KE59-2970.

Sample KE59-2980, collected 5 days after emplacement from the west fissure system, also displayed Fe-rich material on its surface, but with a different morphology than that observed on KE59-2970. Dendritic bunches of crystals on the surface were rare; instead, Fe-rich material was concentrated along a network of lineations defining

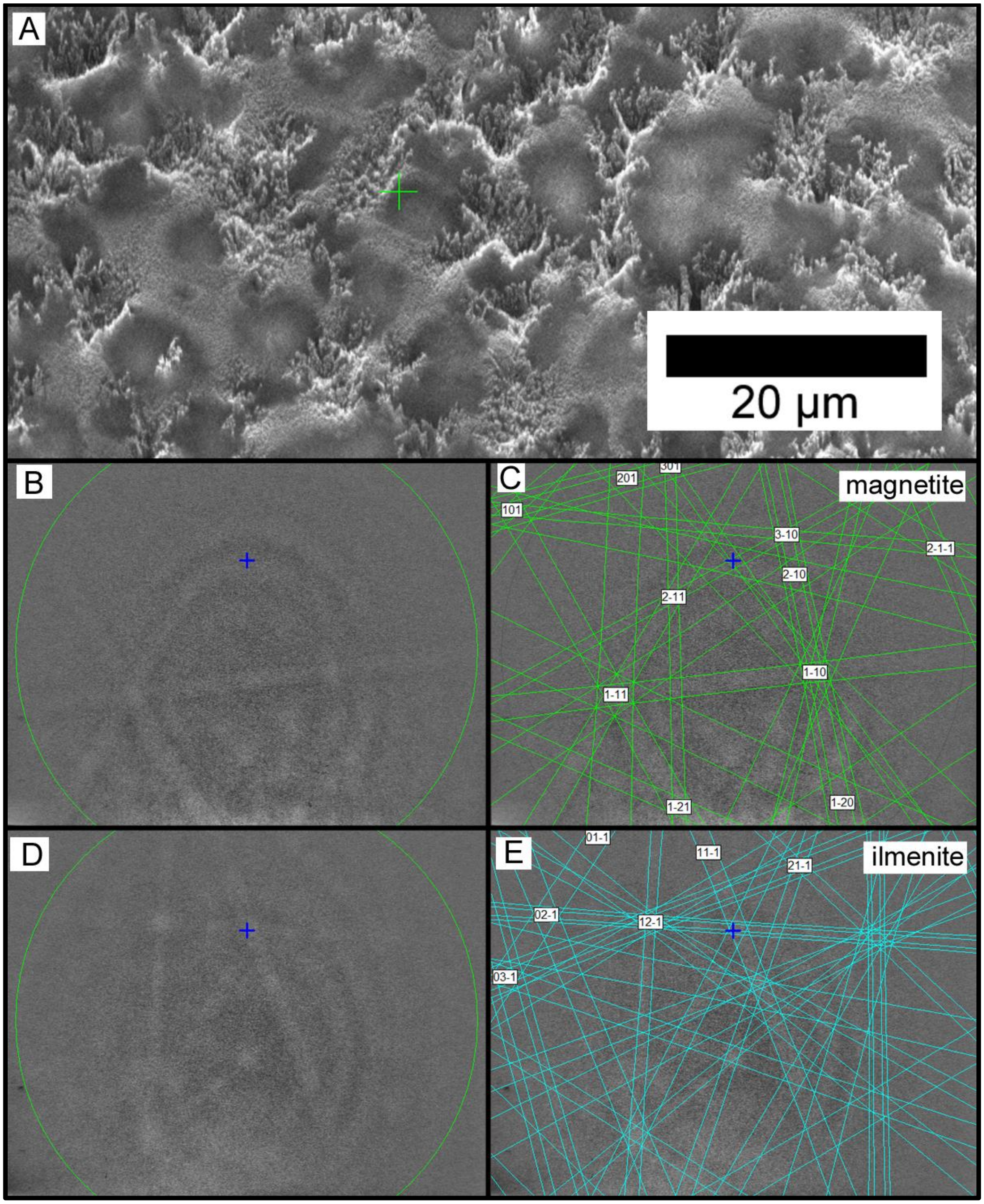

Figure A1. Electron backscatter diffraction patterns of Fe-rich crystallites on Kamoamoa samples. A) Variable pressure SEM image of natural surface of sample KE59-2970. B) EBSD pattern corresponding to magnetite. C) Indexed pattern from (b). D) EBSD pattern corresponding to ilmenite, less commonly observed on this sample. E) Indexed pattern from (d).

subequant polygons of 3-6 sides (**Fig. 14c**). This texture appears to indicate expansion and stretching of the glass surface. Other parts of the surface of sample KE59-2980 are covered with particulate matter, 0.5–5 µm in diameter, with no apparent chemical contrast with the basalt substrate (**Fig. 14d**).

Sample KE59-2979, collected 8 days after emplacement from the west fissure system, displayed the most surface chemical heterogeneity of the fresh spatter samples. The surface texture is dominated by circular pockmarks; in some places, the pockmarks merge into continuous lineations as seen in other spatter samples (**Fig. 15a–b**). This heterogeneous texture also defines a chemical heterogeneity: areas between the pockmarks are more Fe-rich than the pockmark interiors, which have basaltic composition (**Fig. 15c–e**). Fe-rich materials on the surface of KE59-2979 are either defined by polygonal platelets ~200–400 nm across (**Fig. 15f**) or by masses of tiny crystals too fine to resolve (**Fig. 15b**). Additionally, localized regions of the pockmarks, particularly adjacent to vesicle edges, have the composition of amorphous silica (**Fig. 15b**).

Kamoamoa eruption, 1 year later: When we visited in March 2012, the holistic appearance of Kamomoa flow field was fresh, black and unaltered. The lava flow emanating to the north of the westernmost fissure is composed of a’a and shelly pahoehoe. Pahoehoe toes at the northern front of this flow appeared mostly unaltered but displayed faint white coloration on some surfaces. On the interior of the flow, numerous fissures were still emitting acidic vapors, resulting in sulfur mineralization and apparent basalt staining (**Fig. 16a**). Lavas near the most productive vent on the west fissure system, featuring ~6 m spatter ramparts, displayed heterogeneous colors and surface properties. Some surfaces had developed the pale brown color that commonly develops from light oxidation of glass but were otherwise unaltered. A piece of basalt collected from the spatter rampart (NC-11-008) had iridiescent coloration, suggesting thin film interference **(Fig. 16b)**. Some dense lava surfaces developed a matte brown coating criss-crossed by white mineralization along cracks, reminiscent of silica coatings observed in other field locations. A ~25-cm volcanic bomb (NC-11-010) displayed colors that varied sharply across its surface (blue, yellow and brown) (**Fig. 16a**).

Sample NC-11-008, from the westernmost spatter rampart, is a highly vesicular piece of spatter featuring blue, purple and yellow iridescent coloration. In SEM-EDS images of the sample, the surface is matte and relatively featureless. However, EDS element maps suggest a modest chemical contrast near vesicles; vesicle rims are enriched in Al, Mg, Fe and Al, while Si shows no noticeable change (**Fig. 16c–f)**. This contrast suggests that much of the surface features a thin Si-rich coating that is not present near the vesicle rim. Because the basaltic elements are detectable away from the vesicle rim, the coating thickness is likely less than the penetration depth of the electron beam (i.e., < 1–2 μm). Elsewhere on the surface, primary deformation lineations similar to those seen on the fresh KE59 samples were observed; these defined similar chemical contrasts, also suggesting the presence of a thin Si-rich coating.

SEM-EDS images of sample NC-11-010, the volcanic bomb collected at the westernmost spatter rampart, show that much of its surface is covered with a coating, divided into polygons 3–10 μm across by shallow cracks or troughs criss-crossing the surface (**Fig. 17b**). The coating appears to be highly porous (**Fig. 17c**). The coating is not present at the edges of some surface vesicles; at those locations, EDS elemental maps indicate a strong chemical contrast between the coating, which appears to be composed solely of amorphous silica, and the substrate, which has basaltic composition (**Fig. 17d–**

f). The exposure of the coating at the vesicle edges and the strong chemical contrast in elemental maps suggest a silica coating ~2–3 µm thick.

Spatter ejected onto older tephra was collected from areas along the western fissure system (from locations close to the collection sites of KE59-2979 and KE59-2980 the previous year). These ejecta (sample NC-11-015) have a glassy outer layer and are black to dark blue in color (**Fig. 18a**). Like the freshly collected spatter, deformation lineations are frequently present; unlike those fresh samples, much of the surface of the spatter is covered in desiccation cracks, a texture characteristic of amorphous silica (**Fig. 18b**). A partial cross section of the silica coating where it disappears near a vesicle rim suggests a thickness of ~3–4 µm (**Fig. 18c**). Other parts of the surface feature Fe-rich polygonal deposits, similar to those seen on sample KE59-2980 (**Fig. 18d**). The Si-rich and Fe-rich deposits sometimes occur together, but their occurrences are not obviously correlated.

A4. Mauna Loa, 1984 Eruption

The March 1984 eruption of Mauna Loa consisted of fissure eruptions, fire fountains, and effusive lava flows emanating from fissures along the length of the northeast rift zone. The eruption began at rifts within Mokuaweoweo (the summit caldera of Mauna Loa) and propagated to rifts 15 km from Mokuokaweoweo, at 2770 m elevation (Lockwood et al., 1987). Lava flows from the lower eruptive vents flowed to within 10 km of Hilo and to an elevation of < 1000 m. We visited two locations along the 1984 eruption: fissure vents and associated spatter ramparts in and adjacent to the North

Pit of the Mauna Loa caldera (~4000 m elevation) and the intersection of the Powerline Road with the distal flow (1750 m elevation).

A4.1. Near-summit Fissure Lavas

Spatter from the 1984 eruption adjacent to fissures near the summit of Mauna Loa did not feature visually prominent, brightly colored coatings. The basalts were typically dark brown in color. Some surfaces had apparently spalled, exposing a coarse, vesicular surface. Spatter from spatter ramparts adjacent to the fissures typically retained its dense, glassy surface but were not discolored, as observed in the Ka’u Desert and Mauna Ulu (**Fig. 19a**). Some cinders and spatters displayed iridescent coloration. Snow partially obscured some of the spatter ramparts.

SEM imagery of natural surfaces of Mauna Loa 1984 spatter (sample ML-NS-024) revealed a variety of micro-textures. Some regions displayed sinuous lineations, ~1 µm high, with a spacing of 3-5 µm. Other regions were covered in circular pockmarks, 1–10 µm across (**Fig. 19b**). We interpret these textures as primary deformation features while the spatter surfaces were still hot and viscous. Pockmarked regions perhaps represent areas where the surface expanded; lineated regions represent sheared flow lines on the surface.

SEM imagery and x-ray maps also indicated that Si-rich alteration materials occur on the surface of the spatter in small quantities. A patch of the surface, roughly 300 µm by 500 µm across, was observed in SEM-EDS x-ray maps to be Si-enriched (**Fig. 19c**). In places, the basalt underlying this patch was exposed, indicating that the Si deposit is approximately 2 µm thick. Additionally, x-ray maps indicate that the primary micro-textures described above define finely spaced compositional variation. Depressed regions within the lineations and pockmarks are enriched in Si. This suggests that certain regions of the surface may be more susceptible to alteration.

In summary, near-summit lavas from the Mauna Loa 1984 eruption are not visually obviously altered, but display small quantities of silica coatings irregularly distributed over their surface.

A4.2. Distal Flow, 1750 m

At its intersection with the Powerline Road, the 1984 Mauna Loa lava flow is an a'a flow ~8 m thick. The local surfaces of the flow are roughly textured clinkers with no glassy surface layer. Lichens and mosses grow on large portions of the surface. Localized portions of the flow surface (sample ML-PL-001) featured a white, dusty deposit identified by Raman spectroscopy as amorphous silica (**Fig. 19d**). In places, the silica appeared as nodules within vesicles and large cavities.

A rafted block of pahoehoe was perched on the east edge of the a'a flow, roughly 100 m north of the Powerline Road intersection. The age and provenance of this flow chunk is unknown, but it most likely represents a chunk of the same 1984 lava flow carried from an area upslope of the pahoehoe-a'a transition. The rafted surface retained its smooth surface layer and was colored bright orange (**Fig. 19e**). The orange material (on sample ML-PL-005) is a thin, irregular veneer identified by Raman spectroscopy as lepidocrocite (iron oxyhydroxide). SEM-EDS images indicate that the surface features no Si-rich alteration material (**Fig. 19f)**.

Works Cited

Abrams, M., E. Abbott, and A. Kahle (1991) Combined use of visible, reflected infrared, and thermal infrared images for mapping Hawaiian lava flows. *JGR*, **96**, 475–484.

Byrnes, J. M., M. S. Ramsey, and D. A. Crown (2004) Surface unit characterization of the Mauna Ulu flow field, Kilauea Volcano, Hawai'i, using integrated field and remote sensing analyses. *J. Volcanol. Geotherm. Res.*, **135**, 169–193.

Chemtob, S. M. (2012) Silicon isotope systematics of acidic weathering of fresh basalts, Kilauea Volcano, Hawaii. Thesis Chapter V.

Chemtob, S. M., Jolliff, B. J., Rossman, G. R., Eiler, J. M., and Arvidson, R. E. (2010) Silica coatings in the Ka'u Desert, Hawaii, a Mars analog terrain: a micromorphological, spectral, chemical, and isotopic study. *JGR*, **115**, doi:10.1029/2009JE003473.

Chemtob, S. M., G. R. Rossman, and J. F. Stebbins (2012). Natural hydrous amorphous silica: quantitation of network speciation and hydroxyl content by ^{29}Si MAS NMR and vibrational spectroscopy. *American Mineralogist*, **97,** 203–211.

Crisp, J., A. B. Kahle, and E. A. Abbott (1990) Thermal infrared spectral character of Hawaiian basaltic glasses. *JGR*, **95**, 21657–21669.

Curtiss B., J. B. Adams, and M. S. Ghiorso (1985) Origin, development and chemistry of silica-alumina rock coatings from the semi-arid regions of the island of Hawaii. *Geochimica et Cosmochimica Acta*, **49**, 49–56.

Dorn, R. I. (1998) Digital processing of back-scatter electron imagery: a microscopic approach to quantifying chemical weathering. *GSA Bull.*, **107**, 725–741.

Dorn, R. I. (2012) Formation of silica glaze rock coatings through water vapor interactions. *Physical Geography*, **33**, 21–31.

Elias, T., Sutton, A. J., Stokes, J. B., and Casadevall, T. J. (1998) Sulfur dioxide emission rates of Kilauea Volcano, 1979–1997. USGS Open-File Report Number 98-462.

Elias, T., and Sutton, A. J. (2012) Sulfur dioxide emission rates from Kilauea Volcano, Hawai'I, 2007–2010. USGS Open-File Report 2012-1107, 25 p. (http://pubs.usgs.gov/of/2012/1107/)

Farr, T. G., and J. B. Adams (1984) Rock coatings in Hawaii. *GSA Bulletin*, **95**, 1077–1083.

Fulignati, P., Sbrana, A., Clocchiatti, R., Luperini, W., (2006) Environmental impact of the acid fumarolic plume of a passively degassing volcano (Vulcano Island, Italy). *Environ. Geol.*, **49**, 1139–1155.

Gislason, S. R. and Oelkers, E. H. (2003) Mechanism, rates, and consequences of basaltic glass dissolution: II. An experimental study of the dissolution rates of basaltic glass as a function of pH and temperature. *Geochim. Cosmochim. Acta*, **67**, 3817–3832.

Hausrath, E. M., Navarre-Sitchler, A. K., Sak, P. B., Steefel, C. I., and Brantley, S. L. (2008) Basalt weathering rates on Earth and the duration of liquid water on the plains of Gusev Crater, Mars. *Geology*, **36**, 67–70.

Hurwitz, S., Goff, F., Janik, C. J., Evans, W. C., Counce, D. A., Sorey, M. L., and Ingebritsen, S. E. (2003) Mixing of magmatic volatiles with groundwater and interaction with basalt on the summit of Kilauea Volcano, Hawaii. *JGR*, **108**, doi:10.1029/2001JB001594.

Kahle, A. B., Gillespie, A. R., Abbott, E. A., Abrams, M. J., Walker, R. E., and Hoover, G. (1988) Relative dating of Hawaiian lava flows using multispectral thermal infrared images: a new tool for geologic mapping of young volcanic terranes. *JGR*, **93**, 15239–15251.

Lockwood, J. P., Dvorak, J. J., English, T. T., Koyanagi, R. Y., Okamura, A. T., Summers, M. L., and Tanigawa, W. R. (1987) Mauna Loa 1974–1984: a decade of intrusive and extrusive activity. *In* Volcanism in Hawaii, USGS Professional Paper 1350, 537–570.

Morris, R. V., T. G. Graff, S. A. Mertzman, M. D. Lane, and P. R. Christensen (2003) Palagonitic Mars from rock rinds to dust: evidence from visible, near-IR, and thermal emission spectra of poorly crystalline materials. *LPSC XXXIV*, #1874.

Moune, S., Faure, F., Gauthier, P.-J., and Sims, K. W. W. (2007) Pele's hairs and tears: natural probe of volcanic plume. *J. Volcanol. Geotherm. Res.*, **164**, 244–253.

Oelkers, E. H. and Gislason, S. R. (2001) The mechanism, rates and consequences of basaltic glass dissolution: I. An experimental study of the dissolution rates of basaltic glass as a function of aqueous Al, Si and oxalic acid concentration at 25°C and pH = 3 and 11. *Geochim. Cosmochim. Acta*, **65**, 3671–3681.

Oze, C. and J. D. Winter (2005) The occurrence, vesiculation, and solidification of dense blue glassy pahoehoe. *J. Volcanol. Geotherm. Res.*, 142, 285–301.

Prinsloo, L. C., Colomban, P., Brink, J. D., and Meiklejohn, I. (2010) A Raman spectroscopic study of the igneous rocks on Marion Island: a possible terrestrial analogue for the geology on Mars. *J. Raman. Spectroscopy*, doi: 10.1002/jrs.2756.

Schiffman, P., R. Zierenberg, N. Marks, J. L. Bishop, and M. D. Dyar (2006) Acid-fog deposition at Kilauea volcano: a possible mechanism for the formation of siliceous-sulfate rock coatings on Mars. *Geology*, **34**, 921–924.

Seelos, K. D., R. E. Arvidson, B. L. Jolliff, S. M. Chemtob, R. V. Morris, D. W. Ming, and G. A. Swayze (2010), Silica in a Mars analog environment: Ka'u Desert, Kilauea Volcano, Hawai'i, J. Geophys. Res., doi:10.1029/2009JE003347.

Skok, J. R., Mustard, J. F., Ehlmann, B. L., Milliken, R. E., and Murchie, S. L. (2010) Silica deposits in the Nili Patera caldera on the Syrtis Major volcanic complex on Mars. *Nature Geosci.*, doi: 10.1038/NGEO990.

Spadaro, F. R., Lefèvre, R. A., and Ausset, P. (2002) Experimental rapid alteration of basaltic glass: Implications for the origins of atmospheric particulates. *Geology*, **30**, 671–674.

Temple, A. K. (1966) Alteration of ilmenite. *Econ. Geol.*, **61,** 695–714.

White, A. H., and Brantley, S. (2003) The effect of time on the weathering of silicate minerals: why do weathering rates differ in the laboratory and field? *Chem. Geol.*, **202**, 479–506.

Wilmoth, R. A. and G. P. L. Walker (1993) P-type and S-type pahoehoe: a study of vesicle distribution patterns in Hawaiian lava flows. *J. Volcanol. Geotherm.*, **55**, 129–142.

Chapter IV. Natural Hydrous Amorphous Silica: Quantitation of Network Speciation and Hydroxyl Content by ^{29}Si MAS NMR and Vibrational Spectroscopy

Originally published as:
Chemtob, S. M., G. R. Rossman, and J. F. Stebbins (2012) Natural hydrous amorphous silica: quantitation of network speciation and hydroxyl content by ^{29}Si MAS NMR and vibrational spectroscopy. *American Mineralogist*, **97**, 203–211.

Abstract

Natural and synthetic hydrous amorphous silicas were investigated with single-pulse ^{29}Si magic-angle spinning (MAS) NMR and with vibrational spectroscopic methods. Samples included a volcanically derived silica coating on young basalt from Kilauea, Hawaii, as well as hyalite (opal-AN), silica sinters, and synthetic silica gels and silicic acid. Pulse delays of up to an hour were employed for silica samples with slow spin lattice relaxation rates, and nearly fully relaxed spectra (90–100%) were demonstrably achieved for all samples. ^{29}Si NMR spectra consisted of two broad, overlapping peaks at -111 and -102 ppm and a smaller peak at -92 ppm, corresponding to Q^4, Q^3 and Q^2 sites, respectively. The Hawaiian silica coating and silicic acid samples displayed high Q^3 and Q^2 contents; in particular, the structural Si-OH content of the coating was unusually high for a natural silica (5.4 ± 0.4 wt.% H_2O). Saturation-recovery spectra of the Hawaiian silica with increasing delay times were consistent with "stretched exponential" relaxation behavior and three-dimensional distribution of paramagnetic centers. Attenuated total reflectance infrared (ATR-IR) and Raman spectra of the silica powders indicated fully amorphous structures, and displayed hydrous (SiO_3OH) and anhydrous silicate vibrational bands in positions consistent with previous work. Raman spectra of some samples indicated modest grain to grain heterogeneity. Inferred Si-OH contents from ATR-IR band ratios were strongly correlated with hydroxyl contents calculated from NMR spectra. The high Si-OH content of the Hawaiian silica coating suggests it is diagenetically immature and has not been exposed to elevated temperatures.

1. Introduction

The detailed structural characterization of hydrous amorphous silica phases holds importance both for geological problems and in various technological and industrial applications (e.g., desiccants, aerogels, SiO_2 films in semiconductors). In natural settings, amorphous silica (SiO_2) occurs as a secondary phase in a variety of geological environments. Opal is common in neutral-pH hydrothermal settings, where it precipitates from supersaturated spring waters as silica sinter (Rodgers et al., 2002). Precipitation of abiotic and biogenic silica (e.g., diatoms) is a dominant control on the silica concentration of marine waters (Morel and Hering, 1993). Amorphous silica may also be formed in acidic environments as a residual or depositional product of weathering, and also is found as rock coatings in basaltic weathering environments such as the island of Hawaii (Farr and Adams, 1984; Minitti et al., 2007; Chemtob et al., 2010), Vulcano (Fulignati et al., 2002) and Craters of the Moon in Idaho (Faye and Miller, 1973). The chemical, structural and morphological properties of secondary silica deposits are a function of numerous environmental factors, including temperature, pH, water availability, and timescale of formation. Thus, material characterization of silica phases from both the modern and ancient geological record may constrain environmental conditions at the time of their formation. Specifically, the measurement of water content and speciation in silica phases has been the subject of much attention. Here we apply ^{29}Si magic-angle spinning (MAS) NMR, together with Raman and infrared spectroscopy, to hydrous amorphous silicas, including silica coatings formed by acid-sulfate alteration of Hawaiian basalt.

NMR has been applied to various aspects of the structure of hydrous, amorphous silica in numerous studies of naturally-occurring and synthetic materials (see reviews in Engelhardt and Michel (1987), MacKenzie and Smith (2002)). Several early papers on natural opals used simple, ^{29}Si MAS NMR ("single-pulse" spectra, with little or no manipulation of the ^{1}H spin system) and reported broad, slightly asymmetric, single peaks attributable to the predominant type of silica tetrahedra, which are connected to other tetrahedra through four bridging oxygens (Q^4 groups) (deJong et al., 1987; Graetsch et al., 1990). More extensive studies, with higher-quality spectra, also reported an additional, smaller peak due to silicons with single attached OH groups (Q^3) in some opal-CT samples (Graetsch et al., 1994; Brown et al., 2003). However, this species, reaching 20–25% of some spectra, may have been over-represented, because the problem of differential relaxation was not thoroughly explored: collection of such spectra with insufficient delays between NMR pulses can exaggerate the intensity of more rapidly-relaxing components. Cross-polarization (CP) MAS spectra, in which spin energy is transferred from abundant ^{1}H nuclei to nearby Si, was shown to give much higher overall signal-to-noise ratios, to greatly enhance the Q^3 signal and to reveal small amounts of Q^2 groups in some samples (Graetsch et al., 1994; Brown et al., 2003; Paris et al., 2007). However, this method generally cannot be considered to be quantitative, because the signal intensities depend in complex ways on not only silicate speciation, but on the spatial distribution of protons, their interactions, and on the dynamics of proton mobility (e.g. rotation of water molecules, site hopping, etc.) (Engelhardt and Michel, 1987; MacKenzie and Smith, 2002). ^{29}Si{^{1}H} CPMAS NMR can be very useful for exploring the distribution (e.g., surface vs. interior) and dynamics of protons in such materials, as demonstrated in early papers (Maciel and Sindorf, 1980; Sindorf and Maciel, 1982) on silica gels, and in later work on surface protonation as a function of pH (Carroll et al., 2002), but usually cannot accurately determine overall Si-OH contents.

For this study, we collected only "single-pulse" ^{29}Si MAS NMR spectra, in which the ^{29}Si spins are excited directly by a simple radiofrequency pulse at the ^{29}Si Larmor frequency. Single-pulse spectra can be quantitative, if different sites are allowed to undergo complete spin-lattice relaxation between pulses, or if such relaxation rates are the same for different sites. The latter is usually the case for a homogeneous material such as a single mineral phase or a glass, but is often *not* the case for hydrous amorphous silicas. These may be heterogeneous at a variety of length scales, and, if OH-rich regions contain higher concentrations of the paramagnetic impurities that are thought to dominate the relaxation process (e.g., transition metal cations), then Q^3 and Q^2 (if present) may relax faster than Q^4 groups. Proton dynamics may also contribute to ^{29}Si spin-lattice relaxation. The result of such differential relaxation will be an accentuation of the peak areas Q^3 and Q^2 in spectra collected with pulse repetition rates too rapid to allow all sites to relax fully ("partially saturated"). In very pure silicas, such relaxation can take many minutes to even hours (Gladden et al., 1986; Malfait and Halter, 2008), posing a challenge to obtaining data from enough pulses to yield a useful signal-to-noise ratio *and* quantitative peak areas. By careful study of such differential relaxation, we have managed to acquire such data for a number of hydrous amorphous silica samples. These show that the Hawaiian silica coatings appear to be distinctly different from other “opaline” silica in that they contain a much higher proportion of Si-OH groups.

Vibrational spectroscopic methods have been used extensively to describe natural and synthetic amorphous silicas. The effects of network-modifying cations on the spectra of silicate glasses have been well documented (e.g., McMillan,1984; Mysen and Richet, 2005). Davis and Tomozawa (1996) presented a thorough analysis of infrared-active features of water-related species in silica glass. Many authors have characterized the vibrational properties of silica gels and their maturation with time or heat (Bertoluzza et al., 1982; Mulder and Damen, 1987; Almeida and Pantano, 1990; Theil et al., 1990; Matos et al., 1992; Kamitsos et al., 1993). Specifically, the intensity of bands related to Si-OH vibrations is commonly reported to decrease with maturation. Certain silica gel bands display strong polarization in their Raman spectra (Mulder and Damen, 1987). In studies of natural, amorphous silica, micro-Raman analysis has been especially useful in resolving fine-scale mineralogical heterogeneity and in assessing relative mineralogical maturity (Champagnon et al., 1997; Rodgers and Hampton, 2003; Ilieva et al., 2007). Schmidt et al. (2001) illustrated a strong correlation between relative intensity of the IR Si-OH asymmetric stretch band and diagenetic maturation in marine diatom silica. Because the study of silica by vibrational methods is well developed, here we use IR and Raman spectra to supplement and corroborate the ^{29}Si NMR results.

Table 1. Chemical analysis of PU-009 coating by EPMA*

		Normalized (anhydrous basis)
SiO_2	81.89 ± 1.78	97.60 ± 2.12
TiO_2	0.50 ± 0.03	0.59 ± 0.03
Al_2O_3	0.13 ± 0.03	0.15 ± 0.03
FeO*	0.66 ± 0.22	0.79 ± 0.26
MgO	0.07 ± 0.04	0.08 ± 0.05
CaO	0.32 ± 0.15	0.38 ± 0.18
Na_2O	0.11 ± 0.07	0.13 ± 0.09
K_2O	0.05 ± 0.01	0.06 ± 0.02
MnO	0.03 ± 0.02	0.03 ± 0.02
SO_3	0.11 ± 0.07	0.14 ± 0.08
P_2O_5	0.03 ± 0.02	0.04 ± 0.02
Total	**83.89**	**100.00**

*Average of two spot analyses with similar oxide totals (85.5% and 82.2%); other analyses from the same EPMA session produced similar results but lower totals. Reported errors are ±2σ.

2. Methods and Materials

2.1. Samples

The primary natural sample explored in this study (PU-009) was collected on the rim of Pu'u O'o, a basaltic cone along Kilauea's east rift zone on the island of Hawaii. The Pu'u O'o eruption is one of Hawaii's longest-lived historical eruptions, having continued vigorously since 1983. Although the cone itself only occasionally produces new lava flows, it has continuously produced a plume of SO_2-rich gas and aerosols (Porter et al., 2002). The sample is comprised of basaltic volcanic bombs collected on the surface of 1997–98 overflow lavas about 10 m from the cone rim. The bombs were blebs of molten lava that were ejected from the cone and that struck the nearby surface before cooling. The subaerial surfaces of the bombs are covered by a bluish-white coating, up to 50 micrometers thick, composed of hydrous amorphous silica. Similar coatings from Kilauea's southwest rift zone have previously been shown to form by acid-sulfate leaching of basalt, removing divalent and trivalent cations to leave behind a residual silica layer (Chemtob et al., 2010). The amorphous silica coating material was prepared for NMR by manually scraping 16 mg off its basaltic substrate, then carefully removing most dark-colored material by hand picking and by magnetic separation. (Field photos and SEM imagery of PU-009 may be found in **Supplemental Figure 1**)

For comparison, several additional natural, hydrous amorphous silicas were selected. These included a hyalite (opal-AN) from the well-studied (e.g., Langer and Flörke, 1974, Graetsch et al., 1990) locality of Valeç, Czech Republic (glass-clear, colorless, botryoidal deposits up to 5 mm thick, Stanford University collection no. 66406) and two samples of silica sinter deposits collected from flowing, near-neutral hot springs in Yellowstone National Park (courtesy of D.R. Lowe, labeled yel10-1 and yel4-5, Braunstein and Lowe, 2001). We also report data on a sample of 95% ^{29}Si-enriched amorphous silicic acid precipitated by addition of HCl to a basic, concentrated aqueous solution of silica during the routine separation of this material from previously synthesized alkali glass samples (Stebbins and McMillan, 1993). The latter was dried at 110 ˚C only. For comparison, we collected extensive data sets on high purity reagent-grade (Baker AR) silica gel and (Baker AR) silicic acid n-hydrate reagent. For convenience, these are labeled below as “silica gel reagent” and “silicic acid reagent”, while noting that these terms can be applied to a variety of hydrous amorphous silicas of varying OH and H_2O contents.

2.2. Experimental methods

Single-pulse ^{29}Si MAS NMR spectra were collected at Stanford University with a Varian Infinity 400 spectrometer (9.4 T field) at 79.4 MHz and are referenced to

Table 2. Mean chemical shifts (cs) and peak widths (full width at half maximum height, FWHM) for fitted components to ^{29}Si spectra of hydrated amorphous silicas, in ppm.

sample	pd for fit*	Q^2		Q^3		Q^4	
		cs	FWHM	cs	FWHM	cs	FWHM
PU-009 coating	5	92.1	4.6	101.6	6.1	111.1	7.6
hyalite	10	–	–	101.9	7.8	111.8	8.4
yel4-4 sinter	30	91.5	4.6	101.9	7.7	111.6	8.2
yel10-1 sinter	3600	–	–	100.3	6.8	111.4	9.2
silica gel reagent	120	–	–	101.7	6.5	111.4	8.3
silicic acid reagent	30	92.4	4.9	101.8	6.8	111.0	7.8
95% ^{29}Si silicic acid	10	91.8	4.9	101.6	6.3	111.2	7.4

*Pulse delay (s) of spectrum used to obtain parameters shown; see text for details. Uncertainties in mean chemical shifts are ±0.2 ppm; in peak widths ±0.5 ppm

tetramethylsilane. A Varian/Chemagnetics “T3-type” probe with 3.2 mm diameter rotors, spinning at 14 to 15 kHz, was used for most samples, with 0.7 ms pulses at about 130 kHz pulse power (RF tip angle about 30˚) and sample weights of 15 to 25 mg. (The latter are about ten times smaller than used in most previous studies of such materials, necessitated by the nature of the thin silica coating that was the initial impetus for this study.) ^{1}H decoupling was not employed, as dipolar broadening is negligible under these conditions. Spectra were collected with delays between pulses (pd) ranging from seconds to about 1 hr to study the effects of differential relaxation and to approach fully relaxed spectra. Data from hundreds or thousands of pulses were averaged for the shorter pulse delays; this number was limited to typically 24 to 80 pulses for the longest delays. For comparisons of absolute peak areas, we ran a sample of synthetic forsterite (Mg_2SiO_4) (Stebbins et al., 2009) with a pulse delay of 1 hr. For several samples, we also obtained a more precise picture of the relaxation process by collecting saturation-recovery spectra as a function of a relaxation delay τ following a train of 90˚ pulses to saturate the magnetization (Stebbins et al., 2009). More limited data sets were collected for the Yellowstone silica sinters and the 95% ^{29}Si-enriched silicic acid, using a similar 9.4 T spectrometer and a Varian probe with 7 mm diameter rotors (ca. 200 mg of sample) and spinning speeds of 6.5 kHz. NMR spectra were fitted with two or three Gaussian components, in some cases using constraints on peak positions obtained from less noisy, partially relaxed spectra for fitting data from longer delay times. For the spectra collected at 14 to 15 kHz spinning rate, spinning sideband intensities were very low, totaling less than 2% of total peak areas. In spectra collected at the lower spinning speeds, when more intense spinning sidebands were observed, their relative proportions of component peaks were very similar to those of the central peaks. We thus did not include analysis of sideband intensities in the determinations of relative peak areas discussed below.

To attempt to estimate contents of H_2O in different states in the silicas, for several samples we determined the weight loss on heating for about 12 h at 120 ˚C (sorbed and other readily-lost molecular H_2O) and on heating for about 12 h at 1020 ˚C (all H_2O and OH).

Major and minor elemental composition of PU-009 was determined by electron probe microanalysis (EPMA) using a JEOL JXA-8200 probe at Caltech. Quantitative data were acquired using wavelength dispersive spectrometry, operating at 15 kV accelerating voltage and 20 nA beam current. Glasses of various compositions, including anhydrous fused silica glass, were used for standardization. Many analyses of the PU-009 coating suffered from totals well below 100%, likely the result of surface roughness, high porosity, and high water content (**Table 1**). Despite the low totals, the EPMA data illustrates that the PU-009 silica coating has only minor concentrations of components besides SiO_2. Moderate co-enrichment in FeO* and TiO_2 suggest the presence of Fe-Ti oxides, which are associated with silica coatings in other Hawaiian settings (Chemtob et al. 2010).

Raman spectra were collected at Caltech using a Renishaw M1000 micro-Raman spectrometer with a 514.5 nm green laser. The spot size depended on the objective used but was typically 1–5 µm. Peak positions were calibrated against a silicon standard. Because the Raman bands in amorphous silica are characteristically weak, spectra were corrected for the machine blank and manually corrected by spline fitting for broad fluorescence (centered near 620 nm) from the sample. Attenuated total reflectance (ATR) infrared spectra of powdered silica samples were collected using a SensIR Durascope ATR accessory plate with a Nicolet Magna-IR spectrometer, an uncooled pyroelectric deuterated triglycine sulfate (DTGS) detector with a KBr window (400–4000 cm^{-1}) and a KBr beamsplitter.

3. Results from NMR

3.1. Structure and Si-OH contents

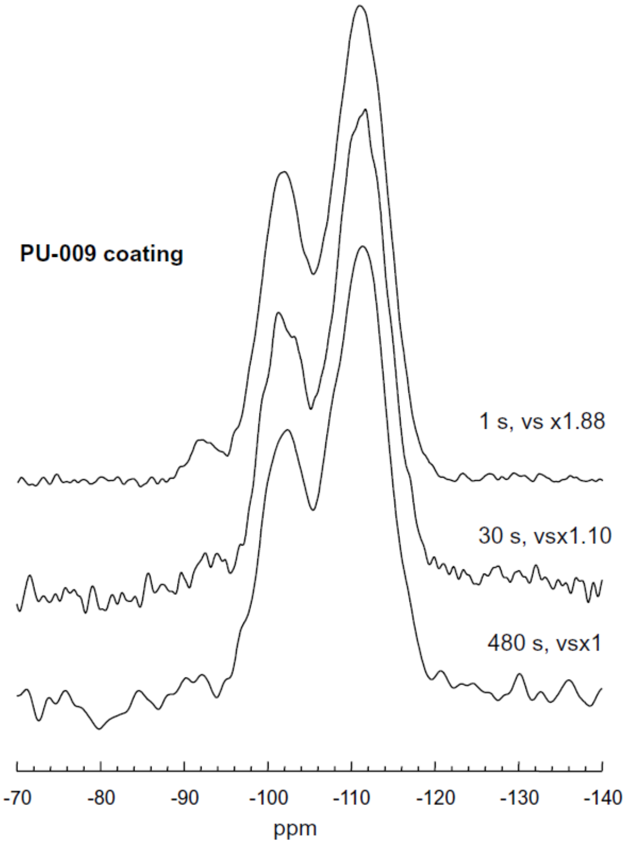

Figure 1. Selected ^{29}Si MAS NMR spectra of Hawaii silica coating sample PU-009, collected with varying pulse delays as labeled. The short-delay spectrum shows lower relative abundance of Q^4 groups because of slower relaxation; the spectra with the two longer delays are indistinguishable at the obtained signal-to-noise ratio. Here and in other figures, intensities are normalized to that of the highest peak to allow ready comparison of component areas, but vertical scale multipliers relative to that of the longest-delay spectrum are shown.

As has been reported in numerous ^{29}Si MAS and CPMAS NMR studies of synthetic silica gels and naturally-occurring hydrous amorphous silicas (Maciel and Sindorf, 1980; Sindorf and Maciel, 1982; Graetsch et al., 1990; Adams et al., 1991; Graetsch et al., 1994; Brown et al., 2003; Paris et al., 2007), the spectra for all of our samples are comprised primarily of two relatively broad (6–8 ppm full-width at half maximum intensity, FWHM), partially overlapping peaks centered at about –111 and –102 ppm (**Figs. 1 to 5**). These can be unambiguously assigned (Engelhardt and Michel, 1987; MacKenzie and Smith, 2002) to the predominant, fully-connected Q^4 sites (–111 ppm) and a smaller component of Q^3 with single OH groups (–102 ppm). Peak widths reflect the disorder in bond angles and distances inherent in an amorphous phase. In PU-009 (**Fig. 1**) and the silicic acid samples (**Fig. 2**, most obviously in the shorter-delay spectra with better

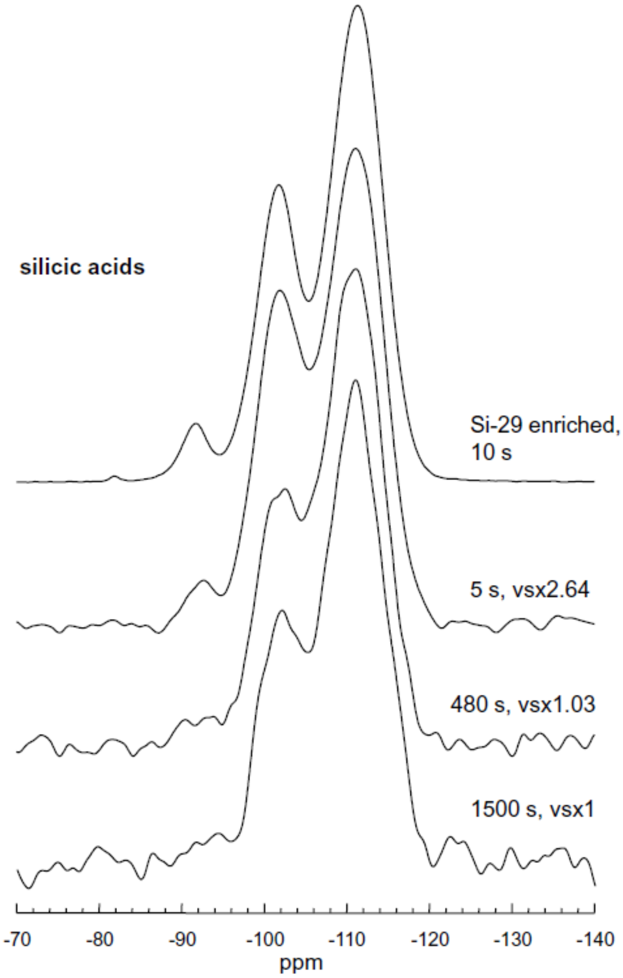

Figure 2. Selected ^{29}Si MAS NMR spectra of silicic acid reagent (lower three) and ^{29}Si-enriched silicic acid (uppermost). For the former, relaxation delays shown were chosen to illustrate differential relaxation as in Fig. 1; the latter displayed no differential relaxation.

signal-to-noise ratios and in the ^{29}Si-enriched sample), a third, smaller peak at about –92 ppm, due to Q^2 groups (two Si-OH bonds), can be seen. The latter was below detection level (about 1%) in the other samples, given the noise levels and lower OH contents. The very high signal-to-noise ratio obtained for the ^{29}Si-enriched silica revealed an even smaller peak at –82 ppm that may correspond to Q^1 groups (**Fig. 2**). As shown in **Table 2**, results from fitting the spectra indicate that the mean chemical shifts (i.e. centers of the Gaussian components) and peak widths vary only slightly among all of the samples described here, with some tendency towards slightly narrower peaks for the samples with higher total OH contents (PU-009 and silicic acid). We note that the low analyzed contents of other chemical components in the natural silica coating (**Table 1**; some of which in any case may be present as small amounts of separate oxide phases, Chemtob et al., 2010) demonstrate that non-bridging oxygens other than Si-OH groups must be of negligible concentration. The close similarity of the spectra of PU-009 and silicic acid reagent also confirms the purity of the former, as other cations would be expected to broaden or shift the peaks.

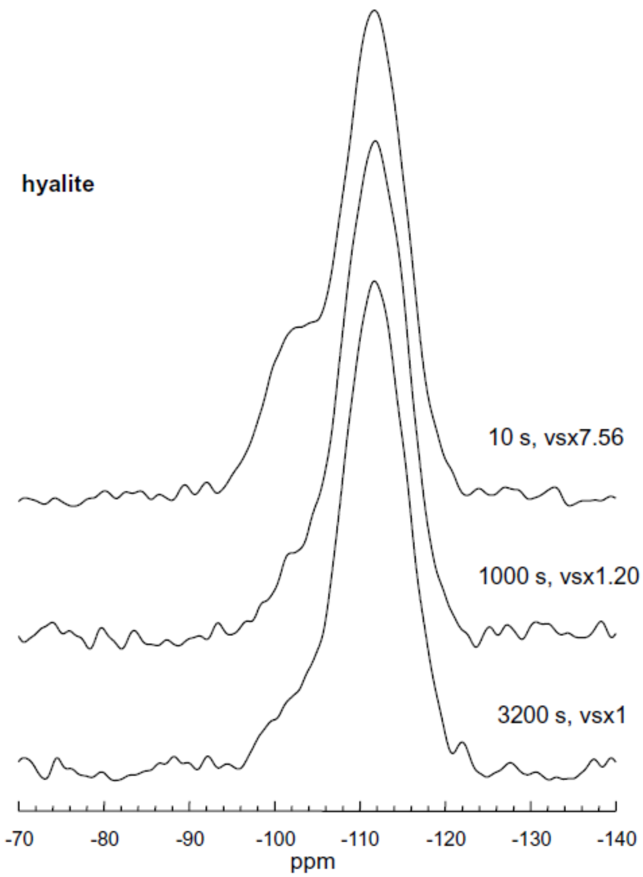

Figure 3. Selected ^{29}Si MAS NMR spectra of Valeç hyalite, chosen as described for Fig. 1.

As has been previously noted in studies of both crystalline and amorphous silicas (Gladden et al., 1986; Malfait and Halter, 2008), the ^{29}Si spin lattice relaxation rates tend to be very slow, often resulting in partial saturation of peak intensities for pulse delays shorter than 5 to 10 minutes up to even an hour, depending on the contents of paramagnetic impurity ions (e.g., Fe^{3+}). In Figures 1 to 5, the intensities of spectra (signal averages over many pulses) are normalized to the same maximum height to allow ready comparison of the component peaks, but the actual intensities relative to the most relaxed, longest-delay spectra are also indicated by the vertical scale multipliers shown. For all samples except for the 95% ^{29}Si-enriched silicic acid, there is a significant increase in the relative area of the Q^4 peak with increasing pulse delay, i.e., this component relaxed more slowly than the Q^3 and Q^2 signals. This was most pronounced in the hyalite sample (**Fig. 3**). The *lack* of such “differential relaxation” in the isotopically

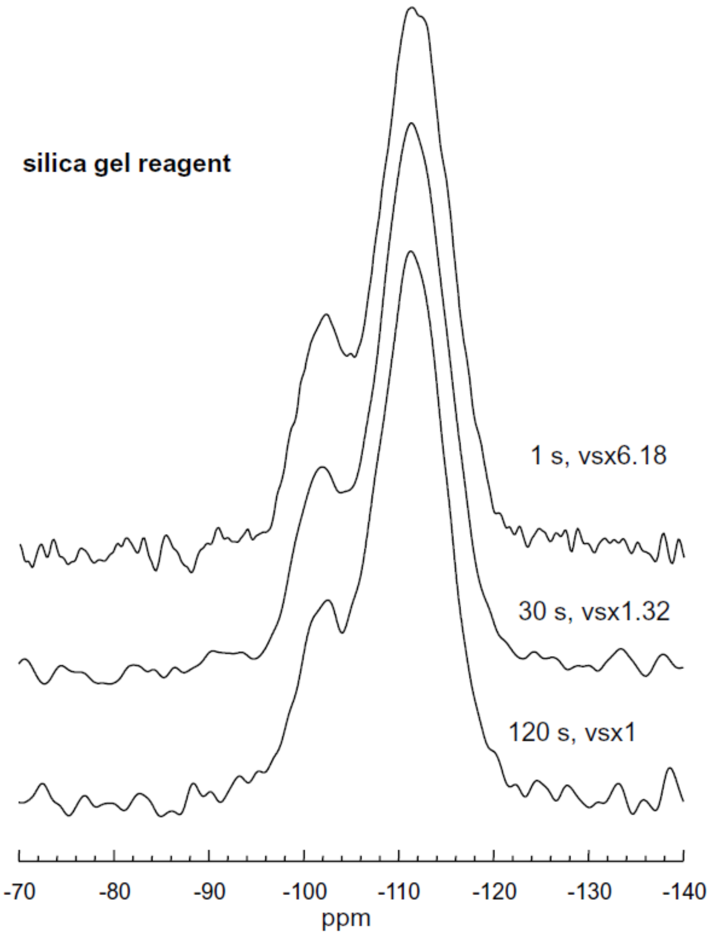

Figure 4. Selected ^{29}Si MAS NMR spectra of silica gel reagent, chosen as described for Fig. 1.

enriched sample may indicate rapid spin diffusion among the adjacent ^{29}Si nuclei, which should be much slower in the isotopically dilute materials (4.7 % ^{29}Si), but this phenomenon has not been studied in detail in such materials.

To estimate the true Q^3 (and Q^2 where observable) proportions and thus the content of Si-OH, we compared spectra with increasing delay times up to a point when a change of at least a factor of 3 or 4 showed no difference in overlaid peak shapes, confirmed by no difference within error of the fitted ratio of Q^3 to Q^4. The figures show selected data only, with a typical short-delay spectrum and two longer-delay spectra that illustrate when the latter condition was reached. The spectra with the longest delays are in general noisier because fewer acquisitions could be made during practical periods of spectrometer time (up to a several days per spectrum). The limiting values of Q^3 (and Q^2) abundances are given in **Table 3**, based typically on averages of the fits to the two or

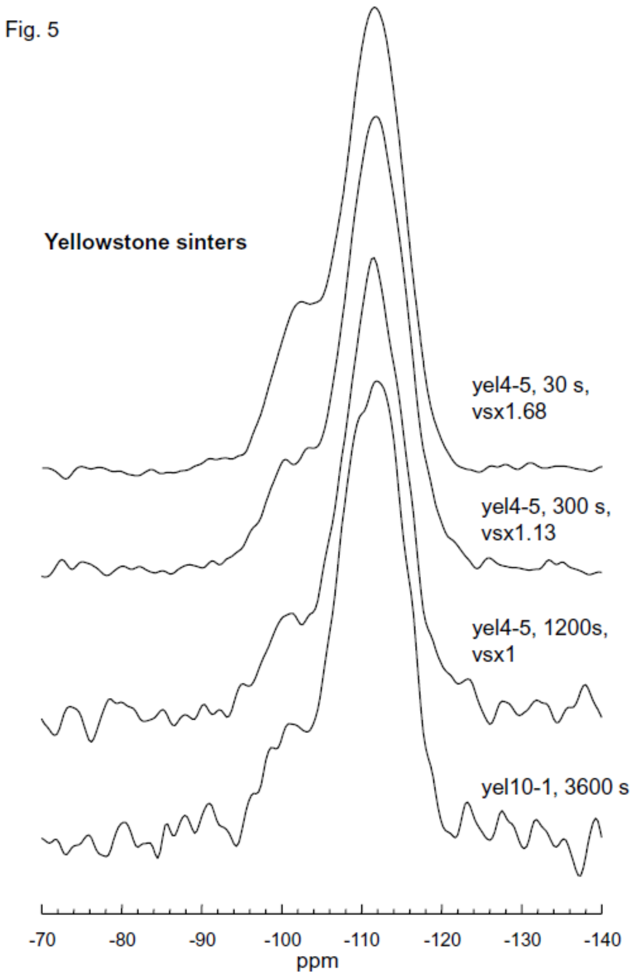

Figure 5. Selected ^{29}Si MAS NMR spectra of Yellowstone sinter samples, chosen as described for Fig. 1.

three most relaxed spectra. The changes in the fitted Q^3 content, and variations in the uncertainty, are plotted for all of the spectra collected in **Figure 6**.

To further assess the problem of slow relaxation rates, we compared integrated total peak areas for most of the samples, normalized per gram (dry weight) of silica, with the standard of synthetic forsterite. The most relaxed spectra recorded are within 90 to 100 % of fully relaxed intensity, with some uncertainty introduced by the relatively low signal-to-noise ratios of these data (**Table 3**). In the “worst case” of all un-relaxed signal being due to Q^4 sites, these uncertainties would translate to roughly only a 10% additional relative error in the relative proportion of the Q^3 species (e.g., 9% Q^3 instead of 10% Q^3 for the hyalite). This kind of assessment would be particularly important for other silicas that are thought to be multi-phased, e.g., opal-CT, as the crystalline components may relax even more slowly than the amorphous material.

Table 3. Speciation and estimated Si-OH contents of hydrated amorphous silicas

sample	max. pulse delay, s	% relaxed	Q^2, %	Q^3, %	NBO/Si	Si-OH, NMR*	Si-OH, wt. loss*†
PU-009 coating	3200	95 ± 10	3 ± 1	32 ± 2	0.38 ± 0.02	5.4 ± 0.4	–
hyalite	3200	95 ± 5	< 1	9.9 ± 0.5	0.10 ± 0.01	1.5 ± 0.2	3.3 ± 0.3
yel4-5 sinter	1200	–	< 1	15 ± 2	0.15 ± 0.02	2.2 ± 0.3	–
yel10-1 sinter	3200	–	< 1	13 ± 3	0.13 ± 0.03	1.9 ± 0.5	–
silica gel reagent	480	92 ± 5	< 1	19.9 ± 0.5	0.20 ± 0.02	2.9 ± 0.3	3.0 ± 0.2
silicic acid reagent	3600	100 ± 10	2 ± 0.5	28 ± 2	0.32 ± 0.02	4.6 ± 0.3	4.5 ± 0.4
95% ^{29}Si silicic acid	60	**	4.3 ± 0.3	32.1 ± 0.3	0.407 ± 0.006	5.8 ± 0.2	–

* from NMR-based NBO/Si, as weight % H_2O

† as weight % H_2O, based on difference between measured weight loss at 1000˚C and that at 120 ˚C

** no differential relaxation observed

The moles of OH per 100 Si, and thus the mean number of non-bridging oxygens (NBO) per Si, can be simply calculated from these results as $0 \times \%Q^4 + 1 \times \%Q^3 + 2 \times \%Q^2$. From this, the total Si-OH content can be readily calculated and converted to weight % OH as H_2O (**Table 3**). We tested this approach by estimating Si-OH contents from the "loss on ignition", i.e., the weight loss on heating at 1020 ˚C, vs. that on drying at 120 ˚C (**Table 3**). For the highly-porous, finely powdered silica gel and silicic acid reagents, the agreement between this estimate and that from the NMR was excellent.

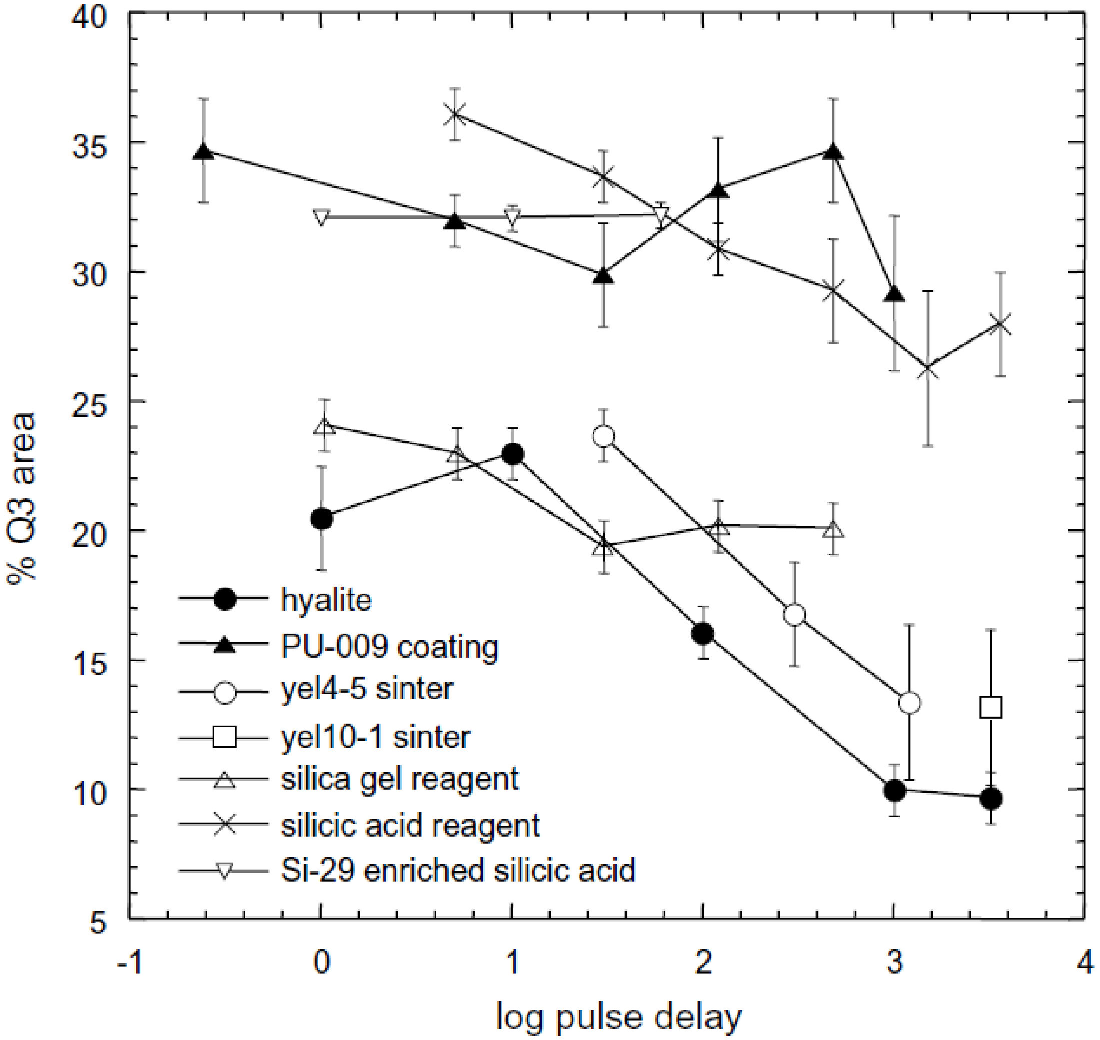

Figure 6. Relative areas of Q^3 peaks vs. $\log_{10}$ of pulse delays, for hydrous amorphous silicas.

However, the high-temperature weight loss for the hyalite sample was twice that from the NMR estimate, presumably because not all of the molecular H_2O was removed from this sample by drying a coarsely-ground sample at 120 ˚C. For this sample, the NMR-estimate of the Si-OH content (1.5 ± 0.2 wt% as H_2O) is equal to that determined by FTIR for several samples of hyalite from this well-studied locality (Langer and Flörke, 1974). The latter paper also demonstrated the complexity of differential thermal analysis

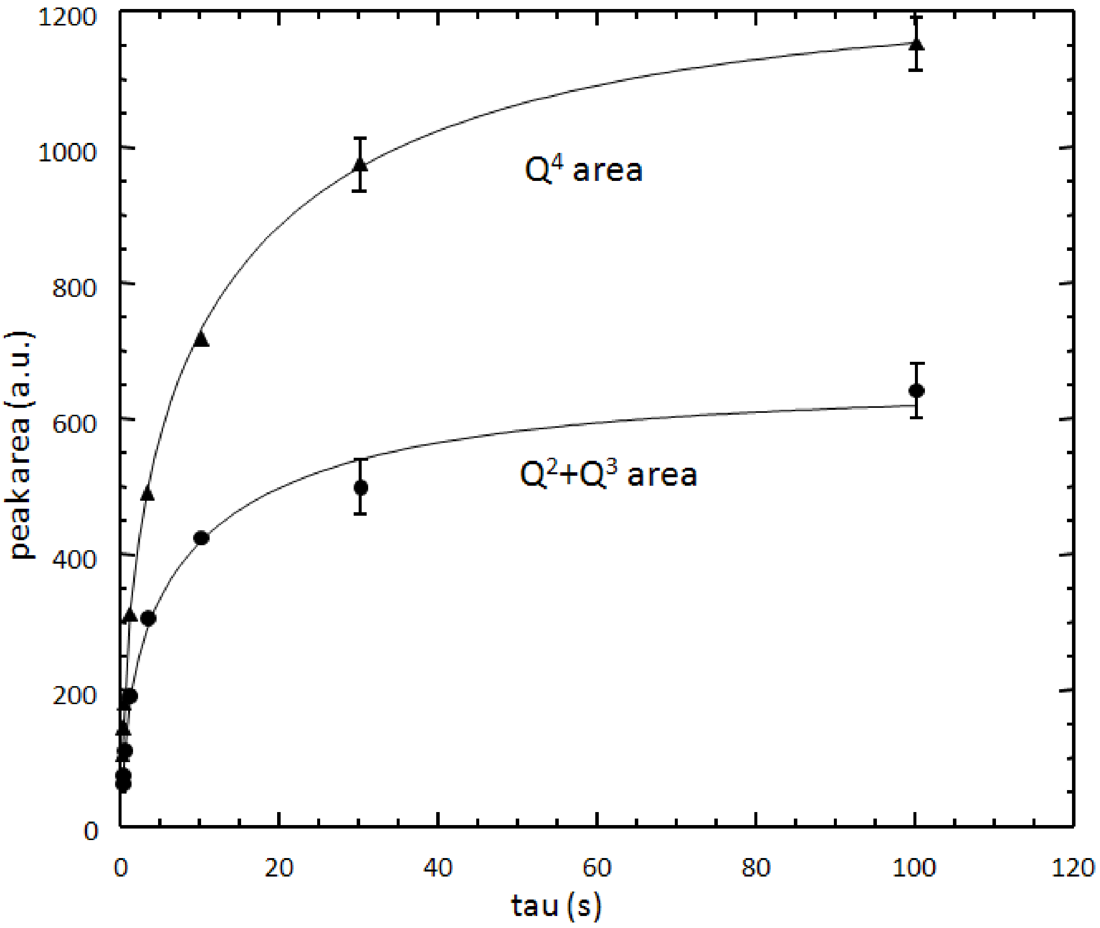

Figure 7. Relative areas of Q^4 and combined Q^3+Q^2 peaks in coating sample PU-009, vs. relaxation delay (τ). Curves are best fits to stretched exponential functions, as described in text. Typical uncertainties are shown.

curves for natural opal samples, showing that much of the molecular H_2O may be retained to temperatures above 250 ˚C; i.e., that contributions from this species and Si-OH are not always readily separable by DTA or weight-loss measurements.

The Hawaiian silica coating sample (PU-009) and the two synthetic silicic acid samples (reagent and ^{29}Si-enriched) are similar in Q^3 (28 to 32 %) and Q^2 (2 to 4 %) contents, while the hyalite and silica sinters have much lower contents of these structural groups (about 10 to 15 % Q^3, Q^2 < 1%). Whether or not these dramatic differences in degree of network connectivity provide systematic clues to the mechanisms of formation,

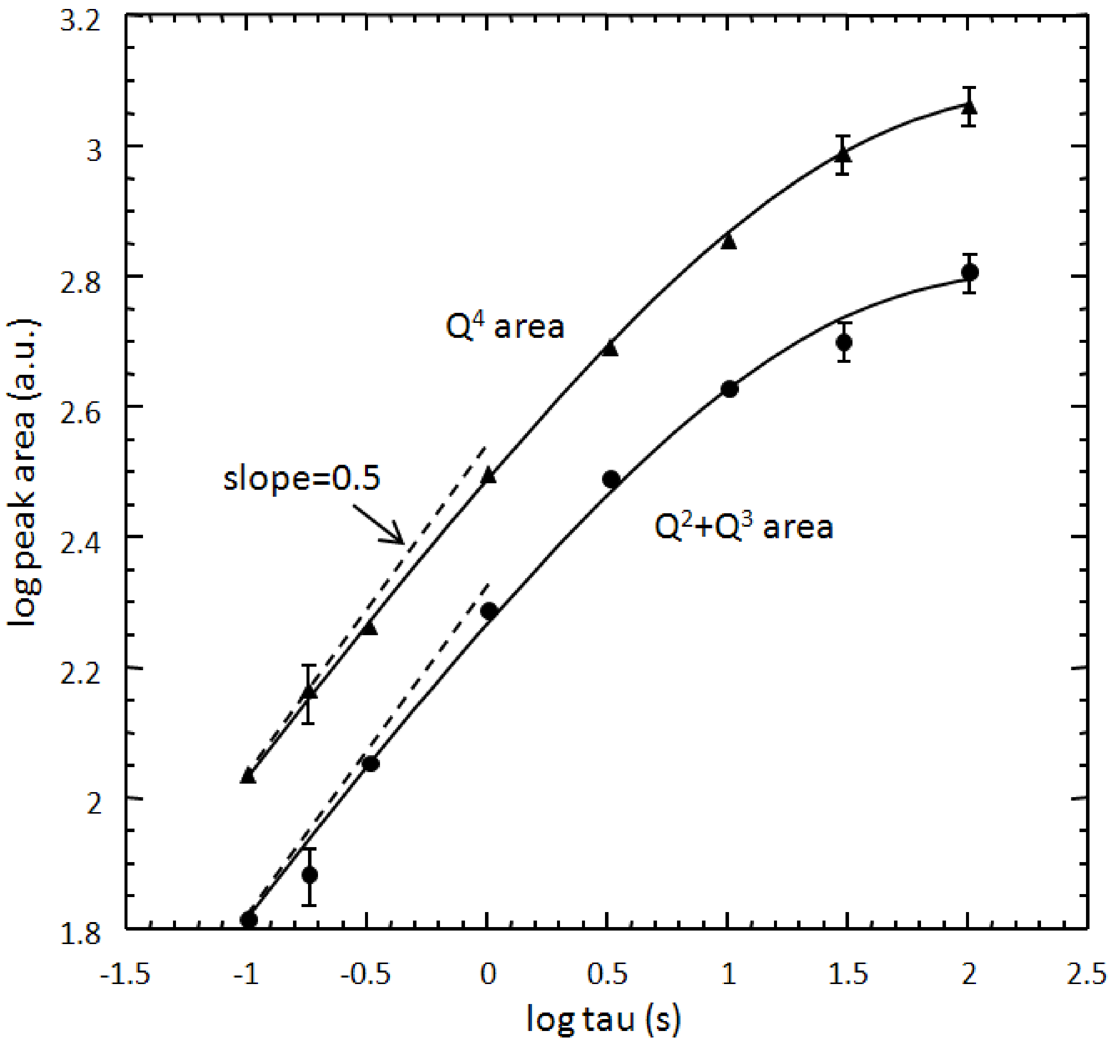

Figure 8. Relative areas of Q^4 and combined Q^3+Q^2 peaks in coating sample PU-009, vs. relaxation delay (tau), plotted in $\log_{10}$-$\log_{10}$ space to show approach to linearity with slope of 0.5 at shortest delays. The curves are the same fits as shown in Fig. 7, recalculated in the variables plotted here. Typical uncertainties are shown.

or subsequent thermal histories, of these types of materials will probably require detailed experimental study and comparison with more of the wide range of naturally-occurring hydrous amorphous silicas. However, this experimental approach does appear to give a robust measurement of this key structural and energetic variable.

The concentrations of Q^2, Q^3, and Q^4 species in the high-OH samples can be analyzed in terms of the apparent equilibrium constant for the reaction $2Q^3 = Q^2 + Q^4$, as has been done for alkali silicate glasses (Maekawa et al., 1991), although it is not clear that the hydrous silicas formed under equilibrium conditions. Resulting values of about 0.18 are considerably higher than those for alkali silicates (e.g. ca. 0.08 for Li, 0.02 for Na, 0.01 for K), perhaps consistent with the smaller size and higher "cation field strength" of H^+.

3.2. Detailed NMR Relaxation Time Study

For the Hawaiian coating sample, we carried out a more detailed study of the spin-lattice relaxation by obtaining high-quality spectra with relaxation delays of up to 100 s, following an initial train of pulses to saturate the magnetization. Spectra were fitted as above, combining the relatively imprecise and small Q^2 areas with the Q^3 areas. The Q^2+Q^3 areas and the Q^4 areas were independently fitted with "stretched exponential" functions, which have been shown to be much more appropriate for this type of relaxation in a solid than the conventional exponential (Hartman et al., 2007; Stebbins et al., 2009). Here, the magnetization (peak area) grows as a function of the relaxation delay τ, with a limiting value of M_∞ and a time constant of T':

$$M(\tau) = M_\infty \{1 - \exp[-(\tau/T')^{1/2}]\} \qquad (1)$$

Data were fitted in linear space (area vs. delay time) to properly weight the uncertainties, and results shown in **Figure 7**. The fitted lines are re-drawn in a log-log plot (**Fig. 8**), which illustrates the excellent agreement at short as well as long times. The slope at short times of both the fit and the data approaches 0.5, as expected for a three-dimensional distribution of paramagnetic centers in the material. This result is in sharp contrast to the reduced dimensionality reported in amorphous silica formed in rice-husk ash (Abreu et

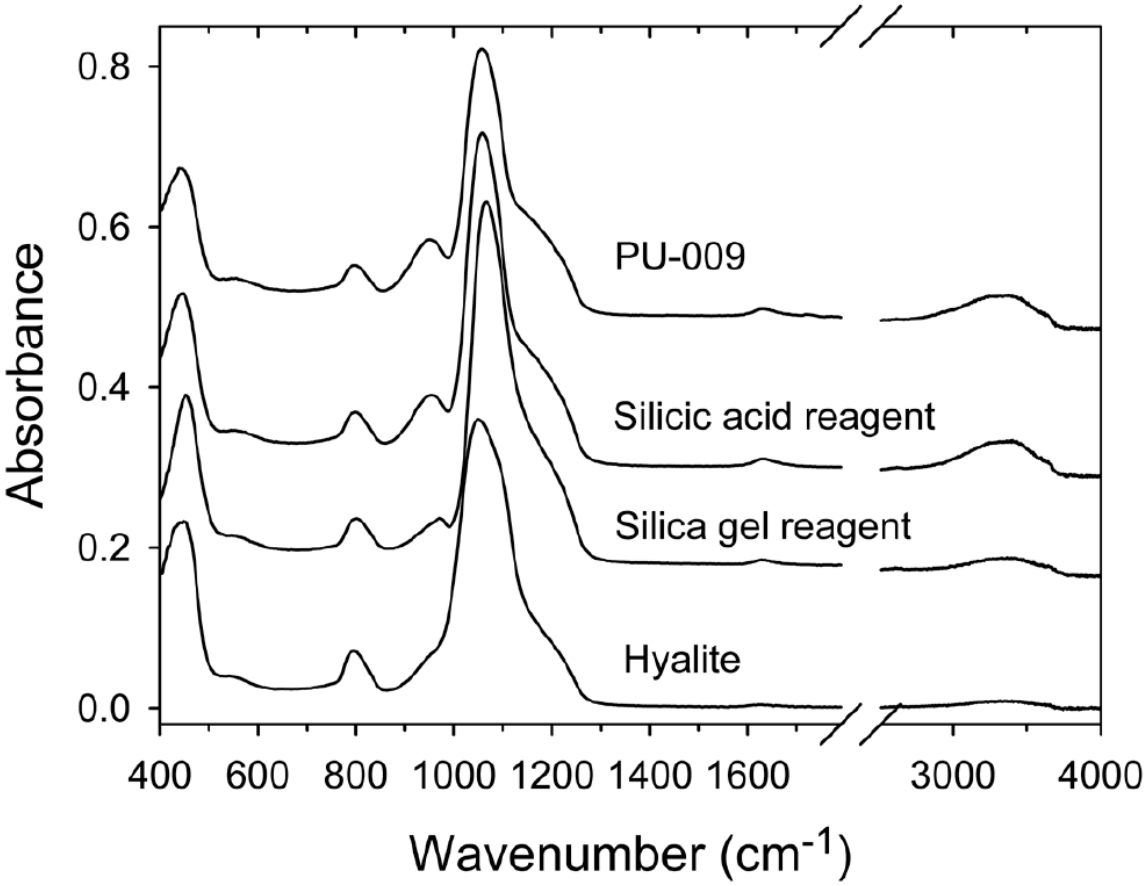

Figure 9. ATR-IR spectra of silica samples. Note the break and change of scale in the wavenumber axis to illustrate the fundamental H_2O/OH stretch region.

al., 2005) and in a silica aerogel (Devreux et al., 1990). On extrapolation to infinite time, the ratio of the Q^2+Q^3 area to the total (i.e. the ratio $M_{\infty,Q3}$/ [$M_{\infty,Q4}$+ $M_{\infty,Q3}$]) is 0.34±0.02, very close to that determined above from the limiting behavior of the single-pulse spectra.

4. Results from Vibrational Spectroscopy

ATR-IR spectra of the PU-009 scrapings feature strong bands centered at 447 cm^{-1}, 798 cm^{-1}, 955 cm^{-1}, and 1059 cm^{-1} (**Fig. 9**). Three of these bands are associated

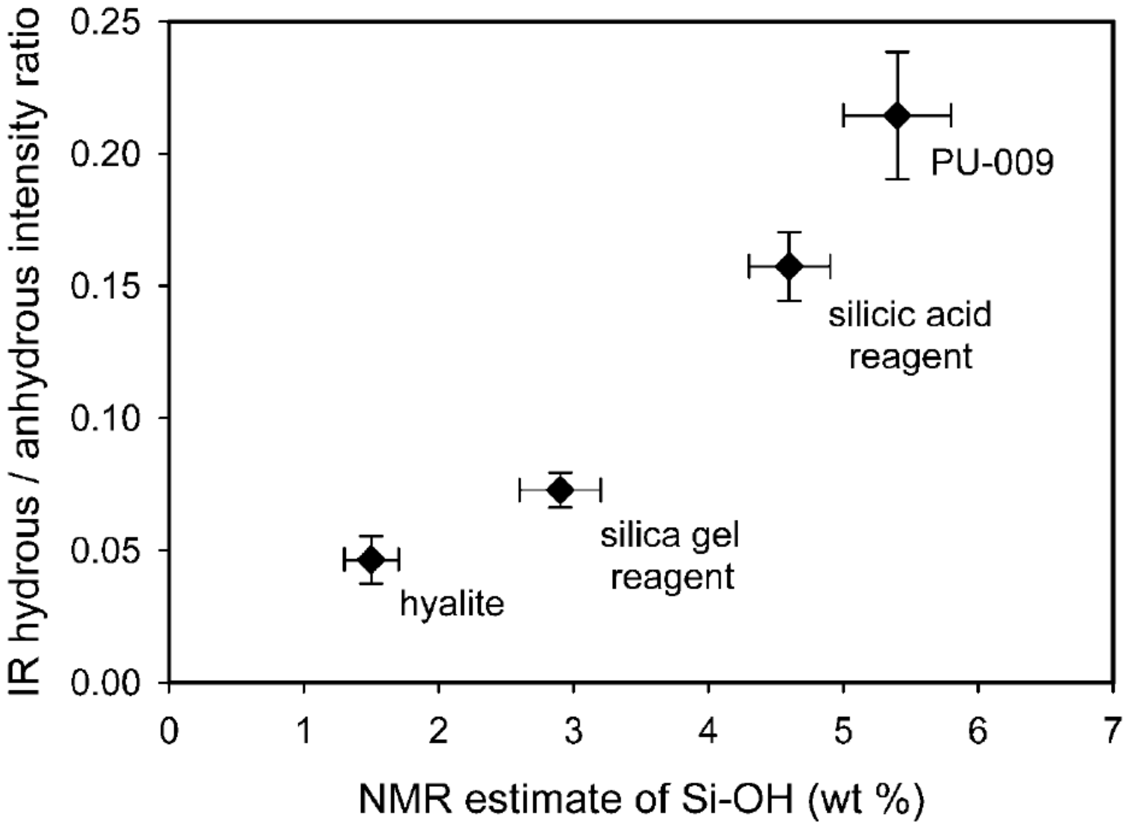

Figure 10. Si-OH contents from ATR-IR vs. ^{29}Si NMR data. Silicate bands in ATR-IR spectra were modeled as overlapping pseudo-Voigt functions. Intensities (band areas) were calculated from the best fit parameters. The ratio of the 955 cm^{-1} band intensity (hydrous Si-OH asymmetric stretch) to the 1059 cm^{-1} band intensity (anhydrous Si-O asymmetric stretch) is plotted on the vertical axis. Errors were estimated by bootstrap Monte Carlo methods. Calculations of Si-OH contents and errors from NMR spectra are described in the text.

with fundamental vibrations of non-hydroxylated silica tetrahedra; bands at 447 cm^{-1}, 798 cm^{-1} and 1059 cm^{-1} correspond to the Si-O-Si bending mode, symmetric stretch, and asymmetric stretch (AS), respectively (Davis and Tomozawa. 1996). The broad shoulder centered at 1210 cm^{-1} has previously been assigned to a second AS mode in which adjacent oxygens move out of phase with each other (Kamitsos et al., 1993). The peak at 955 cm^{-1} corresponds to the AS mode of a silica tetrahedron with one hydroxyl group (O_3SiOH) (Davis and Tomozawa, 1996). A weak band at 552 cm^{-1} has been tentatively assigned to Si-OH rocking modes (Almeida and Pantano, 1990), and is consistent with calculated vibrational frequencies for three- and four-membered siloxane rings (Monsivais-Gámez et al., 2007). A small band near 1630 cm^{-1} corresponds to the bending mode of molecular water.

Other natural and synthetic hydrous silica samples produce ATR-IR spectra largely similar to those of the Hawaiian silica coating (PU-009). In particular, the spectrum of the silicic acid reagent is nearly identical to that of the coating, suggesting it may be the best analog material. The spectra of the silica gel reagent and hyalite samples show reduced intensity of the Si-OH AS band relative to that of the anhydrous asymmetric stretching band. In addition, the Si-OH AS band is shifted in frequency in the silica gel reagent spectrum, to 980 cm^{-1} from 955 cm^{-1}. This shift may correspond to a smaller contribution from Si-OH asymmetric stretching in silanols that are hydrogen bonded to neighboring silanols or molecular water molecules; this hydrogen-bonded AS mode occurs at a lower frequency, around 944 cm^{-1} (Davis and Tomozawa, 1996). The absolute intensities of ATR-IR spectra are strongly influenced by grain size, but peak area ratios more accurately indicate relative abundances of the structural units that contribute to the spectra. A strong correlation is observed between the ratio of the hydrous to anhydrous AS peak areas and the derived Si-OH contents from NMR (**Fig. 10**). These observations corroborate the NMR results and suggest that ATR-IR spectra may be effective at quantifying water content of such materials with minimal preparation.

Raman spectra were collected of both intact silica coatings on basalt and of the scraped silica material PU-009 (**Fig. 11**). The Raman spectra of the intact coating are largely consistent with the ATR-IR spectra, with a broad, multi-component feature

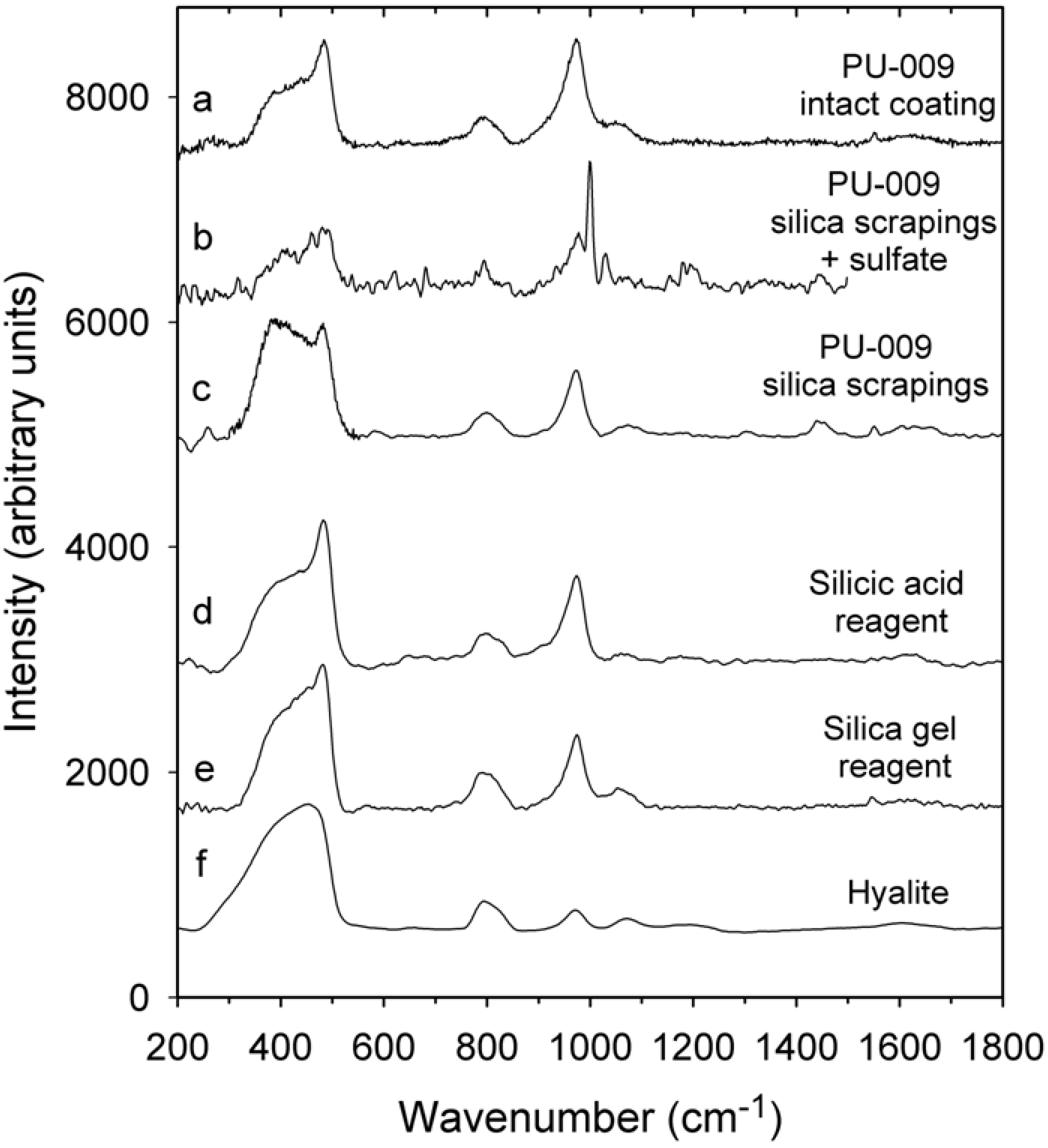

Figure 11. Selected Raman spectra of silicate samples. a) Hawaiian silica coating, intact on basalt surface. b) Scraped Hawaiian silica with prominent sulfate peaks near 1000 cm^{-1}. c) Scraped Hawaiian silica. d) Silicic acid reagent. e) Silica gel reagent. f) Valeç hyalite.

centered at ~440 cm^{-1} (Si-O-Si bending mode), a sharp overlapping band at 480 cm^{-1} (isolated O_3SiOH symmetric stretch) (Mulder and Damen, 1987), and bands at 796 cm^{-1} (Si-O-Si symmetric stretch), 971 cm^{-1} (Si-OH AS) and 1068 cm^{-1} (Si-O-Si AS, TO mode) (**Table 4**). Spectra of scrapings of the Hawaiian coatings were generally similar to those of the intact coatings, as expected, but some heterogeneity was observed. Some spectra displayed sharp peaks near 1000 cm^{-1} that are commonly associated with sulfates, probably jarosite. Electron microprobe analyses of silica coatings from other Hawaiian localities have indicated up to percent-level contents of sulfur, so the presence of sulfate minerals is not unexpected (Chemtob et al., 2010). Individual grains show subtle variation in relative peak intensities for the hydrous and anhydrous asymmetric stretching bands, possibly indicating minor grain heterogeneity in the amount of structural water in the coating or loss during grinding and transport.

Raman spectra of the other natural and synthetic silicas are similar to those of the Hawaiian silica. The silicic acid reagent and silica gel reagent spectra have nearly identical band shapes and positions to those of the Hawaiian silica coatings. The hyalite has a characteristically different spectrum distinguishable by a particularly broad band at 453 cm^{-1} (Si-O-Si bending mode) and no overlapping O_3SiOH symmetric stretch band. The hyalite spectra also feature a weak but detectable band centered at 1180 cm^{-1} corresponding to the LO mode of the Si-O-Si asymmetric stretch. The LO mode is possibly present in the spectra of some of the other samples (**Fig. 11a,d**), but the peak height is often close to the detection limit. As in the corresponding ATR-IR spectra, the silica gel reagent and hyalite spectra feature a more intense anhydrous AS band at 1068 cm^{-1} relative to the Si-OH AS band, consistent with lower structural OH contents.

5. Discussion

The amorphous silica samples probed in this study have, to first order, quite similar short-range structures. NMR spectra of all samples display broad peaks associated with Q^4, Q^3 and (in some) Q^2 species in the same positions as previously reported in synthetic and natural amorphous silicas, differing primarily in their relative peak heights.

	Probable band assignment					
Sample	Si-O bending mode	O_3SiOH symmetric stretch	Si-O symmetric stretch	Si-OH asymmetric stretch	Si-O asymmetric stretch	Sulfate stretching modes
PU-009 coating (in situ)	425	484	796	974	1068	n.p.
PU-009 silica scrapings	420	485	794	972	1073	n.p.
PU-009, sulfate-bearing	390	488	795	978	1074	998, 1030
silicic acid reagent	432	482	796	974	1066	n.p.
silica gel reagent	438	482	793	974	1069	n.p.
hyalite	452	n.p.	795	972	1073	n.p.

Table 4. Raman band positions and assignments (given in cm^{-1}). *n.p. = not present

Structural water content (Si-OH) appears to be the primary variable controlling the spectroscopic properties of the silicas. Variations between samples in the vibrational spectra were also closely correlated to Si-OH abundance. Although all silica samples are generally similar in their spectroscopic properties to the Hawaiian silica coatings, the silicic acid reagent is perhaps the closest analog material because it has the most similar hydroxyl content.

The analyses presented here provide new constraints on the formation mechanism and subsequent history of the Hawaiian silica. Silica coatings in Hawaii have previously been attributed to numerous mechanisms, including alteration of externally deposited ash (Farr and Adams 1984), stoichiometric dissolution of basaltic substrate followed by silica re-precipitation, and non-stoichiometric dissolution (i.e., leaching). The calculated hydroxyl content of the scraped Hawaiian silica (5.4 ± 0.4% as wt% H_2O) is substantially higher than that reported for most natural opals, both paracrystalline (opal-CT) and amorphous (opal-AN or opal-AG) (Graetsch et al., 1994; Brown et al., 2003). This exceptionally high Si-OH content, along with the lack of evidence for any crystalline silica phases, suggests that the Hawaiian coatings are immature materials that were not exposed to elevated temperatures or diagenetic events after their formation. NMR and vibrational spectra of the Hawaiian coating cannot distinguish between depositional and leaching mechanisms. The closest synthetic analog analyzed in this study, the silicic acid reagent, was presumably manufactured by chemical deposition from solution. However, multicomponent silicate glasses leached in acidic solutions also can produce silica gel with equally high proportions of Q^2 and Q^3 and, thus, high hydroxyl contents (Angeli et al., 2006).

The detailed ^{29}Si MAS NMR analyses at long delay times to produce fully relaxed spectra presented here represent, to the knowledge of the authors, the first of such measurements on such a small mass of sample (15–25 mg). The useful quality of the resultant spectra demonstrates that single-pulse NMR may glean valuable information about many geologic samples on a small spatial scale. Potential volume-limited targets include opaline silica in volcanic vugs, silica cements in sedimentary rocks, and individual strata in biologically mediated silica deposits (e.g., sinters, stromatolites).

Acknowledgements

We thank Don Lowe (Stanford University) for the Yellowstone silica samples, and two anonymous reviewers for helpful comments. This research was supported by the National Science Foundation, through grant EAR-1019596 (J.F. Stebbins), by the White Rose Foundation (G.R. Rossman), and by a National Aeronautics and Space Administration graduate student fellowship (NESSF).

References

Abreu, R.F., Schneider, J., and Cincotto, M.A. (2005) Structure and hydration kinetics of silica particles in rice husk ash studied by ^{29}Si high-resolution nuclear magnetic resonance. Journal of the American Ceramic Society, 88, 1514–1520.

Adams, S.J., Hawkes, G.E., and Curzon, E.H. (1991) A solid state ^{29}Si nuclear magnetic resonance study of opal and other hydrous silicas. American Mineralogist, 76, 1863–1871.

Almeida, R.M. and Pantano, C.G. (1990) Structural investigation of silica gel films by infrared spectroscopy. Journal of Applied Physics, 68, 4225–4232.

Angeli, F., Gaillard, M., Jollivet, P., and Charpentier, T. (2006) Influence of glass composition and alteration solution on leached silicate glass structure: A solid-state NMR investigation. Geochimica et Cosmochimica Acta, 70, 2577–2590.

Bertoluzza, A., Fagnano, C., Morelli, M.A., Gottardi, V., and Guglielmi, M. (1982) Raman and infrared spectra on silica gel evolving toward glass. Journal of Non-Crystalline Solids, 48, 117–128.

Braunstein, D. and Lowe, D.R. (2001) Relationship between spring and geyser activity and the deposition and morphology of high temperature (>73 ˚C) siliceous sinter, Yellowstone National Park, Wyoming, U.S.A. Journal of Sedimentary Research, 71, 747–763.

Brown, L.D., Ray, A.S., and Thomas, P.S. (2003) ^{29}Si and ^{27}Al NMR study of amorphous and paracrystalline opals from Australia. Journal of Non-Crystalline Solids, 332, 242–248.

Carroll, S.A., Maxwell, R.S., Bourcier, W., Martin, S., and Hulzey, S. (2002) Evaluation of silica-water surface chemistry using NMR spectroscopy. Geochimica et Cosmochimica Acta, 66, 913–926.

Champagnon, B., Panczer, G., and Chemarin, C. (1997) Differentiation of natural silica glasses using Raman microspectrometry. Chemie der Erde-Geochemistry, 57, 289–296.

Chemtob, S.M., Joliff, B.L., Rossman, G.R., Eiler, J.M., and Arvidson, R.E. (2010) Silica coatings in the Ka-u Desert, Hawaii, a Mars analog terrain: A micromorphological, spectral, chemical and isotopic study. Journal of Geophysical Research, 115, E04001.

Davis, K.M. and Tomozawa, M. (1996) An infrared spectroscopic study of water-related species in silica glasses. Journal of Non-Crystalline Solids, 201, 177–198.

deJong, B.H.W.S., van Hoek, J., Veeman, W.S., and Manson, D.V. (1987) X-ray diffraction and ^{29}Si magic-angle-spinning NMR of opals: incoherent long- and short-range order in opal CT. American Mineralogist, 72, 1195–1203.

Devreux, F., Boilot, J.P., Chaput, F., and Sapoval, B. (1990) NMR determination of the fractal dimension in silica aerogels. Physical Review Letters, 65, 614–617.

Engelhardt, G. and Michel, D. (1987) High-Resolution Solid-State NMR of Silicates and Zeolites, Wiley, New York, 485 p.

Farr, T.G. and Adams, J.B. (1984) Rock coatings in Hawaii. GSA Bulletin, 95, 1077–1083.

Faye, G.H. and Miller, R.M. (1973) “Blue Dragon” basalt from Craters of the Moon National Monument, Idaho: origin of color. American Mineralogist, 58, 1048–1051.

Fulignati, P., Sbrana, A., Luperini, W., and Greco, V. (2002) Formation of rock coatings induced by the acid fumarole plume of the passively degassing volcano of La Fossa (Vulcano Island, Italy). Journal of Volcanology and Geothermal Research, 115, 397–410.

Gladden, L.F., Carpenter, T.A., and Elliot, S.R. (1986) ^{29}Si MAS NMR studies of the spin-lattice relaxation time and bond-angle distribution in vitreous silica. Philosophical Magazine, 53, L81–L87.

Graetsch, H., Gies, H., and Topalovic, I. (1994) NMR, XRD and IR study on microcrystalline opals. Physics and Chemistry of Minerals, 21, 166–175.

Graetsch, H., Mosset, A., and Gies, H. (1990) XRD and ^{29}Si MAS-NMR study on some non-crystalline silica minerals. Journal of Non-Crystalline Solids, 119, 173–180.

Hartman, J.S., Narayanan, A., Rigby, S.S., Sliwinski, D.R., Halden, N.M., and Bain, A.D. (2007) Heterogeneities in sol-gel-derived paramagnetics-doped forsterites and willemites-Electron microprobe analysis and stretched-exponential ^{29}Si NMR spin-lattice relaxation studies. Canadian Journal of Chemistry, 85, 56–65.

Ilieva, A., Mihailova, B., Tsintsov, Z., and Petrov, O. (2007) Structural state of microcrystalline opals: a Raman spectroscopic study. American Mineralogist, 92, 1325–1333.

Kamitsos, E.I., Patsis, A.P., and Kordas, G. (1993) Infrared-reflectance spectra of heat-treated, sol-gel-derived silica. Physical Review B, 48, 12499–12505.

Langer, K. and Flörke, O.W. (1974) Near infrared absorption spectra (4000–9000 cm^{-1}) of opals and the role of "water" in these $SiO_2 \cdot nH_2O$ minerals. Fortschritte der Mineralogie, 52, 17–51.

Maciel, G.E. and Sindorf, D.W. (1980) Silicon-29 nuclear magnetic resonance study of the surface of silica gel by cross polarization and magic-angle spinning. Journal of the American Chemical Society, 102, 7606–7607.

MacKenzie, K.J.D. and Smith, M.E. (2002) Multinuclear Solid-State NMR of Inorganic Materials, Pergamon, New York, 727 p.

Maekawa, H., Maekawa, T., Kawamura, K., and Yokokawa, T. (1991) The structural groups of alkali silicate glasses determined from ^{29}Si MAS-NMR. Journal of Non-Crystalline Solids. 127, 53–64.

Malfait, W.J. and Halter, W.E. (2008) Structural relaxation in silicate glasses and melts: High-temperature Raman spectroscopy. Physical Review B, 77, 14201–1–6.

Matos, M.C., Ilharco, L.M., and Almeida, R.M. (1992) The evolution of TEOS to silica gel and glass by vibrational spectroscopy. Journal of Non-Crystalline Solids, 147–148, 232–237.

McMillan, P. (1984) Structural studies of silicate glasses and melts—applications and limitations of Raman spectroscopy. American Mineralogist, 69, 622–644.

Minitti, M.E., Weitz, C.M., Lane, M.D., and Bishop, J.L. (2007) Morphology, chemistry, and spectral properties of Hawaiian rock coatings and implications for Mars. J. Geophys. Res., 112, E05015, doi:10.1029/2006JE002839.

Monsivais-Gámez, E., Ruiz, F., and Martínez, J.R. (2007) Four-membered rings family in the Si-O extended rocking IR band from quantum chemistry calculations. Journal of Sol-Gel Science and Technology, 43, 65–72.

Morel, F.M.M. and Hering, J.G. (1993) Principles and applications of aquatic chemistry, John Wiley and Sons, New York, 588 p.

Mulder, C.A.M. and Damen, A.A.J.M. (1987) The origin of the “defect” 490 cm^{-1} Raman peak in silica gel. Journal of Non-Crystalline Solids, 93, 387–394.

Mysen, B.O. and Richet, P. (2005) Silicate Glasses and Melts, Properties and Structure, Elsevier, Amsterdam, 544 p.

Paris, M., Fritsch, E., and Aguilar Reyes, B.O. (2007) ^{1}H, ^{29}Si and ^{27}Al NMR study of the destabilization process of a paracrystalline opal from Mexico. Journal of Non-Crystalline Solids, 353, 1650–1656.

Porter, J.N., Horton, K.A., Mouginis-Clark, P.J., Lienert, B., Sharma, S.K., Lau, E., Sutton, A.J., Elias, T., and Oppenheimer, C. (2002) Sun photometer and lidar measurements of the plume from the Hawaii Kilauea Volcano Pu’u O’o vent: Aerosol flux and SO_2 lifetime. *Geophys. Res. Lett.*, 29(16), 1783, doi:10.1029/2002GL014744.

Rodgers, K.A., Cook, K.L., Browne, P.R.L., and Campbell, K.A. (2002) The mineralogy, texture and significance of silica derived from alteration by steam condensate in three New Zealand geothermal fields. Clay Minerals, 27, 299–322.

Rodgers, K.A. and Hampton, W.A. (2003) Laser Raman identification of silica phases comprising microtextural components of sinters. Mineralogical Magazine, 67, 1–13.

Schmidt, M., Botz, R., Rickert, D., Bohrmann, G., Hall, S.R., and Mann, S. (2001) Oxygen isotopes of marine diatoms and relations to opal-A maturation. Geochimica et Cosmochimica Acta, 65, 201–211.

Sindorf, D.W. and Maciel, G.E. (1982) Cross-polarization/magic-angle-spinning silicon-29 nuclear magnetic resonance study of silica gel using trimethylsilane bonding as a probe of surface geometry and reactivity. Journal of Physical Chemistry, 86, 5208–5219.

Stebbins, J.F. and McMillan, P. (1993) Compositional and temperature effects on five coordinated silicon in ambient pressure silicate glasses. Journal of Non-Crystalline Solids, 160, 116–125.

Stebbins, J.F., Smyth, J.R., Panero, W.R., and Frost, D.J. (2009) Forsterite, hydrous and anhydrous wadsleyite and ringwoodite (Mg_2SiO_4): ^{29}Si NMR results for chemical shift anisotropy, spin-lattice relaxation, and mechanism of hydration. American Mineralogist, 94, 905–915.

Theil, J.A., Tsu, D.V., Watkins, M.W., Kim, S.S., and Lucovsky, G. (1990) Local bonding environments of Si-OH groups in SiO2 deposited by remote plasma-enhanced chemical vapor deposition and incorporated by postdeposition exposure to water vapor. Journal of Vacuum Science and Technology A, 8, 1374–1381.

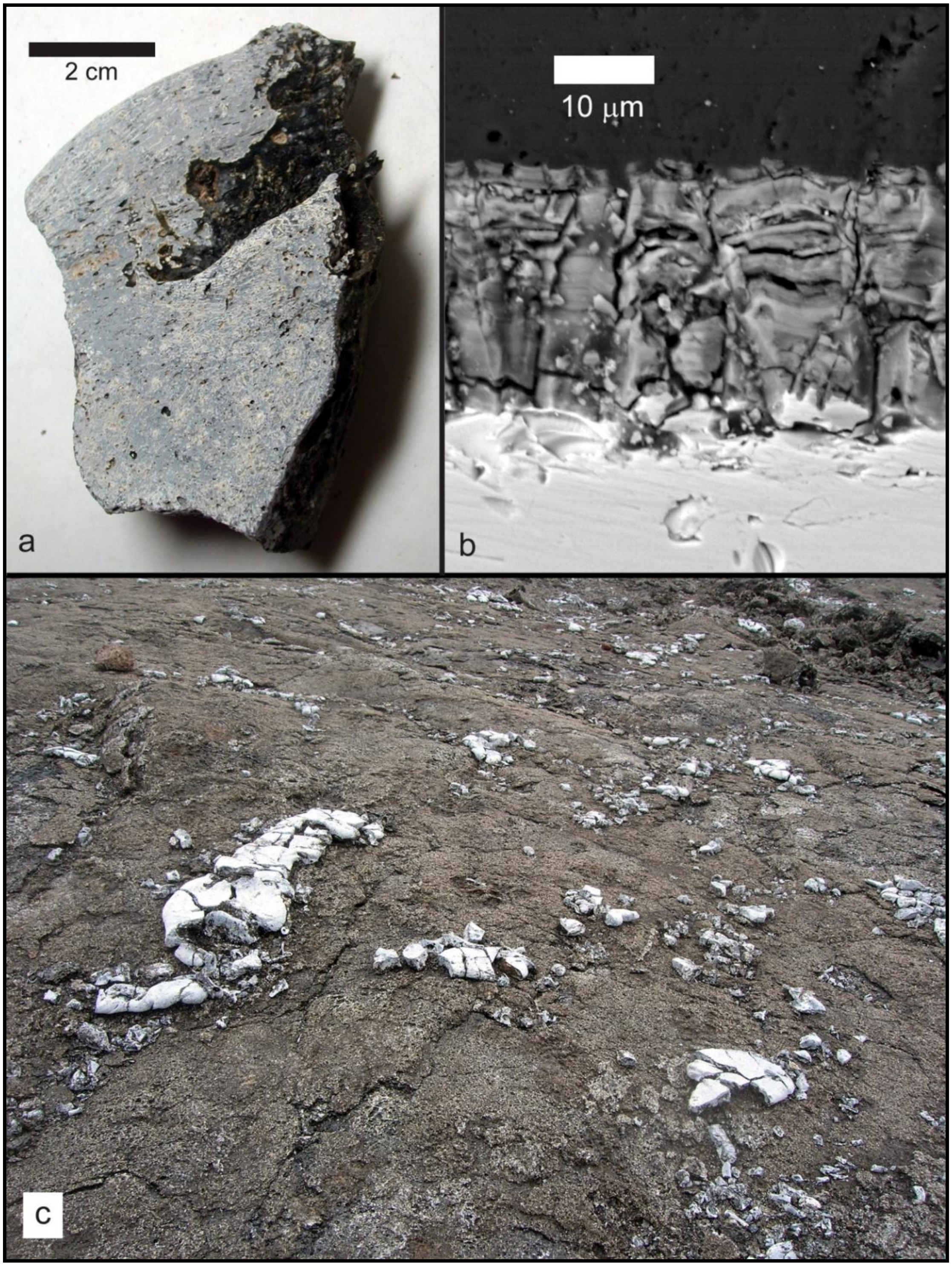

Supplemental Figure 1. Imagery of PU-009. a) Hand sample, illustrating bluish-white coating on basaltic surface. b) SEM backscatter electron image of the PU-009 coating in thick section. The bright region at the bottom of the image corresponds to the basalt substrate, capped by a ~40 µm silica coating (gray). c) Field photo of coated volcanic bombs strewn across the landscape near the rim of the Pu'u O'o cone.

Chapter V. Silicon Isotope Systematics of Acidic Weathering of Fresh Basalts, Kilauea Volcano, Hawaii

Abstract

Silicon isotopes are fractionated by a host of low-temperature aqueous processes, making them potentially useful as a weathering proxy. In most previous reports, clays and opals were ^{28}Si-enriched relative to the dissolved reservoirs from which they precipitated. Here we show that amorphous silica coatings and cements on basalt flows, the products of acidic weathering and leaching, at Kilauea Volcano, Hawaii, are ^{30}Si-enriched relative to their basaltic substrate ($\delta^{30}Si_{NBS-28}$ = + 0.92 to +1.36‰). These compositions are difficult to reconcile with previously reported fractionation factors (for which $\Delta^{30}Si_{solid-aqueous} < 0$‰). Silica coating morphology and δ^{30}Si are most consistent with *in situ* basalt alteration with an atypical direction of Si isotope fractionation ($\Delta^{30}Si_{solid-aqueous} > 0$‰) driven by complex aqueous Si speciation. Laboratory experiments in which fresh glassy basalt gravel was partially dissolved in hydrochloric or hydrofluoric acids replicated Hawaiian amorphous silica layer morphology. Fluid samples from HCl-bearing experiments were ^{30}Si-enriched; however, HF-bearing experiments produced fluids with ^{28}Si-enrichments, demonstrating the role of aqueous speciation in Si isotope fractionation. These results indicate that fluid chemistry and environmental conditions may impact on the direction and magnitude of Si isotope fractionation during weathering.

1. Introduction

Chemical weathering is the process by which silicate rocks break down and decompose to more stable phases in natural environments. Weathering controls the distribution of primary and secondary minerals at the Earth's surface. The rates of chemical weathering are strongly influenced by temperature, rainfall rates, and environmental chemistry (Raymo et al., 1988; Riebe et al., 2004; Das et al., 2005). Evidence for the extent and style of chemical weathering in a geologic record may provide information about the environmental conditions from that time period. Therefore, the development of geochemical and isotopic proxies for weathering is of interest for understanding climatic and environmental histories.

Variations in stable silicon isotope ratios ($^{30}Si/^{28}Si$ and $^{29}Si/^{28}Si$) are a potentially useful tool for probing the environmental and weathering history of modern and ancient low-temperature aqueous systems. The usefulness of this isotope system relies on the observation that low-temperature processes, such as clay precipitation and silica adsorption, produce large fractionations in silicon isotope composition ($\delta^{30}Si$) [1], while primary igneous variations in $\delta^{30}Si$ are observable but small (Douthitt, 1982; Savage et al., 2010, 2011)). Dissolved Si in natural surface waters is enriched in $^{30}Si/^{28}Si$ relative to source materials (De La Rocha et al., 2000; Ding et al., 2004; Georg et al., 2007). This fractionation is generally understood to occur as a result of the weathering of silicate rocks and the precipitation of secondary minerals, such as clays and opals, which tend to be enriched in ^{28}Si. Soil $\delta^{30}Si$ reflects a range of fractionating processes, including

---

[1] $\delta^{30}Si = (R_{sample} - R_{std}) / R_{std} \cdot 1000$, where $R = {}^{30}Si/{}^{28}Si$; throughout this paper, the standard used in this notation is NBS-28, a quartz sand sample that serves as the international silicon isotope standard.

weathering of primary phases, adsorption of silica on iron oxide particles, and biological uptake of silica (Ziegler et al., 2005; Delstanche et al., 2009; Opfergelt et al., 2010)), as well as the input of wind-blown dust (Bern et al., 2010). Particularly ^{28}Si-enriched samples, such as pedogenic silcretes (as light as δ^{30}Si = -5.4‰) may have undergone multiple cycles of dissolution and re-precipitation (Basile-Doelsch et al., 2005). Groundwater from the Navajo Sandstone aquifer, Nevada, spans the range of primary and secondary mineral δ^{30}Si, potentially reflecting varying degrees of redissolution of secondary clays and silcretes (Georg et al., 2009). The precipitation of biogenic silica, incorporated into the shells of diatoms and radiolaria in marine environments and into plant phytoliths in terrestrial environments, may also impose significant fractionations on the dissolved silicon budget (Leng et al., 2009; Opfergelt et al., 2006). These observed fractionations have allowed the use of silicon isotopes as a proxy for environmental conditions in several geologic records, including siliceous diatoms over the period of the Last Glacial Maximum (De La Rocha et al., 1998), Precambrian oceanic cherts (Robert and Chaussidon, 2006; van den Boorn et al., 2010) and banded-iron formations (Heck et al., 2011; Chakrabarti et al., 2012).

Several factors complicate the interpretation of Si isotope compositions in natural samples. One complicating factor is that many of the above-mentioned low-temperature processes, including precipitation, adsorption on nanophase oxide particles, and biouptake, produce silicon isotope signatures indistinguishable from one another. Determining environmental conditions and formation mechanisms may be difficult if multiple fractionating processes operated simultaneously. Another unresolved issue is that isotopic fractionation factors (α) associated with precipitation of clays and opals are

Publication	**Fractionation factor (1000 ln α)**	**Experiment description**
Ziegler et al. (2002)	-0.7‰	Allophane precipitation from aqueous Si-Al solution: Rayleigh fractionation
Li et al. (1994)	-1.0‰	Opal precipitation from monosilicic acid
de la Rocha et al. (1997)	-1.1‰	Biogenic silica formation by diatoms from seawater
Geilert et al. (2011)	-1.2‰	Controlled opal precipitation from solution, flow-through setup
Ziegler et al. (2002)	-1.3‰	Allophane precipitation from aqueous Si-Al solution: equilbrium fractionation
Milligan et al. (2004)	-1.5‰	Biogenic silica formation by diatoms from seawater
Douthitt (1982)	-3.5‰	Observation of secondary minerals vs. associated fluid bodies in natural settings

Table 1. Si isotope fractionation factors associated with mineral precipitation and adsorption reported in the literature.

poorly constrained. Many previous experimental and analytical studies have achieved a value of 1000 ln $\alpha_{\text{precip-aqueous}} \cong -1‰$ (Table 1), but variations in α with fluid chemistry, Si concentration, and temperature have not been explored. The relative effects of equilibrium and kinetic fractionation are poorly understood. Effective interpretation of δ^{30}Si compositions of ancient rocks requires continued study of weathering under different conditions in natural and experimental settings.

In this study, we focus on chemical weathering of fresh basalt flows at Kilauea Volcano on the island of Hawai'i. Young basalt flows frequently feature brightly colored white, yellow, orange or blue coatings, up to 50 μm thick, composed largely of hydrous amorphous silica (Minitti et al., 2007; Chemtob et al., 2010; Chemtob et al., 2012). These coatings form over a period of months to years by interaction of the fresh basalt surface with volcanically-derived acids. However, the immediate source of Si and the degree of Si mobility during coating formation is unclear.

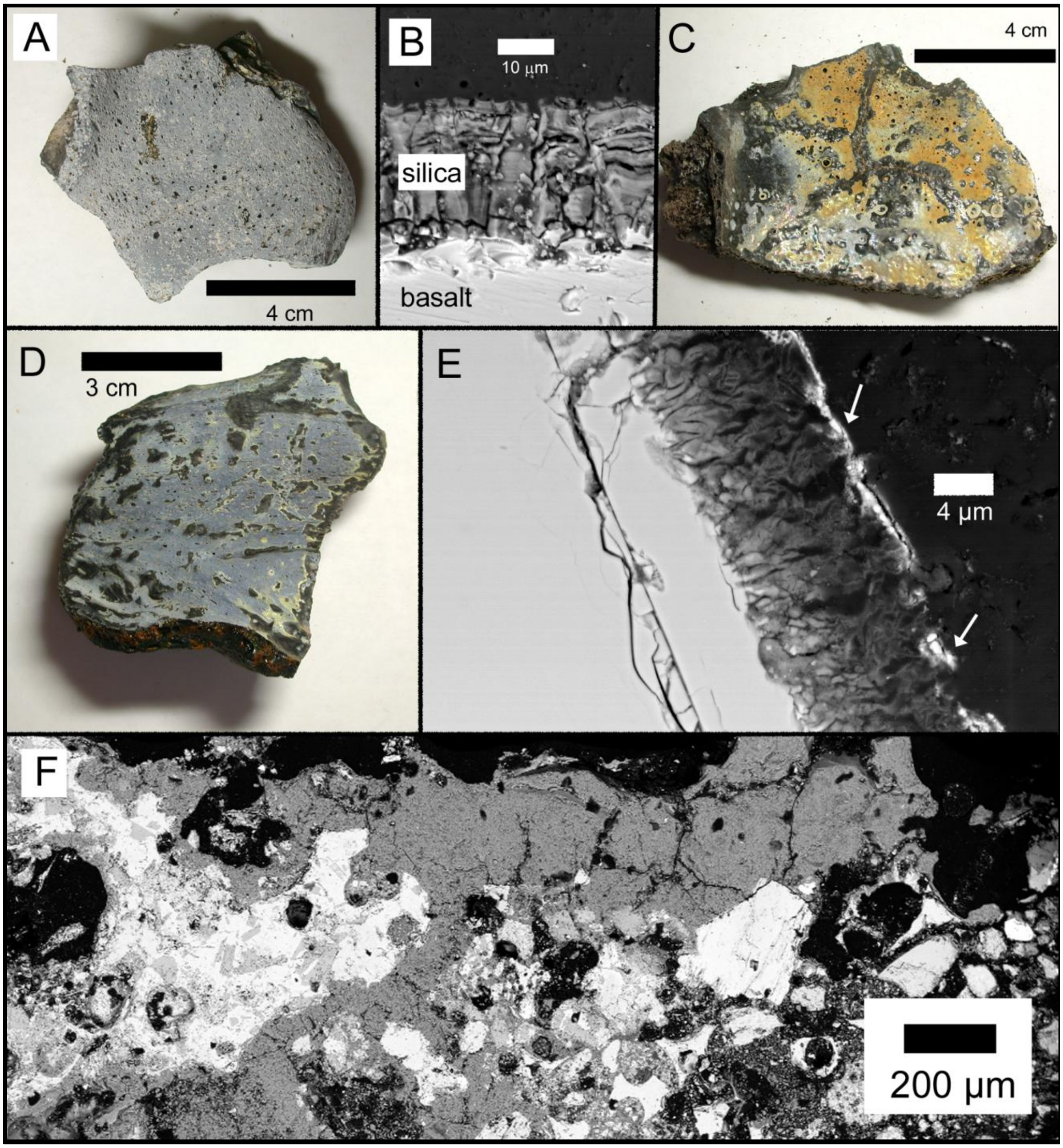

Figure 1. Optical and backscattered electron (BSE) images of Hawaiian siliceous samples. a) Sample PU-009, silica-coated volcanic bomb from the rim of the Pu'u O'o cone. Note that the spalled basalt on which the bomb was deposited is uncoated. b) BSE image of cross-section of PU-009. Dark zone at top of image is epoxy, bright zone at bottom is the basalt substrate, and the gray zone is a 25–30 µm thick layer of hydrous amorphous silica. c) Coated underside of PU-010, a 2 cm thick pahoehoe shell from the rim of Pu'u O'o. d) Hand sample of KD-003, a 1974 coated spatter sample collected along Kilauea's Southwest Rift Zone in the Ka'u Desert. e) Cross-sectional BSE view of KD-003. Coatings at this location consist of a 10 µm layer of amorphous silica capped by a 1 µm layer of Fe-Ti oxide (marked by arrows). f) BSE image of polished cross section of indurated ash sample S-12-41. Abundant gray-colored material is amorphous silica cement. Darker-colored spots are void space, carbonaceous material, or epoxy.

This study presents Si isotope data, determined both by multiple-collector inductively coupled plasma-source mass spectrometry (MC-ICP-MS) and by secondary ion mass spectrometry (SIMS), for Kilauean basalts and silica coatings and cements. By measuring δ^{30}Si of these coatings, we seek to determine whether silica layers form by *in situ* alteration and replacement of basalt surfaces, or by transport and external deposition of Si. Previous studies on Si isotope fractionation during basalt weathering have focused either on the composition of dissolved Si in rivers draining basaltic watersheds (Georg et al., 2007) or on the composition of soil profiles developed on much older Hawaiian basalts (Ziegler et al., 2005). This is, to our knowledge, the first study of Si isotope fractionation of small-scale solid alteration products of young lava. Here we show that silica coatings display anomalously heavy δ^{30}Si relative to their basaltic substrates.

In addition to analyses of natural samples, we conducted laboratory alteration experiments of fresh basaltic glass in acidic solutions and present chemical, morphologic and Si isotopic characteristics of the reacted solids and solutions. Previous basalt alteration experiments with similar experimental setups (Tosca et al., 2004; Hurowitz et al., 2005) included no isotopic analysis of solid or liquid products. The objectives of these experiments were to replicate natural silica coating morphologies and to characterize the Si isotope signature of basalt weathering in a controlled environment. The experiments presented here show that Si speciation profoundly affects the direction and magnitude of silicon isotope fractionation during weathering and precipitation.

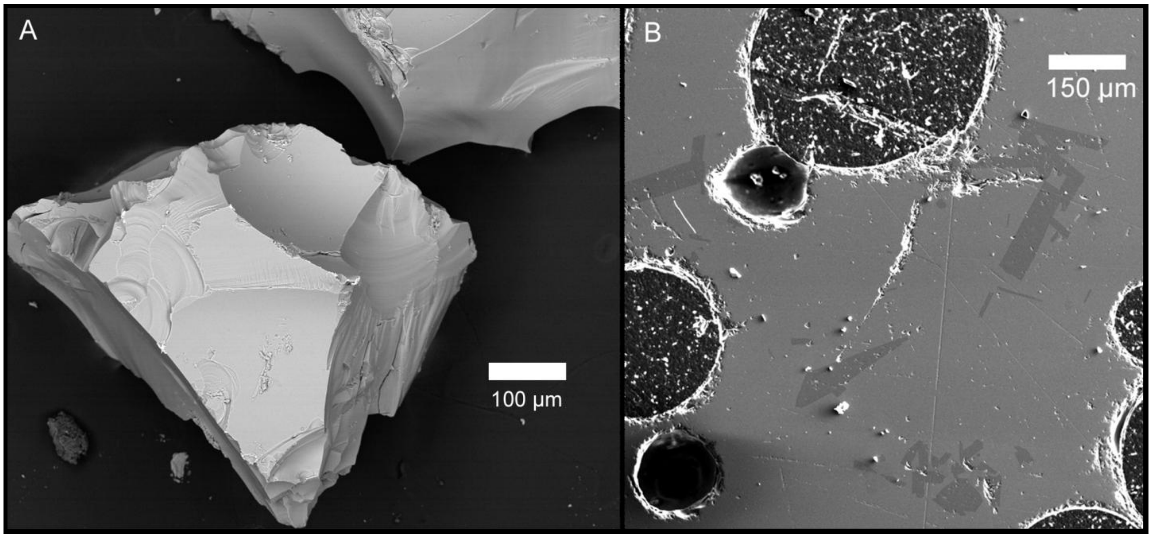

Figure 2. SEM images of KP-fresh, glassy basalt collected freshly from an active lava flow near Kalapana in 2010. a) KP-fresh gravel, 300-600 μm grain size fraction. b) Polished cross section, illustrating high vesicularity, high glass content and plagioclase laths.

2. Sample Locales and Descriptions

Samples of young basalts featuring silica coatings were collected from flows of various ages along Kilauea's southwest (SWRZ) and east (ERZ) rift zones. The samples labeled PU-009 and PU-010 were collected in 2010 on the northeast rim of Pu'u O'o, a basaltic cone on the ERZ. The Pu'u O'o eruption began in 1983 and is one of the island's longest-lived historical eruptions. Pu'u O'o has continuously produced a plume dominated by water vapor and SO_2 but also containing CO_2, H_2, reduced sulfur species, HCl, and HF (Gerlach, 1993). These samples were collected on the surface of 1997 overflow pahoehoe lavas produced as part of Kilauea's Episode 55 eruption. Much of the subaerial surface of these lavas is covered by a bluish-white coating, 30–80 μm thick, composed primarily of hydrous amorphous silica (Figure 1a,b). The pahoehoe features a 2–3 cm thick outer shell and a hollow center, where still-molten lava drained. In some cases, both the outer and inner surfaces of the shells are coated by silica. PU-010 comprises a doubly-coated pahoehoe shell (Figure 1c); the underside coating was scraped for analysis. PU-009 comprises heavily coated basaltic volcanic bombs strewn over the pahoehoe surface. The PU-009 silica coating sample was the subject of a previous study on water content and speciation in the silica coatings as determined by infrared spectroscopy and ^{29}Si NMR (Chemtob et al., 2012). Samples KD-003, KD-005 and EA-30 were collected from coated spatter ramparts and pahoehoe toes erupted in 1974 in the Ka'u Desert along Kilauea's SWRZ, roughly 5 km downwind of Halema'uma'u Crater (Figure 1d,e). Samples from the same locality were described in Chemtob et al. (2010).

Amorphous silica is observable at Kilauea not only as coatings on fresh basalts, but as cement in soils and regoliths (Seelos et al., 2010; Ziegler et al., 2005). The region near the south rim of Halema'uma'u Crater features a number of manmade soil berms, bulldozed by the U.S. military during World War II. These piles have since developed a ~1 cm indurated rind; samples of these rinds (S-12-41) were collected in April 2012 by Don Swanson. SEM and infrared spectroscopic analysis of the cements indicates they are composed primarily of gypsum and amorphous silica (Figure 1f). Amorphous silica cements were scraped and collected for analysis.

A sample of still-molten lava (KP-fresh) was collected using a steel pole in 2010 from an active lava channel sourced at the Episode 58 vent, ~1 km east of Pu'u O'o. The collection site was roughly 7 km southeast of the source vent. The sample is unaltered, highly vesicular and composed largely of glass, with ~10% phenocrysts (primarily plagioclase, An_{71}, with rare olivine) (Figure 2). The chemical composition of KP-fresh as determined by electron microprobe analysis is given in Table 2.

Table 2. Electron microprobe analyses of KP-fresh basalt glass[1]

SiO_2	51.84 ± 0.30
TiO_2	2.46 ± 0.08
Al_2O_3	13.21 ± 0.16
FeO*	11.26 ± 0.16
MgO	6.38 ± 0.10
CaO	10.66 ± 0.13
Na_2O	2.36 ± 0.08
K_2O	0.43 ± 0.02
Cr_2O_3	n.d.
MnO	0.16 ± 0.04
P_2O_5	0.23 ± 0.04
SO_3	n.d.
Total	99.04

[1] Average of four spot analyses. Errors are 2σ.

3. Methods

3.1. Experimental Procedures

Partial dissolution experiments were carried out using a variety of setups and environmental conditions (Table 3). Starting material for all experiments was KP-fresh basalt (described in Section 2), ground, sieved to a grain size fraction of 300–600 μm, and ultrasonicated to remove clinging fine particles. Experiments FT.A and FT.B were conducted using packed-bed flow-through reactors constructed using PEEK and Teflon tubing manufactured by Upchurch Scientific, as described in Hurowitz et al. (2005). Reacting solution was pumped through the sample chambers using a syringe pump at 10 μL/min. The starting fluids were prepared from Seastar Baseline ultra-pure acids and 18.1 mΩ H_2O; fluid compositions were a mixture of H_2SO_4 and HCl, with SO_4:Cl set to replicate the composition of Kilauea volcanic gases (Greenland et al., 1985) and diluted to pH 1 (FT.A) or pH 3 (FT.B). Exps. FT.A and FT.B were maintained at 50° C by submerging the flow-through apparatus in a heated water-bath. Fluid samples were collected in Teflon beakers and diluted in 18.1 mΩ H_2O. The effluent pH was monitored for both flow-through experiments. The B-HCl and B-HF experimental series were batch experiments conducted in screw-top Teflon vials. KP-fresh basalt in the 300–600 μm size fraction was loaded into experimental vials. In Exps.

Experiment	Apparatus	Fluid composition	T (° C)	Duration	Initial basalt (g)	Initial fluid (mL)	W/R ratio	Fluid collection procedure
Flow-through experiments								
FT.A	PEEK tubing	74.5 mM H_2SO_4, 18.6 mM HCl	50	14 days	1	n.a.	201.6	Steady solution output
FT.B	PEEK tubing	0.75 mM H_2SO_4, 0.19 mM HCl	50	14 days	1	n.a.	201.6	Steady solution output
Batch HCl experiments								
B-HCl.A	PTFE vial	0.1 M HCl	60	30 days	0.625	1.25	1.9	Periodic
B-HCl.B	PTFE vial	0.1 M HCl	60	30 days	0.312	2.96	9.5	Periodic
B-HCl.C	PTFE vial	0.1 M HCl	60	30 days	0.117	11.42	97.6	Periodic
Batch HF experiments								
B-HF.A	PTFE vial	1 M HF	60	16 days	0.102	1.02	10	Periodic
B-HF.B	PTFE vial	1 M HF	60	16 days	0.106	1.06	10	Only at conclusion
B-HF.C	PTFE vial	1 M HF	60	16 days	0.242	0.725	3	Periodic
B-HF.D	PTFE vial	1 M HF	60	16 days	0.242	0.726	3	Only at conclusion
B-HF.E	PTFE vial	1 M HF	60	7 days	0.0998	0.998	10	Only at conclusion
B-HF.F	PTFE vial	0.1 M HF	60	7 days	0.0996	0.996	10	Only at conclusion

Table 3. Log of experimental conditions.

B-HCl.A through C, the starting fluid composition was 0.1 M HCl. The water/rock mass ratios (W/R) for Exps. B-HCl.A, B, and C were set to 2, 10, and 100, respectively. In Exps. B-HF.A through E, the starting fluid composition was 1 M HF; in experiment B-HF.F, the fluid composition was 0.1 M HF. Water/rock ratios were set to W/R = 10 for Exps. B-HF.A, B, E, and F and to W/R = 3 for Exps. B-HF.C and D. The batch experiments were heated inside of a drying oven, or on a hot plate, set to 60° C. Fluid samples were periodically collected from some experiments using an adjustable volume syringe. Volumes of collected fluid were typically small (50–100 μL) and were typically diluted in 18.1 mΩ H_2O after collection. Solid samples of basalt gravel were also periodically collected. For other experiments, fluid samples were collected only at the experiment conclusion. Fluid samples were stored in Teflon sample bullets for later analysis.

Solid samples were mounted in epoxy and polished for morphological analysis using a LEO 1550 VP field emission scanning electron microscope (SEM) at Caltech. An Oxford Inca x-ray energy dispersive spectrometer (EDS) was used for concurrent elemental analyses and for elemental mapping. The major and minor element compositions of alteration materials were determined by wavelength dispersive spectrometry using a JEOL JXA-8200 electron probe microanalyzer (EPMA). The probe was operated at 15 kV accelerating voltage and 20 nA beam current.

Concentrations of dissolved Si, Ti, Al, Mg, Ca, Fe, Mn, Na, K, P, and S in effluent samples were determined using a Thermo iCap 6300 radial view inductively coupled plasma optical emission spectrometer (ICP-OES) at the Jet Propulsion Laboratory. Standard solutions were prepared for each element at concentrations of 0.1, 1, 10, and 50 ppm using spec solutions. Samples and standards were matrix-matched in 2% HNO_3.

3.2. Isotopic Analytical Methods

3.2.1. SIMS Methods

Initial characterization of the silicon isotope content of the PU-009 silica coatings was performed on a Cameca 7f ion microprobe at Caltech. Analyses of the silica coating were standardized to quartz from the Rose Quartz Mine (San Diego County, CA) (RSQ). Because the silica coating is amorphous and contains up to 5.5% structural H_2O (Chemtob et al., 2012), additional materials were analyzed to test whether RSQ was a sufficiently matrix-matched standard. To assess the magnitude of a matrix effect associated with crystallinity, Ge 214 silica glass was analyzed. To assess the matrix effects associated with water content, a series of albite glasses with identical chemical composition but varying water content was analyzed. Anhydrous albite glass (AmAb) and albite glasses with 3 wt% H_2O (Ab 3%) and 7 wt% H_2O (Ab 7%) were synthesized as part of a previous study (Silver et al., 1985). Samples and standards were mounted in epoxy, polished using diamond and alumina papers, and coated with 50 nm Au before analysis. Cameca 7f measurements were made with an O^- primary beam, focused to a ~30 μm spot. Secondary ^{28}Si and ^{30}Si ions were measured with two Faraday cups by magnetic peak switching. Typical count rates were ~3.6 x 10^7 cps for ^{28}Si and ~1.1 x 10^6 cps for ^{30}Si.

3.2.2. MC-ICP-MS Methods

Silicon isotope compositions were also determined using a ThermoFinnigan Neptune multiple-collector inductively coupled plasma-source mass spectrometer (MC-ICP-MS) at UCLA, over three sessions in 2012. Silica coatings and cements were scraped from their basalt substrates using dental tools and were purified by manual picking and magnetic separation. Silica digestions were performed following the methods of De La Rocha et al. (1996) and Ziegler et al. (2010). Silica samples, basaltic substrates, and standards (NBS-28; RSQ; Ge 214 silica glass; Ab 3%; Ab 7%) were dissolved in 2.5 M ultrapure HF at ~120° C in sealed Teflon screw-cap vials. The volume of HF added is proscribed by the Si concentration of the sample such that the final concentration of fluorosilicate ions is kept below the threshold required for volatilization of SiF_4 gas. In some digestions, equal volumes of ultrapure HNO_3 were added to accelerate dissolution.

Purification of Si from digestions was achieved by ion-exchange chromatography. 2 mL of BioRad cation exchange resin DOWEX 50W-X12 (200–400 mesh) was added to each of twelve ion exchange columns. Columns were loaded with 3.6 μg Si in 0.02% HF and eluted with 6 mL of 18.1 mΩ H_2O. The resin retains cationic species, but Si species do not bind to the resin, producing Si-purified solutions with ~0.5 ppm Si. This purification method has been demonstrated in previous studies to achieve complete Si yield (Shahar et al., 2009; Ziegler et al., 2010). HF concentrations in the final purified solutions are 0.0023%, low enough not to cause signal instability on the MC-ICPMS (Shahar et al., 2009). Some natural Hawaiian samples contain percent-level concentrations of sulfate, a species not retained by the resin; test runs of NBS-28 standard

Sample number	**δ^{29}Si**	**2 s.e.**	**δ^{30}Si**	**2 s.e.**	**Δ^{29}Si**	**2 s.e.**	**# blocks**	**# analyses**
Standards								
RSQ quartz	-0.023	0.052	0.021	0.078	-0.034	0.063	4	1
Ge214 silica glass	0.214	0.052	0.378	0.032	0.018	0.061	6	1
Amorphous albite, anhyd.	0.059	0.038	0.127	0.054	-0.006	0.022	6	1
Amorphous albite, 7% H2O	0.272	0.033	0.434	0.045	0.047	0.05	12	2
Basalts								
KP-fresh	-0.039	0.045	-0.186	0.043	0.057	0.046	6	1
KP-fresh (dup.)	-0.061	0.046	-0.096	0.039	-0.01	0.059	4	1
KD-005 basalt	-0.461	0.052	-0.836	0.039	-0.028	0.064	6	1
PU-009 basalt	-0.103	0.054	-0.11	0.134	-0.046	0.048	5	1
PU-010 basalt	-0.17	0.033	-0.246	0.124	-0.043	0.042	6	1
Silica coatings and Cements								
PU-009 coating	0.815	0.029	1.36	0.045	0.111	0.041	6	1
PU-009 coating (dup.)	0.725	0.051	1.172	0.073	0.118	0.074	5	1
PU-010 underside coating	0.499	0.054	1.073	0.033	-0.057	0.055	9	2
KD-003 coating	0.471	0.034	0.923	0.041	-0.007	0.049	6	1
S-12-41 cement	0.591	0.051	1.104	0.055	0.02	0.042	5	1

Table 4. MC-ICP-MS silicon isotope compositions for standards, basalts, and Hawaiian silica coatings and cements.

Sample number	δ^{29}Si	2 s.e.	δ^{30}Si	2 s.e.	Δ^{29}Si	2 s.e.	# blocks	# analyses
HCl Batch Experiments								
B-HCl.A.3	0.336	0.021	0.531	0.045	0.061	0.034	6	1
B-HCl.A.6	0.882	0.027	1.730	0.029	-0.014	0.029	5	1
B-HCl.B.3	-0.088	0.017	-0.205	0.035	0.019	0.029	6	1
B-HCl.B.6	0.500	0.013	0.898	0.018	0.035	0.017	6	1
B-HCl.C.3	-0.082	0.018	-0.149	0.015	-0.005	0.023	6	1
B-HCl.C.6	-0.003	0.013	-0.037	0.056	0.016	0.025	6	1
B-HCl.D.final	1.150	0.063	2.291	0.060	-0.036	0.062	4	1
HF Batch Experiments								
B-HF.A.3	-1.093	0.109	-2.011	0.194	-0.052	0.033	10	2
B-HF.A.6	-2.442	0.048	-4.745	0.047	0.015	0.030	6	1
B-HF.B.final	-2.594	0.133	-5.076	0.223	0.034	0.037	10	2
B-HF.C.3	-2.714	0.043	-5.253	0.047	0.006	0.033	9	2
B-HF.C.6	-1.917	0.008	-3.709	0.023	0.004	0.013	5	1
B-HF.D.final	-4.566	0.058	-8.931	0.068	0.058	0.033	9	2
B-HF.E.final	-1.759	0.086	-3.474	0.119	-0.006	0.087	4	1
B-HF.F.final	-1.067	0.155	-1.968	0.144	-0.047	0.083	3	1

Table 5. MC-ICP-MS silicon isotope compositions for effluent samples from batch alteration experiments.

material with added sulfate produced no measurable matrix effects. Si-purified samples were matrix-matched to the standard solutions in 2% HNO_3.

Purified solutions were run on the Neptune MC-ICP-MS in dry plasma mode using the Cetac Aridus I desolvating system, the Cetac PFA microconcentric Aspire nebulizer, and a PFA spray chamber. $^{28}Si^+$, $^{29}Si^+$, and $^{30}Si^+$ ions were all measured simultaneously. Ion beam intensities were for experimental solutions were typically around 3.0 V for $^{28}Si^+$, 160 mV for $^{29}Si^+$, and 110 mV for $^{30}Si^+$. The MC-ICP-MS was operated at a mass resolving power of ~9,500. The primary standard solution was NBS-28, which by definition has $\delta^{30}Si \equiv 0$‰. Samples and standards were diluted to match peak heights to within 5–10%. Corrections for instrumental mass bias were performed by sample-standard bracketing. Measurements were performed in blocks of 20 cycles, with 4–6 blocks performed per sample.

4. Results

4.1. MC-ICP-MS Results

4.1.1. Standards

Zero enrichment analyses of NBS-28 standard solutions as unknowns by MC-ICP-MS were frequently performed to assess internal reproducibility. Individual zero enrichment analyses were typically ±0.10‰ or better for both $\delta^{29}Si$ and $\delta^{30}Si$; daily averages of zero enrichment analyses were typically ±0.05‰ or better.

Measurements of three inter-laboratory standards for silicon isotope MC-ICP-MS analysis (IRMM-018a, Diatomite, and “Big Batch”), performed by identical sample preparation and analytical techniques, are reported elsewhere (Ziegler et al., 2010).

Derived values for those materials matched recommended values (Reynolds et al., 2007). Several in-house standards were measured to establish external reproducibility and to determine silicon isotope compositions of materials to be used for SIMS standardization. RSQ was measured as δ^{30}Si = 0.02 ± 0.08‰ (2 s.e.), which is in good agreement with the measurement reported by Chmeleff et al. (2008) (δ^{30}Si = 0.10 ± 0.13‰). Silicon isotope compositions of Ge 214, AmAb and Ab 7% glasses were also determined; their δ^{30}Si are listed in Table 4 and discussed below in Section 4.2.1.

4.1.2. Basalts

Basalt δ^{30}Si isotope compositions are listed in Table 4. KP-fresh, the fresh lava sample that was used as precursor material for dissolution experiments, was dissolved and analyzed twice, resulting in measurements of δ^{30}Si = -0.19 ± 0.04 and -0.10 ± 0.04 (2 s.e.). Hereafter, the average value of these two compositions, -0.14 ± 0.03‰, will be used for comparison to experimental effluent compositions.

Two basalt samples collected at the rim of Pu'u O'o, PU-009 and PU-010, had isotope compositions of δ^{30}Si = -0.11 ± 0.13 and -0.25 ± 0.12 (2 s.e.), respectively. KD-005, collected from the July 1974 pahoehoe flow on Kilauea's Southwest Rift Zone, was measured as δ^{30}Si = -0.84 ± 0.04‰.

4.1.3. Silica Coatings and Cements

All MC-ICP-MS analyses of Hawaiian silica coatings and cements showed ^{30}Si-enriched compositions relative to Hawaiian basalt (Table 4). PU-009 silica coatings were dissolved and analyzed twice, resulting in measurements of δ^{30}Si = 1.36 ± 0.05‰ and

1.17 ± 0.07‰. Coatings from the underside of the pahoehoe shell sample PU-010, collected adjacent to PU-009, had δ^{30}Si = 1.07 ± 0.03. The coating from the Ka’u Desert sample KD-003 had δ^{30}Si = 0.92 ± 0.04. Separated amorphous silica cement from the indurated soil sample S-12-41 had δ^{30}Si = 1.10 ± 0.06.

4.1.4. Experimental Effluent Samples

δ^{30}Si of fluid samples from dissolution experiments are shown in Table 5. These results will be discussed in Section 4.3 in the context of each individual experiment.

4.2. SIMS Results

The results of SIMS analyses, including tests of matrix effects and δ^{30}Si measurements of Hawaiian silicas, are included in Appendix A. The analyses suffered from poor reproducibility between sessions and across different epoxy mounts of the same sample. The lack of reproducibility may result from unexpected matrix effects, heterogeneity within the coatings, or uneven topography, as the coatings tend to polish poorly. Because of these complicating factors, we prefer the MC-ICP-MS δ^{30}Si and focus our interpretations on those values.

4.3. Experimental Results

4.3.1. Flow-Through Experiments

4.3.1.1. Effluent Chemistry

ICP-OES analyses of the effluent samples from the two flow-through experiments are displayed in Table 6 and Figure 5. The Exp. FT.A data suggest accelerated

Sample number	Hours elapsed	Sample pH	Flow rate (µL/min)	Dilution factor	P	Si	Ti	Al	Ca	Fe	K	Mg	Mn	Na
Experiment FT.A														
FT.A.1	11.4	1.05	6.30	7.0	92 (15)	8873 (414)	562 (3.7)	8665 (38)	5223 (280)	5803 (176)	2775 (3)	7182 (225)	73 (3.7)	2329 (67.3)
FT.A.2	23.6	0.98	12.05	5.6	77.4 (0.4)	5643 (202)	148 (8.1)	4961 (14)	2716 (81)	2085 (19)	2052 (76.6)	3956 (44)	24.2 (0.3)	949 (11)
FT.A.3	47.9	0.97	9.90	5.6	83.1 (0.4)	3891 (153)	104 (5.2)	4377 (51)	5457 (130)	1197 (28)	144 (82)	2019 (53)	14.7 (0.4)	888 (12.1)
FT.A.4	79.6	0.98	7.54	5.9	55.5 (2.5)	3494 (63)	123 (2.9)	4545 (35)	4073 (56)	1069 (0.6)	101 (62)	1483 (9)	13.7 (0.1)	913 (20)
FT.A.5	98.3	0.96	10.53	5.4	76.5 (1.5)	3474 (241)	139 (11)	4125 (76)	3405 (95)	932 (15.3)	107 (34)	1143 (21)	11.8 (0.3)	865 (3)
FT.A.6	143.7	0.98	11.71	5.3	33.5 (1.2)	2807 (30)	134 (0.2)	3083 (35)	1660 (85)	762 (12.3)	n.d.	709 (12)	9.9 (0.1)	702 (12)
FT.A.7	168.0	NA	9.65	5.2	29.7 (1.0)	2938 (162)	153 (9.4)	3097 (40)	1551 (33)	855 (30.8)	41 (31)	695 (25)	11.2 (0.5)	718 (16)
FT.A.8	190.9	0.96	10.36	5.4	42.1 (1.0)	2731 (206)	144 (12)	2661 (3.9)	1606 (110)	769 (0.8)	63 (24)	588 (4)	10.2 (0.1)	649 (8)
FT.A.9	215.2	NA	10.82	5.6	42.9 (1.2)	2662 (136)	140 (8.1)	2558 (4.6)	1801 (16)	768 (43.2)	n.d.	568 (28)	10.3 (0.9)	628 (32)
FT.A.10	245.8	0.92	8.26	5.2	38.4 (1.8)	3153 (155)	176 (8.5)	2772 (44)	1511 (152)	859 (4.8)	77.3 (44)	616 (3.6)	11.4 (0.1)	679 (0.6)
FT.A.11	290.0	NA	12.22	5.8	35.3 (1.1)	2846 (93)	153 (8.5)	2344 (10)	1283 (91)	810 (17.5)	n.d.	556 (10)	11.1 (0.3)	611 (16)
FT.A.12	336.0	0.93	12.08	5.8	37.0 (0.7)	3120 (82)	182 (9.5)	2484 (0.8)	1418 (48)	962 (27.8)	n.d.	650 (24)	12.9 (0.6)	664 (41)

Table 6. ICP-OES chemical analyses of effluent samples from flowthrough experiments FT-A and FT-B. n.d. = not detected.

Sample number	Hours elapsed	Sample pH	Flow rate (µL/min)	Dilution factor	P	Si	Ti	Al	Ca	Fe	K	Mg	Mn	Na
Experiment FT.B														
FT.B.1	11.4	3.38	8.84	5.7	7.0 (1.3)	648 (7)	n.d.	389 (1.8)	1834 (28)	162 (1.6)	381 (3.4)	169 (2.9)	n.d.	219 (0.7)
FT.B.2	23.6	3.05	12.57	5.1	2.2 (0.2)	448 (11)	n.d.	290 (1.2)	718 (15)	137 (1.1)	152 (4.3)	173 (1.2)	n.d.	124 (5.8)
FT.B.3	47.9	3.06	9.27	6.0	2.3 (0.2)	492 (19)	n.d.	270 (1.8)	736 (2.1)	119 (2.5)	108 (15.3)	178 (3.8)	n.d.	129 (2.5)
FT.B.4	79.6	NA	5.60	5.8	n.d.	522 (6)	n.d.	292 (0.4)	308 (6.3)	126 (2.5)	n.d.	194 (2.0)	n.d.	119 (1.4)
FT.B.5	98.3	3.05	9.68	5.5	3.1 (0.3)	629 (15)	n.d.	330 (2.3)	504 (10.1)	124 (0.8)	210 (33)	188 (2.5)	n.d.	117 (9.5)
FT.B.6	143.7	NA	12.90	5.7	1.4 (0.1)	464 (7)	n.d.	265 (0.6)	212 (1.8)	101 (1.6)	67 (15)	138 (2.3)	n.d.	108 (9.9)
FT.B.7	168.0	NA	9.49	5.7	9.3 (0.5)	538 (7)	n.d.	271 (0.8)	294 (0.4)	118 (0.9)	57 (24)	175 (2.3)	n.d.	108 (10.3)
FT.B.8	190.9	3.04	10.45	5.5	3.9 (0.4)	536 (11)	n.d.	293 (5)	625 (14.2)	112 (3.2)	63 (13)	171 (6.1)	n.d.	108 (2.7)
FT.B.9	215.2	NA	8.79	6.0	3.0 (0.2)	587 (13)	n.d.	304 (1.4)	454 (0.5)	115 (2.8)	68 (24)	170 (5.2)	n.d.	131 (0.4)
FT.B.10	245.8	3.11	6.49	5.9	4.0 (0.9)	671 (10)	n.d.	340 (1.4)	286 (1.4)	134 (2.2)	60 (27)	204 (2.5)	n.d.	134 (5.0)
FT.B.11	290.0	NA	12.73	5.6	4.3 (0.6)	521 (5)	n.d.	310 (3.5)	177 (0.2)	101 (0.9)	35 (5.2)	134 (0.7)	n.d.	118 (4.1)
FT.B.12	336.0	2.95	12.94	5.4	2.5 (0.1)	506 (0.8)	n.d.	296 (2.1)	190 (3.3)	101 (2.1)	47 (19)	130 (4.1)	n.d.	112 (1.5)

Table 6. (continued)

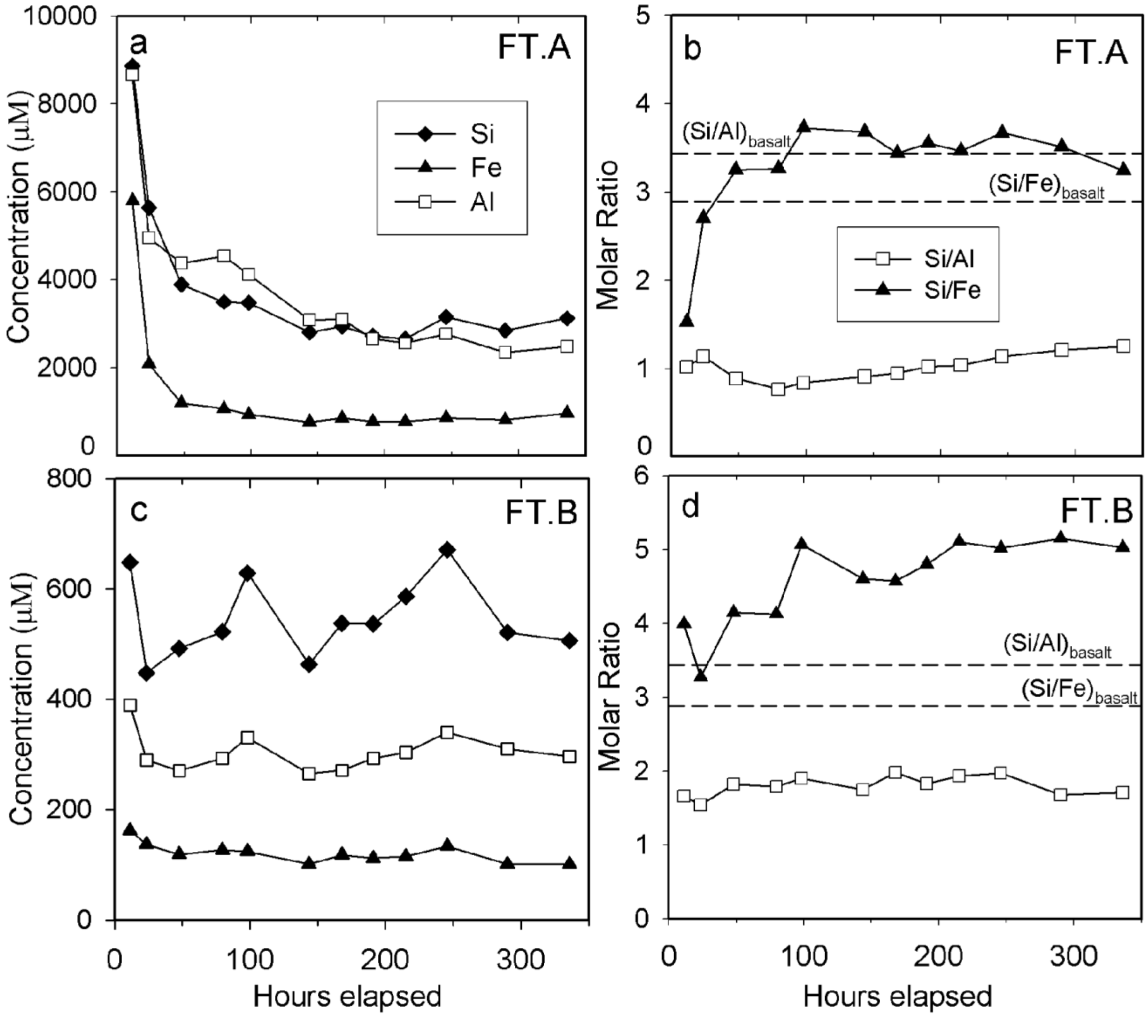

Figure 3. Elemental concentrations and molar ratios of effluent samples from experiments FT-A and FT-B as a function of time. a) Concentrations (in µM) of Si, Al, and Fe from Exp. FT-A. b) Molar ratios from Exp. FT-A. The molar ratios of KP-fresh basalt are indicated as dotted horizontal lines. c) Concentrations from Exp. FT-B. Legend from (a) applies. d) Molar ratios from Exp. FT-B. Legend from (b) applies.

dissolution of all elements at the onset of the experiment, followed by an approach to steady-state behavior within the first 50–100 hours of reaction (Figure 3a). This early spike in fluid concentration has been observed in previous studies with similar experimental setups (Hurowitz et al., 2005) and is likely attributable to the fast dissolution of clinging fine particles, trace soluble phases, and reactive broken edges. Dissolution of basalt in these conditions is apparently non-stoichiometric. Throughout the

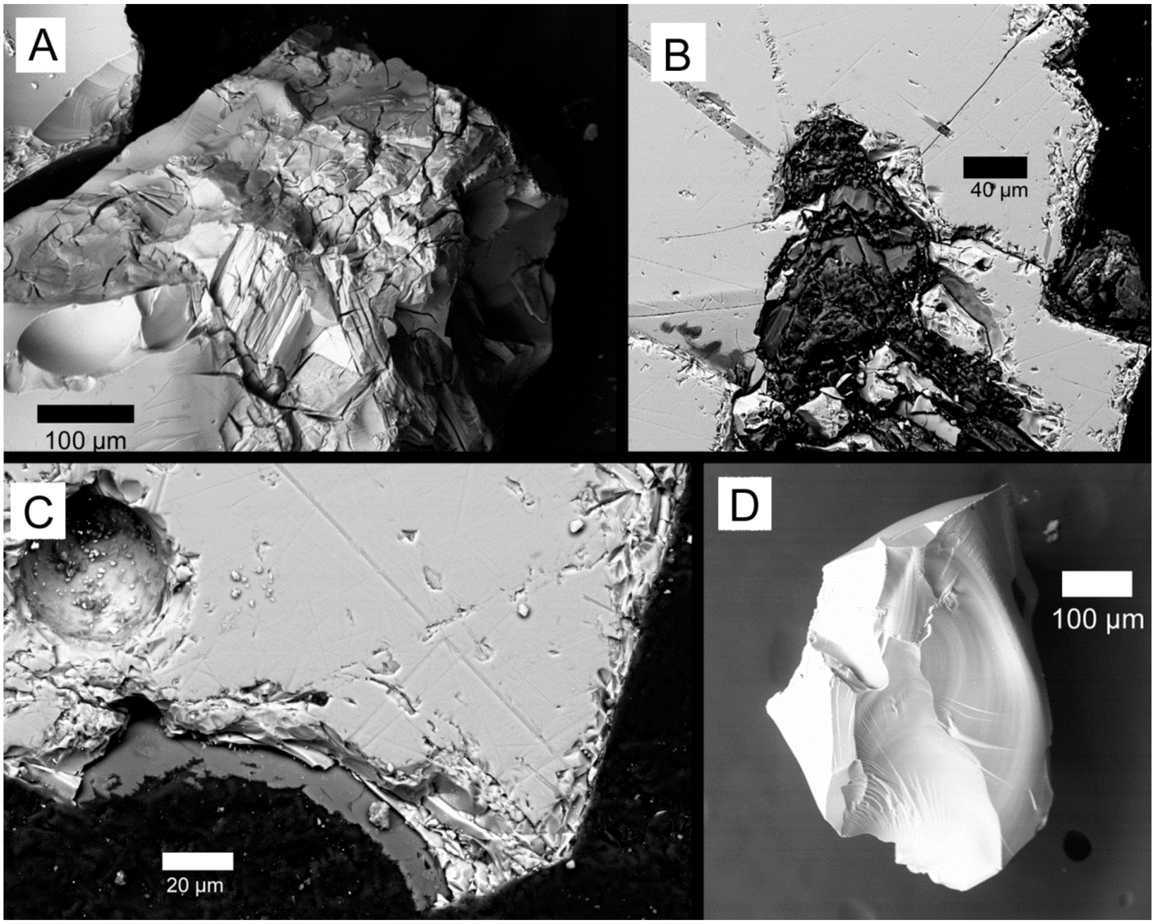

Figure 4. Alteration product morphologies from flow-through experiments. a) Grain from experiment FT-A with desiccation cracks characteristic of an amorphous silica coating. b) Exp. FT-A grain with plagioclase lath replaced by amorphous silica. c) Exp. FT-A grain with 6-10 μm silica coating, observable on one edge only. d) Basalt grain from Exp. FT-B with no visually apparent alteration.

experiment, the molar Si/Al ratio of solutions is relatively constant at ~1.1, compared to $(Si/Al)_{basalt}$ = 3.45 (Figure 3b). This ratio indicates that during both initially accelerated dissolution and later steady-state dissolution, Al is preferentially mobilized relative to Si, implying a Si-rich residual phase. The dissolution of basalt in the experimental chamber was insufficient to buffer the acidic fluid, as indicated by the essentially unmodified pH (Table 6).

Exp. FT.B, the experiment run in pH 3 fluid, displayed relatively constant levels of dissolved metals in effluent samples throughout the experiment (Figure 3c). Dissolved metal concentrations were typically 6-10x lower than in the equivalent samples from Exp FT.A. Enhanced initial dissolution was evident but more subtle than in the pH 1 experiment. As in Exp. FT.A, dissolution is apparently non-stoichiometric, but the molar Si/Al ratio (~1.8) is closer to basalt stoichiometry (Figure 3d).

4.3.1.2. Solid Reactant Mineralogy and Morphology

Residual solid grains from Exp. FT.A were essentially unchanged in color or physical appearance from the starting basaltic glass, but under SEM observation displayed textures and chemical signatures consistent with moderate alteration. Some grains have surface desiccation cracks characteristic of amorphous silica deposits (Figure 4a). Backscatter electron images of polished thick sections of the residual grains revealed irregularly distributed Si-rich alteration layers 3–6 μm thick (Figure 4c). Additionally, large plagioclase laths extending well into the interior of the basalt grains appeared to be entirely replaced by amorphous silica (Figure 4b).

Residual grains from Exp. FT.B appeared unaltered in SEM images (Figure 4d). This lack of distinct alteration phases is consistent with the low measured dissolved solids from that experiment.

4.3.1.3. Solution δ^{30}Si

Effluent samples from Exps. FT.A and FT.B were not analyzed for δ^{30}Si because of difficulty in isolating dissolved Si from these samples. Sulfate is not easily separable from the silicate anion by cation exchange chromatography. The high sulfate contents of

Sample number	Hours elapsed	W/R ratio	Dilution factor	P	Si	Ti	Al	Ca	Fe	K	Mg	Mn	Na
Experiment B-HCl.A													
B-HCl.A.1	1.53	1.88	143.10	188 (25)	3394 (192)	204 (13)	3295 (98)	5743 (170)	2428 (157)	n.d.	2852 (214)	14.4 (3.1)	4843 (464)
B-HCl.A.2	9.93	1.79	123.59	269 (8)	16629 (432)	242 (24)	6329 (69)	7630 (653)	8208 (658)	n.d.	17035 (1336)	82.2 (4.2)	4243 (540)
B-HCl.A.3	22.75	1.71	115.94	163 (25)	27681 (322)	112 (10)	8466 (72)	6591 (600)	14837 (1143)	n.d.	31286 (2048)	153 (13)	3409 (229)
B-HCl.A.4	165.10	1.50	141.26	147 (19)	1103 (70)	3.2 (2.0)	5649 (168)	5157 (617)	9133 (844)	n.d.	23394 (2101)	102 (14)	2138 (465)
B-HCl.A.5	307.98	1.47	132.24	113 (6.6)	1151 (21)	n.d.	6039 (331)	4385 (595)	9809 (986)	n.d.	30554 (3271)	135 (16)	1645 (252)
B-HCl.A.6	693.43	1.54	34.67	21 (8.9)	807 (53)	n.d.	5208 (45)	14134 (486)	6744 (211)	366 (134)	38376 (1756)	188 (7.6)	1808 (61)
Experiment B-HCl.B													
B-HCl.B.1	1.65	9.44	67.77	n.d.	931 (32)	n.d.	908 (45)	n.d.	635 (40)	n.d.	746 (130)	n.d.	12548 (9526)
B-HCl.B.2	10.10	9.28	66.85	n.d.	4584 (235)	87 (46)	2614 (164)	16592 (707)	2021 (78)	n.d.	4258 (372)	n.d.	370 (95)
B-HCl.B.3	22.97	8.95	53.90	25 (21)	9925 (178)	104 (9.7)	4670 (51)	7683 (328)	4262 (184)	n.d.	9167 (470)	44 (3.8)	764 (11)
B-HCl.B.4	165.18	7.81	64.71	n.d.	19168 (1412)	70 (51)	7382 (321)	7250 (457)	9194 (663)	n.d.	22638 (2481)	109 (24)	1092 (180)
B-HCl.B.5	308.10	7.48	65.47	31.6 (2.8)	19878 (1035)	55 (6.9)	7845 (112)	6913 (158)	10059 (218)	n.d.	23941 (2216)	111 (3.4)	1172 (279)
B-HCl.B.6	693.92	7.57	7.39	27.9 (1.6)	20062 (1162)	96 (4.7)	7630 (99)	4823 (133)	9523 (249)	n.d.	20917 (829)	129 (4.2)	1567 (27)

Table 7. ICP-OES chemical analyses of fluid samples from batch HCl experiments.

Sample number	Hours elapsed	W/R ratio	Dilution factor	P	Si	Ti	Al	Ca	Fe	K	Mg	Mn	Na
Experiment B-HCl.C													
B-HCl.C.1	1.78	97.61	22.36	n.d.	357 (318)	n.d.	100 (13)	1190 (71)	70 (43)	n.d.	93 (89)	n.d.	n.d.
B-HCl.C.2	10.20	96.69	23.01	13.7 (6.2)	455 (16)	2.7 (1.5)	343 (5.6)	733 (28)	323 (16)	n.d.	359 (15)	21 (0.9)	n.d.
B-HCl.C.3	23.17	98.69	21.61	12.2 (5.4)	901 (10)	7.8 (3.2)	652 (4.4)	445 (62)	899 (83)	n.d.	660 (69)	105 (10.5)	n.d.
B-HCl.C.4	165.40	96.70	23.02	20.4 (2.4)	3330 (322)	55 (2.1)	2317 (9.6)	1157 (80)	1546 (62)	n.d.	1756 (28)	115 (7.3)	398 (65)
B-HCl.C.5	308.18	96.56	21.21	22.4 (1.7)	3869 (27)	91 (4.4)	2950 (43)	1343 (95)	1749 (108)	n.d.	1923 (121)	118 (8.0)	586 (49)
B-HCl.C.6	694.03	96.46	6.76	24.2 (2.0)	4657 (27)	162 (6.1)	3810 (13)	1979 (77)	2142 (90)	137 (8)	2189 (158)	126 (5.2)	903 (62)

Table 7. (continued)

these solutions were expected to produce a significant matrix effect during MC-ICP-MS analysis, so the analyses were not performed.

4.3.2. Batch HCl Experiments

Batch experiments B-HCl.A, B-HCl.B and B-HCl.C were run using 0.1 M HCl at water-rock mass ratios of 2, 10, and 100, respectively. The experimental vessels were weighed periodically throughout the course of the experiment to monitor the W/R ratio. Changes in W/R ratio were observed for all three experiments; these changes were particularly significant, around 25%, for Exps. B-HCl.A and B-HCl.B (Table 7). The changes are attributable to loss of fluid during sample collection and to evaporative loss. In an attempt to keep W/R ratios constant, fluid and solids were extracted in proportions

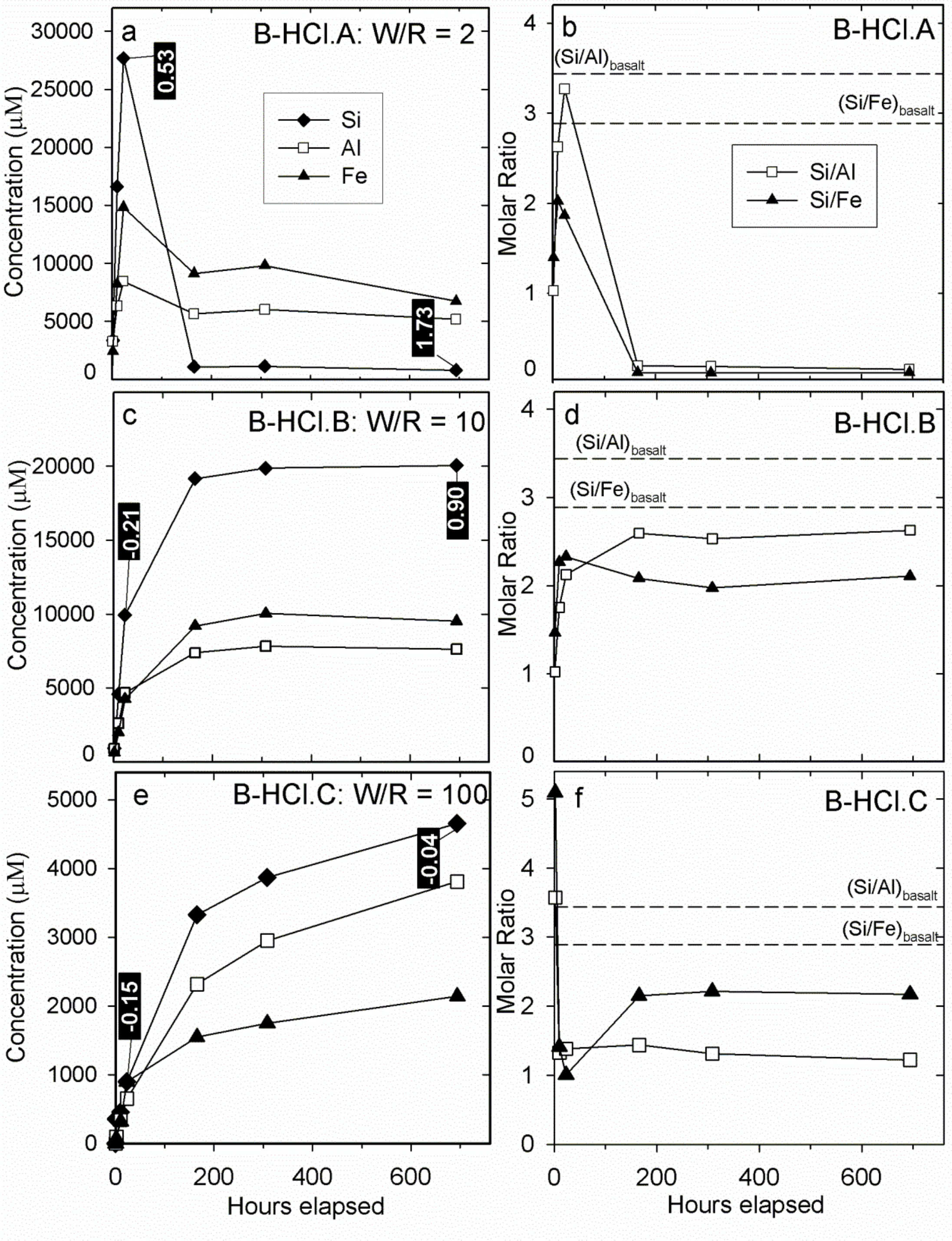

Figure 5. Elemental concentrations, molar ratios, and silicon isotope compositions of effluent samples from the batch HCl experiments (B-HCl.A, B & C) as a function of time. Concentrations are given in µM. Si isotope compositions were determined by MC-ICP-MS; for samples for which δ^{30}Si was measured, δ^{30}Si is indicated by a black box with white text. a) Concentrations from Exp. B-HCl.A. b) Molar ratios from Exp. B-HCl.A. c) Concentrations from Exp. B-HCl.B. Legend as in (a). d) Molar ratios from Exp. B-HCl.B. Legend as in (b). e) Concentrations from Exp. B-HCl.C. Legend as in (a). f) Molar ratios from Exp. B-HCl.C. Legend as in (b).

equal to the overall W/R ratio for each experiment, but additional fluid may have been lost from the system during opening and manipulation of the experimental vessels. Additionally, the experiments lost up to 10 mg between sampling sessions, presumably by evaporative loss. In later sampling sessions, additional starting fluid was added to each experiment after sample collection in an attempt to prevent further W/R ratio change; a corresponding modest increase in W/R ratio is apparent in sample B-HCl.B.6 (Table 7).

4.3.2.1. Fluid Chemistry

ICP-MS analyses of fluid samples from Exp. B-HCl.A indicate a dramatic rise in dissolved solid concentration for most elements within the first 24 hours of reaction, followed by a drop in all element concentrations by the next sampling session at 165 hours (Figure 5a).

Sample B-HCl.A.3 featured the highest Si concentration, 28 mM (~700 ppm); this is well above the concentration for saturation of amorphous silica at 60° C, 4.5 mM (Alexander et al., 1954). Dissolution within the initial 24 hours was apparently non-stoichiometric; compared to the basalt composition, the first three effluent samples are depleted in Si relative to Al, Fe and Mg (Figure 5b). The drop in element concentrations between the third and fourth samples likely resulted from the precipitation of a secondary phase. Si concentration dropped from 28 mM to 1.1 mM, while most other elements also dropped in concentration but less dramatically, suggesting that the precipitate was Si-rich.

Exp. B-HCl.B effluent samples indicate a monotonic increase in the concentration of Si, Ti, Al, Fe, and Mg for the first 165 hours of the experiment and relatively constant concentrations for the remainder of the experiment (Figure 5c). Sample B-HCl.B.1

showed anomalously high concentrations of Na and Ca, but for other effluent samples Na and Ca displayed the pattern indicated by the other elements. Similarly to Exp. B-HCl.A, basalt dissolution was non-stoichiometric. Initial samples were strongly depleted in Si relative to Al and Fe, but Si/Al and Si/Fe rose over the course of the experiment (Figure 5d). Relative mobility, or tendency to be released into solution during weathering of major elements, appears to be Mg > Al ≅ Fe > Si (Table 7). The non-stoichiometric solution chemistry implies that dissolution left a Si-rich residual phase. Unlike Exp. B-HCl.A, Exp. B-HCl.B apparently featured no major precipitation event, instead reaching a steady state. Samples B-HCl.B.4–6 are supersaturated with respect to amorphous silica; therefore, the constant concentrations are likely related to kinetic inhibition of precipitation, rather than the achievement of equilibrium.

Effluent samples from Exp. B-HCl.C, the highest water-rock ratio setup, indicate a monotonic increase in the concentration of all elements over the entire course of the experiment (Figure 5e). Si concentration reached a maximum of 4.7 mM in sample B-HCl.C.6, just over the level of amorphous silica saturation. As in the other batch HCl experiments, dissolution was apparently non-stoichiometric (Figure 5f). Si/Al stabilized at a lower value than that the steady-state value observed in Exp. B-HCl.B. The observation that dissolved solute concentrations did not level out over the course of the experiment suggests that the weathering capacity of the fluid had not yet been exhausted. Although [Si] for B-HCl.C.6 is less than for B-HCl.B.6, the total dissolved Si (Si_{tot} = [Si] · V) for the two experiments are roughly equal ($Si_{tot,B\text{-}HCl.B}$ = 44.3 μmol; $Si_{tot,B\text{-}HCl.C}$ = 46.0 μmol). However, this dissolved flux occurred over a small number of total

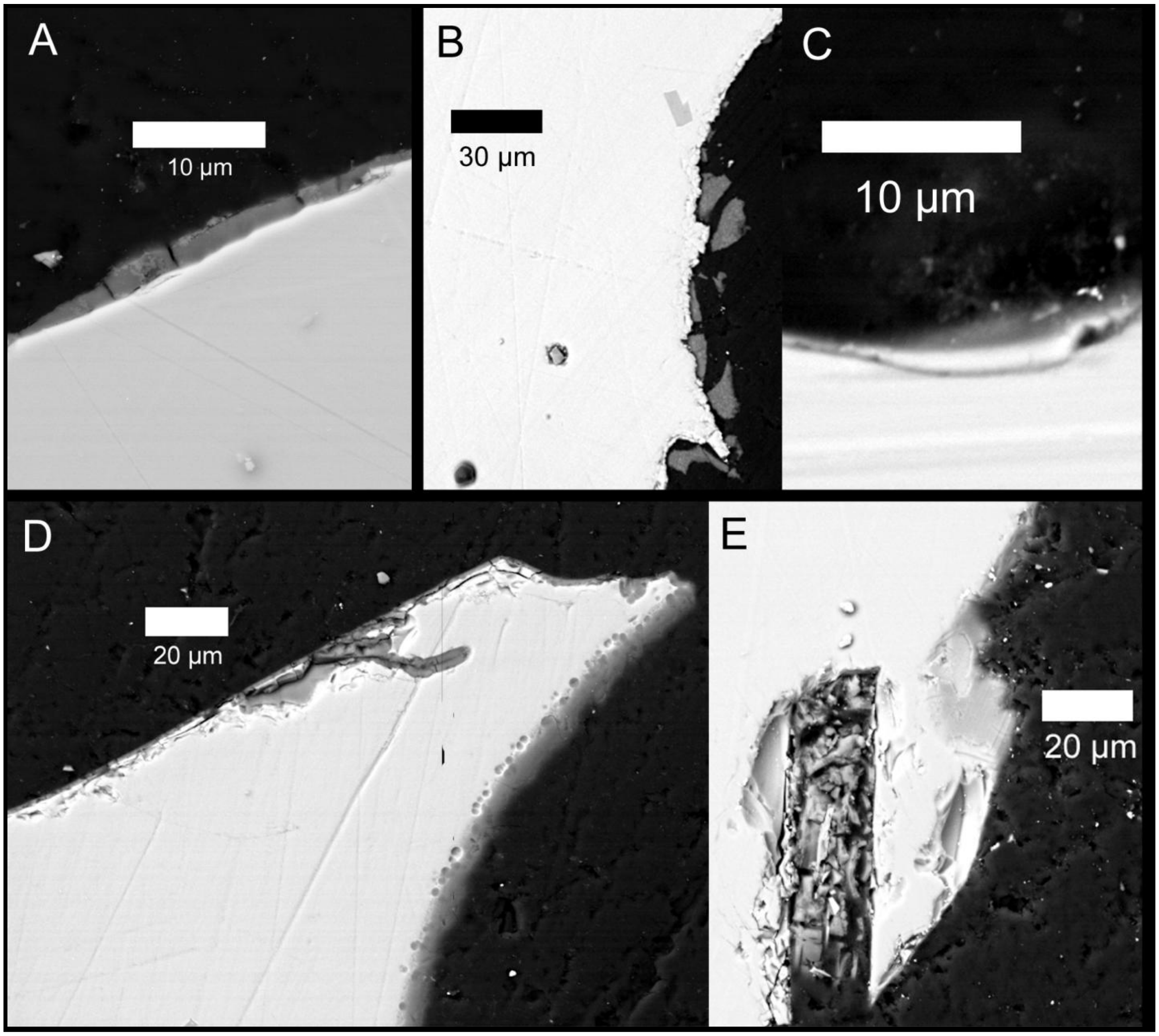

Figure 6. Alteration product morphologies from batch HCl experiments. a) Siliceous coating, ~2 µm thick, on a grain collected along with fluid sample B-HCl.A.4. b) Grain from Experiment B-HCl.A, collected after experiment completion, with a broken layer of Si-rich precipitate 12 µm thick. c) Exp. B-HCl.B grain. Grains from this experiment showed minimal evidence of alteration products; maximum coating thicknesses observed were 0.5–1 µm. d) Grain from Exp. B-HCl.C, featuring a 6 µm thick silica alteration layer (on right) and amorphous silica replacing basalt along an interior crack (on left). e) Replacement of a plagioclase lath by silica in a grain from Exp. B-HCl.C.

grains in Exp. B-HCl.C, suggesting that residual leached zones in Exp. B-HCl.C should be thicker and/or more abundant.

4.3.2.2. Solid Reactant Mineralogy and Morphology

Reacted basalt grains from Experiments B-HCl.A, B-HCl.B and B-HCl.C by optical microscope showed no visual changes in color or grain morphology. Upon opening the Exp. B-HCl.A vial and removing the fluid and basaltic grains, a white precipitate was observed caked on the sides of the vial. This precipitate may have formed in the period between the collection of samples B-HCl.A.3 and B-HCl.A.4, resulting in the drop in dissolved solid content. The precipitate was not retrieved from the vial.

Polished thick sections of basalt grains from each experiment examined by SEM showed evidence of leaching layers and alteration textures. Grains collected concurrently with B-HCl.A.4 were irregularly coated with alteration layers up to 2 µm thick (Figure 6a). Basalt grains collected with B-HCl.A.6 displayed secondary deposits up to 12 µm thick (Figure 6b). Electron probe microanalyses indicate that these alteration materials are ~75% SiO_2 and ~20% FeO* (Table A2). A sharp boundary separated the Si-rich alteration layers from the basaltic glass substrates. The presence a sharp boundary does not distinguish between external deposition of the alteration mineral from solution and a replacement reaction, which can produce boundaries sharp even at the nm-scale (Putnis, 2009).

Reacted basalt samples from Exp. B-HCl.B showed little evidence of alteration layers; in rare cases, 0.5–1 µm thick Si-rich layers were detected (Figure 6c).

Exp. B-HCl.C basalt grains featured alteration layers up to 6 µm thick (Figure 6c). The chemistry of the alteration layers from this experiment was heterogeneous. Some layers displayed the Si- and Fe-rich chemistry described in Exp. B-HCl.A; other layers were nearly pure silica (Table A2). In places, acid alteration of the basalt grains penetrated the interiors of grains along cracks (Figure 6d). Mineral laths were occasionally replaced by silica (Figure 6e), as previously described for Exp. FT-A.

4.3.2.3. Solution $\delta^{30}Si$

Two fluid samples from each experiment were analyzed by MC-ICP-MS for δ^{30}Si (Table 5; Figure 5). Fluids from all three experiments showed trends of ^{30}Si enrichment relative to KP-fresh. Samples from Exp. B-HCl.A were the most ^{30}Si-enriched; sample B-HCl.A.6 had δ^{30}Si = 1.73 ± 0.03‰. Samples B-HCl.B.3 and B-HCl.C.3 both had δ^{30}Si compositions roughly equal to the composition of KP-fresh, indicating minimal isotopic fractionation early in those experiments. By the end of the experimental period, Exp. B-HCl.B and B-HCl.C fluids had evolved to δ^{30}Si = 0.90 ± 0.02‰ and δ^{30}Si = -0.04 ± 0.05‰, respectively.

4.3.3. Batch HF Experiments

4.3.3.1. Fluid Chemistry

Experiments B-HF.A, B-HF.B and B-HF.E were run with a W/R ratio of 10. Sample B-HF.A.1, collected 2 hours after initiation, had [Si] = 147 mM (Figure 7a, Table 8). Si concentrations fluctuated around this initial level for most of the rest of the experiment and rose to 241 mM in the final fluid sample. The Si/Fe ratio remained relatively constant over the course of the experiment, but the Si/Al displayed unique behavior (Figure 7b). Initial fluid samples showed Si/Al < $(Si/Al)_{basalt,}$ but this ratio evolved to 14.8 over the course of the experiment. This is explained by Al concentrations decreasing from 62 mM to 16 mM as [Si] increased, and suggests the retention of Al in a

Sample number	Hours elapsed	Dilution factor	P	Si	Ti	Al	Ca	Fe	K	Mg	Mn	Na
Experiment B-HF.A												
B-HF.A.1	2.17	133.33	0.81 (0.30)	147 (2.5)	6.1 (0.1)	62 (1.0)	43.5 (1.3)	32 (0.6)	n.d.	20 (0.7)	0.4 (0.1)	15 (0.7)
B-HF.A.3	20.67	133.33	0.90 (0.06)	181 (1.5)	8.1 (0.3)	82 (0.7)	52 (1.5)	43 (1.2)	1.5 (0.7)	30 (1.1)	0.5 (0.04)	23 (0.9)
B-HF.A.4	69.17	133.33	0.95 (0.01)	180 (3.8)	8.3 (0.3)	81 (1.5)	45 (2.2)	46 (2.1)	2.9 (0.3)	35 (1.5)	0.6 (0.03)	23 (1.1)
B-HF.A.5	169.50	133.33	0.87 (0.04)	141 (1.2)	7.8 (0.1)	22 (0.2)	36 (0.5)	45 (0.6)	2.1 (0.3)	12 (0.1)	0.6 (0.01)	18 (0.4)
B-HF.A.6	381.25	133.33	1.63 (0.12)	241 (2.7)	16.2 (0.4)	16 (0.3)	74 (2.4)	93 (2.6)	3.9 (0.5)	13 (0.5)	1.2 (0.1)	31 (1.2)
Experiment B-HF.B												
B-HF.B.final	381.25	133.33	1.4 (0.03)	219 (2.0)	15 (0.2)	28 (0.1)	58 (0.5)	80 (0.8)	3.7 (0.7)	10 (0.2)	1.0 (0.01)	29.6 (0.4)
Experiment B-HF.C												
B-HF.C.1	2.17	133.33	0.92 (0.17)	151 (8.6)	7.9 (0.9)	74 (3.9)	44.2 (5.4)	42 (5.2)	1.2 (0.7)	29 (3.3)	0.5 (0.07)	21 (2.5)
B-HF.C.2	5.25	133.33	1.1 (0.1)	128 (0.8)	7.5 (0.1)	58 (0.4)	33 (0.4)	41 (0.6)	1.4 (1.0)	29 (0.6)	0.6 (0.02)	33 (0.9)
B-HF.C.3	20.67	133.33	0.47 (0.07)	97 (0.5)	7.3 (0.3)	7.8 (0.1)	32 (1.6)	45 (2.1)	0.9 (0.3)	7.5 (0.4)	0.54 (0.04)	6.7 (0.4)
B-HF.C.4	69.17	133.33	0.21 (0.04)	89 (1.5)	8.7 (0.2)	2.6 (0.1)	13 (0.4)	59 (1.3)	1.4 (0.4)	8.2 (0.2)	0.8 (0.02)	6.4 (0.1)
B-HF.C.5	169.50	133.33	0.22 (0.05)	85 (0.3)	8.3 (0.3)	2.8 (0.02)	13 (0.5)	58 (2.3)	2.0 (0.4)	7.6 (0.3)	0.88 (0.3)	10 (0.6)
B-HF.C.6	381.25	66.67	0.95 (0.02)	266 (3.6)	20.2 (0.4)	12.6 (0.2)	44 (1.0)	130 (2.7)	3.7 (0.5)	23 (0.4)	1.8 (0.04)	17 (0.2)

Table 8. ICP-OES chemical analyses of fluid samples from batch HF experiments.

Sample number	Hours elapsed	Dilution factor	P	Si	Ti	Al	Ca	Fe	K	Mg	Mn	Na
Experiment B-HF.D												
B-HF.D.final	381.25	24.21	0.07 (0.003)	93 (3.1)	8.0 (0.2)	9.6 (0.2)	22 (0.8)	60 (2.0)	0.8 (0.1)	28 (0.8)	0.9 (0.03)	6.5 (0.1)
Experiment B-HF.E												
B-HF.E.final	168.00	100	0.93 (0.09)	146 (1.0)	7.4 (0.3)	31.8 (0.2)	41.2 (0.9)	41.6 (1.0)	1.8 (0.7)	22.4 (0.4)	0.6 (0.04)	27 (0.5)
Experiment B-HF.F												
B-HF.F.final	168.00	100	0.03 (0.002)	7.5 (0.1)	1.1 (0.06)	4.4 (0.05)	0.4 (0.01)	6.4 (0.3)	0.24 (0.06)	0.25 (0.002)	0.1 (0.006)	3.9 (0.2)

Table 8. (continued)

secondary phase. Si/Mg ratios were also higher than basalt stoichiometry for the duration of the experiment. These fluid compositions suggest the following relative element mobility: Si ≅ Fe > Al > Mg. This observed element mobility, nearly reversed from that observed in Exp. B-HCl.A through C and described in Section 4.3.3.1, is likely facilitated by variable solubility of metal fluoride complexes and the precipitation of fluoride minerals. Experiments B-HF.B and B-HF.E were identical to Exp. B-HF.A except that in those experiments the vials were kept closed and no samples were collected until completion of the experiment (16 days and 7 days, respectively); the composition of final collected fluid samples from Exps. B-HF.B and B-HF.E were similar to samples collected close to the same time from Exp. B-HF.A.

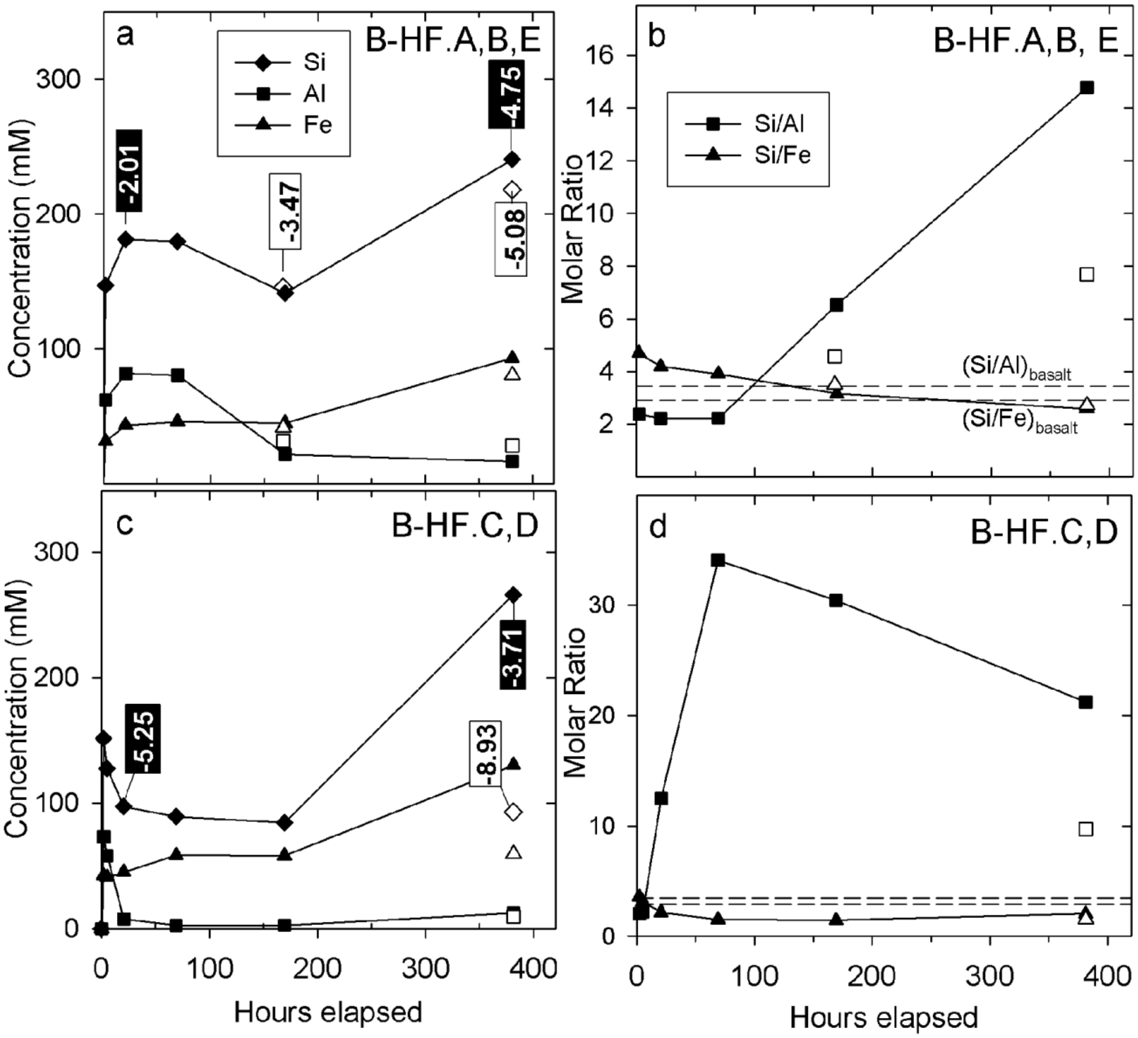

Figure 7. Elemental concentrations, molar ratios, and silicon isotope compositions of effluent samples from the batch HF experiments. Experiments B-HF.A and B-HF.C were opened periodically for fluid sample collection; data from those experiments are indicated by filled symbols. Experiments B-HF.B, B-HF.D, and B-HF.E were kept closed for the duration of the experiment (382 hours for B-HF.B and B-HF.D, and 168 hours for B-HF.E), after which fluids were collected; data for those experiments are indicated by open symbols. Silicon isotope compositions are given for open-sampled experiments by black boxes with white text, and for closed experiments by white boxes with black text. a) Concentrations for batch HF experiments with W/R ratio = 10. Exp. B-HF.A is given by closed symbols; Exp. B-HF.B (382 hours) and B-HF.E (168 hours) are given by open symbols. b) Molar ratios of W/R = 10 experiments. c) Concentrations for batch HF experiments with W/R ratio = 3. Exp. B-HF.C is given by closed symbols; Exp. B-HF.D is given by open symbols. Legend as in (a). d) Molar ratios of W/R = 3 experiments. Legend as in (b).

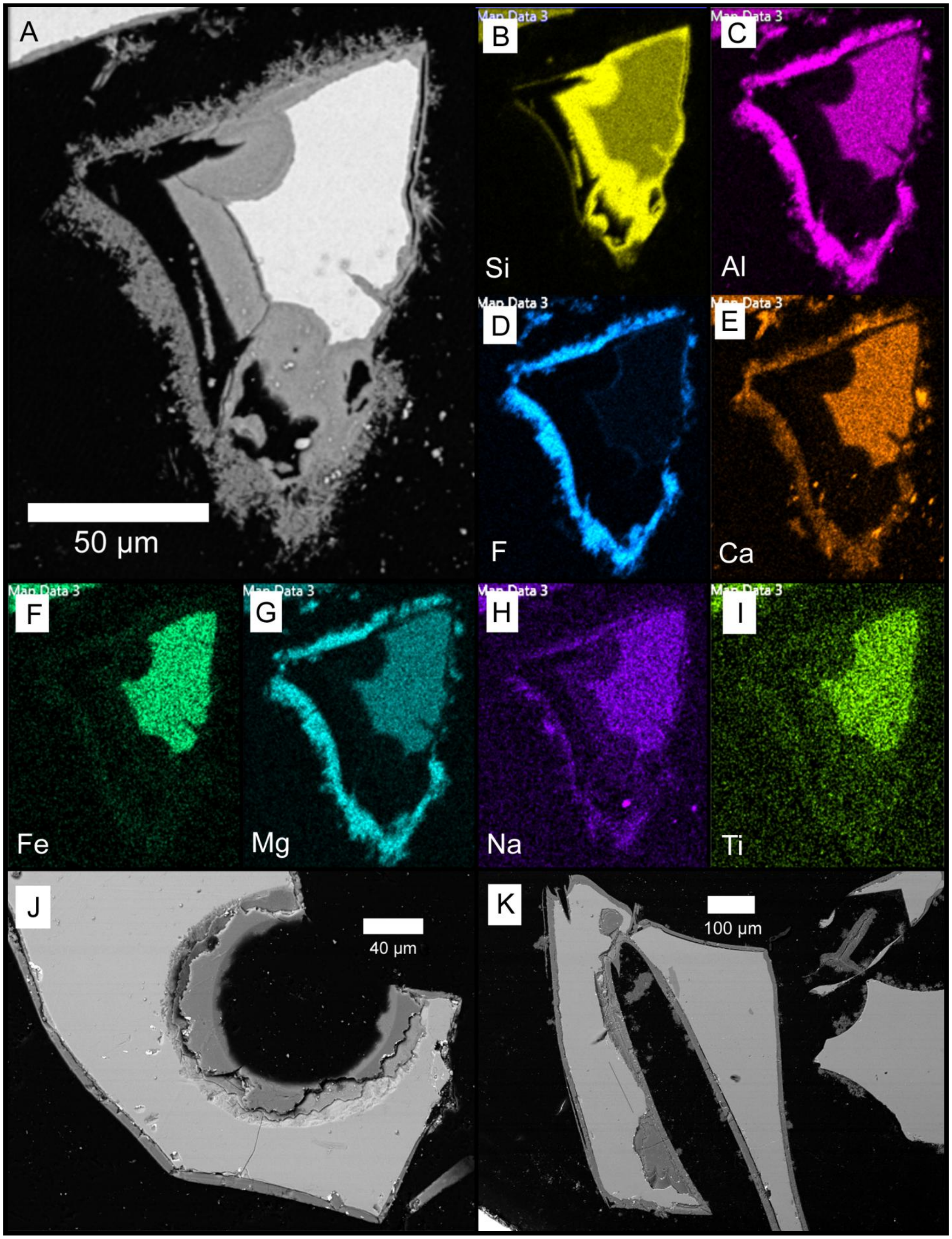

Figure 8. Alteration product morphologies from batch HF experiments. a) Grain from Exp. B-HF.A, featuring Si-rich leached layers up to 30 µm thick and acicular fluoride crystals. b-i) EDS maps of the grain from (a), illustrating that the fluoride deposit contains Ca, Al, Mg, Na, and Fe, but not Si. j) Grains from Exp. B-HF.B, with Si-rich alteration layers up to 100 µm thick. k) Grain from Exp. B-HF.C with 5 µm and 30 µm Si-rich alteration layers.

Exps. B-HF.C and B-HF.D were run with a lower W/R ratio of 3. Dissolved concentrations in samples from Exp. B-HF.C showed similar trends to those from Exp. B-HF.A. High dissolved concentrations of many elements were detected in the first sample, B-HF.C.1. [Si] dropped to ~100 mM in samples B-HF.C.2 through B-HF.C.4, then rose to 260 mM in the final fluid sample (Figure 7c). As in Exp. B-HF.A, Si/Fe ratios remained relatively constant throughout the experiment, but Si/Al and Si/Mg evolved to well above basalt stoichiometric levels (Fig 7d). These compositions imply a relative element mobility of Si ≅ Fe > Mg > Al. Exp. B-HF.D was identical to Exp. B-HF.C except that no samples were collected until the completion of the experiment. ICP-MS analysis of sample B-HF.D.final indicated a considerably lower Si concentration compared to B-HF.C.6 (93 mM instead of 266 mM). Al and Mg concentrations in sample B-HF.D.final were roughly the same, producing lower Si/Al and Si/Mg ratios than in the open-system experiment. These ratios suggest that secondary minerals in the Exp. B-HF.D system are more Si-rich, but are still depleted in Si relative to the basalt glass.

Exp. B-HF.F was run with identical conditions to Exp. B-HF.E (closed-vial, 7 days, W/R ratio = 10), but with 0.1 M HF instead of 1 M HF. All measured dissolved elemental concentrations were lower than any of the 1 M HF experiments. The Si concentration from sample B-HF.F.final was 8.2 mM. Unlike fluid samples from the other HF experiments, the Si/Fe and Si/Al ratios of the fluid sample from B-HF.F were lower than basalt stoichiometric ratios. The enhanced Si mobility observed in Exps. B-HF.A through D must depend on high concentrations of HF for effective Si complexation.

4.3.3.2. Solid Reactant Mineralogy and Morphology

Residual solids from all B-HF experiments were mixtures of dark basalt grains and fine white precipitated material. SEM-EDS analysis of polished mounts of the solid products of these experiments revealed extensive alteration, leaching layers, and crystalline precipitates. Exp. B-HF.A basalt grains were bounded by alteration layers, composed of nearly pure silica, up to 30 μm thick (Figure 8a; Table A2). Additionally, acicular crystals up to 10 μm long were observed to have grown on many substrate surfaces. EDS elemental maps indicate that these crystals are Mg-, Al- and Ca- bearing fluorides (Figure 8b-i). The fluoride domains contain no more than 10 wt% SiO_2 (Figure 8b; Table A2). Solid products from Exp. B-HF.B displayed similar textures; in cases, Si-rich leached layers were up to 100 μm thick (Figure 8j).

Alteration textures for Exps. B-HF.C and B-HF.D were similar to those from Exps. B-HF.A and B-HF.B. Acicular fluoride grains were observed, but not as commonly as in Exp. B-HF.A-B. Silica-rich alteration layers were typically 5–10 μm thick, but in some cases 30-μm-thick layers were observed (Figure 8k).

4.3.3.3. Solution δ^{30}Si

Two fluid samples from each Exps. B-HF.A and B-HF.C, and one fluid sample from each of Exps. B-HF.B, B-HF.D, B-HF.E, and B-HF.F, were analyzed by MC-ICP-MS for δ^{30}Si (Table 5; Figure 7). In contrast to the batch HCl experiments, all fluid samples from the B-HF experiments analyzed for δ^{30}Si showed ^{28}Si-enrichment. Fluids in Exp. B-HF.A decreased in δ^{30}Si over the course of the experiment and eventually achieved δ^{30}Si values of -4.75 ±0.05‰ (Figure 7a). Exp. B-HF.B, which featured identical conditions to Exp. B-HF.A except that the vial remained closed throughout the experiment, evolved to a similar δ^{30}Si of -5.08 ± 0.22‰. Exp. B-HF.E, another closed-vial experiment run for 7 days instead of 16, evolved to $\delta^{30}Si = -3.47 \pm 0.12$‰ (Figure 7a).

Exp. B-HF.C displayed an irregular trend in silicon isotope evolution, first achieving a strongly ^{28}Si-enriched composition before becoming more ^{30}Si-enriched by the end of the experiment. Sample B-HF.C.3 had $\delta^{30}Si = -5.25 \pm 0.05$‰, and sample B-HF.C.6 had $\delta^{30}Si = -3.71 \pm 0.02$‰. Unlike Exps. B-HF.A and B-HF.B, which had closely matching ending δ^{30}Si compositions, Exps. B-HF.C and B-HF.D differed significantly in their ending δ^{30}Si compositions. Sample B-HF.D.6 had $\delta^{30}Si = -8.93 \pm 0.07$‰, the most ^{28}Si-enriched composition measured in this study and a composition that is more ^{28}Si-enriched than the range of previously reported natural terrestrial δ^{30}Si variation.

The final collected fluid from Exp. B-HF.F, the experiment run in 0.1 M HF, had $\delta^{30}Si = -1.97 \pm 0.14$‰. This composition is the least ^{28}Si-enriched of the fluid samples from HF dissolution experiments.

5. Discussion

5.1. Basalt δ^{30}Si Measurements

Measured values of δ^{30}Si composition of the Pu'u O'o-derived basalts KP-fresh, PU-009 and PU-010 are somewhat more ^{30}Si-enriched than those previously reported for basalts. Savage et al. (2010) measured a variety of basalts, including USGS geostandards (BHVO-1, BHVO-2, and BCR-1), Atlantic and Pacific mid-ocean ridge basalts, and ocean island basalts (Marianas, South Sandwich). Measurements of δ^{30}Si for all of these basalts were narrowly clustered between -0.32 and -0.22‰. In contrast, our measurements of δ^{30}Si for Pu'u O'o basalts fell between -0.24‰ and -0.10‰. This difference of ~0.1–0.2‰ may represent a matrix effect produced by incomplete purification of solutions during ion exchange chromatography. Alternately, individual igneous systems may have more primary variability in silicon isotope composition than previously suggested. Silicon isotope heterogeneity among basalts may be caused by varying amounts of phenocryst crystallization and fractionation (Savage et al., 2011) or variable magmatic gas content.

In contrast to the Pu'u O'o lavas, Ka'u Desert basalt sample KD-005 is ^{30}Si-depleted (δ^{30}Si = -0.84‰) compared to previously reported basalt compositions. This basalt sample, erupted in 1973, is older than the Pu'u O'o lavas, and has undergone weathering, at least at its surface. Perhaps the ^{30}Si-depleted composition indicates that weathering has affected the interior of the basalt as well. In contrast to weathering trends described for the silica coatings below, which deviate from previously described silicon isotope fractionations, this putative weathering trend is consistent with that previously described for basalt weathering (Ziegler et al., 2005; Georg et al., 2007).

5.2. Experimental δ^{30}Si Measurements

5.2.1. HCl Batch Experiments

To interpret the silicon isotope fractionations measured in Exp. B-HCl.A through C, we employ a simple model for silicon isotope fractionation in a batch dissolution experiment. The model involves two steps: dissolution of an aliquot of basalt (with no associated fractionation), followed by precipitation of a fraction of dissolved Si as a secondary phase (with an associated fractionation factor α). For each experiment, we assess whether bulk chemical and δ^{30}Si measurements are consistent with such a model.

In the model, initial dissolution of basalt (with composition $\delta^{30}Si_{bas}$) produces no fractionation, such that the bulk reservoir of mobilized silicon has $\delta^{30}Si_{tot} = \delta^{30}Si_{bas}$. Then, a fraction of the dissolved Si (f_{precip}) precipitates out of solution. The isotopic composition of the precipitate follows the following mass balance:

$$f_{precip}\ \delta^{30}Si_{precip} + (1 - f_{precip}) \cdot \delta^{30}Si_{fluid} = \delta^{30}Si_{bas} \ (1)$$

The isotopic composition of the precipitate can be calculated using one of two endmember models: a Rayleigh fractionation, in which solids are isolated from the remaining solution as they precipitate:

$$R_{precip} = \alpha \cdot R_{bas} \cdot (1 - f_{precip})^{\alpha - 1} \ (2)$$

or as a steady-state fractionation, in which precipitates remain in equlibrium with the fluid:

$$R_{precip} = f_{precip} \cdot R_{bas} + (1 - f_{precip}) \cdot \alpha \cdot R_{bas} \ (3)$$

We use 1000 ln α = -1.2‰, from Geilert et al. (2011), which is roughly the median value of the range of fractionation factors determined by previous researchers (Table 1). Using the above equations, we determine ranges of values of f_{precip} and $\delta^{30}Si_{precip}$ that are consistent with our measurements of $\delta^{30}Si_{bas}$ and $\delta^{30}Si_{fluid}$. If we choose a value of f_{precip}, the total mass of Si in secondary precipitate can be calculated:

$$m_{precip} = (28.0855\ g/mol) \cdot V \cdot [Si] \cdot f_{precip} / (1 - f_{precip}) \ (4)$$

where V is the volume of fluid in the experiment. In many experiments, a large proportion of the secondary precipitate occurred as coatings or leaching layers on the surface of the basalt grains. By approximating the basalt grains as spheres with d = 500 μm and assuming values for the coating density (2.1 g/cm^3) and silica content of the precipitates (91 wt% SiO_2), the total m_{precip} can be converted to an effective average thickness of silica coating. Thus, the calculated allowable ranges of f_{precip} can be compared to measured coating thicknesses as estimated from SEM imagery to determine the validity of this model. Below, we apply this model to δ^{30}Si results from each of the three HCl batch experiments.

5.2.1.1. Exp. B-HCl.A

Fluid sample B-HCl.A.3 had 28 mM Si and δ^{30}Si = 0.53‰. Using equations (1)-(3), it can be shown that this Si isotopic composition is inconsistent with Rayleigh fractionation, but is consistent with steady-state fractionation for values of f_{precip} above 0.44 (Figure 9a). The model suggests that at least half of the mobilized Si precipitated from solution as secondary phases. The minimum m_{precip} calculated from equation (4) is 0.68 mg Si, which corresponds to a uniform coating 0.27 μm thick. This minimum coating thickness is consistent with observed alteration morphologies; grains collected partway through Exp. B-HCl.A had coatings up to 2 μm thick (as described in section 4.3.2.2).

Later in the course of Exp. B-HCl.A, the concentration of Si and all other analyzed elements dropped significantly, suggesting a precipitation event. The occurrence of a precipitation event is supported by the observation of late-forming white precipitate caked on the sides of the experimental vessel. Fluid sample B-HCl.A.6 had 0.81 mM Si and δ^{30}Si = 1.73‰. The Si loss compared to sample B-HCl.A.3, in which [Si] = 28 mM, indicates an $f_{precip} = (1 – 0.81/28) = 0.97$. Given this f_{precip}, we use

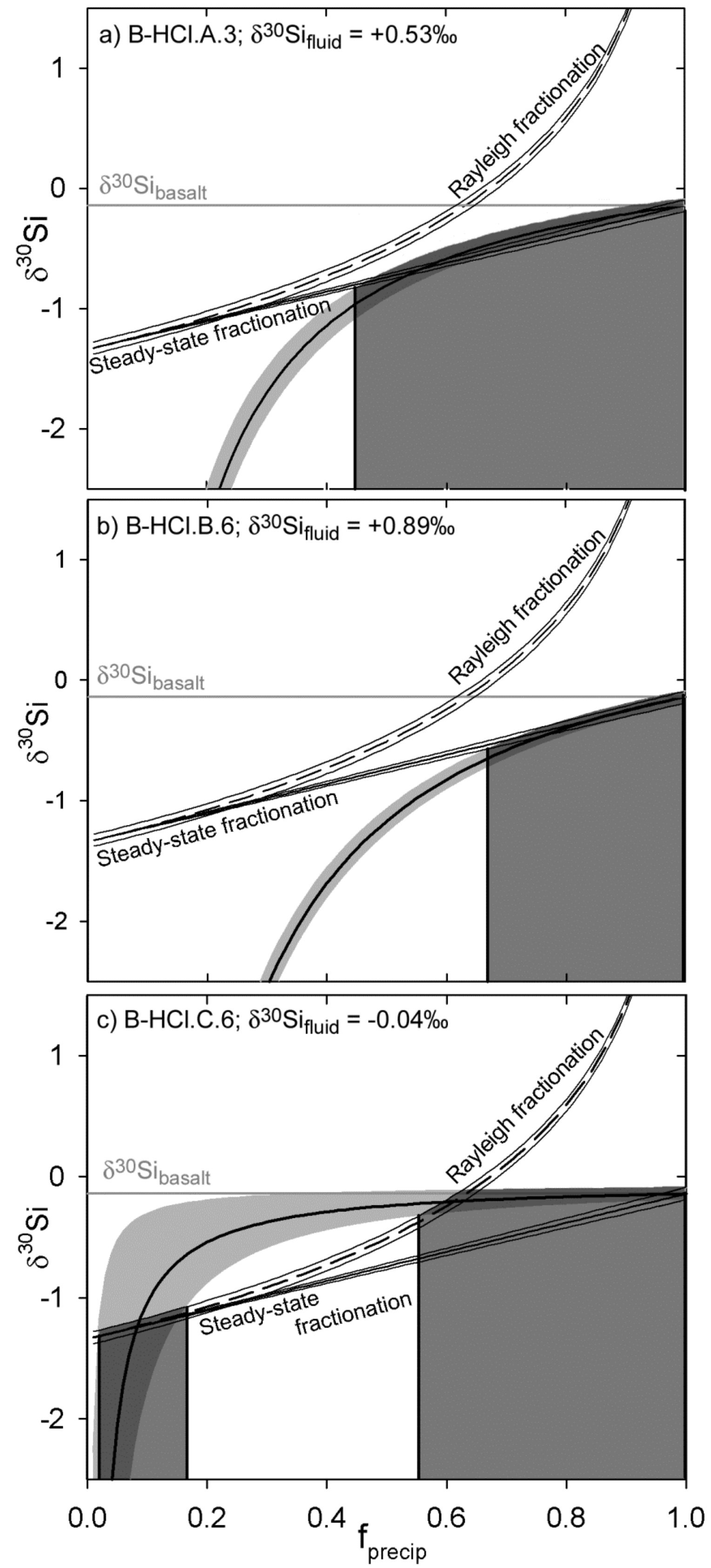

Figure 9. Mass balance models of isotopic fractionation in batch HCl experiments. The horizontal gray line represents the isotopic composition of the basalt experimental starting product. The black curve in each figure represents the modeled δ^{30}Si of the silica precipitate as a function of the proportion of precipitated Si (f_{precip}), as determined by equation (1) in the text. Error bars are notated in light gray, ± 1σ. Dark gray regions correspond to values of f_{precip} in which modeled silica δ^{30}Si are consistent with steady-state and/or Rayleigh fractionation models (see text). a) Sample B-HCl.A.3. b) Sample B-HCl.B.6. c) Sample B-HCl.C.6.

equations (2) and (3) to calculate the predicted δ^{30}Si and compare these predictions to the measured value. From (2), Rayleigh fractionation with f_{precip} = 0.97 would give $\delta^{30}Si_{modeled}$ = 3.54‰. From (3), steady-state fractionation gives $\delta^{30}Si_{modeled}$ = 1.70‰. The measured Si isotopic composition is highly consistent with the steady-state modeled value. In summary, silicon isotope compositions of Exp. B-HCl.A are consistent with steady-state fractionation by precipitation in the simple model described above.

5.2.1.2. Exp. B-HCl.B

Fluid sample B-HCl.B.3 was measured to have [Si] = 10 mM and δ^{30}Si = -0.21‰, slightly lighter than $\delta^{30}\mathrm{Si}_{bas}$. Apparently, this dissolution step caused no significant isotopic fractionation.

Fluid sample B-HCl.B.6 had 20 mM Si and δ^{30}Si = 0.89‰. As in Exp. B-HCl.A, this composition is calculated to be inconsistent with Rayleigh fractionation, but is consistent with steady-state fractionation for values of f_{precip} above 0.69 (Figure 9b). The minimum m_{precip} for the experiment is 2.5 mg Si, which corresponds to a uniform silica coating 2.23 µm thick. This thickness is inconsistent with SEM mounts of grains from Exp. B-HCl.B; generally, Si-rich alteration layers were not common, and if present, the layers were less than 1 µm thick. Therefore, the results of Exp. B-HCl.B are apparently inconsistent with the two-step fractionation model.

5.2.1.3. Exp. B-HCl.C

Fluid sample B-HCl.C.3 also showed no significant fractionation from $\delta^{30}\mathrm{Si}_{bas}$. As in Exp. B-HCl.B, considerable dissolution had already occurred by the collection of sample B-HCl.C.3 but apparently had no effect on the Si isotopic composition of the fluid.

Fluid sample B-HCl.C.6 had 4.6 mM Si and δ^{30}Si = -0.04‰. This isotopic composition is consistent with f_{precip} less than 0.17 and above 0.55 (Figure 9c). Very high values of f_{precip} (> 0.80) are not consistent with the observed extent of alteration as they would require that the majority of Si in the initial basalt was dissolved and mobilized. The two possible ranges for f_{precip}, 0–0.17 and 0.55–0.80, correspond to effective coating thicknesses of < 0.61 μm and 3.6–11.4 μm, respectively. Alteration layers up to 6 μm thick were observed on basalt grains from Exp. B-HCl.C (Figure 6c). Thus, the isotopic fractionation observed in Exp. B-HCl.C is most consistent with f_{precip} = 0.55–0.80. That range represents mixtures between Rayleigh-dominated and steady state-dominated fractionation. The apparent contribution of Rayleigh-like behavior is perhaps the result of the development of thicker alteration layers, leading to the isolation of some precipitated material from solution.

It is worth noting that fluids from Exp. B-HCl.C bear the silicon isotope signature of secondary precipitation even though the Si concentration did not exceed amorphous silica saturation. This suggests that isotope fractionation may occur simply as a result of replacement reactions during incongruent dissolution. Isotopic resetting during *in situ* coupled dissolution-reprecipitation reactions has been observed in other systems, such as the replacement of KCl with KBr using a ^{40}K tracer (Putnis, 2009). Apparently, no kinetically-controlled supersaturation and precipitation event, as observed in Exp. B-HCl.A, is necessary to cause a Si isotope fractionation.

5.2.1.4. Synthesis of Results from Batch HCl Experiments

Rayleigh and steady-state models are consistent with much of the silicon isotope variation in the HCl batch experiments. The calculated fraction of precipitated silica, f_{precip}, appears to decrease with the experimental water-rock ratio. Minimum fractions of precipitated silica for experiments B-HCl.A, B-HCl.B, and B-HCl.C, with W/R ratios of 2, 10, and 100, respectively, are 0.97, 0.69, and 0.55. This trend suggests that lower water-rock ratio environments may experience larger isotopic fractionations, provided that enough fluid is present to transport away fractionated solutions.

There are two primary features of the data that are inconsistent with these models. First, samples B-HCl.B.3 and B-HCl.C.3 both showed δ^{30}Si essentially unchanged from basalt, despite considerable incongruent dissolution. One possible explanation is that the fractionation factor α is concentration-dependent, such that precipitates from fluids with low degrees of supersaturation fractionate Si less strongly than fluids with high degrees of supersaturation. Under this hypothesis, early-collected samples with relatively low Si concentration would not show statistically significant Si isotope fractionation.

A second inconsistency with the precipitation model is that the silicon isotope composition of sample B-HCl.B.6 suggests a larger volume of precipitate than was observed via SEM. One possible explanation is that the SEM images did not reflect the true amount of precipitate that formed in this experiment. The silica coatings may not have been adequately preserved during the polishing process, or some precipitate at the bottom of the vial may not have been collected. Alternately, deviation from the precipitation model may indicate that in addition to precipitated and dissolved silica, some mobilized silicon may back-react with exposed basalt surfaces. Isotopic exchange between dissolved Si and bulk basalt is unlikely to occur without leaving detectable alteration minerals. This putative back-reaction is most likely characterized as adsorption of dissolved silica onto basalt surfaces. The extent of adsorption depends on the reactive sites available on the basaltic glass surface and the dissolved Si concentration; because [Si] rose above supersaturation in Exp. B-HCl.B, adsorption may have been significant. Adsorption of Si on iron oxide surfaces has been shown to produce Si isotope fractionations (Delstanche et al., 2009). If adsorption is a significant factor, then the calculated values of f_{precip} are overestimates.

5.2.2. HF Batch Experiments

In contrast to fluids from the HCl batch experiments, which showed evolution towards ^{30}Si-enriched compositions over the course of a given experiment, all samples from the batch HF experiments produced ^{28}Si-enriched fluids. These results are inconsistent with a Rayleigh model using the literature fractionation factor $1000 \ln \alpha =$ -1.2‰, which would drive solution δ^{30}Si to ^{30}Si-enriched values.

One possible explanation for the ^{28}Si-enriched fluid compositions is that the experiments, despite best efforts, were open-system and leaked Si-bearing vapor. The experimental vials for Exps. B-HF.A through D were hand-tightened only; Exp. B-HF.E and B-HF.F were wrench-tightened. The silicon isotope fractionation factors between gaseous SiF_4 and aqueous silica, or between gaseous SiF_4 and solid silicates, have not been measured experimentally. A calculation of the equilibrium fractionation factor between gaseous SiF_4 and solid SiO_2, based on isotope-substituted IR spectra of SiF_4, is given in Appendix B. The calculation suggests a fractionation factor $1000 \ln \alpha_{SiF4\text{-}qtz} =$

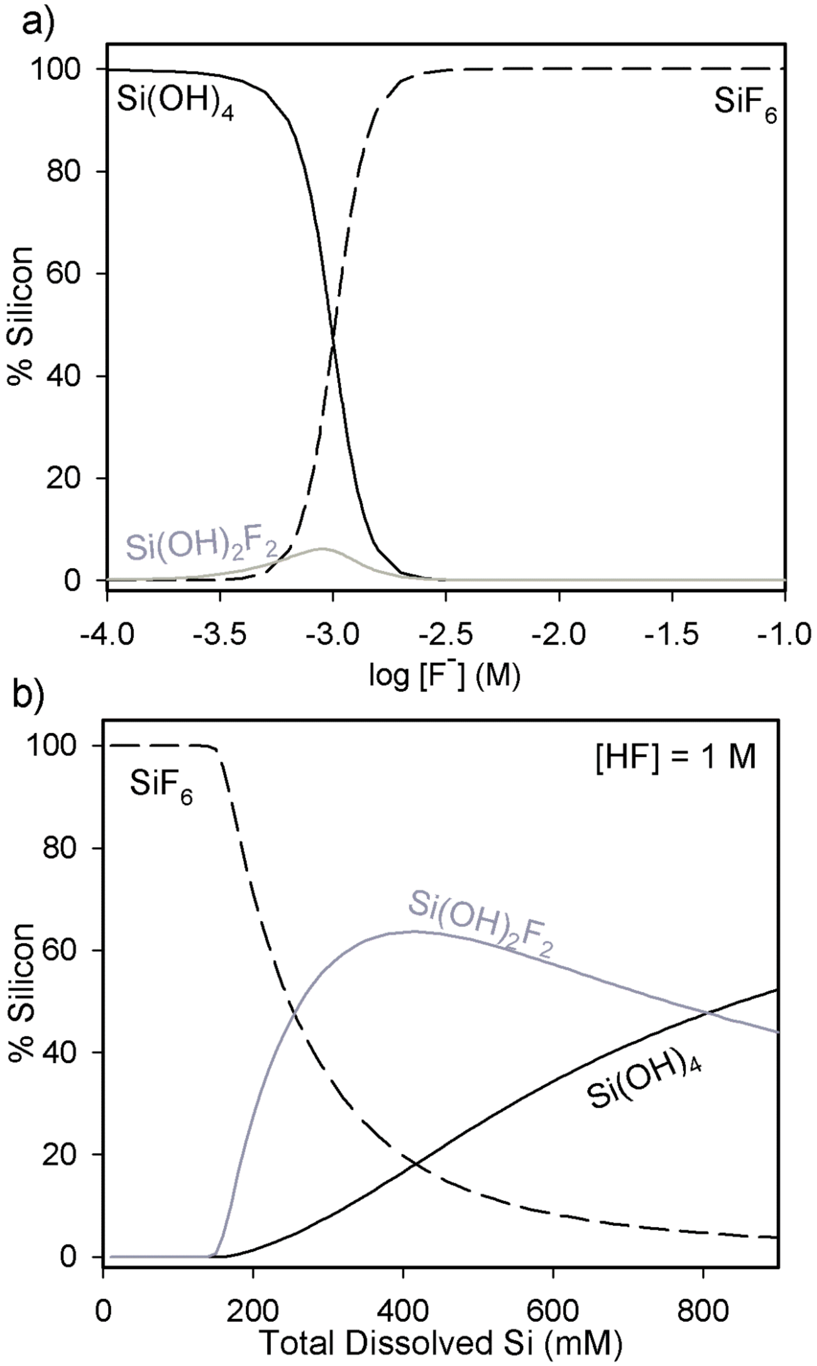

Figure 10. Fluorosilicate speciation models. In both models, dissolved metals other than Si are ignored and speciation is limited to the three species displayed ($Si(OH)_4$, $Si(OH)_2F_2$, and SiF_6^{2-}). a) Silica speciation at low concentrations of Si with varying [F^-]. After Busey et al. (1980). B) Silica speciation as a function of total dissolved Si at fixed [HF] = 1 M. Equilibrium constants from Busey et al. (1980) and Golovnev et al. (2003). The displayed results were numerical solutions calculated in MATLAB.

14.9‰ at 25° C, with ^{30}Si concentrating in the SiF_4 vapor. Thus, escaped SiF_4 gas would drive the residual fluid towards ^{28}Si-enriched compositions. However, open-system behavior cannot explain entirely the negative δ^{30}Si. Exps. B-HF.E and B-HF.F were weighed before and after reaction and lost only 2.5 and 2.9 mg, respectively, but still produced solutions with negative δ^{30}Si. If the vapor leaked from those experiments had Si contents equal to that of the liquids, the fraction of Si lost would be 1.2% and 1.4%, respectively; however, the vapors in equilibrium with dilute H_2SiF_6 solutions are ~10x depleted relative to the solution (Munter et al., 1947), so Si loss fractions would instead be 0.12% and 0.14%. To produce the isotopic compositions of the final fluids ($\delta^{30}Si_{B\text{-}HF.E.final}$ = -3.47‰; $\delta^{30}Si_{B\text{-}HF.F.final}$ = -1.97‰) by Rayleigh fractionation of SiF_4 gas with 1000 ln α = 14.9‰ would require 20% and 12% of dissolved Si to be lost from the system, respectively. The losses of SiF_4 vapor are insufficiently large to explain observed fractionations, so we dismiss the hypothesis that the HF batch experiments are dominated by open-system behavior.

A second possible interpretation is that silicon isotope fractionations occurred between Si-bearing aqueous species in the experiments, and that one set of aqueous species was more likely to be incorporated into solid precipitates than the other. Many members of the family of Si-hydroxyfluoride complexes of the form $SiF_x(OH)_y^{4-x-y}$ are theoretically possible, but the dominant species at high F concentrations are SiF_6^{2-} (hexafluorosilicate) and, to a lesser extent, $Si(OH)_2F_2$ (Busey et al., 1980). At 25° C, the association reaction for hexafluorosilicate,

$$Si(OH)_4 + 4\ H^+ + 6\ F^- \leftrightarrow SiF_6^{2-} + 4\ H_2O \qquad (5)$$

has a measured equilibrium constant of $10^{29.5}$ (Busey et al., 1980; Golovnev et al., 2003). The association reaction for $Si(OH)_2F_2$

$$Si(OH)_4 + 2\ H^+ + 2\ F^- \leftrightarrow Si(OH)_2F_2 + 2\ H_2O \qquad (6)$$

has a calculated equilibrium constant of $10^{11.09}$ (Busey et al., 1980). At low Si concentrations, Si speciation is dominated either by $Si(OH)_4$ or by SiF_6^{2-} over the entire range of HF concentration. The crossover point at which $[Si(OH)_4] = [SiF_6^{2-}]$ depends on pH and $[F^-]$; at pH 3, $[F^-]_{crit}$ = 1 mM (Figure 10a).

In solutions with higher Si concentrations, such that the molar ratio of Si to F is less than 1/6, Si speciation becomes more complex. We can calculate the expected Si speciation given total concentrations of Si and HF, ignoring other dissolved cations. The relevant equilibria are equations (5) and (6), the dissociation of water ($H^+ + OH^- \leftrightarrow H_2O$, $K_w = 10^{-14}$), and the dissociation of HF ($HF + H_2O \leftrightarrow H_3O^+ + OH^-$, $K_d = 10^{-3.46}$). The last equations are for charge balance and mass balance for Si and F:

$$F_{total} = [HF] + [F^-] + 2\ [Si(OH)_2F_2] + 6[SiF_6^{2-}] \qquad (7)$$

$$Si_{total} = [Si(OH)_4] + [Si(OH)_2F_2] + [SiF_6^{2-}] \qquad (8)$$

$$[H^+] – [OH^-] – [F^-] – 2\ [SiF_6^{2-}] = 0 \qquad (9)$$

We calculate Si speciation for F_{total} = 1 M and Si_{total} varying from 0 to 1000 mM. The calculation indicates that at 1 M HF, SiF_6^{2-} is the dominant Si-bearing species up to concentrations of ~250 mM Si, after which $Si(OH)_2F_2$ becomes dominant (Figure 10b). Most of the B-HF experiments had at least one fluid sample at or near this Si concentration, suggesting that the experiments may have achieved conditions in which multiple Si-bearing aqueous species coexisted.

A Si isotope fractionation in the HF experiments opposite in sign to that observed in the HCl experiments could be produced by differences in Si speciation in one of two ways. First, precipitation of a F-bearing silica phase with a different associated α could reverse the sign of the isotopic fractionation. However, SEM-EDS elemental maps of solids from the B-HF experiments indicate that Si is not a significant component in precipitated fluoride minerals (Figure 8b,d), so this mechanism is not valid. Alternately, there could be preferential incorporation of one isotopically fractionated aqueous species into the precipitate over other species. The isotopic fractionations between silicic acid and F-bearing aqueous silica species have not been calculated or measured experimentally, and doing so is beyond the scope of this paper. Interspecies fractionations would have to be large, on the order of several per mil, to produce the observed ^{28}Si-enriched fluid compositions. Regardless, these results imply that Si speciation can have drastic effects on the isotopic signature of precipitation and weathering.

5.3. Understanding ^{30}Si-Enriched Hawaiian Silica Coatings

All of the Hawaiian silica coatings and cements analyzed in this study are ^{30}Si-enriched to varying degrees relative to their basaltic substrates. This is, to our knowledge, the first report of alteration materials with higher δ^{30}Si than their putative source materials. The range of reported fractionation factors 1000 ln $\alpha_{\text{precip-dissolved}}$ is -3.5‰ to -0.4‰ (Table 1), such that for low f_{precip}, secondary precipitates are expected to be ^{28}Si-enriched. Here we consider a number of hypotheses explaining the unusual direction of fractionation observed for these coatings: 1) External clastic input; 2) Extreme Rayleigh fractionation; 3) Vapor transport of silicon; 4) Fractionation impacted by Si speciation;

5) Varying influence of kinetic and equilibrium fractionation factors; and 6) Solution buffering by basalt.

5.3.1. External Clastic Input

Ziegler et al. (2005) report that Hawaiian soils of increasing age incorporate increasing proportions of quartz and mica. These minerals are not found in unaltered Hawaiian igneous rocks and are attributed to input of wind-blown dust from Asia (Kurtz et al., 2001). Additionally, wind-blown basaltic ash is a primary contributor to Hawaiian soils, is deposited on and around the surfaces of modern flows, and has been detected embedded in surficial silica coatings (Minitti et al., 2007; Farr and Adams, 1984). However, external clastic input cannot account for the high δ^{30}Si of the silica coatings. The silicon isotope compositions of Hawaiian soils from Ziegler et al. (2005) with high proportions (> 80%) of Si from windblown dust range from δ^{30}Si = -1.0 to -0.3‰. Basaltic ash would only contribute material of bulk basaltic composition to the coatings, that is δ^{30}Si = -0.3 to -0.1‰. There are no obvious isotopically heavy clastic inputs available in this setting, so we eliminate the possibility of a clastic or aeolian control on δ^{30}Si.

5.3.2. Extreme Rayleigh Fractionation

Here we address the possibility that the elevated δ^{30}Si signatures of Hawaiian silica coatings could form by simple steady-state or Rayleigh fractionation governed by published values of α. We consider the composition of the PU-009 coating, which is the most fractionated of all of the alteration materials observed; for the purpose of these

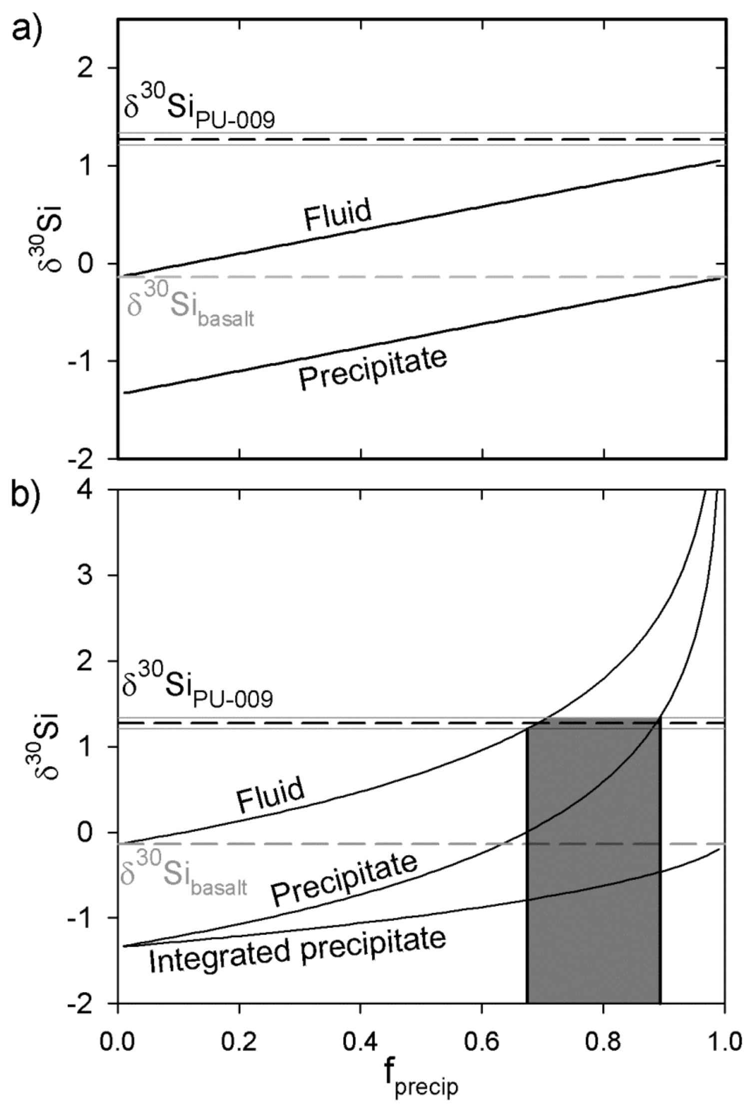

Figure 11. Modeling of PU-009 silica coating δ^{30}Si using fractionation factor from Geilert et al. (2011). a) Steady-state fractionation model. No value of f_{precip} produces fluids or precipitates as ^{30}Si-enriched as the silica coating. b) Rayleigh fractionation model. The gray box corresponds to values of f_{precip} that are consistent with Rayleigh fractionation (see text).

calculations, we use the average of the two duplicate measured values, δ^{30}Si = +1.27‰. The evolution of solutions and precipitates by Rayleigh and steady-state fractionation are given by equations (2) and (3), respectively. Neither fluids nor precipitates can achieve the PU-009 composition by steady-state fractionation, because $\Delta_{coating\text{-}basalt} > \alpha$ (Figure 11a). However, the PU-009 composition can be achieved by precipitation from a Rayleigh-fractionated reservoir (Figure 11b). This case can be defined by two endmember scenarios. In one endmember case, defined by where the Rayleigh solution curve intersects $\delta^{30}Si_{coating}$, a large fraction (f_{precip} = 0.68) of Si precipitates from solution. Then, the remaining solution is transported to the surface, where it evaporates such that all the remaining Si is deposited. In the second endmember case, defined by where the Rayleigh *precipitate* curve intersects $\delta^{30}Si_{coating}$, the majority (f_{precip} = 0.90) of dissolved Si precipitates from solution; then a small fraction of the remaining dissolved reservoir precipitates to form the coatings. Both of these endmember cases require that the initial precipitation event (of f_{precip} = 0.68 or 0.90) occur elsewhere, and that the remaining dissolved reservoir be transported to the site of coating or cement deposition. The scenario in which all Rayleigh-fractionated precipitates cumulate together cannot produce δ^{30}Si compositions as ^{30}Si-enriched as PU-009 (Figure 11b).

Rayleigh fractionation is a mathematically possible explanation for the development of ^{30}Si-enriched coating compositions, but it has two implications for the coating formation mechanism that are difficult to reconcile with morphological observations of the coatings. First, it requires that the coatings be depositional, forming from Si transported from elsewhere rather than forming *in situ*. An explanation invoking a depositional formation mechanism conflicts with observations of residual texture in the coatings, such as regions where the silica layer bridges near-surface vesicles, and surface-selective alteration morphologies (Chemtob et al., 2010; Chemtob, 2012). A second implication of Rayleigh fractionation is that it requires the formation of large deposits of ^{28}Si-enriched precipitates, 2–8x larger in volume than the observed coatings. No such isotopically light silica has been detected; even cements such as S-12-41, formed by groundwater transport of dissolved silica, are ^{30}Si-enriched. The absence of an observable solid reservoir of isotopically light Si suggests that coating formation by extreme Rayleigh fractionation is unlikely.

5.3.3. Vapor transport of silicon

Here we address the possibility that Si in the Hawaiian coatings was transported to sites of deposition by vapor transport. Vapor pressures of SiO at ambient temperatures are vanishingly small (Nuth and Ferguson, 2006), so SiO cannot be a significant contributor of silica to basalt surfaces. The most likely candidate species for vapor transport of silicon is SiF_4 gas. Silica delivered by SiF_4 would likely be ^{30}Si-enriched relative to the basalt substrate (Appendix B). Fluorine has been shown by previous researchers to play a significant role in basaltic surface chemistry. Hydrofluoric acid is a small but significant component of gases emitted from Kilauea. Typical gas compositions for Kilauean eruptions in 1983-1984 were 0.20 mol% HF for the East Rift (Gerlach, 1993) and 0.25 mol% HF for the summit (Greenland et al., 1985); in earlier eruptions, HF concentrations of up to 2.1 mol% have been detected (Murata et al., 1964). X-ray photoelectron spectroscopic (XPS) studies of fresh Hawaiian basalt surfaces show fluorine enrichment and Si depletion, attributed to the continued degassing of F-bearing gas from cooling basalt flows and volatilization of SiF_4 at the surface (White and Hochella, 1992). At Lewotolo Volcano, Eastern Sunda Arc, Indonesia, calc-alkaline volcanic rocks ranging from basalts to trachyandesites sometimes display vesicles partially filled with cristobalite, attributed to vapor-phase crystallization from SiF_4-bearing gas (de Hoog et al., 2005). At Klyuchevskoy Volcano, Kamchatka, Russia, altered rocks near fumaroles were strongly depleted in silica and enriched in fluorine by gaseous metasomatism (Naboko, 1957).

Vapor deposition of silica coatings could occur by one of two mechanisms. In one mechanism, SiF_4-bearing gases are transported to fresh basalt surfaces and conditions change such that the equilibrium SiF_4/HF ratios drop, allowing silica to sublimate. A drop in the SiF_4/HF ratio can be produced by: 1) an increase in system temperature, 2) a decrease in system pressure, or 3) a decrease in the partial pressure of HF (de Hoog et al., 2005). Sublimation could account for silica precipitation immediately next to eruptive vents, where the vapor pressure drops and HF is diluted with atmospheric gases; however, it could not account for coatings on distal flows, where vapor pressure is already close to 1 atm. An alternate mechanism to sublimation is reaction of gaseous SiF_4 with liquid water on the surface of flows, producing fluorosilicic acid, followed by evaporation. In the H_2O-rich end of the HF-H_2O-H_2SiF_6 system, liquids are highly enriched in H_2SiF_6 relative to equilibrating vapors (Munter et al., 1947); therefore, any liquid water on the surface may scour the vapor of most of its silica content.

The vapor deposition mechanism for producing ^{30}Si-enriched silica coatings has several weaknesses. First, this mechanism implies that most of the silica deposition should occur shortly after eruption, when volcanic gas emissions are most voluminous. Observation of one-year old lavas along Kilauea’s East Rift Zone shows development of alteration layers roughly 4 μm thick, but no 10–50 μm coatings as seen on older flows (Chemtob, 2012). It appears that silica coating development continues for years after flow emplacement. White and Hochella (1992) observed fluorine and silicon contents by XPS on successive samples from distal ends of the 1987 Kilauea flow; they observed an anti-correlation of Si and F and the disappearance of the F signal within 270 days. Fluorine was not a detectable surface species after 270 days, and so probably did not contribute to Si mobility on distal flow surface after that period. Additionally, Hawaiian volcanic vapors have far higher concentrations of SO_2 than HF. Solutions interacting with SiF_4-

bearing vapors would inevitably dissolve SO_2 as well as SiF_4, producing acidic solutions that may interact and leach nearby basalt. Si mobilized by acidic leaching of basalt would likely drown out the isotopic signature of vapor-tranported Si. Therefore, a vapor deposition mechanism for the coatings is unlikely.

5.3.4. Fractionation Impacted by Aqueous Si Speciation

Here we assess the possibility that the δ^{30}Si fractionation factor is impacted by the speciation of Si in solution. In most experimental and natural aqueous systems explored by other researchers, concentrations of dissolved species other than Si are dilute. In dilute systems at low or neutral pH, silicic acid is speciated entirely as $Si(OH)_4$. However, because of the influence of acidic volcanic gases and the low water/rock ratio, fluids accumulating on the surface of Hawaiian lava flows may develop unusually high ionic strength. We consider potential alternate species of Si that may exist in altering fluids at Kilauea and assess their potential contribution to silicon isotope fractionation.

Organic and inorganic ligands have been shown to affect silica solubility and dissolution rate (Chen and Marshall, 1982; Öhman et al., 1991; Azaroual et al., 1997; Bai et al., 2009). Increasing dissolved concentrations of NaCl, $MgCl_2$, and $MgSO_4$ were shown to decrease silica solubility at all temperatures; however, increasing dissolved concentrations of Na_2SO_4 decreased silica solubility at temperatures below 150° C but increased silica solubility at higher temperature (Chen and Marshall, 1982). These authors suggested the existence of a weakly hydrogen-bonded sulfate-silicic acid aqueous complex to explain this enhanced solubility (Marshall and Chen, 1982). The association reaction for this complex,

$$Si(OH)_4 + SO_4^{2-} \leftrightarrow Si(OH)_4 \cdot SO_4^{2-} \qquad (10)$$

has a calculated equilibrium constant, K_{assoc}, of $10^{-0.42}$ M^{-1} (Marshall and Chen, 1982). Such a complex has never been detected spectroscopically, but its existence has been postulated by multiple authors (Öhman et al., 1991). If it exists, the silica-sulfate complex may be an important Si-bearing species in SO_2-rich Kilauean fluids. Typical groundwater samples from 1999-2001 from the NSF well adjacent to Kilauea Caldera had [S] = 4000 ppm as sulfate; fumarolic condensates have been detected with as much as 21200 ppm S as sulfate (Hurwitz et al., 2001). If all Si is speciated either as $Si(OH)_4$ or as the silica-sulfate complex, then the proportion of Si in the complex is given by

$$Si_{complex}/Si_T = K_{assoc}[SO_4^{2-}] / (1 + K_{assoc}[SO_4^{2-}]). \qquad (11)$$

Thus, groundwater samples may have as much as 4.5%, and fumarolic condensates as much as 20.1% of total Si in the proposed silica-sulfate complex.

Another potentially important silica speciation in Hawaiian solutions is Si-fluoride complexes, as discussed in Section 5.2.2. As stated in Section 5.3.3., Hawaiian volcanic gases have HF concentrations of ~0.25 mol%. The speciation of Si in solutions influenced by volcanic vapors depends on the degree of dilution of those vapors and the degree of Si saturation in leachate solutions; under certain circumstances, these solutions may include SiF_6^{2-} and $Si(OH)_2F_2$ in significant proportions.

To date, there has been insufficient experimental and theoretical work on the effects of silica speciation on $\delta^{30}Si$ fractionation to assess the potential impact of sulfate or fluoride complexes on the Kilauea silica coatings. However, there are several scenarios in which speciation could affect isotopic fractionation. First, as discussed in Section 5.2.2., if a non-unity fractionation factor exists between two Si-bearing aqueous species coexisting in subequal proportions, then if one aqueous species is more likely to be incorporated into solid precipitates than the other, an isotopic fractionation could be observed. Any altering sulfate or fluoride in the solid precipitates could be removed from the coatings during later wetting events. Second, if Si speciation is dominated by a single species that is not silicic acid (i.e., SiF_6^{2-}), a different kinetic fractionation factor might apply if the diffusive properties of that species are markedly different from silicic acid. Lastly, increased ionic strength has been shown to increase the rate and extent of silica polymerization (Icopini et al., 2005), which may in turn affect Si isotope fractionation. The effect of silica polymerization on Si isotope fractionation remains unstudied. Futher experimental work is required to quantify the potential effect of Si speciation on the δ^{30}Si of Hawaiian silica coatings.

5.3.5. Varying Influence of Kinetic and Equilibrium Fractionation Factors

The Si isotope fractionations observed in most natural systems, many of which are characterized by solid precipitates and/or adsorbates being enriched in ^{28}Si relative to the residual pool, are thought to be controlled by kinetic processes (Ding et al., 2004; De La Rocha et al., 2000). Equilibrium fractionation could be characterized by a different fractionation factor. β factors have not yet been published for aqueous silica species, so equilibrium α for $Si(OH)_{4(aq)}$ - $SiO_{2\ (s)}$ cannot be calculated directly. However, in analogy with the oxygen isotope system, an equilibrium fractionation factor is likely to favor heavy, rather than light, isotopes in the precipitate. A recent study in which silica was repeatedly precipitated and redissolved at 24-hour intervals for 130 days showed that solutions evolved to high δ^{30}Si, then declined again to the initial δ^{30}Si. The authors took this decline as an approach to the equilibrium fractionation, in which $\Delta_{solid\text{-}fluid} \geq 0$ (Oelze et al., 2012). Preliminary molecular dynamics simulations of equilibrium fractionation between silicic acid and quartz at 25° C suggest that $\alpha_{SiOH(4)qtz\text{-}aq}$ = +3‰ (M. Meheut, pers. comm.).

Under what circumstances would equilibrium, rather than kinetic, fractionation factors apply to the case of acidic basalt alteration? DePaolo (2011) argues that equilibrium isotopic fractionations will be achieved in regimes in which the net precipitation rate is slow relative to backward reaction (dissolution) rate, and in which fluid transport rates are fast such that solutions remain well mixed. These conditions are achieved at low degrees of supersaturation. The degree to which Hawaiian silica precipitates approach equilibrium with altering fluids is unclear. Silica coating morphology suggests coupled *in situ* dissolution-reprecipitation (Chemtob, 2012; Putnis, 2009) The formation of silica layers in Hawaii is likely characterized by low W/R ratios, high degrees of supersaturation, and numerous cycles of rewetting-evaporation. An approach to equilibrium fractionation factors under these conditions is possible but unlikely.

5.3.6. Solution Buffering by Basalt

In all the above interpretations of elevated δ^{30}Si signatures of the Hawaiian silica coatings, an implicit assumption was made that no Si isotopic fractionation occurs during dissolution of basalt. Here we assess the validity of that assumption and determine the plausibility of a coating formation mechanism involving buffering of solutions to basalt δ^{30}Si during incongruent dissolution. Evidence for Si isotope fractionation during incongruent dissolution is equivocal. Ziegler et al. (2005) measured the leachates of a basalt dissolution experiment in water and observed that for low degrees of alteration, fluids were up to 3‰ lighter than the substrate basalt. This trend reversed itself at higher degrees of dissolution and was more pronounced for crystalline basalts than for glassy basalts. In the iron isotope system, Beard et al. (2002) observed no δ^{56}Fe fractionation during dissolution of hematite. Brantley et al. (2004) observed Fe isotope fractionation during dissolution of hornblende, but only in the presence of bacteria and/or organic chelating agents.

Two potential scenarios involving isotopically incongruent dissolution of basalt could produce ^{30}Si silica precipitates. First, basalt dissolution could produce a Si isotope fractionation in the opposite sense from mineral precipitation, releasing low δ^{30}Si material to solution and retaining high δ^{30}Si material in the leached product. This scenario mirrors the dissolution experiment reported in Ziegler et al. (2005) and would directly account for the coating δ^{30}Si, but is inconsistent with results of dissolution experiments from this study and with δ^{30}Si trends observed in natural weathering environments. In the B-HCl experiments, we observed that leachates undersaturated with respect to amorphous silica were isotopically unfractionated or modestly ^{30}Si-enriched (Table 5). Terrestrial river waters are typically ^{30}Si-enriched relative to the rocks they weather; if initial leachates were indeed ^{28}Si-enriched, then substantial secondary phase precipitation would have to occur to cancel the ^{30}Si "deficit", and ^{28}Si-rich waters might still be detectable in some locations. Thus, an opposite-sense fractionation from dissolution seems unlikely.

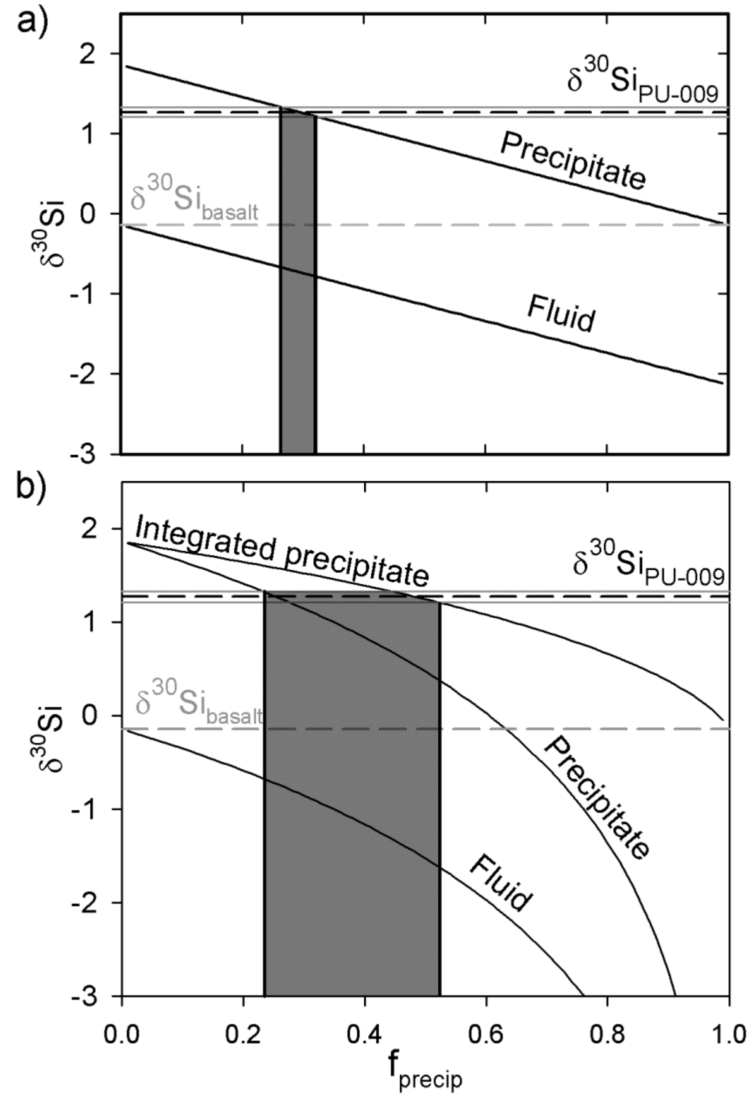

Figure 12. Modeling of PU-009 silica coating δ^{30}Si using α = 1.002. a) Steady-state fractionation model. The coating δ^{30}Si is reproduced if 26–32% of dissolved Si is precipitated as amorphous silica. b) Rayleigh fractionation model. The first precipitates with $\delta^{30}Si = +1.27‰$ are produced at $f_{precip} = 0.23$. The integrated Rayleigh precipitate achieves the δ^{30}Si composition of PU-009 at $f_{precip} = 0.52$. These two values of f_{precip} represent endmember cases consistent with measured δ^{30}Si.

In a second scenario, interacting solutions are buffered by the basalt and exhibit an isotopic fractionation in the same direction and magnitude as seen during precipitation (i.e. those α listed in Table 1). Because the total amount of mobilized Si is small relative to undissolved Si in the basalt substrate, the δ^{30}Si of near-surface basalt would remain essentially unaffected. Altering fluids would become ^{30}Si-enriched; solids precipitated from such fluids at high f_{precip} would also be ^{30}Si-enriched. Solution buffering by basalt appears to be a valid explanation for producing isotopically heavy silica coatings, but it has several implications for the coating formation mechanism. Solution buffering likely requires a volume interaction with unaltered basalt to produce an isotopic fractionation. For changes in δ^{30}Si of the residual solid to remain undetectable by analytical methods, isotopic exchange with the fluid would have to occur over a large volume of basalt relative to the volume of the silica coating. These conditions require that silica coatings be depositional in origin, apparently contradicting morphological evidence of *in situ* alteration in some coatings (Chemtob, 2012).

5.4. Preferred Interpretations

The viable mechanisms for producing ^{30}Si-enriched silica coatings on young Kilauean basalts described in Section 5.3 can be clustered into two groups: 1) Delivery of external, ^{30}Si-enriched silica to sites of coating deposition (Rayleigh fractionation, 5.3.2; Vapor transport, 5.3.3.; Buffering 5.3.6), and 2) Derivation of silica by local leaching with a fractionation factor $\alpha_{\text{precip-SiO2(aq)}}$ greater than 1 (Effects of speciation 5.3.4; equilibrium fractionation, 5.3.5). We prefer the second group of explanations because they are more consistent with the morphology and physical distribution of coatings observed in the field. Silica coating appearance on Kilauea is strongly dependent on surface properties; specifically, coatings tend to form on dense, glassy surfaces (Chemtob, 2012). This observation implies that the silica alteration materials are products of the breakdown of those glassy layers. Formation mechanisms involving delivery of isotopically fractionated silica to lava surfaces would likely produce roughly uniformly distributed deposits, rather than the surface-specific product observed in the field.

At this time, we cannot distinguish between mechanisms producing a fractionation factor greater than unity. Explanations involving α influenced by aqueous speciation of Si and equilibrium fractionation are both potentially valid. However, for local derivation of silica coatings, 1000 ln α must be larger than $\Delta_{silica-basalt}$; for the most ^{30}Si-enriched coating, $\Delta_{silica-basalt}$ is ~1.4‰. Assuming an arbitrary value of 1000 ln α = +2‰, we can recreate a potential history for formation of the PU-009 silica alteration layer (Figure 12). SO_2 and HF-bearing vapors interact with liquids on the surface of young, unaltered basalt (either rainwater or condensed plume water vapor) and acidify them. These acidic liquids dissolve aliquots of near-surface basalt. Because water-rock ratios are low and ionic strength is high in these solutions, Si displays complex speciation in solution. A fraction (f_{precip} = 0.26–0.32 for steady-state fractionation, or 0.23–0.52 for Rayleigh fractionation) of dissolved Si precipitates in place as amorphous silica. The residual solutions percolate into the porous flows, carrying the remaining dissolved load.

6. Conclusions

Amorphous silica coatings on young Kilauean basalts are, to varying degrees, enriched in ^{30}Si relative to their basalt substrate. This direction of isotopic fractionation appears inconsistent with previously determined fractionation factors for the precipitation of amorphous silica from solution. The preferred explanation for ^{30}Si-enrichment in the Hawaiian silica coatings is a shift in the fractionation factor resulting from a change in aqueous Si speciation. The potential impact of aqueous speciation on isotopic fractionation factor is demonstrated by the batch HCl and HF dissolution experiments presented in this study. Incongruent dissolution was observed in both sets of experiments;

however, in the B-HCl experiments, fluid δ^{30}Si evolved to ^{30}Si-enriched compositions, and in the B-HF experiments, fluids were ^{28}Si-enriched. Isotopic fractionations were more extreme at low water-rock ratios.

These results have potential implications for the future use of silicon isotopes as a weathering proxy. Previous studies documenting silicon isotope systematics in Hawaii illustrate that Hawaiian soils become increasingly ^{28}Si-enriched with age (Ziegler et al., 2005) and that Hawaiian groundwater and stream waters are ^{30}Si-enriched (Georg et al., 2007). The silica coatings and cements observed in this study show the opposite sense of fractionation. However, the volume of these weathering products is insignificant compared to the volume of Hawaiian soils and the dissolved cation flux transported to the oceans. Even if unusual speciation is producing an opposite-sense fractionation in these localized silica deposits, this process is clearly overwhelmed by the primary fractionation. Thus, use of silicon isotopes as a proxy for long-term weathering trends should still be considered valid.

Nevertheless, the existence of ^{30}Si-enriched secondary precipitates, even in small proportions, suggests that the fractionation factor varies as a function of fluid composition. Interpretations of δ^{30}Si of individual occurrences of secondary minerals in the geologic record should be context-dependent. Future researchers should investigate in greater detail, through molecular-dynamics simulations and additional experiments, the effects of aqueous speciation and water-rock ratio on silicon isotope composition to enhance its use as an effective proxy.

7. Acknowledgements

We thank Samantha Ingalls (UCLA) for assistance with MC-ICP-MS data collection, Yunbin Guan (Caltech) for assistance with SIMS methods, and Don Swanson (HVO-USGS) for samples and discussion. This work was supported by the White Rose Foundation and by a NASA graduate student fellowship.

Appendix A. SIMS Results

A.1. Matrix Effects

Effective stable isotopic analysis by ion probe requires that standards are matrix-matched in composition and structure as closely as possible to the samples of interest (Eiler et al., 1997). Deviations from precisely matched standards may produce matrix effects in the form of instrumental mass ratio offsets. The Hawaiian silica coatings are composed of hydrous amorphous silica with up to 5.5% structural water by weight (Chemtob et al., 2012). No hydrous amorphous silica standards were readily available, so a series of tests were conducted to determine the instrumental matrix effects associated with amorphousness and with water content.

The test for the matrix effect associated with amorphousness was performed by analyzing, in the same SIMS session, raw (crystalline) Ge 214 quartz and fused SiO_2 glass synthesized from Ge 214 quartz. We assume that fusion of the Ge 214 quartz sample produced no silicon isotope fractionation, such that $\delta^{30}Si_{raw} = \delta^{30}Si_{fused} = 0.38 \pm 0.03‰$ (2 s.e.; Table 4). SIMS analysis of raw Ge 214 quartz produced a value of $\delta^{30}Si_{raw} = -65.68 \pm 0.63‰$ (2σ), pre-instrumental mass fractionation (IMF) (Figure A1). The SIMS measurement for fused Ge 214 quartz showed $\delta^{30}Si_{fused} = -65.45 \pm 0.81‰$, pre-

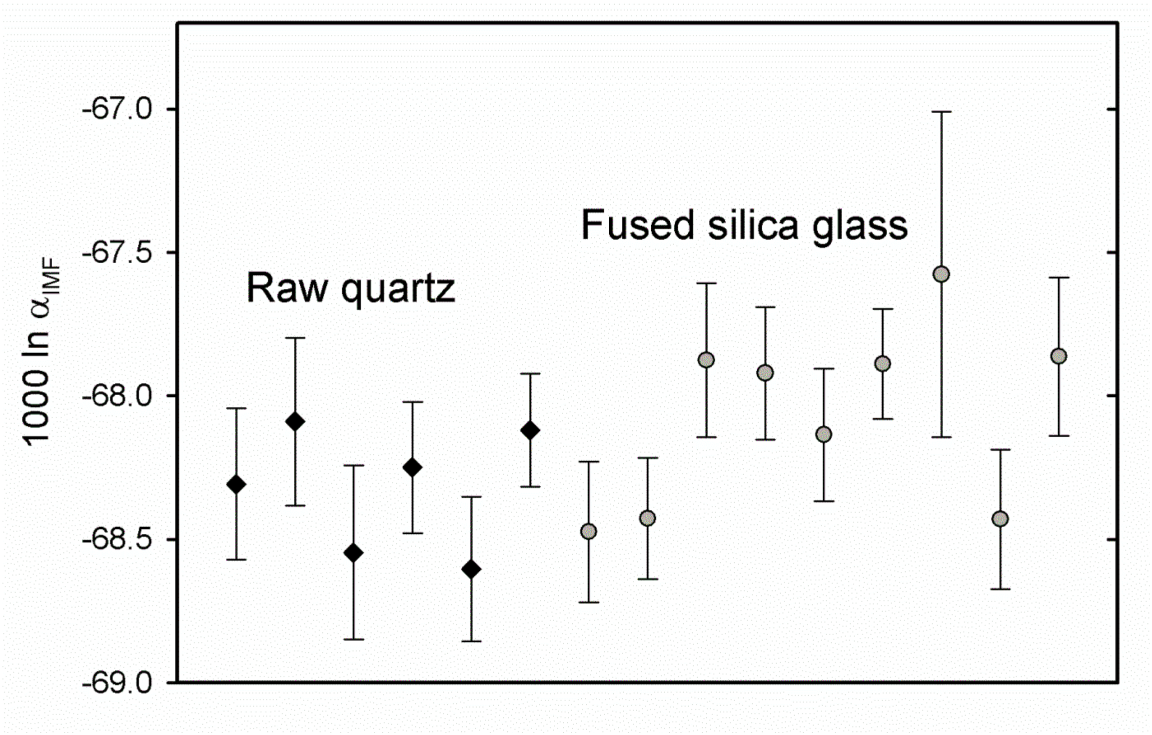

Figure A1. Test for SIMS matrix effect associated with amorphousness, evaluated by individual spot analyses of Ge 214 quartz and fused Ge 214 silica glass. IMF is calculated based on MC-ICP-MS analyses of Ge 214 fused glass.

IMF. From these measurements, we determine that, for anhydrous silica glass, α_{IMF} = 0.9342 ± 0.0008 (2σ). Additionally, we calculate the crystalline-amorphous matrix effect to be 1000 ln $\alpha_{fused-raw}$ = 0.25 ± 0.55‰ (1σ). In short, there was no statistically significant matrix effect, even at the 1σ level, associated with crystallinity for silicon isotope measurements of silica glass.

The test for matrix effects associated with hydrous content was conducted by analyzing a series of albite glasses with varying water contents, synthesized by Silver et al. (1985). The δ^{30}Si compositions of the AmAb and Ab 7% glasses were 0.13 ± 0.05‰ and 0.43 ± 0.05‰, respectively (Table 4). Insufficient quantities of Ab 3% glass were available for MC-ICP-MS analysis, so further discussion will be limited to AmAb and Ab 7%. Pre-IMF analyses of the AmAb and Ab7 % glasses were δ^{30}Si = -65.9 ± 0.6‰ and

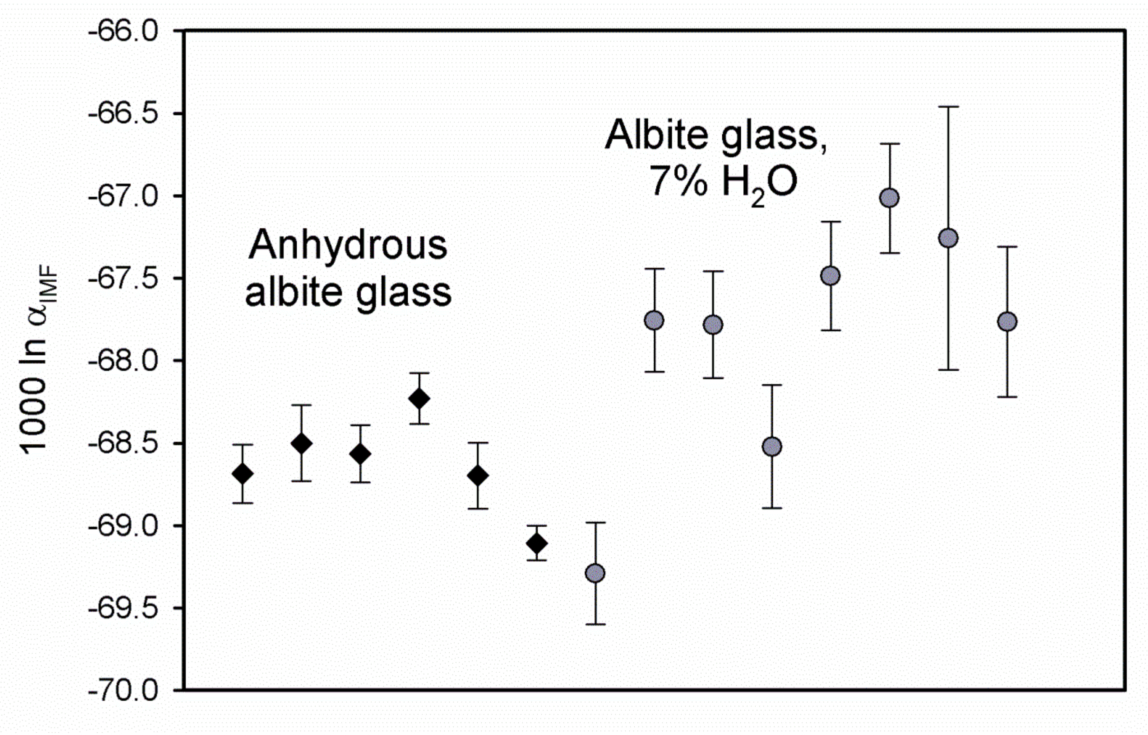

Figure A2. Test for SIMS matrix effect associated with water content, evaluated by individual spot analyses of anhydrous albite glass and albite glass containing 7% H_2O. IMF is calculated based on MC-ICP-MS analyses of each material.

-65.5 ± 1.6‰, respectively (Figure A2). These values imply that for AmAb, α_{IMF} = 0.9337 ± 0.0003, and for Ab 7%, α_{IMF} = 0.9344 ± 0.0008 (2σ). The matrix effect associated with this difference in hydrous content is calculated by dividing these two IMFs; we calculate 1000 ln $\alpha_{7\%\text{-dry}}$ = 0.77 ± 0.91‰ (1σ). The matrix effect for hydrous content in glasses appears to be larger than the matrix effect associated with amorphousness, but it is not statistically significant even at the 1σ level. This lack of statistical significance is largely due to the large spread of data points for the Ab 7% glass, including a potential outlier more than 0.7‰ lighter than the next lightest analysis (Figure A2). Recalculation of the matrix effect omitting the outlying point gives 1000 $\ln_{\%\text{-dry}}$ = 0.97 ± 0.91‰ (1σ). In summary, no matrix effects associated with amorphousness or with hydrous content were significant at the 2σ level, and so no systematic corrections will be made to Hawaiian silica measurements; however, some evidence suggests that water content may affect measured silicon isotope compositions by up to 1‰.

A.2. Hawaiian Silica δ^{30}Si

Ion probe measurements of the silicon isotope composition of the PU-009 silica coatings were attempted in two sessions, in February 2011 and January 2012. In Feb. 2011, analyses were conducted on a thick section of PU-009 was mounted with the RSQ standard in Petroepoxy. In Jan. 2012, analyses were conducted on a coated piece of PU-009 polished at a low angle with respect to the natural surface, exposing a coated area hundreds of micrometers across, and mounted with the Ge 214 fused silica standard. Sample EA-30 was prepared with the same low-angle polish and was also analyzed in the Jan. 2012 session.

In the Feb. 2011 session analyses of PU-009, isotope ratios were collected for 21 spots on the exposed coating layer, 6 spots on the basalt substrate, and 12 spots on the RSQ standard. In this session, the instrumental mass fractionation as determined for RSQ was $\alpha_{IMF} = 0.9276 \pm 0.0012$ (2σ). Basalt analyses were approximately 14‰ lighter than RSQ standards, indicating a substantial matrix effect associated with the difference in chemistry between these materials. Spread in apparent δ^{30}Si of ~7‰ was observed for the 14 silica coating spot analyses (Figure A3). Isotope ratios of the silica coating may have been affected by topography and the potential contaminating influence of

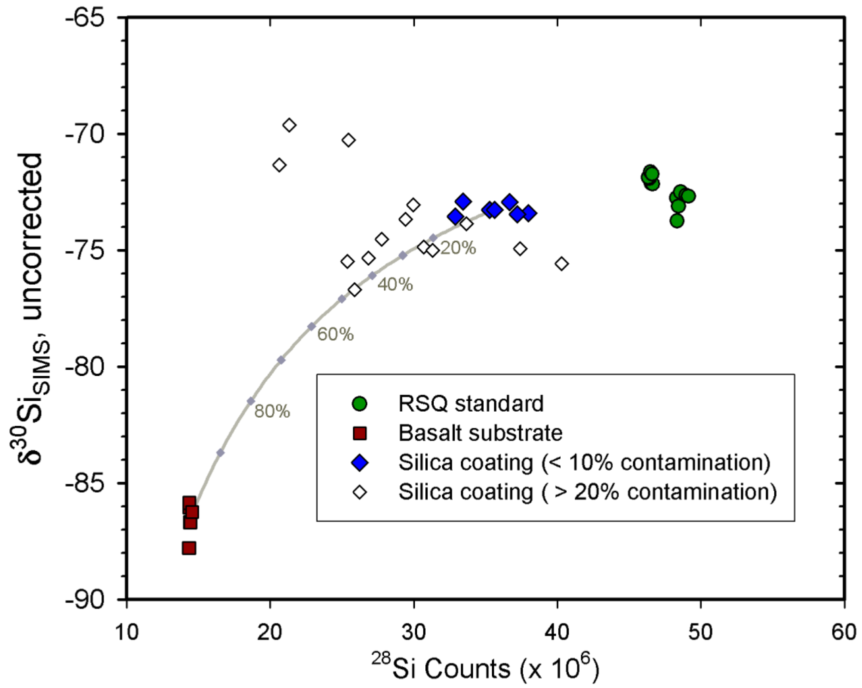

Figure A3. SIMS analyses of PU-009 silica coating, February 2011. δ^{30}Si values are not corrected for IMF. The standard, Caltech Rose Quartz, has $\delta^{30}\mathrm{Si} = 0.02 \pm 0.08‰$ (Table 4). The basalt substrate has $-0.11 \pm 0.13‰$ but has a significantly different IMF. The gray line represents a mixing trend (curved in ^{30}Si/^{28}Si vs. ^{28}Si space) between the average zero-contamination silica coating analyses and the average basalt analysis.

basalt. Because the silica coatings are roughly the same width as the ion beam, selected spots frequently overlapped both the coating and the near-surface basalt substrate (Figure A4). The potential influence of basalt contamination was assessed by determining, via image processing, the proportion of basalt included in each spot (f_{bas}). This metric split the analyses into two populations. Spots with apparent f_{bas} less than or approximately equal to 10% (7 of the original 21) formed a tighter cluster in ^{30}Si/^{28}Si; the IMF-corrected apparent composition for these spots was $\delta^{30}\mathrm{Si} = -0.90 \pm 1.53‰$ (2σ). The remaining 14 spots all had $f_{bas} > 20\%$; their ^{30}Si/^{28}Si compositions were highly variable. We plotted ^{30}Si/^{28}Si against ^{28}Si counts to determine if the spot analyses with high f_{bas} were affected by basalt contamination. A simple mixing line between the average basalt analysis and the average basalt-free coating analysis forms curved trends in this space (Figure A3). Some of the high f_{bas} spots appeared to follow this mixing trend, suggesting

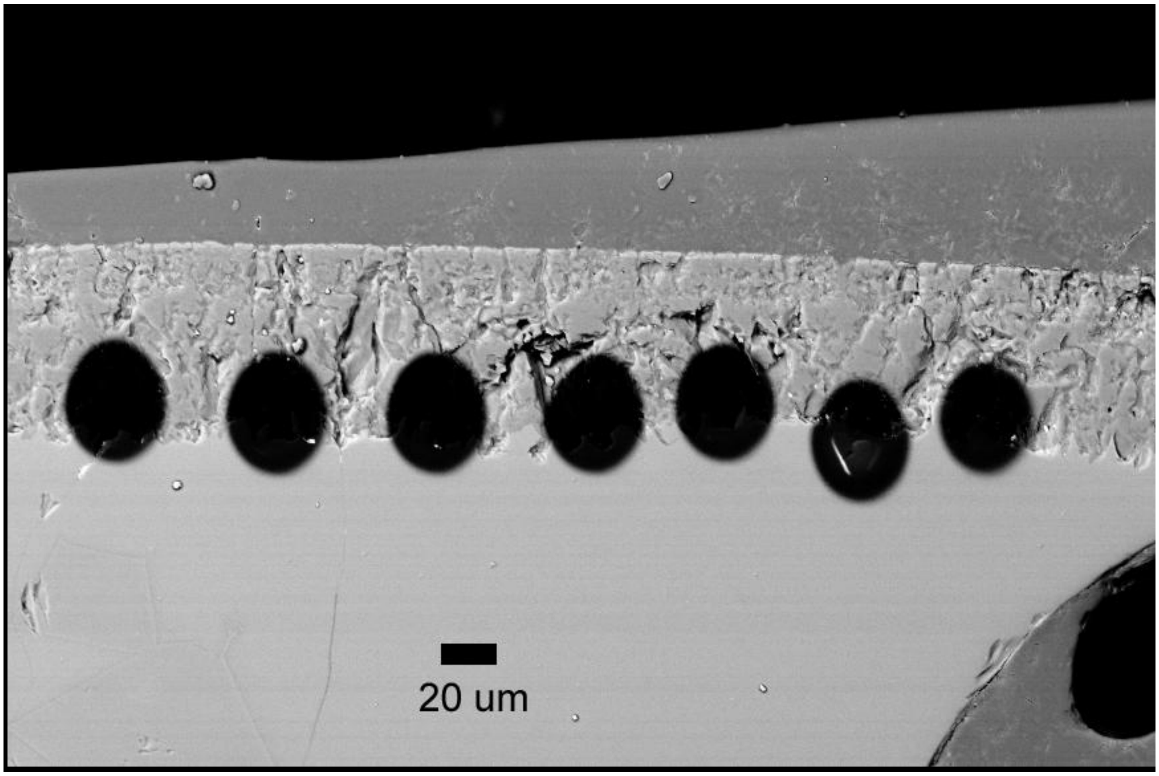

Figure A4. SEM image of SIMS pits on PU-009 coating from February 2011 session. SIMS pits frequently sampled both the silica coating and the basalt substrate, so tests were performed to assess the degree of basalt contamination (see Figure A3).

the influence of basalt mixing; other spots did not follow the mixing trend. This observation suggests that high f_{bas} spots may be equally affected by the ionization of basalt and the fractionating effect of irregular topography. For this session, we favor the low f_{bas} composition for the PU-009 silica composition, δ^{30}Si = -0.90 ± 1.53‰ (2σ).

In the Jan. 2012 session analysis of PU-009, isotope ratios were collected for 35 spots on the low-angle polished natural coated surface, 7 spots on the basalt substrate, and 22 spots on the Ge 214 standard. The IMF determined for Ge 214 for this session was $\alpha_{IMF} = 0.9421 \pm 0.0008$ (2σ). As in the previous session, spread in apparent δ^{30}Si of ~7‰ was observed for the silica coating spot analyses (Figure A5). Isotope ratios may have been affected by surface heterogeneity and topography. Although the surface was macroscopically flat, profilometer images of the analyzed surface showed highly

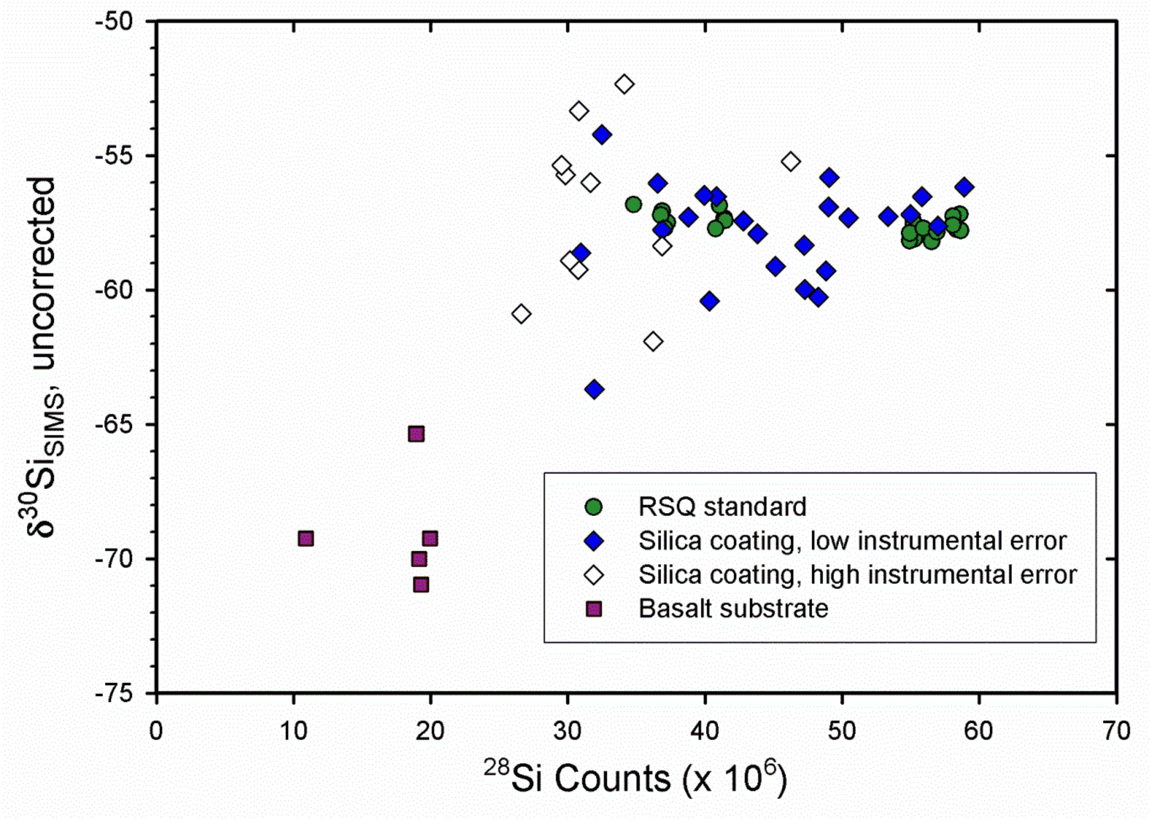

Figure A5. SIMS analyses of PU-009 silica coating, January 2012.

irregular topography and up to 20 µm of relative relief across SIMS traverses (Figure A6), which may have a significant effect on measured isotope ratios. Because ion beam spots did not visually overlap with the polished basalt substrate, estimates of substrate contamination could not be determined as in the previous session. However, isotope ratios from pits within 10-20 µm of the basalt edge were highly variable, suggesting that those points may have penetrated the basalt substrate (Figure A5); these pits were excluded from analysis. Additionally, data were filtered by instrumental error; points

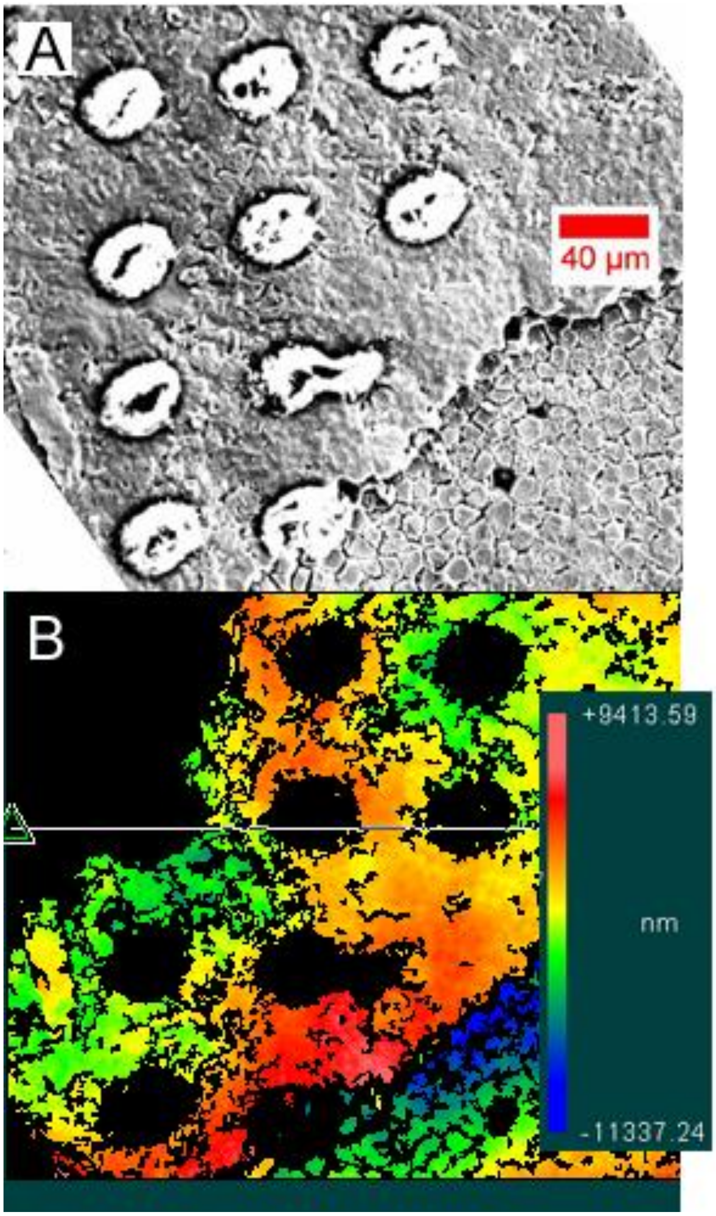

Figure A6. Imagery of SIMS pits on natural surface of PU-009 coating from January 2012 session. A) SEM secondary electron image. B) Profilometry, illustrating the presence of significant topography across the surface region where SIMS analyses were conducted.

with higher error may have sampled sections of the surface with more irregular topography and/or greater heterogeneity. Data with $\sigma_{\delta30Si} < 0.4$‰ were retained (Figure A5). The IMF-corrected apparent composition for this subset of data is $\delta^{30}Si = +0.35 \pm 2.79$‰ ($2\sigma$).

In the same SIMS session, sample EA-30 was also analyzed; isotope ratios were collected for 22 spots on the natural coated surface, 2 spots on the basalt substrate, and 18 spots on the Ge 214 standard. The IMF determined for Ge 214 was $\alpha_{IMF} = 0.9425 \pm 0.0013$ (2σ). Isotope ratios of the coated surface showed less spread than either of the PU-009 sessions (Figure A7), despite considerable topography and relative relief on the coated surface. Data filtering procedures were similar to those described for the PU-009 Jan. 2012 session.

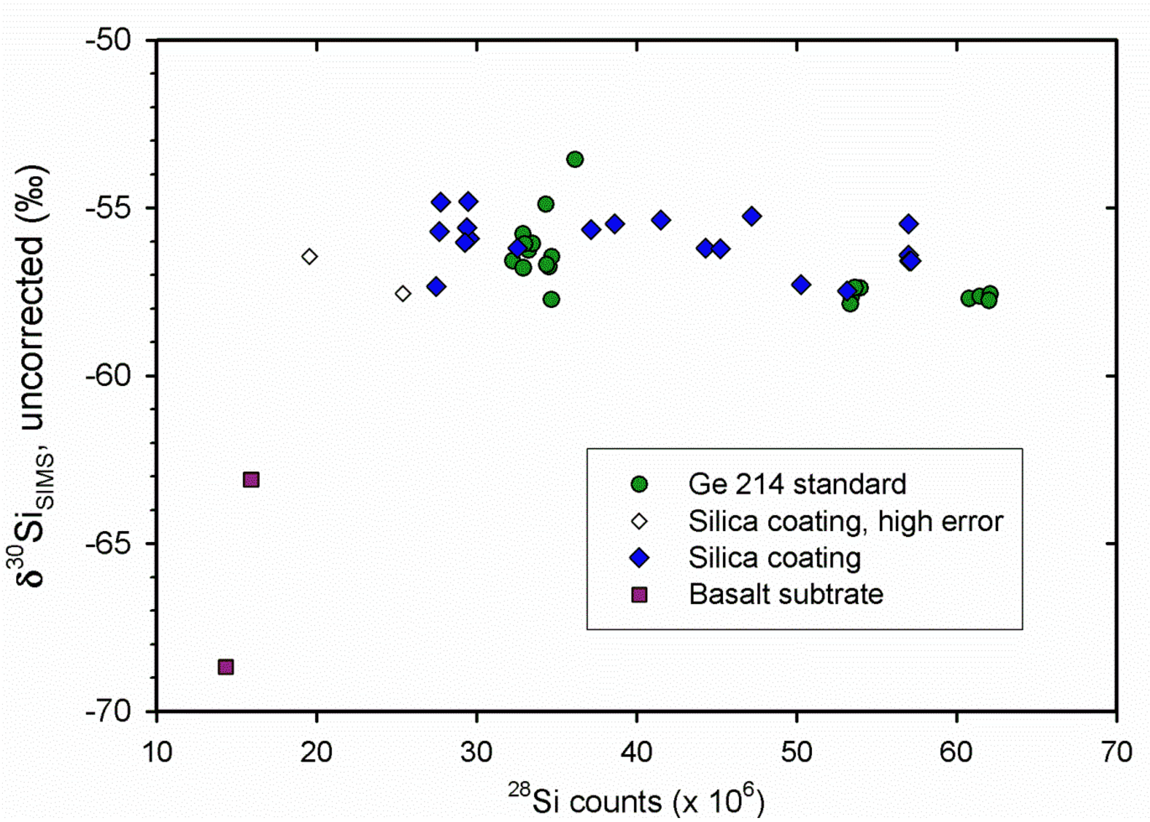

Figure A7. SIMS analysis of EA-30 silica coating, standardized against Ge 214 silica glass ($\delta^{30}Si$ = 0.37 ± 0.03‰).

The IMF-corrected apparent composition for EA-30 is $\delta^{30}Si = +1.53 \pm 2.17‰$ (2σ).

A.3. Comparison with ICP-MS Results

Comparison of the silicon isotope compositions for silica coatings derived by SIMS with those derived by MC-ICP-MS shows mixed agreement. For the PU-009 coating, the measured ICP-MS compositions were $\delta^{30}Si = +1.36 \pm 0.05‰$ and +1.17 ± 0.07‰ (2 s.e.). The SIMS compositions from two separate sessions, after culling data and correcting for instrumental mass fractionation, were $\delta^{30}Si = -0.90 \pm 1.53‰$ and +0.35 ± 2.79‰ (2σ). Although the values determined by the two SIMS sessions are within error of each other, the first SIMS session is not in agreement with the MC-ICP-MS values. EA-30 and KD-003 are not the same sample, but were collected within ~1 km of each other in the Ka’u Desert. The ICP-MS composition of KD-003 (δ^{30}Si =+0.92 ± 0.04‰) and the SIMS composition of EA-30 (δ^{30}Si = +1.53 ± 2.17‰) are in good agreement.

The poor precision and accuracy of the SIMS data relative to the ICP-MS data illustrate that the Hawaiian coatings are poorly suited for ion probe analysis. The coating materials are composed of easily abradable, fine-grained hydrous amorphous silica, and tend to spall and disintegrate instead of polish when sandpapers are applied. These poorly polished surfaces may have sharp topographic variability. Topographic variation may produce an instrumental mass fractionation, but the sign and magnitude of this fractionation for Si isotopes is unclear. We attempted to filter data most strongly affected by basalt contamination or topography, but such filtering may have biased the derived result. Additionally, microprobe analyses of coated basalts mounted in epoxy typically show low totals, which may result from high porosity (Chemtob et al., 2010). In Section A.1, we showed that matrix effects associated with crystallinity or with water content are less than 1‰ in magnitude. Porosity, which was not explored, may also produce an unpredictable matrix effect. Because of these complicating factors, we prefer the MC-ICP-MS results and focus our interpretations on those values.

Appendix B. Calculation of Eequilibrium Si Isotope Fractionation Factor Between Gaseous SiF_4 and Solid Silicates

In interpreting the Si isotope fractionation observed in HF-bearing dissolution experiments, it is useful to calculate the equilibrium fractionation factor associated with the mobilization of Si in fluoride compounds. Potentially relevant aqueous Si-fluoride species include SiF_6^{2-} and $Si(OH)_2F_2$ (Busey et al., 1980); however, no isotopically substituted spectroscopic data are available for those dissolved species. We make use of infrared spectra of isotopically-substituted SiF_4 gas, collected at 25° C from Heicklen and Knight (1964) (Table A1).

Mode	Symmetry	^{28}Si	^{29}Si	^{30}Si
ν_1	A_1	264	264	264
ν_2	E	801	801	801
ν_3	F_2	1031.8 ± 0.3	1022.9 ± 0.3	1014.4 ± 0.3
ν_4	F_2	389.35 ± 0.15	387.8 ± 0.5	386.35 ± 0.10

Table A1. Frequencies of fundamental vibrational modes, in cm^{-1}, of isotopically-substituted SiF_4, from Heicklen and Knight (1964). The ν_1 and ν_2 modes are infrared-forbidden, and are derived from the positions of combination modes.

The β-factor of a phase *a* is the isotopic fractionation factor of an element Y between the molecule and a perfect gas of Y atoms (Meheut et al., 2009). The fractionation factor (α) between any two phases can be expressed as the ratio of two β-functions. The β-function can be computed using the vibrational properties of the molecule.

$$\beta = (Q'/Q)_a / (Q'/Q)_{gas} \qquad \text{(A1)}$$

where Q' is the partition function of the system with all Y atoms in the phase *a* substituted with the unusual isotope. The ratio of partition functions for phase *a* and for the perfect gas are given by the Teller-Redlich Spectrosopic Theorem:

$$Q'/Q = (Q'/Q)_{trans} \cdot (Q'/Q)_{rot} \cdot (Q' / Q)_{vib} \qquad \text{(A2)}$$

But, $(Q'/Q)_{trans,a} = (Q'/Q)_{trans,gas}$, and $(Q'/Q)_{rot,gas} = (Q'/ Q)_{vib,gas} = 1$. So, the β-factor for phase a can be expressed as

$$\beta = (Q'/Q)_{rot} \cdot (Q'/Q)_{vib} = (\sigma/\sigma') \cdot \Pi_i \,[\, (\nu_i'/\nu_i) \cdot (e^{-ui'/2} / e^{-ui/2}) \cdot (1 - e^{-ui}) / (1 - e^{-ui'}) \qquad \text{(A3)}$$

where σ is the symmetry number, ν_i is the frequency of each vibrational mode, $u_i = h\nu_i / kT$, h is Planck's constant, k is the Boltzmann constant and T is temperature in Kelvin.

In the ν_1 and ν_2 vibrational modes of a tetrahedral molecule, the central atom does not move; therefore, only the ν_3 and ν_4 modes contribute to the β-factor. Both ν_3 and ν_4 are triply degenerate modes, so their partition function contributions are cubed in equation A3. Based on the spectroscopic data from Heicklen and Knight, the β-factor for substitution of ^{30}Si for ^{28}Si in SiF_4 gas is 1.08696.

Meheut et al. (2009) calculated Si isotope β-factors for several silicate minerals (quartz, kaolinite, forsterite, enstatite and lizardite). At 25 °C, differences between β-factors for these minerals were ~5‰ or less. The β-factor for quartz at 25 °C is 1.0709. Therefore, $1000 \ln \alpha_{\text{SiF4-quartz}} = 1000 \ln (\beta_{\text{SiF4}} / \beta_{\text{quartz}}) = 14.88‰$. Fractionation factors for less fully polymerized silicate minerals were larger than $\alpha_{\text{SiF4-quartz}}$. This equilibrium calculation of α suggests that SiF_4 in equilibrium with silicates should be strongly ^{30}Si-enriched.

Appendix C: Electron Probe Analyses of Batch Experiment Alteration Materials

	Exp B-HCl.A			Exp B-HCl.C		Exp B-HF.A (Silica)		Exp B-HF.A (Fluoride)	
	Raw	Normalized	Endmember, basalt removed	Raw	Normalized	Raw	Normalized	Raw	Normalized
SiO_2	49.17	63.73	73.47	66.14	98.74	93.82	99.20	7.07	10.45
TiO_2	0.89	1.16	0.00	0.13	0.20	0.02	0.02	0.12	0.17
Al_2O_3	5.69	7.37	2.16	0.03	0.04	0.04	0.05	18.89	27.92
FeO*	12.13	15.73	19.57	0.33	0.49	0.26	0.28	0.75	1.11
MgO	2.06	2.67	-0.52	0.01	0.01	0.00	0.00	11.65	17.22
CaO	4.04	5.24	0.55	0.04	0.06	0.05	0.06	4.66	6.89
Na_2O	0.57	0.73	-0.61	0.01	0.02	0.02	0.02	0.45	0.66
K_2O	0.19	0.24	0.08	0.01	0.01	0.01	0.01	0.12	0.17
Cr_2O_3	0.04	0.06	0.08	0.02	0.03	0.00	0.00	0.00	0.00
MnO	0.06	0.08	0.01	0.02	0.03	0.00	0.00	0.03	0.04
P_2O5	0.13	0.17	0.10	0.02	0.02	0.03	0.03	0.06	0.09
SO_3	0.39	0.50	0.91	0.01	0.02	0.00	0.00	0.00	0.00
F	1.80	2.33	4.19	0.23	0.34	0.33	0.35	23.85	35.27
Total	77.15	100.00	100.00	66.99	100.00	94.58	100.00	67.63	100.00

Table A2. Representative electron microprobe analyses of alteration materials from B-HCl and B-HF experiments. Alteration layers formed in Exp. B-HCl.A were too thin to analyze independently of the basalt substrate, so the endmember alteration composition was estimated by subtracting basalt composition and assuming a TiO_2 content of zero.

Works Cited

Alexander, G. B., Heston, W. M., and Iler, R. K. (1954). The solubility of amorphous silica in water. *J. Phys. Chem.*, **58,** 453–455.

Azaroual, M., Fouillac, C., and Matray, J. M. (1997) Solubility of silica polymorphs in electrolyte solutions, I. Activity coefficient of aqueous silica from 25° to 250° C, Pitzer's parameterisation. *Chem. Geol.,* **140**, 155–165.

Bai, S., Urabe, S., Okaue, Y., and Yokoyama, T. (2009) Acceleration effect of sulfate ion on the dissolution of amorphous silica. *J. Colloid Int. Sci.,* **331**, 551–554.

Basile-Doelsch, I., Meunier, J. D., and Perron, C. (2005). Another continental pool in the terrestrial silicon cycle. *Nature,* **433,** 399–402.

Brantley, S. L., Liermann, L. J., Guynn, R. L., Anbar, A., Icopini, G. A., and Barling, J. (2004) Fe isotopic fractionation during mineral dissolution with and without bacteria. *Geochim. Cosmochim. Acta,* **68**, 3189–3204.

Chakrabarti, R., Knoll, A. H., Jacobsen, S. B., and Fischer, W. W. (2012). Si isotope variability in Proterozoic cherts. *Geochim. Cosmochim. Acta,* in press.

Chemtob, S. M. (2012) Distribution and temporal evolution of Hawaiian silica coatings. Thesis Chapter III.

Chemtob, S. M., Jollliff, B. L., Rossman, G. R., Eiler, J. M., and Arvidson, R. E. (2010). Silica coatings in the Ka'u Desert, Hawaii, a Mars analog terrain: A micromorphological, spectral, chemical, and isotopic study. *JGR,* **115,** doi:10.1029/2009JE003473.

Chemtob, S. M., Rossman, G. R. and Stebbins, J. F. (2012). Natural hydrous amorphous silica: Quantitation of network speciation and hydroxyl content by ^{29}Si MAS NMR and vibrational spectroscopy. *Am. Min*, **97,** 203–211.

Chen, C.-T. A. and Marshall, W. L. (1982) Amorphous silica solubilites – IV. Behavior in pure water and aqueous sodium chloride, sodium sulfate, magnesium chloride, and magnesium sulfate solutions up to 350° C. *Geochim. Cosmochim. Acta*, **46**, 279–288.

Chmeleff, J., Horn, I., Steinhoefel, G., and von Blanckenburg, F. (2008) In situ determination of precise stable Si isotope ratios by UV-femtosecond laser ablation high-resolution multi-collector ICP-MS. *Chem. Geol.*, **249**, 155–166.

Das, A., Krishnaswami, S., Sarin, M. M., and Pande, K. (2005) Chemical weathering in the Krishna Basin and Western Ghats of the Deccan Traps, India: Rates of basalt weathering and their controls. *Geochim. Cosmochim. Acta*, **69**, 2067–2084.

de Hoog, J. C. M., van Bergen, M. J., and Jacobs, M. H. G. (2005) Vapour-phase crystallisation of silica from SiF_4-bearing volcanic gases. *Annals of Geophysics*, **48**, 775–785.

De La Rocha, C. L., Brzezinski, M. A., and Deniro, M. J. (1996). Purification, recovery, and laser-driven fluorination of silicon from dissolved and particulate silica for the measurement of natural stable isotope abundances. *Anal. Chem.* **68**, 3746–3750.

De La Rocha, C. L., Brzezinski, M. A., and Deniro, M. J. (2000) A first look at the distribution of the stable isotopes of silicon in natural waters. *Geochim. Cosmochim. Acta,* **64,** 2467–2477.

De La Rocha, C. L., Brzezinski, M. A., and Deniro, M. J., and Shemesh, A. (1998). Silicon-isotope composition of diatoms as an indicator of past oceanic change. *Nature*, **395**, 680–683.

Delstanche, S., Opfergelt, S., Cardinal, D., Elass, F., André, L., and Delvaux, B. (2009). Silicon isotopic fractionation during adsorption of aqueous monosilicic acid onto iron oxide. *Geochim. Cosmochim. Acta*, **73,** 923–934.

DePaolo, D. J. (2011) Surface kinetic model for isotopic and trace element fractionation during precipitation of calcite from aqueous solutions.. *Geochim Cosmochim. Acta*, **75**, 1039–1056.

Ding, T., Wan, D., Wang, C., and Zhang, F. (2004). Silicon isotope compositions of dissolved silicon and suspended matter in the Yangtze River, China." *Geochim Cosmochim. Acta*, **68**, 205–216.

Douthitt, C. B. (1982). The geochemistry of the stable isotopes of silicon." *Geochim Cosmochim. Acta*, **46**, 1449–1458.

Eiler, J. M., Graham, C., and Valley, J. W. (1997) SIMS analysis of oxygen isotopes: matrix effects in complex minerals and glasses. *Chemical Geology*, **138**, 221–244.

Farr, T. G. and Adams, J. B. (1984) Rock coatings in Hawaii. *GSA Bulletin*, **95**, 1077–1083.

Georg, R. B., Reynolds, B. C., West, A. J., Burton, K. W., and Halliday, A. N. (2007). Silicon isotope variations accompanying basalt weathering in Iceland. *EPSL*, **261**, 476–490.

Gerlach, T. M. (1993) Oxygen buffering of Kilauea volcanic gases and the oxygen fugacity of Kilauea basalt. *Geochim. Cosmochim. Acta*, **57**, 795–814.

Greenland, L. P. Rose, W. I., and Stokes, J. B. (1985) An estimate of gas emissions and magmatic gas content from Kilauea volcano. *Geochimica et Cosmochimica Acta*, **49**, 125–129.

Heck, P. R., Huberty, J. M., Kita, N. T., Ushikubo, T., Kozdon, R., and Valley, J. W. (2011) SIMS analyses of silicon and oxygen isotope ratios for quartz from Archean and Paleoproterozoic banded iron formations. *Geochim. Cosmochim. Acta*, **75**, 5879–5891.

Heicklen, J., and Knight, V. (1964) The infrared spectrum of SiF_4. *Spectrochimica Acta*, **20**, 295–298.

Hurowitz, J. A., McLennan, S. M., Lindsley, D. H., and Schoonen, M. A. A. (2005). Experimental epithermal alteration of synthetic Los Angeles meteorite: Implications for the origin of Martian soils and identification of hydrothermal sites on Mars. *JGR*, **110**, doi:10.1029/2004JE002391.

Hurwitz, S., Goff, F., Janik, C. J., Evans, W. C., Counce, D. A., Sorey, M. L., and Ingebritsen, S. E. (2003) Mixing of magmatic volatiles with groundwater and interaction with basalt on the summit of Kilauea Volcano, Hawaii. *JGR*, **108**, doi:10.1029/2001JB001594.

Icopini, G. A., Brantley, S. L., and Heaney, P. J. (2005) Kinetics of silica oligomerization and nanocolloid formation as a function of pH and ionic strength at 25° C. *Geochim. Cosmochim. Acta*, **69**, 293–303.

Kurtz, A. C., Derry, L. A., and Chadwick, O. A. (2001) Accretion of Asian dust to Hawaiian soils: isotopic, elemental, and mineral mass balances. *Geochim. Cosmochim. Acta*, **65**, 1971–1983.

Leng, M. L., Swann, G. E. A., Hodson, M. J., Tyler, J. J., Patwardhan, S. V., and Sloane, H. J. (2009) The potential use of silicon isotope composition of biogenic silica as a proxy for environmental change. *Silicon*, **1**, 65–77.

Li, Y. H., Ding, T. P. and Wan, D. F. (1994) Experimental study of silicon isotope dynamic fractionation and its geological application. *Mineral Deposits*, **13**, 282-288.

Marshall, W. L., and Chen, C.-T. A. (1982) Amorphous silica solubilities – VI. Postulated sulfate-silicic acid solution complex. *Geochim. Cosmochim. Acta*, **46**, 367–370.

Meheut, M., Lazzeri, M., Balan, E., and Mauri, F. (2009) Structural control over equilibrium silicon and oxygen isotopic fractionation: a first-principles density-functional theory study. *Chem. Geol.*, **258**, 28–37.

Minitti, M. E., Weitz, C. M., Lane, M. D., and Bishop, J. L. (2007). Morphology, chemistry and spectral properties of Hawaiian rock coatings and implications for Mars. *JGR*, **112**, doi:10.1029/2006JE002839.

Munter, P. A., Aepli, O. T., and Kossatz, R. A. (1947) Hydrofluoric acid – water and hydrofluoric acid – hydrofluosilicic acid – water. *Industrial and Engineering Chemistry*, **39**, 427–431.

Murata, K. J., Ault, W. U., and White, D. E. (1964) Halogen acids in fumarolic gases of Kilauea volcano. *Bull. Volcanol.*, **27**, 365–368.

Naboko, S. I. (1957) A case of gaseous fluorine metasomatism at an active volcano. *Geochemistry*, **1957**, 452–455.

Nuth, J. A., and Ferguson, F. T. (2006). Silicates do nucleate in oxygen-rich circumstellar outflows: new vapor pressure data for SiO. *Astrophys. J.*, **649**, 1178–1183.

Oelze, M., von Blanckenburg, F., Höllen, D., Dietzel, M., and Bouchez, J. (2012) On the competition between kinetic and equilibrium isotope fractionation during low-T silica precipitation. *Goldschmidt Proceedings*.

Öhman, L.-O., Nordin, A., Sedeh, I. F., and Sjöberg, S. (1991) Equilibrium and structural studies of silicon(IV) and aluminum(III) in aqueous solution. 28. Formation of soluble silicic acid-ligand complexes as studied by potentiometric and solubility measurements. *Acta Chemica Scandinavica*, **45**, 335–341.

Opfergelt, S., Cardinal, D., Henriet, C., Draye, X., André, L., and Delvaux, B. (2006) Silicon isotope fractionation by banana (*Musa* spp.) grown in a continuous nutrient flow device. *Plant Soil*, **285**, 333–345.

Opfergelt, S., D. Cardinal, L. André, C. Delvigne, L. Bremond, and B. Delvaux (2010). Variations of δ30Si and Ge/Si with weathering and biogenic input in tropical basaltic ash soils under monoculture. *Geochim. Cosmochim. Acta*, **74**, 225–240.

Putnis, A. (2009) Mineral replacement reactions. *In* Oelkers, E. H. and Schott, J., Eds., Thermodynamics and Kinetics of Water-Rock Interaction, **70**, 87–124. *Reviews in Mineralogy and Geochemistry*, Mineralogical Society of America, Chantilly, Virginia.

Reynolds, B. C., Aggarwal, J., André, L., Baxter, D., Beucher, C., Brzezinski, M. A., Engström, E., Georg, R. B., Land, M., Leng, M. J., Opfergelt, S., Rodushkin, I., Sloane, H. J., van den Boorn, H. J. M., Vroon, P. Z. and Cardinal, D. (2007) An inter-laboratory comparison of Si isotope reference materials. *J. Anal. At. Spectrom.*, **22**, 561–568.

Robert, F., and Chaussidon, M. (2006). A palaeotemperature curve for the Precambrian oceans based on silicon isotopes in cherts. *Nature* **443**, 969–972.

Savage, P. S., Georg, R. B., Armytage, R. M. G., Williams, H. M., and Halliday, A. N. (2010). Silicon isotope homogeneity in the mantle. *EPSL*, **295**, 139–146.

Savage, P. S., Georg, R. B., Williams, H. M., Burton, K. W., and Halliday, A. N. (2011). Silicon isotope fractionation during magmatic differentiation. *Geochim. Cosmochim. Acta*, **75**, 6124–6139.

Seelos, K. D., Arvidson, R. E., Jolliff, B. L., Chemtob, S. M., Morris, R. V., Ming, D. W., and Swayze, G. A. (2010). Silica in a Mars analog environment: Ka'u Desert, Kilauea Volcano, Hawaii. *JGR*, **115**, doi:10.1029/2009JE003347.

Shahar, A., Ziegler, K., Young, E. D., Ricolleau, A., Schauble, E. A., and Fei, Y. (2009). Experimentally determined Si isotope fractionation between silicate and Fe metal and implications for Earth's core formation. *EPSL*, **288**, 228–234.

Silver, L., and Stolper, E. (1985). A thermodynamic model for hydrous silicate melts. *J. Geology*, **93**, 161–177.

Skulan, J. L., Beard, B. L., and Johnson, C. M. (2002) Kinetic and equilibrium Fe isotope fractionation between aqueous Fe(III) and hematite. *Geochim. Cosmochim. Acta*, **66**, 2995–3015.

Tosca, N. J., McLennan, S. M., Lindsley, D. H., and Schoonen, M. A. A. (2004). Acid-sulfate weathering of synthetic Martian basalt: the acid fog model revisited. *JGR*, **109**, doi:10.1029/2003/JE002218.

van den Boorn, S. H. J. M., van Bergen, M. J., Vroon, P. Z. de Vries, S. T., and Nijman, W. (2010) Silicon isotope and trace element constraints for the origin of ~3.5 Ga cherts: implications for Early Archaean marine environments. *Geochimica et Cosmochimica Acta*, **74**, 1077–1103.

White, A. F. and Hochella, M. F. (1992) Surface chemistry associated with the cooling and subaerial weathering of recent basalt flows. *Geochim. Cosmochim. Acta*, **56,** 3711–3721.

Ziegler, K., Chadwick, O. A., Brzezinski, M. A., and Kelly, E. F. (2005). Natural variations of δ^{30}Si ratios during progressive basalt weathering, Hawaiian Islands. *Geochim. Cosmochim. Acta*, **69**, 4597–4610.

Ziegler, K., Young, E. D., Schauble, E. A., and Wasson, J. T. (2010). Metal–silicate silicon isotope fractionation in enstatite meteorites and constraints on Earth's core formation. *EPSL*, **295**, 487–496.

Chapter VI. Future Work and Appendices

1. Future Work

The research presented in this thesis has revealed a great deal about the development and evolution of silica coatings on Hawaiian lava flows and associated geochemical signatures, but leaves open potentially fruitful avenues of work for the future. Periodic visits to the 2011 Kamoamoa eruption site over the next several years would allow for direct documentation of surface evolution at a single site. Changes in coating thickness (or lack thereof) would constrain the relative contributions of acidity from syneruptional gases and regional plume gases at this site.

Partial-dissolution experiments presented in Chapter V reproduced amorphous silica alteration layers similar in appearance to natural Hawaiian silica coatings, but did not produce Fe-Ti oxide coating layers. The simple experimental setups employed in this study, in which basalt gravels remained submerged for the duration of the experiment, may not be sufficient to reproduce this feature of Hawaiian lava surfaces. Future experiments may employ more complex setups, including repeated cycles of wetting and drying to encourage precipitation of components mobilized during dissolution.

The surprising results of our silicon isotope study, in which a variety of Hawaiian silica coatings were found to be anomalously ^{30}Si-enriched relative to their basalt substrates, invite additional experimental, theoretical, and analytical studies to determine the range of conditions in which such fractionations should be observed. Experiments using acidic solutions of different compositions and different ionic strengths should be conducted to further explore the effects of Si speciation on Si isotope fractionation. Calculations of equilibrium Si isotope fractionations between various solid silicate phases and aqueous Si-bearing species would constrain the expected range of fractionation factors. Lastly, by scraping coatings off basalt samples for MC-ICP-MS analysis, I lost spatial context and the ability to identify isotopic heterogeneity within the coatings. Procedures for preparing and analyzing alteration minerals for δ^{30}Si analysis by SIMS should continue to be refined. For example, improved precision and spatial resolution might allow the distinguishing of residual and deposited silica material at the scale of coating thickness by δ^{30}Si alone.

2. Data and Sample Repositories

Raw datasets will be stored on external electronic media (flash drives or external hard drives) and kept in the possession of Prof. Rossman and myself. These raw datasets include:

- Cameca 7f and NanoSIMS oxygen isotope measurements of Ka'u Desert basalt, silica, and Fe-Ti oxides (Chapter II)
- SIMS silicon isotope measurements of silica coatings and associated standards (Chapter V)
- MC-ICP-MS silicon isotope measurements (raw counts) (Chapter V)
- ICP-OES fluid compositions (raw counts) (Chapter V)
- Infrared and Raman spectra of natural and synthetic amorphous silicas (x-y data) (Chapter IV)

Select representative spectra of amorphous silicas will be published on Prof. Rossman's mineral spectroscopy website. Other raw data will be made available to interested parties upon request.

Hawaiian basalt samples will be distributed as follows. Select representative samples of coated basalts will be kept with Prof. Rossman at Caltech. I will also take with me a representative suite of samples. Many sampling sites collected for this study (Ka'u Desert, Keanakakoi Crater, Mauna Ulu, Napau Crater, Mauna Loa) fell within the boundaries of Hawaii Volcanoes National Park. The research permits issued to me by the National Park Service require that samples, if not designated for a permanent collection, be returned to the park when research is complete. I will contact NPS officials to determine how to proceed with the disposal of these samples.